SOLAR ENERGY

THE JOURNAL OF SOLAR ENERGY SCIENCE AND ENGINEERING

VOLUME V 1961 1

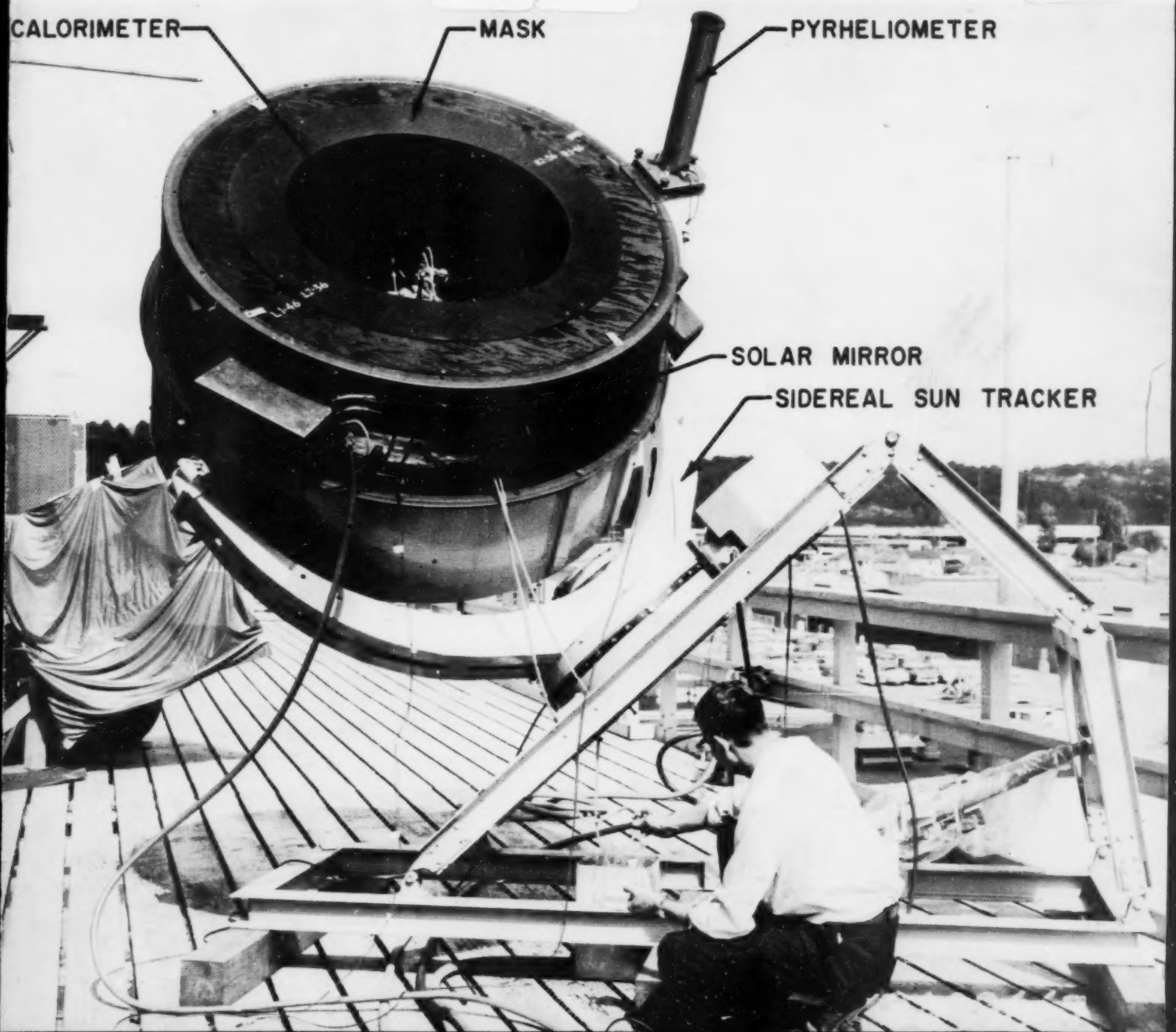

THE ASSOCIATION FOR APPLIED SOLAR ENERGY

ARIZONA STATE UNIVERSITY
TEMPE, ARIZONA

SOLAR ENERGY

THE JOURNAL OF SOLAR ENERGY SCIENCE AND ENGINEERING

VOLUME V JANUARY-MARCH, 1961 NUMBER 1

PUBLISHED QUARTERLY BY
THE ASSOCIATION FOR APPLIED SOLAR ENERGY
ARIZONA STATE UNIVERSITY, TEMPE, ARIZONA

EXECUTIVE COMMITTEE

H. WALMSLEY, *President*
Brig. Gen., USA Retired
JAN OOSTERMEYER, *Vice President*
Retired President, Shell Chemical Corporation
WALTER T. LUCKING, *Vice President*
President, Arizona Public Service Company
HENRY SARGENT, *Vice President*
President, American & Foreign Power Co., New York
WALTER BIMSON
Chairman of the Board, Valley National Bank
WELDON B. GIBSON
Vice President, Stanford Research Institute
SHERMAN HAZELTINE
Chairman of the Board, First Nat'l Bank of Arizona
JOHN M. JACOBS
Owner, John Jacobs Farms
JOHN MILLS
Chairman of the Board, Associated Federal Hotels
FRANK SNELL
Partner, Snell & Wilmer

EDITORIAL BOARD

A. B. Stafford, *Editor*
Sidney W. Wilcox, *Assoc. Editor*

ADVISORY AND CONTRIBUTING EDITORS

JOHN P. DECKER
U.S. Forest Service
FRANK E. EDLIN
E. I. DuPont de Nemours & Co.
MERRITT KASTENS
Union Carbide International
RUSSELL L. RIESE
Arizona State University

SUBSCRIPTIONS

The Journal is sent to AFASE members as one of their membership benefits. Non-members may purchase single copies of this issue at $3 per copy, or may obtain a subscription at $10 per year. Please send all communications and inquiries regarding back numbers, dues, etc., to AFASE at the above address. All correspondence regarding manuscripts should be addressed to A. B. Stafford, Arizona State University.

TABLE OF CONTENTS

Experimental Study of the Intermittent Vapour Absorption Refrigeration Cycle Employing the Refrigerant-Absorbent Systems of Ammonia-Water and Ammonia-Lithium Nitrate 1
J. C. V. Chinnappa

Current Developments in Pyrheliometric Techniques 19
A. J. Drummond

Lightweight Solar Concentrator Development 24
Roger Gillette, Howard E. Snyder, and Thomas Timar

A Direct-Current Integrator for Radiation Measurements 29
P. Schoffer and V. E. Suomi

Solar Abstracts 33

Cover Photo:

Calorimeter test setup, see Gillette, Snyder, and Timar article, page 26

VOL. 5 1961

SOLAR ENERGY

THE JOURNAL OF SOLAR ENERGY SCIENCE AND ENGINEERING

VOLUME V | APRIL-JUNE, 1961 | NUMBER 2

PUBLISHED QUARTERLY BY
THE ASSOCIATION FOR
APPLIED SOLAR ENERGY
ARIZONA STATE UNIVERSITY,
TEMPE, ARIZONA

EXECUTIVE COMMITTEE

H. WALMSLEY, *President*
Brig. Gen., USA Retired
JAN OOSTERMEYER, *Vice President*
Retired President, Shell Chemical Corporation
WALTER T. LUCKING, *Vice President*
President, Arizona Public Service Company
HENRY SARGENT, *Vice President*
President, American & Foreign Power Co., New York
WALTER BIMSON
Chairman of the Board, Valley National Bank
WELDON B. GIBSON
Vice President, Stanford Research Institute
SHERMAN HAZELTINE
Chairman of the Board, First Nat'l Bank of Arizona
JOHN M. JACOBS
Owner, John Jacobs Farms
JOHN MILLS
Chairman of the Board, Associated Federal Hotels
FRANK SNELL
Partner, Snell & Wilmer

EDITORIAL BOARD

A. B. Stafford, *Editor*
Sidney W. Wilcox, *Assoc. Editor*

ADVISORY AND CONTRIBUTING EDITORS

JOHN P. DECKER
U.S. Forest Service
FRANK E. EDLIN
E. I. DuPont de Nemours & Co.
MERRITT KASTENS
Union Carbide International
RUSSELL L. RIESE
Arizona State University

SUBSCRIPTIONS

The Journal is sent to AFASE members as one of their membership benefits. Nonmembers may purchase single copies of this issue at $3 per copy, or may obtain a subscription at $10 per year. Please send all communications and inquiries regarding back numbers, dues, etc., to AFASE at the above address. All correspondence regarding manuscripts should be addressed to A. B. Stafford, Arizona State University.

TABLE OF CONTENTS

A Solar Energy Pilot Plant for Northern Chile 37
Julio G. Hirschmann

Photochemical Systems for Solar Energy Conversion—Nitrosyl Chloride 44
Rudolph J. Marcus and Henry C. Wohlers

Some Considerations Relative to a Solar-Powered Savery Water Pump 58
James R. Jenness, Jr.

Theoretical Concentrations for Solar Furnaces 61
M. H. Cobble

Solar Abstracts 73

Cover Photo:

Salt stack at Lake Grassmere produced by solar evaporator at 42 degrees below the equator.
Dominion Salt Ltd., Marlborough, New Zealand

SOLAR ENERGY

THE JOURNAL OF SOLAR ENERGY SCIENCE AND ENGINEERING

VOLUME V JULY-SEPTEMBER NUMBER 3

PUBLISHED QUARTERLY BY
THE ASSOCIATION FOR
APPLIED SOLAR ENERGY
ARIZONA STATE UNIVERSITY,
TEMPE, ARIZONA

EXECUTIVE COMMITTEE

H. WALMSLEY, *President*
Brig. Gen., USA Retired
JAN OOSTERMEYER, *Vice President*
Retired President, Shell Chemical Corporation
WALTER T. LUCKING, *Vice President*
President, Arizona Public Service Company
HENRY SARGENT, *Vice President*
President, American & Foreign Power Co., New York
WALTER BIMSON
Chairman of the Board, Valley National Bank
WELDON B. GIBSON
Vice President, Stanford Research Institute
SHERMAN HAZELTINE
Chairman of the Board, First Nat'l Bank of Arizona
JOHN M. JACOBS
Owner, John Jacobs Farms
JOHN MILLS
Chairman of the Board, Associated Federal Hotels
FRANK SNELL
Partner, Snell & Wilmer

EDITORIAL BOARD

A. B. Stafford, *Editor*
Sidney W. Wilcox, *Assoc. Editor*

ADVISORY AND CONTRIBUTING EDITORS

JOHN P. DECKER
U.S. Forest Service
FRANK E. EDLIN
E. I. DuPont de Nemours & Co.
MERRITT KASTENS
Union Carbide International
RUSSELL L. RIESE
Arizona State University

SUBSCRIPTIONS

The Journal is sent to AFASE members as one of their membership benefits. Non-members may purchase single copies of this issue at $3 per copy, or may obtain a subscription at $10 per year. Please send all communications and inquiries regarding back numbers, dues, etc., to AFASE at the above address. All correspondence regarding manuscripts should be addressed to A. B. Stafford, Arizona State University.

TABLE OF CONTENTS

Photosynthesis of Hydrogen Peroxide by Crystal Phosphors 77
V. A. Garten and K. Eppinger

The Present State-Of-The-Art of Photovoltaic Solar Energy Conversion .. 83
M. Wolf

Solar Radiation at the Earth's Surface 95
H. E. Landsberg

Plastic-Replica Mirror Segments for a Solar Furnace 99
J. Bolin, C. J. Tenukest, and C. J. Milner

Atmospheric Radiation Near the Surface of the Ground: A Summary for Engineers 103
Raymond W. Bliss, Jr.

Cover Photo: Magnetogram of the sun made with the solar magnetograph in the 150-foot tower telescope of the Mount Wilson Observatory. The degree of brightening of the trace is proportional to magnetic-field intensity, while the magnetic polarity is shown by the slant to right or left of the short recording line.

VOL. 5 1961

SOLAR ENERGY

THE JOURNAL OF SOLAR ENERGY SCIENCE AND ENGINEERING

VOLUME V | OCTOBER-DECEMBER | NUMBER 4

PUBLISHED QUARTERLY BY THE ASSOCIATION FOR APPLIED SOLAR ENERGY ARIZONA STATE UNIVERSITY, TEMPE, ARIZONA

EXECUTIVE COMMITTEE

H. WALMSLEY, *President*
Brig. Gen., USA Retired
JAN OOSTERMEYER, *Vice President*
Retired President, Shell Chemical Corporation
WALTER T. LUCKING, *Vice President*
President, Arizona Public Service Company
HENRY SARGENT, *Vice President*
President, American & Foreign Power Co., New York
WALTER BIMSON
Chairman of the Board, Valley National Bank
WELDON B. GIBSON
Vice President, Stanford Research Institute
SHERMAN HAZELTINE
Chairman of the Board, First Nat'l Bank of Arizona
JOHN M. JACOBS
Owner, John Jacobs Farms
JOHN MILLS
Chairman of the Board, Associated Federal Hotels
FRANK SNELL
Partner, Snell & Wilmer

EDITORIAL BOARD

A. B. Stafford, *Editor*
Sidney W. Wilcox, *Assoc. Editor*

ADVISORY AND CONTRIBUTING EDITORS

JOHN P. DECKER
U.S. Forest Service
FRANK E. EDLIN
E. I. DuPont de Nemours & Co.
MERRITT KASTENS
Union Carbide International
RUSSELL L. RIESE
Arizona State University

SUBSCRIPTIONS

The Journal is sent to AFASE members as one of their membership benefits. Non-members may purchase single copies of this issue at $3 per copy, or may obtain a subscription at $10 per year. Please send all communications and inquiries regarding back numbers, dues, etc., to AFASE at the above address. All correspondence regarding manuscripts should be addressed to A. B. Stafford, Arizona State University.

TABLE OF CONTENTS

Flow Systems in the Solar Furnace and the Photolysis of Nitrosyl Chloride 121
Rudolph J. Marcus and Henry C. Wohlers

Equilibrium Temperatures of Ideal Spectrally Selective Surfaces 129
R. R. Hibbard

On Radiant Energy in High-Temperature Research 133
Tibor S. Laszlo

Notes on a Solar Collector with Unique Air Permeable Media 138
M. J. Shoemaker

Solar Abstracts 142

Cover Photo: Flow system in a solar furnace, see Marcus and Wohlers article page 121.

VOL.
5
1961

Experimental Study of the Intermittent Vapour Absorption Refrigeration Cycle Employing the Refrigerant-Absorbent Systems of Ammonia Water and Ammonia Lithium Nitrate

By J. C. V. Chinnappa

Department of Mechanical Engineering, University of Ceylon, Colombo

A systematic investigation is attempted in this paper of the intermittent vapour absorption refrigeration cycle employing the refrigerant-absorbent combinations of ammonia water and ammonia-lithium nitrate. A description is given of the actual cycle, and the differences between the actual and theoretical cycles are traced together with the effects of these differences on the values of the coefficient of performance and the effective cooling per lb of initial mass of the solution. A simplified approximate expression is given for the theoretical coefficient of performance of the ammonia-water system, as also expressions for the theoretical coefficient of performance of the ammonia-lithium nitrate system suitable for use with the corresponding data charts. Some comments are made regarding condenser performance and evaporator design.

INTRODUCTION

There has been in recent years a renewed interest in the intermittent vapour absorption refrigeration cycle. The main reason for this interest has been the fact that this cycle affords a ready application of solar energy which is itself an intermittent heat source. Trombe and Foex[1] have reported preliminary experiments with a pilot plant using the ammonia-water system. Williams, Chung, Lof, Fester, and Duffie[2,3] have described a comprehensive investigation which included a theoretical estimate of the performance of four different binary systems (methanol-silica gel, acetone-silica gel, ammonia-water, and Freon 21—tetra-ethylene glycol dimethyl ether), and an experimental study of two of these systems. In both the above investigations the heat source was solar radiation focussed onto the generator by means of a reflector.

Eisenstadt, Flanigan and Farber[14] have conducted tests on an experimental intermittent refrigerator employing the NH_3-H_2O system with solution concentrations varying from 0.4 to 0.7 and with maximum generator temperatures from 140 to 180 F. These tests have demonstrated the feasibility of the use of this cycle for air-conditioning.

Another recent investigation, which however was not a solar energy application, has been reported by Andrews.[4] He described a successful attempt to develop an absorption refrigerator using the ammonia-calcium chloride system.

Early work on this cycle took place 20 to 30 years ago. Portable refrigerators working on this cycle were marketed in the U.S.A. employing the ammonia-water combination.[5] Refrigerators were also built using solid absorbents.[6] Hulse reported the design of an adsorption system using sulphur dioxide and silica-gel employed in freight-car refrigeration.[7]

When this investigation was commenced in March, 1957, there was not available in the published work to the author's knowledge any detailed information describing the intermittent absorption cycle as it occurs in practice and giving values for the coefficient of performance (COP) with heat source temperatures up to 250 F; temperatures which could normally be expected with conventional designs of the different types of solar heat collector. This investigation was therefore intended to obtain a comparison between the theoretical and actual performance of a refrigerator working on the intermittent vapour absorption cycle with these heat source temperatures.

An artificial heat source was employed to obtain these temperatures because the experiments were conducted in London where solar energy is rarely available in winter, while its customary fickleness and varying character during the remaining months would make the achievement of controlled conditions a matter of chance.

Two binary systems were chosen for systematic

investigation: ammonia water and ammonia-lithium nitrate. In the case of the NH_3-H_2O system, tables[8] and a chart[9] are available giving the values of the required thermodynamic properties, and so the problem resolved itself into an attempt to study and describe the actual cycle, and to evaluate the theoretical and actual COP. In the case of the NH_3-$LiNO_3$ system however, the data concerning the thermodynamic properties[10,11] were not comprehensive enough to include the lower part of the range of the heat source temperatures under investigation. The required properties were therefore first evaluated. Thereafter the actual cycle was studied, and values for the theoretical and actual COP were obtained.

Since NH_3 is absorbed by $LiNO_3$ to form a clear, syrupy liquid, it was possible to use the same apparatus to study both systems.

The author is not aware of any other published work on the use of the NH_3-$LiNO_3$ combination in an intermittent vapour absorption refrigeration cycle. With regard to the NH_3-H_2O system, this investigation has attempted a rather more detailed examination and analysis than that reported in similar recent investigations. It has also been possible to gain some insights into the performance of the condenser (cooled by stagnant cooling water) and the evaporator of a refrigerator working on this cycle. The results obtained and presented herein therefore would appear to be of some use as design data particularly in further research connected with solar refrigeration. These experiments, preliminary in nature, were in fact conducted by the author in order that experimental results under controlled conditions would be available for comparison with the performance of an intermittent refrigerator operated by solar energy. Such an investigation is currently under way.

NOMENCLATURE

c	Specific heat of NH_3-$LiNO_3$ solutions
c_L	Specific heat of liquid ammonia
c_m	Mean specific heat of NH_3-$LiNO_3$ solutions over a temperature range
h	Local coefficient of heat transfer
H	Enthalpy of solution
H_v	Enthalpy of vapour
H'	Enthalpy of liquid ammonia (distillate)
k_1, k_2	Constants in Dühring equation
k', k''	Constants in equation
L	Latent heat of ammonia
L_d	Differential heat of evaporation
P	Pressure
Q	Heat supplied or transferred
Q_e	Effective cooling
Q_e	Heat absorbed by the oil bath and generator-absorber vessel
Q_L	Heat lost from oil bath
Q_s	Heat supplied to solution during regeneration
t	Temperature of solution
t_b	Temperature of oil bath
t'	Temperature of distillate or pure ammonia
T	Absolute temperature
v	Specific volume of superheated vapour of ammonia
w	Balance weight at end of balance arm
w (with suffix)	Equivalent weight of part of refrigerator
W	Weight of solution
W_e	Water equivalent of either generator heating arrangement (oil bath, etc.), or condenser-evaporator depending on context
W'	Weight of distillate or absorbent
X_A	Concentration of solution, weight of absorbent per unit weight of solution
X_R	Concentration of solution, weight of refrigerant per unit weight of solution
x_R	Concentration of vapour, weight of refrigerant per unit weight of vapour
δ	Signifies small change, e.g., δt, δW
Δ	Signifies finite change, e.g., Δt_b
θ_m	Mean temperature difference between oil bath and atmosphere
τ	Time

Numerical suffixes, unless otherwise specified in the context, refer to state points in the refrigeration cycles.

THE THEORETICAL CYCLE

Description

Two forms of the theoretical cycle are proposed as suitable for comparison with the actual cycles obtained in the present investigation. These two cycles are shown plotted for the NH_3-H_2O system with initial concentration (X_{R1}) = 0.48, and maximum generator (or solution) temperature (t_4) = 255 F in Fig. 2. The cycles for the solution occur in the middle of the chart, while the temperatures of the refrigerant (or distillate) corresponding to the various points in the cycles are shown on the right of the chart for X_R = 1.00. Similar cycles can be plotted for the NH_3-$LiNO_3$ system on the corresponding P-t-X chart.

The first form of the theoretical cycle may be designated "the theoretical cycle with absorption at constant pressure", or more briefly "the constant pressure absorption cycle", and it is represented in Fig. 2 by 2-3-4-5-2.

The second form of the theoretical cycle may be designated "the theoretical cycle with absorption at constant temperature", or more briefly "constant temperature absorption cycle", and it is represented in Fig. 2 by 1-3-4-6-1.

In the constant pressure absorption cycle regenera-

VOL. 5 1961

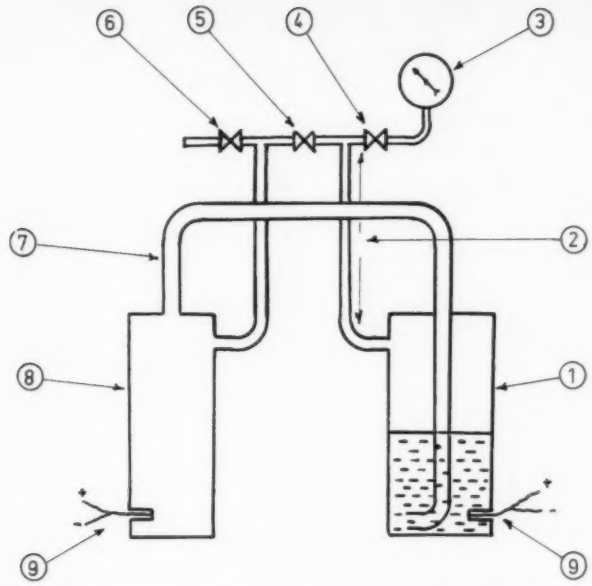

FIG. 1—Schematic Diagram of Experimental Refrigerator.
1. Generator-Absorber
2. Rectifying Section of distillation pipe:
   not insulated for NH_3-H_2O tests
   insulated for NH_3-$LiNO_3$ tests
3. Pressure Gauge
4. Gauge valve A
5. Valve B: open during regeneration
   closed during refrigeration
6. Valve C for charging
7. Absorption pipe
8. Condenser-evaporator
9. Thermocouples.

tion consists of two processes, 2-3 and 3-4. Likewise refrigeration also consists of two processes: 4-5 and 5-2. During process 4-5 adiabatic cooling of the distillate takes place down to the temperature of heat abstraction (32 F in Fig. 2). Effective cooling takes place during process 5-2.

In the constant temperature absorption cycle regeneration consists of the two processes 1-3 and 3-4. In the refrigeration phase, during adiabatic cooling process 4-6, the solution is cooled, usually by immersion in a water-bath, to a temperature (t_6) which is equal to the initial temperature (t_1). Effective cooling takes place during process 6-1.

The numbers on the right represent the corresponding state points of the distillate. There is no distillate in the condenser-evaporator during process 2-3 or 1-3.

The constant pressure absorption cycle (2-3-4-5-2) is the more efficient of the two cycles due to the fact that less refrigerant is used up during the process 4-5 than during the process 4-6, leaving more refrigerant to produce effective cooling. However, the constant pressure absorption cycle is more difficult to realise in practice. The difficulty mainly arises in the control of the rate of cooling of the generator-absorber during the refrigeration stage, for it is necessary to regulate during the process 4-5, the cooling rate of the generator-absorber so that the distillate will be cooled to t_5' (the temperature at which heat abstraction should take place) and no further. Thereafter, during the process 5-2, the cooling rate needs to be so adjusted that absorption at constant pressure is maintained.

In the present series of tests no attempt was made to realise constant pressure absorption. Instead, just prior to the commencement of the refrigeration stage the generator-absorber was immersed in a cooling tank. The temperature of the solution fell quite rapidly to 80 F, and remained approximately at that temperature during the rest of the refrigeration stage. Therefore, of the two cycles proposed for comparison with the actual cycle, the constant temperature cycle is more realistic.

Coefficient of Performance

Where enthalpy of vapour, solution, and refrigerant may be obtained from appropriate tables and charts, Williams, et al,[2] have stated the following expression for the COP of the constant pressure absorption cycle:

$$\text{COP} = Q_c/Q_s = \frac{W_5' \times L_5}{W_4 H_4 - W_2 H_2 + \int_{W_4}^{W_2} H_v \, dW} \qquad [1]$$

where

Q_c = effective cooling
Q_s = heat to solution during regeneration
W_5' = weight of refrigerant (distillate) at the commencement of process 5-2
L_5 = latent heat of refrigerant ($L_5 = L_2$)
W = weight of solution, suffix indicating point in the cycle
H = enthalpy of solution, suffix indicating point in the cycle
dW = differential mass of vapour boiling out of solution
H_v = enthalpy of the vapour at the temperature at which dW is evaporated

The mass of distillate (or refrigerant) at point 5 may be obtained from the following expression, also stated by Williams, et al.,[2] which gives the ratio of the masses of distillate at the end of and at the commencement of process 4–5:

$$\frac{W_5'}{W_4'} = e^{\frac{(H_5' - H_4')}{L_m}} \qquad [2]$$

where

L_m = mean latent heat of the refrigerant during the process 4-5
H' = enthalpy of the liquid refrigerant, suffix indicating the point in the cycle.

The vapour boiling off from the solution contains

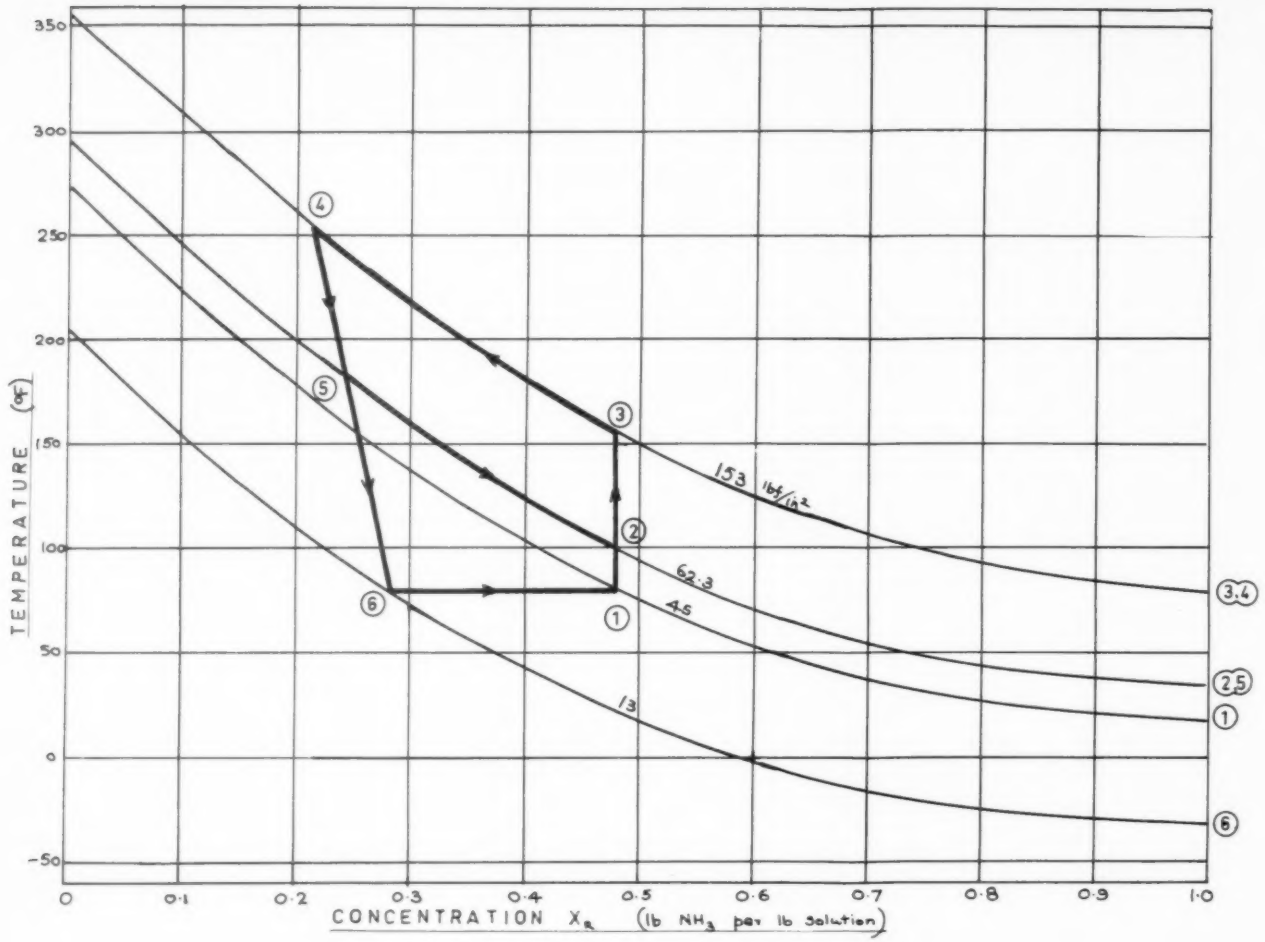

FIG. 2—Theoretical Cycles for NH_3-H_2O System.

an increasing proportion of water vapour as the temperature of distillation rises. Since in the theoretical cycle it is assumed that the distillate is pure NH_3, account must be taken of the rectification of the vapour boiling off. Applying mass balances to the rectifier, it may demonstrated that:

$$dW = \left(\frac{1 - X_R}{x_R - X_R}\right) dW' \qquad [2a]$$

where

dW = mass of vapour leaving solution and entering rectifier at temperature t,

dW' = mass of pure refrigerant vapour leaving rectifier, and

X_R, x_R = refrigerant concentration of solution and vapour at temperature t.

Since the mass of pure refrigerant W' (or dW') is related directly to solution mass and concentration it is now possible to evaluate Eq. [1] for given conditions of t_3, X_{R3}, t_4, and P_4 using Eqs. [2] and [2a], and also the P-t-X chart giving values of enthalpy.

Eq. [1] cannot be applied where values of enthalpy for vapour and solution are not directly available, as is the case for the NH_3-$LiNO_3$ system for which Gensch[10] has presented the data in different form. In addition to the P-t-X chart, Gensch has compiled a chart giving the differential heat of evaporation of NH_3 from NH_3-$LiNO_3$ solutions plotted against boiling point for various concentrations and pressures: and also obtained a curve for the variation of the specific heat of NH_3-$LiNO_3$ solutions with concentration. The same form has been used in this paper for the presentation of the NH_3-$LiNO_3$ data to facilitate comparison with Gensch's charts. The expression for Q_s, the heat supplied to the solution during regeneration, has therefore been modified to make it possible to use the data as presented in the charts.

In its modified form, for p equal changes of δW in the weight of solution during actual distillation (process 3-4) such that $\delta W_1 = \delta W_2 = \cdots = \delta W_n = \cdots = \delta W_p (= \delta W)$,

VOL. 5 1961

$$Q_s = W_3\, c_3(t_3 - t_2) + \left(W_4 + \frac{\delta W}{2}\right) \sum_{n=1}^{n=p} c_{m_n}\, \delta t_n + \sum_{n=1}^{n=p} Ld_{m_n}\, \delta W_n + \delta W \sum_{r=1}^{r=(p-1)} \sum_{n=1}^{n=r} c_{m_n}\, \delta t_n \quad [3]$$

where

W = weight of solution
c = specific heat of solution
t = temperature of solution
δt_n = temperature rise of the solution during which the incremental change in solution weight is δW_n
c_{m_n} = mean specific heat of the solution during the change in concentration due to change in solution weight of δW_n
Ld_m = mean differential heat of evaporation.

The expression for the COP of the NH_3-$LiNO_3$ constant pressure absorption cycle therefore becomes

$$\text{COP} = \frac{W_5' \times L_5}{W_3\, c_3(t_3 - t_2) + \left(W_4 + \frac{\delta W}{2}\right) \sum_{n=1}^{n=p} c_{m_n}\, \delta t_n + \sum_{n=1}^{n=p} Ld_{m_n}\, \delta W_n + \delta W \sum_{r=1}^{r=(p-1)} \sum_{n=1}^{n=r} c_{m_n}\, \delta t_n} \quad [4]$$

The derivation of Eq. [3] and an example of the application of a similar equation is given in Appendix I.

The above expressions for the COP have to be modified slightly for the constant temperature absorption cycle because the refrigeration phase differs from the refrigeration phase in the constant pressure absorption cycle. The expression for the effective cooling becomes

$$Q_c = W_6' \times L_m \quad [5]$$

where

L_m = mean latent heat of the refrigerant during the process 6-1
W_6' = weight of refrigerant at point 6.

Hence for the NH_3-H_2O constant temperature cycle

$$\text{COP} = \frac{W_6' \times L_m}{W_4 H_4 - W_1 H_1 + \int_{W_4}^{W_1} H_v\, dW} \quad [6]$$

For the NH_3-$LiNO_3$ constant temperature cycle

$$\text{COP} = \frac{W_6' \times L_m}{W_3\, c_3(t_3 - t_1) + \left(W_4 + \frac{\delta W}{2}\right) \sum_{n=1}^{n=p} c_{m_n}\, \delta t_n + \sum_{n=1}^{n=p} Ld_{m_n}\, \delta W_n + \delta W \sum_{r=1}^{r=(p-1)} \sum_{n=1}^{n=r} c_{m_n}\, \delta t_n} \quad [7]$$

Eq. [1] has been evaluated for NH_3-H_2O for two values of the initial concentration $X_{R2} = 0.48$ and 0.55. For the solution with $X_{R2} = 0.48$, the initial temperature of the solution, $t_2 = 98$ *F*, while for the solution with $X_{R2} = 0.55$, $t_2 = 80$ F. For both solutions the temperature of heat abstraction, $t_5' = t_2' = 32$ F, and $t_3' = 80$ F. Eq. [6] has been evaluated for two values of $X_{R1} = 0.48$ and 0.55, and for $t_1 = 80$ F, and $t_2' = 80$ F. The values of the COP obtained from both equations have been plotted against maximum generator (or solution) temperature t_4 in Fig. 3.

Similarly for NH_3-$LiNO_3$ Eq. [4] has been evaluated for two values of initial concentration (X_{R2}) = 0.455 and 0.513. For the solution with $X_{R2} = 0.455$, $t_2 = 116$ F, while for the solution with $X_{R2} = 0.513$, $t_2 =$

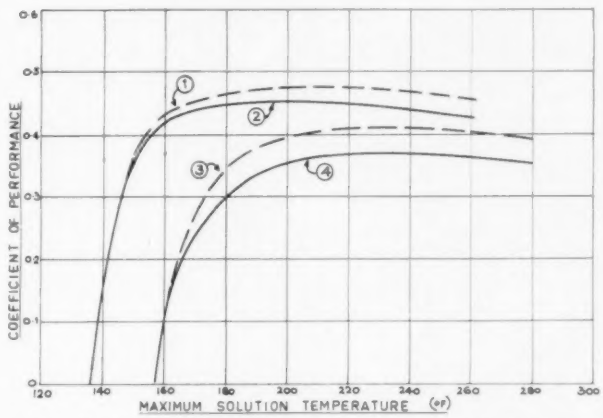

FIG. 3—Variation of the Theoretical Coefficient of Performance with the Maximum Solution Temperature for the NH_3-H_2O System.
constant pressure and constant temperature absorption
1. $X_{R2} = 0.55$, $t_2 = 80°F = t_3'$
2. $X_{R1} = 0.55$, $t_1 = 80°F = t_3'$
3. $X_{R2} = 0.48$, $t_2 = 98°F$, $t_3' = 80°F$.
4. $X_{R1} = 0.48$, $t_2 = 80°F = t_3'$

Suffixes refer to points in cycles in Fig 2.

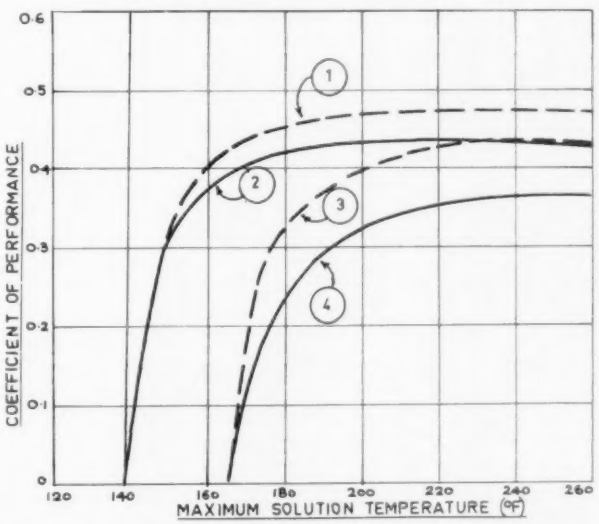

FIG. 4—Variation of the Theoretical Coefficient of Performance with Maximum Solution Temperature for the NH_3-$LiNO_3$ System.
constant pressure and constant temperature absorption
1. $X_{R2} = 0.513$, $t_2 = 89°F$, $t_3' = 80°F$.
2. $X_{R1} = 0.513$, $t_1 = 80°F = t_3'$
3. $X_{R2} = 0.455$, $t_2 = 116°F$, $t_3' = 80°F$.
4. $X_{R1} = 0.455$, $t_1 = 80°F = t_3'$

Suffixes refer to points in the theoretical cycles in Fig 15.

89 F. For both solutions $t_5' = t_2' = 32$ F, $t_3' = 80$ F In the same way Eq. [7] has been evaluated for values of $X_{R1} = 0.455$ and $X_{R1} = 0.513$, $t_1 = 80$ F, $t_3' = 80$ F. The values of the COP so obtained from both these equations have been plotted against maximum solution temperature, t_4 in Fig. 4.

Simplified Expressions for the Theoretical Coefficient of Performance for the NH_3-H_2O System

The evaluation of Eqs. [1], [4], [6], and [7] requires tedious computation, and so an attempt was made to simplify these equations. Some success was forthcoming with Eq. [1] and [4] relating to the NH_3-H_2O system.

For the constant pressure absorption cycle, and for given values of X_{R2}, t_2, t_3', and t_4, the equations given below enable the theoretical COP to be calculated rapidly with the assistance of the P-t-X chart giving enthalpy values:

$$W_4 = \frac{(1 - X_{R2})}{(1 - X_{R4})} \qquad [8]$$

$$\text{Theor. COP} = \frac{485(1 - W_4)}{W_4 H_4 - H_2 - 691.5(1 - W_4)} \qquad [9]$$

For the constant temperature absorption cycle, for given values of X_{R1}, t_1 $(= t_3')$, and t_4, the COP can be obtained from similar equations:

$$W_4 = \frac{(1 - X_{R1})}{(1 - X_{R4})} \qquad [10]$$

$$\text{Theor. COP} = \frac{461.5(1 - W_4)}{W_4 H_4 - H_1 + 691.5(1 - W_4)} \qquad [11]$$

For the range of initial concentrations from 0.40 to 0.55, for values of t_1, t_2, and t_3', between 80 and 100 F, and for values of t_4 up to 260 F, the values for the COP obtained from the simplified equations differ from values obtained from Eqs. [1] and [4] by about 2 per cent or less; the best agreement being obtained in the middle of the range.

Effect of Variation in Initial Concentration

As X_{R1} increases the COP increases (see Figs. 3 and 4). This is due to the fact that for a constant value for the temperature of condensation (t_3') the temperature of the solution at which distillation commences (t_5) becomes less as X_{R1} increases. This results in a greater weight of distillate for the same maximum solution temperature, t_4, with the consequent production of more cooling.

The increase in COP is maintained with increasing X_{R1} till X_{R1} reaches the optimum value at which for a given initial temperature, t_1, the vapour pressure of the solution, P_1, is equal to the vapour pressure of the liquid refrigerant at the maximum value of the temperature at which heat is abstracted. For example, in the NH_3-H_2O system, when the maximum temperature at which heat is abstracted $t_1' = 32$ F, and the initial temperature of the solution is 80 F, the value of the initial concentration corresponds to values of the initial temperature and pressure of 80 F, and 62.3 psi respectively, and is approximately equal to 0.55.

This consideration is critical in determining the value of the initial concentration for the different possible applications of the intermittent vapour absorption cycle, e.g., food preservation, air conditioning, etc.

EXPERIMENTAL PROCEDURE

The main details of the experimental refrigerator are shown diagrammatically in Fig. 1. The actual refrigerator is shown in Fig. 5 where two more details are visible: the knife-edge in the middle of the absorption pipe, and the balance arm.

Fig. 6 shows the rest of the experimental rig. The tank farthest away contained heating oil and was provided with two immersion heaters, 4 kw and 2 kw. It was possible to measure the power supplied to these

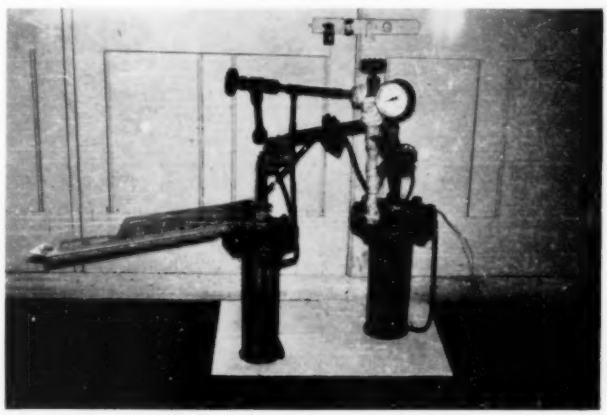

FIG. 5—Experimental Refrigerator.

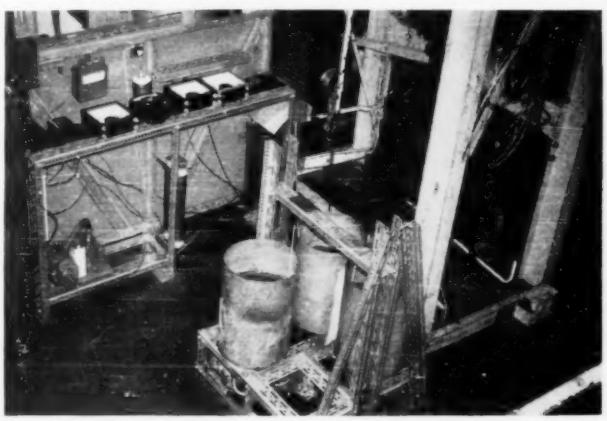

FIG. 6—Test Rig, Showing Heating Tank (farthest away), Cooling Tanks and Instrument Shelf.

VOL. 5 1961

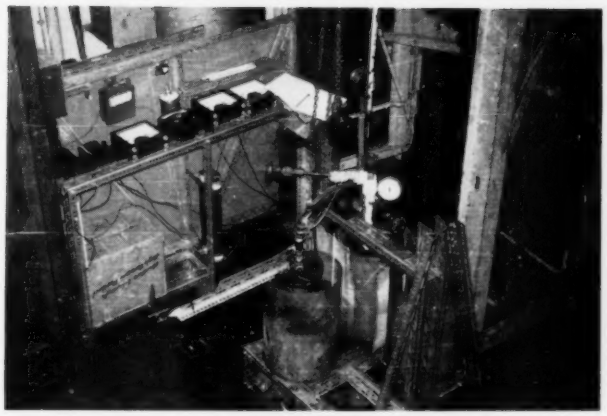

FIG. 7—Regeneration Stage in Progress; NH_3-$LiNO_3$ Tests.

heaters, and also to vary the heating rate. The remaining two tanks were cooling tanks containing water.

Fig. 7 shows the regeneration phase of a test with NH_3-$LiNO_3$ in progress. The experimental refrigerator was supported on a knife-edge with the generator-absorber in the heating tank and the condenser-evaporator in a cooling tank. The knife-edge rested on a hardened pad fixed to the crossbeam of the stand. At the commencement of regeneration valve B (Fig. 1) was opened and the balance arm (Fig. 7) was made roughly horizontal by adding (or taking away) weights. As heating progressed vapour was conveyed through the narrow distillation pipe connecting the two vessels, and as distillation took place the refrigerator swung on the knife-edge, the movement of the pointer at the end of the balance arm indicating the weight of the distillate. The oil bath was used for maximum solution temperatures up to 220 F: for higher temperatures the generator-absorber was heated by a gas flame from a bunsen burner.

Fig. 8 shows refrigeration taking place with frost forming round the condenser-evaporator. During this part of the cycle valve B (Fig. 1) was closed, and vapour passed from the condenser-evaporator to the generator-absorber through the absorption pipe and bubbled through the solution in the generator-absorber. The generator-absorber was cooled by immersion in a tank containing water. During this stage the movement of the pointer indicated the weight of absorbent.

The use of this rig enabled the following observations to be made during regeneration: temperature of oil-bath (t_b), power input to immersion heaters, temperature of solution inside the generator-absorber (t), temperature of distillate (t'), temperature of condenser-evaporator cooling water, pressure in refrigerator, and mass of distillate.

During refrigeration it was possible to observe the temperature of the distillate, the temperature of the solution in the generator-absorber, the temperature of the generator-absorber bath, the pressure in the refrigerator, and the mass of absorbate.

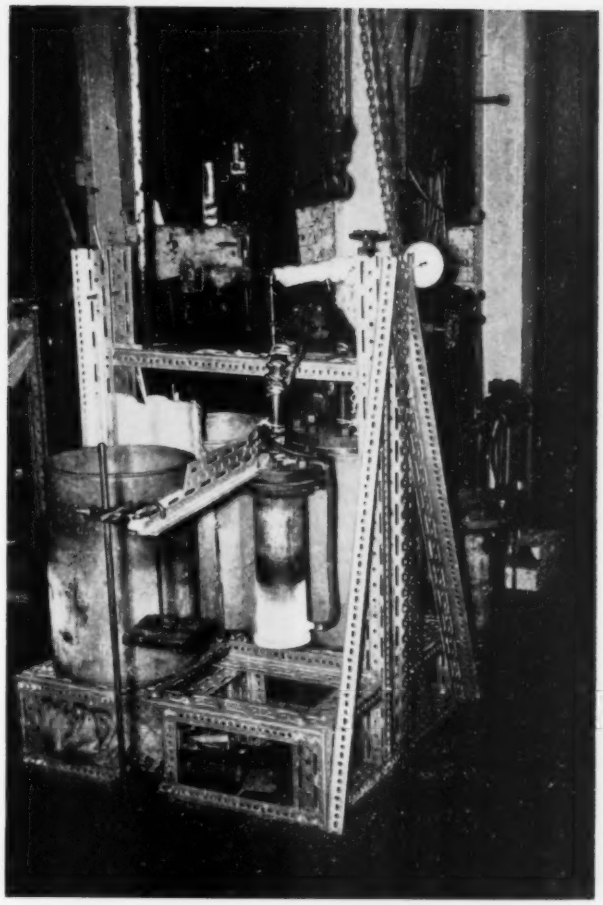

FIG 8—Refrigeration Stage in Progress.

The temperature of the solution and the temperature of the distillate during the cycle were measured by means of thermocouples the hot junctions of which were at the end of tubes inserted into and in good thermal contact with the solution and the distillate. The temperature of the oil-bath and the cooling water tanks were measured directly by thermometers, the readings being taken after stirring.

EXPERIMENTAL RESULTS: AMMONIA-WATER SYSTEM

The Actual Cycle

Six tests were performed ($X_{R1} = 0.48$) with maximum solution temperatures of 180, 200, 220, 237, 255, and 274 F. The temperature of the condenser cooling water during regeneration and the temperature of the absorber cooling water during refrigeration were maintained at about 80 F. Fig. 9 shows the data for the test with maximum solution temperature 255 F: the trends of the various curves are typical of the other

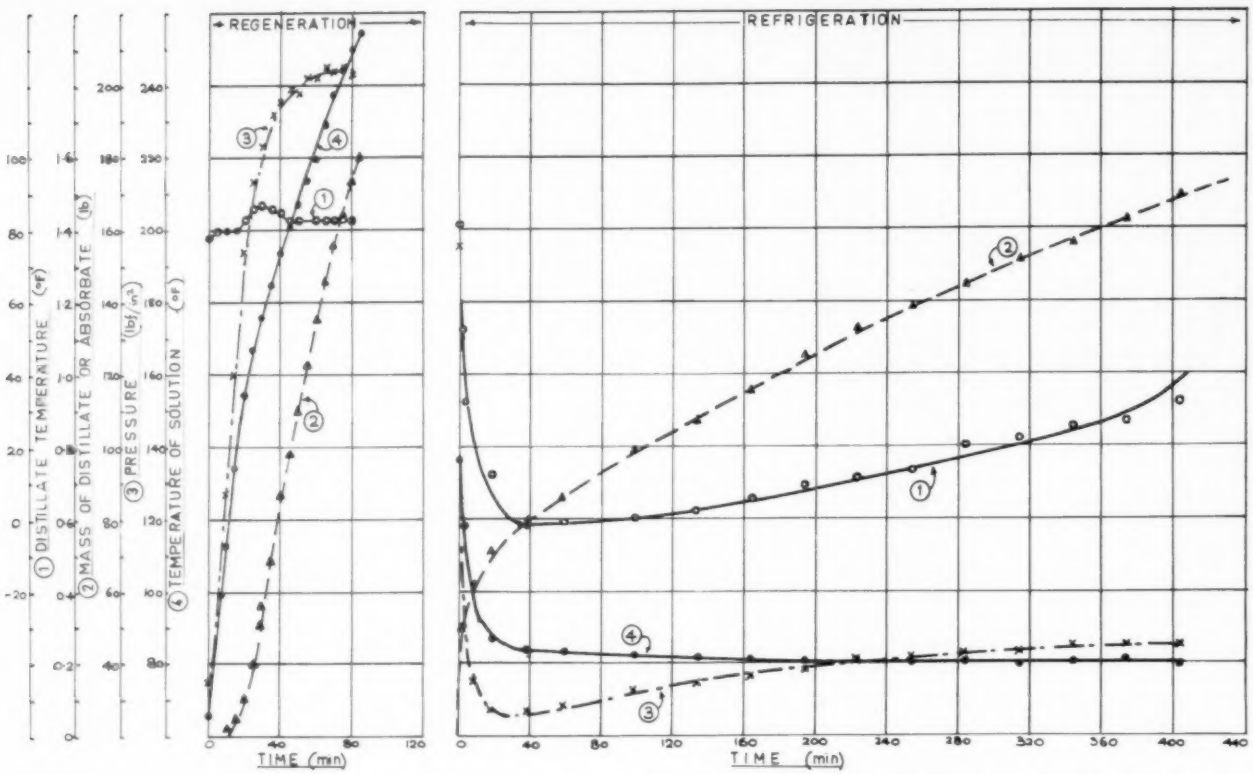

FIG. 9—Data from Test Number 5 (max. solution temp., t_s = 255 °F) for NH_3-H_2O System. Initial Mass of Solution = 5.39 lb.

TABLE 1.—Results of Tests for NH_3-H_2O System for X_{R1} = 0.48, and Comparison with Theoretical Values. Initial Weight of Solution 5.39 lb.

Test No.	Regeneration							Refrigeration					Actual		Theoretical			
										(11) Minimum temp. of distillate					Constant temp. absorption		Constant press. absorption	
(1)	(2) Max. sol. temp. t_s °F	(3) Max. press. psi	(4) Final sol. conc X_{RS}	(5) Temp. of condenser C.W. °F	(6) Wt. of dist. lb	(7) Water in condenser as percentage of distillate	(8) Heat to solution Q Btu	(9) Mean temp. of absorber C.W. °F	(10) Weight of absorbate lb	Observed with vessel °F	Calculated no vessel °F	(12) Total eff. cooling below 32°F Btu	(13) Effective cooling per lb of solution Btu	(14) COP	(15) Effective cooling per lb of solution Btu	(16) COP	(17) Effective cooling per lb of solution Btu	(18) COP
1	180	170	0.427	78.7	0.50	0	935	73	0.50	13.5	11.5	240	44.5	0.287	60	0.301	62	0.348
2	200	183	0.385	78.6–79.5	0.85	0	1257	75	0.85	9	3	404	75	0.322	94.3	0.356	98	0.397
3	220	184	0.335	80.8–82.2	1.23	2	1598	79	1.18	3.5	0.5	563	104.5	0.352	121.8	0.369	126	0.403
4	237	190	0.296	77.4–81.4	1.46	1.4	1834	78.5	1.42	−4.5	−8	686	127	0.374	137	0.369	147	0.407
5	255	203	0.270	80.5–84.6	1.605	2.6	2017	80	1.523	−1	−7.5	709	131.5	0.352	155.5	0.368	165	0.404
6	274	201	0.223	79.5–82.4	1.81	2.2	2261	81	1.73	−6	−14	804	149	0.356	171.5	0.360	181	0.397

tests. Relevant data and results from all the tests are presented in Table 1.

The actual cycle, shown plotted in Fig. 10 as 1-7-8-9-1 together with the corresponding theoretical cycle, differed from the corresponding theoretical cycle in a few notable ways.

First, the actual pressure at which distillation took place was greater than the theoretical pressure. This difference between the actual and theoretical pressures corresponds to the temperature difference between the condensing vapour and the cooling water. This temperature difference is necessary in order that the heat

VOL. 5 1961

of condensation can be transferred to the cooling water. As a result the actual value of the final generator concentration (X_{R8}) was greater than the theoretical value (X_{R4}) for the same value of t_8 (or t_4), i.e., the actual weight of distillate was less than the theoretical quantity. It follows that the greater the rate of heating the less the actual weight of distillate obtained. Keith[5] states that the rate of heating of the generator in the "Icyball" refrigerator should not exceed a certain value. The rate of heating of the solution in relation to the area of condensing surface provided therefore acquires considerable importance, and is discussed more fully in a subsequent section.

Second, at the end of adiabatic cooling (process 8-9) the vapour pressure of the distillate was 5-7 psi greater than the vapour pressure of the absorbing solution. One of the reasons for this difference was probably poor mixing in the absorber. Included in this pressure difference was the pressure head, about 10–15 in. water gauge, required to cause the NH_3 vapour to bubble through the solution. A consequence of this difference in pressure was that the actual minimum temperature of the distillate was greater than the theoretical value. The difference between the vapour pressures of the distillate and the solution gradually decreased during the subsequent process 9-1.

Third, it was not found possible to prevent a small quantity of water from being transferred during regeneration to the condenser-evaporator. The rectifying section of the distillation pipe consisted of a vertical length of bare pipe. The heating rate was adjusted so that the temperature at the top of the pipe was about 120 F. The percentages of water in the distillate shown in column 7 of Table 1 indicated that either this simple form of rectifier did not function efficiently or water was carried over due to entrainment, since the narrow distillation pipe had no baffles.

The presence of water in the distillate produces three effects. The first effect is to cause a reduction in the effective cooling. The water in the distillate has to be cooled during adiabatic cooling from the temperature of condensation (t_8') to the highest temperature at which heat abstraction takes place, which was 32 F in these tests, and NH_3 has to be evaporated to achieve this. In the present series of tests however this particular effect was negligibly small, and the more significant way in which effective cooling is reduced occurs towards the end of process 9-1. Distillate containing

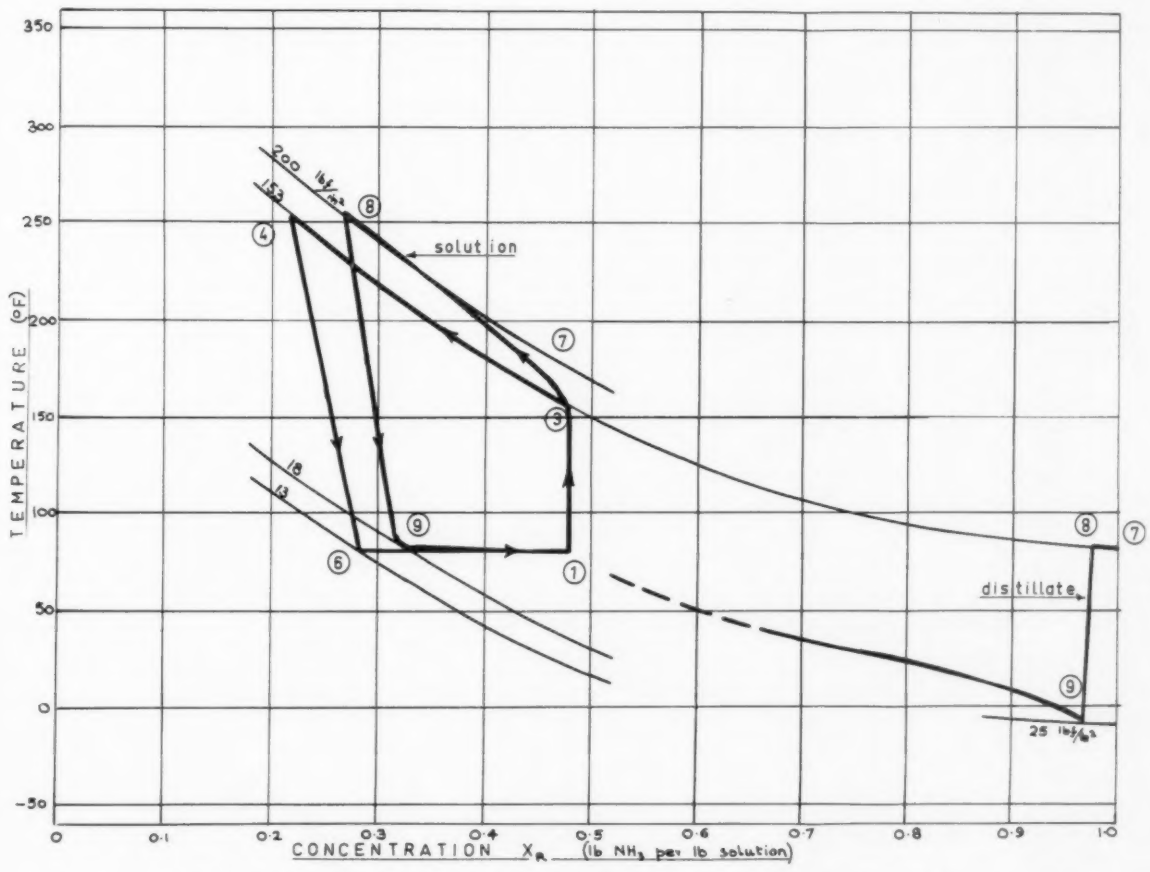

FIG. 10—Actual Cycle for NH_3-H_2O System Compared with the Theoretical Cycle.

water is in reality a solution of high concentration in refrigerant. During process 9-1 (see Fig. 10), the refrigerant concentration of the distillate decreases while the temperature of the distillate increases. These changes continue till the temperature of the distillate exceeds the highest temperature at which refrigeration is required to take place. Further evaporation of refrigerant does not provide 'useful' refrigeration. In the present series of tests the concentration of the distillate at which effective cooling below 32 F ceased was approximately 0.74, corresponding to a pressure of about 44 psi, the vapour pressure of the absorbing solution at 80 F. Hence water in the distillate prevented effective cooling below 32 F being obtained from about 3 times its own weight of NH_3.

A second consequence of water in the distillate is that at the cessation of absorption the cycle is not completed, and provision must be made to purge the residual solution in the condenser-evaporator back to the generator-absorber in order to return the solution to its original concentration. In these tests this was done by tilting the refrigerator.

The third consequence of water in the distillate is that the minimum temperature of the distillate (t_9') is raised. The states of the distillate corresponding to the solution states in the actual cycle are shown on the right in Fig. 10. There is no distillate in the condenser-evaporator during the process 1-7.

Actual Coefficient of Performance

In order to determine the actual COP two quantities need to be calculated from the data collected: Q_s, the heat supplied to the solution, and Q_e, the effective cooling produced.

The heat supplied to the solution for t_5 up to 220 F was obtained by two methods. The first or 'direct method' was the evaluation of the expression

$$Q_s = W_8H_3 - W_1H_1 + \sum_{W_8}^{W_1} H_v\delta W \qquad [12]$$

The values of W_8 and W_1 were obtained from the experimental observations, while values for H_1, H_8, and H_v were obtained from the Kohloss and Scott chart.[9] The third term on the right hand side was evaluated by a graphical method. The first step in this method was the drawing of a graph in which the pressure and the temperature of the solution were plotted against the mass of distillate. Thereafter the mean temperature and pressure for each increment of 0.2 lb (or less) in the mass of the distillate was read off from the plot. The values of H_v corresponding to these mean temperatures and pressures were taken from the Kohloss and Scott chart, and the required summation obtained.

This method of obtaining Q_s was approximate due to the action of the rectifying section. Though the top of this air-cooled pipe was maintained at a temperature (i.e., at about 120 F) which should have made it possible to effect virtually complete rectification, about 2 per cent of the distillate was water. It was not certain whether this water was carried over due to entrainment or whether the rectifier did not function efficiently. It was not possible to estimate the reflux with any degree of exactitude and take it into account in evaluating the third term in Eq. [12], where dW is strictly the mass of vapour leaving the solution and not the mass of distillate.

TABLE 2.—Comparison of the Values for Heat Supplied to Solution by Direct and Indirect Methods (NH_3-H_2O Tests)

Test No.	Max. Sol. Temp. °F	Heat Supplied to Solution [Btu]	
		'Indirect method'	'Direct method'
1	180	1026	1032
2	200	1296	1354
3	220	1703	1690

An approximate estimation for test 5 indicates that the real value of Q_s is about 4 per cent greater than as calculated from Eq. [12], and the actual COP (column 14, Table 1) about one per cent less. This error will be less at lower maximum solution temperatures.

A second method, termed the 'indirect method,' was also employed to estimate Q_s. The heat capacity of the generator tank and contents and the heat loss from the generator tank for various temperature differences between the oil and atmosphere were determined in a separate series of tests. During regeneration the energy input to the immersion heaters in the generator tank were measured, and from these quantities Q_s was obtained by difference.

The values of Q_s obtained by the two methods is shown in Table 2. The agreement is rather closer than it should be as Q_s calculated by the 'direct method' may be expected to be slightly less than that obtained by the 'indirect method'. The agreement however is good enough to create confidence in the 'indirect method' which was later used to check the data of the NH_3-$LiNO_3$ charts.

In order to calculate the effective cooling produced it was first necessary to determine the weight of refrigerant evaporated during adiabatic cooling. This was done by the trial-and-error solution of an equation similar to Eq. [2] for the conditions of the present cycle process 8–9.

During the calculation it was assumed that the difference in the vapour pressures of the distillate and the absorbing solution was 5 psi at state point 9. Also taken into account in the calculation was the effect of water in the distillate, namely, that of preventing effective cooling below 32 F being obtained from three times its own weight of NH_3.

VOL. 5 1961

All the stated differences between the actual and theoretical cycles affect the COP but in different ways. The first difference, i.e., X_{RS} for the actual cycle being greater than that for the theoretical cycle (X_{R4}), would appear not to exercise much influence, since a smaller weight of distillate would waste less refrigerant during the adiabatic cooling process. The second difference, the difference between the solution and distillate vapour pressures at the end of adiabatic cooling, tends to increase the COP, while the presence of water in the distillate reduces it. The net effect of all these factors is seen in a comparison of columns 14 and 16, Table 1. The biggest difference between the theoretical and actual cycle is seen in the effective cooling produced per lb of initial mass of solution.

Where the same vessel is used as condenser and evaporator both the effective cooling per lb of solution and the actual COP are materially reduced due to the heat capacity of the vessel. This is discussed more fully in the section dealing with the evaporator.

Heating Rate and Condenser Performance

The results of an attempt to relate condenser performance to the heating rate are shown in Table 3. Though the variation in the heating rate was not large enough to produce a distinct variation in some of the quantities (e.g., rate of distillation), some interesting trends can be discerned.

The assumptions underlying these calculations were two in number, namely, that the vapour condensing in the condenser was pure NH_3, and that the ammonia vapour entered the condenser proper at the temperature of condensation. There was justification for these assumptions as the top of the rectifying section of the distillation pipe was maintained at a temperature of about 120 F, and the mass of water in the distillate was less than about $2\frac{1}{2}\%$. The vapour was cooled somewhat more in its subsequent passage through the rest of the insulated distillation pipe.

The temperature difference (column 4) was therefore obtained as the difference between the saturation temperature corresponding to the mean pressure of distillation and the temperature of the cooling water. The over-all coefficient of heat transfer was obtained from the heat rejected in the condenser which was the difference between the enthalpy of the vapour and the enthalpy of the distillate (column 5).

An increase in the heating rate (column 3, Table 3) resulted in a decrease in the over-all heat transfer coefficient. However, the decrease was largely offset by

TABLE 3.—Heating Rate and Condenser Performance (NH_3-H_2O tests).

(1) Test No.	(2) Max. Sol. Temp. °F	(3) Rate of Heat Supply during Actual Distillation, Process 6-7, per lb of Solution Btu/min	(4) Temp. Diff. between Condensing Vapour and Cooling Water	(5) Overall Coeff. of Heat Transfer for Condenser Btu/sq ft-hr-°F	(6) Actual Rate of Distillation of Pure NH_3, per lb of Solution ($\times 10^{-1}$) lb/hr	(7) Diff. between Actual wt. of NH_3 in Distillate and Theoretical wt, per lb of Solution ($\times 10^{-2}$) lb	(8) Rate of Heat Supply per lb of Solution per ft² of Condensing Surface Btu/psf-hr
2	200	3.07	6.2	70.7	2.06	4.60	148.0
3	220	2.93	5.8	73	1.915	3.10	140.5
4	237	3.41	8.1	60	2.19	3.85	164
5	255	3.73	10.5	49	2.29	4.15	179
6	274	3.65	11.0	44.5	2.19	4.2	175

TABLE 4.—Results of Tests for NH_3-$LiNO_3$ System and Comparison with Theoretical Values. Initial Weight of Solution: 4.625 lb (Tests 1 to 3) and 4.125 lb (Tests 4 and 5)

Test No.	Regeneration							Refrigeration					Actual		Theoretical			
										Minimum temp. of distillate					Constant temp. absorption		Constant press. absorption	
(1)	(2) Initial Conc X_{A1}	(3) Max. sol. temp. t_5 °F	(4) Max. press. psi	(5) Final sol. conc. X_{A5}	(6) Temp. of condenser C.W. °F	(7) Wt. of dist. lb	(8) Heat to solution Btu	(9) Temp. of absorber C.W. °F	(10) Weight of absorbate lb	(11) Observed with vessel °F	(11) Calculated no vessel °F	(12) Effective cooling below 32°F Btu	(13) Effective cooling per lb of solution Btu	(14) COP	(15) Effective cooling per lb of solution Btu	(16) COP	(17) Effective cooling per lb of solution Btu	(18) COP
1	0.487	209	189	0.608	77.7–78.0	0.93	1017	80	0.92	23	9.5	444	96	0.437	102	0.435	108.5	0.460
2	0.487	221.5	178	0.627	78.4–79.0	1.03	1124	83–77	—	20	6	495	106.5	0.440	113	0.435	120	0.463
3	0.487	256	193	0.667	80.0–81.1	1.25	1361	88–80	1.26	14	−6	588	127	0.432	135	0.430	146	0.462
4	0.545	219	163	0.631	77.7–78.3	0.56	773	83	0.523	12	4	273	66.2	0.353	70	0.352	74.5	0.375
5	0.545	260	168	0.690	80.9	0.865	1092	80	0.840	2	−4	415	100.5	0.380	100.3	0.366	107.5	0.394

the increase in the temperature difference (column 4), so that a more rapid rate of heating did produce an increase in the rate of distillation (column 6). Yet the proportional increase in the rate of heating of the solution was greater than the proportional increase in the distillation rate.

The rate of heat supply per lb of solution per sq ft of condensing surface is a significant quantity as it determines the magnitude of the temperature difference, and consequently the actual mass of distillate obtained. A 50 per cent increase in the heating rate per sq ft of condensing surface resulted in the temperature difference doubling with a consequent increase of about 30 per cent in the amount by which the actual weight of distillate obtained was less than the theoretical maximum weight obtainable.

In these tests the cooling water was stagnant for most of the period of regeneration. This method of cooling the condenser is of some significance for refrigerators operated by solar energy, as it is possible that other sources of energy to drive pumps to circulate cooling water may be either unavailable or uneconomical to use.

The rate at which heat was supplied in these experiments can be obtained from solar radiation with a moderate amount of concentration. Column 8 therefore furnishes quite useful design data for a suitable condenser, and also makes possible the estimation of the actual effective cooling produced for a known rate of solar heat collection.

EXPERIMENTAL RESULTS: AMMONIA-LITHIUM NITRATE SYSTEM

Extension of Data Charts

Gensch[10] prepared three charts giving the data necessary to estimate the performance of a vapour absorption refrigerator using NH_3-$LiNO_3$. The first was a P-t-X chart; the second gave values for the differential heat of evaporation; and the third values of the specific heat of solution. Berestneff[11] has reviewed Gensch's paper and reproduced Gensch's charts. The range of concentrations covered by Gensch's charts extended from $X_A = 0.58$ to $X_A = 0.76$. This range was inadequate for the present series of tests which required a range from $X_A = 0.48$ to $X_A = 0.70$. The first stage of this investigation therefore consisted of an attempt to use such data as were available from the tests to extrapolate Gensch's curves.

The method employed closely followed Gensch's own method and is described in Appendix II. Figs. 11, 12, and 13 show respectively the P-t-X chart, the differential heat of evaporation chart, and the specific heat versus concentration chart for the required range of concentrations and pressure.

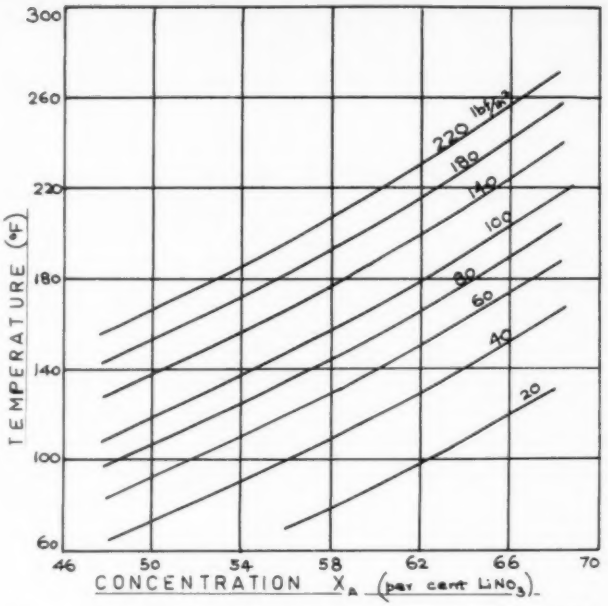

FIG. 11—Pressure-Temperature-Concentration Chart for NH_3-$LiNO_3$ Solutions.

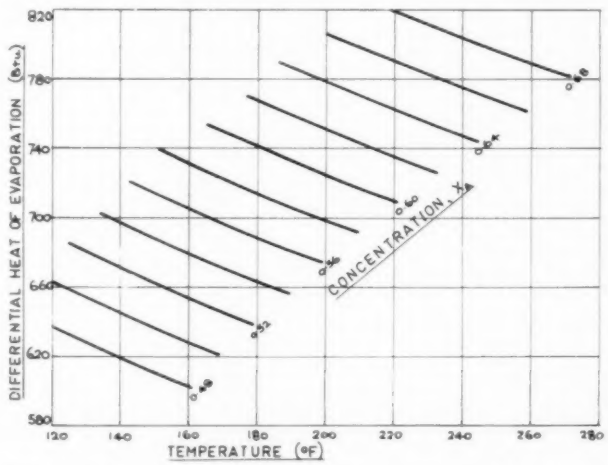

FIG. 12—Differential Heat of Evaporation for NH_3-$LiNO_3$ Solutions.

The Actual Cycle

Five tests were performed. Three of these tests had $X_{A1} = 0.487$, and maximum solution temperatures of 209, 221.5, and 255 F. The remaining two tests had $X_{A1} = 0.545$ and maximum solution temperatures of 219 and 260 F. A summary of the results is presented in Table 4. Fig. 14 is a plot of the data for test number 2: the trend of the curves being similar to those obtained for the remaining tests. The actual cycle for the solution is shown plotted in Fig. 15 as cycle 1–7–8–9–1 together with the corresponding theoretical cycle 1–3–4–6–1.

The difference between the actual cycle and the theoretical cycle during the regeneration stage was

VOL. 5 1961

the same as that noticed for the NH_3-H_2O system, namely, that the actual pressure of distillation was greater than the theoretical pressure. The reason for this difference and its effects have been discussed in the previous section.

During the refrigeration stage there appeared to be one important difference between the actual and theoretical cycles. In the theoretical cycle, at the conclusion of adiabatic cooling (process 4-6), the pressure of the absorbing solution is equal to the pressure of the distillate. However, at the end of process 8-9, in the actual cycle with NH_3-$LiNO_3$, the vapour pressure of the distillate was 20-22 psi greater than the vapour pressure of the absorbing solution. This difference in pressure was apparently due to the viscosity of the NH_3-$LiNO_3$ solution, and the poor mixing in the absorber. The effect of this pressure difference was beneficial in that it prevented the refrigerant (or distillate) being cooled to excessively low temperatures during process 8-9.

At the conclusion of process 8-9, the pressure of the distillate was about 48 psi. Since the vapour pressure of the solution at state point 1 was 53 psi, the absorption process 9-1 for the distillate takes place at nearly constant pressure.

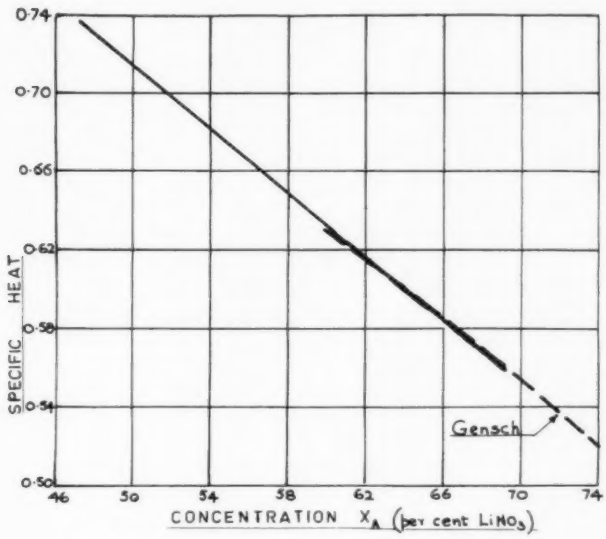

FIG 13—Specific Heat of NH_3-$LiNO_3$ Solutions.

Actual Coefficient of Performance

The actual COP for values of t_s up to 220 F, was obtained by two methods, a 'direct method' using the data charts (Figs. 11, 12, and 13), and an 'indirect method' based on a thermal balance of the heat supplied to the bath from the immersion heaters, the heat gain of the bath and contents, and the heat loss to the environment.

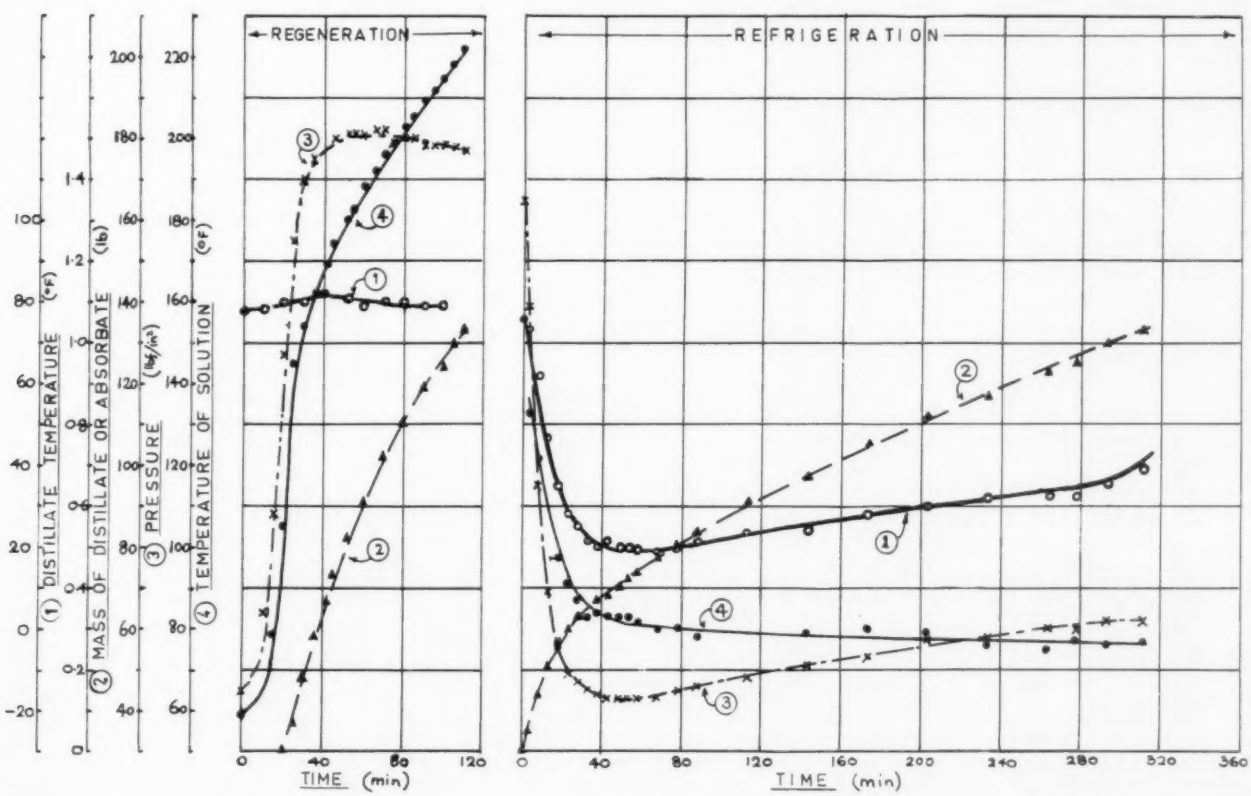

FIG. 14—Data from Test Number 2 (max. solution temp., t_s = 221.5°F) for the NH_3-$LiNO_3$ System. Initial Mass of Solution = 4.625 lb.

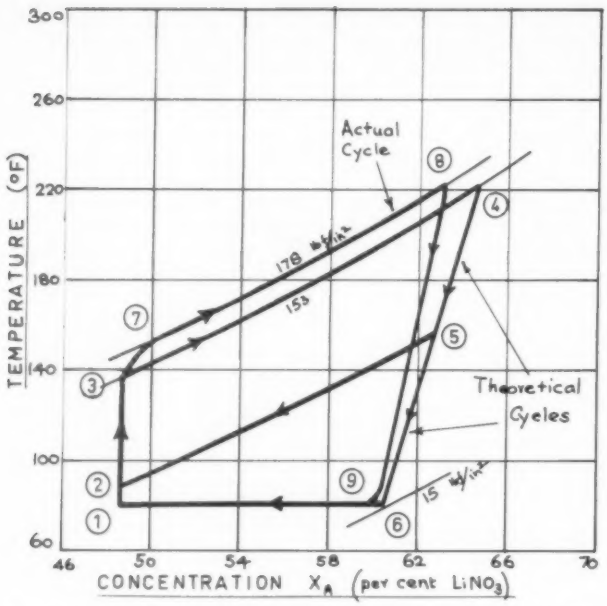

FIG. 15— Actual Cycle for NH_3-$LiNO_3$ System Compared with the Theoretical Cycles.

TABLE 5.—Comparison of the Values of the Heat Supplied to Solution by Direct and Indirect Methods (NH_3-$LiNO_3$ Tests)

Test No.	Initial Conc. X_{A1}	Max. Sol. Temp. t_s	Heat Supplied to Solution [Btu]	
			'Indirect method'	'Direct Method'
1	0.487	209	1017	993
2	0.487	221.5	1195	1187
4	0.545	219	826	800

An example of the application of the direct method is given in Appendix I. The indirect method was essentially the same as that adopted for the NH_3-H_2O system. A comparison of the values calculated by the two methods is given in Table 5, and would appear to justify the proposal of Figs. 11, 12, and 13 as accurate enough for engineering use till better attested data are available. For values of $t_s > 220$ F, only the direct method was used to obtain the heat to solution (Table 4).

The effective cooling was calculated on the basis that: all the distillate was pure NH_3, and that there was no absorbent in the condenser-evaporator; that at the end of process 8-9 the vapour pressure of the distillate was 20 psi greater than the vapour pressure of the absorbing solution; and that the temperature of the absorbing solution during the refrigeration stage was constant.

Even though it reduces the effective cooling per lb of solution, the difference between the theoretical and actual cycle during regeneration, namely, that the actual distillation pressure is greater than the theoretical pressure, does not significantly affect the actual COP. On the contrary the difference between the vapour pressure of the distillate and the vapour pressure of the solution at the end of process 8-9 does have an appreciable effect on the COP, and is largely responsible for the fact that the actual COP obtained exceeds the theoretical COP of the corresponding constant temperature absorption cycle.

SOME CONSIDERATIONS IN EVAPORATOR DESIGN

The actual effective cooling stated in Tables 1 and 4 was determined after computing from Eq. [2] the weight of refrigerant evaporated during the adiabatic cooling process. When the same vessel serves as condenser and evaporator, the actual effective cooling so calculated is a gross effect, and includes both the 'available cooling' and the heat abstracted from the vessel during adiabatic cooling. It is only the 'available cooling' which produces any useful refrigeration outside the evaporator vessel.

For test number 5 with the NH_3-H_2O system (t_s = 255 F), if it be assumed that the evaporator containing the 1.605 lb of distillate were a spherical vessel of just enough capacity the available cooling is about 18 Btu less than the gross effective cooling. This quantity of heat (18 Btu) is the heat abstracted from the vessel in cooling from 83 F (the temperature at the end of the regeneration stage) to 32 F (the highest temperature at which heat is usefully abstracted). Even though the vessel is cooled below 32 F during adiabatic cooling, the cooling effected below 32 F is recovered during the process following.

Where the water equivalent of the containing vessel (W_e) is known, the weight of refrigerant evaporated during adiabatic cooling may be directly determined from the equation

$$\log_e \left[\frac{c_l W_5' + W_e}{c_l W_4' + W_e} \right] = \frac{H_5' - H_4'}{L_m} \qquad [13]$$

where c_l = mean specific heat of liquid refrigerant, and the suffixes 4 and 5 relate to the states of refrigerant (distillate) before and after adiabatic cooling respectively in the constant pressure absorption cycle.

Where the same vessel serves as condenser and evaporator, the weight of that vessel will have to be a minimum in order to obtain the greatest possible amount of available cooling. However, this condition conflicts directly with the requirement that the heat transfer should be as large as possible in order to ensure efficient condenser and evaporator performance. A compromise is therefore inevitable.

The difference between the available cooling and the effective cooling can be reduced by separating the evaporator from the condenser. Ideally, if the evaporator in such a system can be perfectly insulated, then

VOL. 5 1961

the available cooling will be the same as the actual effective cooling. While this arrangement is not feasible for portable units, it is the form which will be adopted in refrigerators of larger capacity.[1]

The evaporator in the intermittent cycle refrigerator is intrinsically different from the evaporator in a refrigerator working on the continuous cycle. In the latter it is a continuous flow pipe system, whilst in the former it is a reservoir. Performance data for intermittent cycle evaporators of sound design are not available at present, and await the development of large capacity units.

SUMMARY AND CONCLUSIONS

1. For the NH_3-H_2O system simplified approximate expressions are stated for the calculation of the theoretical COP, and also the theoretical effective cooling (Eqs. 8, 9, 10, and 11) for the intermittent vapour absorption cycle. For the NH_3-$LiNO_3$ system the data charts of Gensch have been extrapolated using methods similar to those employed by him (Figs. 11, 12, and 13), and suitable expressions obtained to facilitate the calculation of the theoretical COP (Eqs. 4 and 7, and Appendix I).

2. A systematic experimental study has been made of the cycle employing two binary systems—NH_3-H_2O and NH_3-$LiNO_3$ with maximum solution temperatures up to about 270 F. Using solutions with an initial concentration of about 0.50, the effective cooling below 32 F per lb of solution, and the actual COP have been obtained and compared with theoretical values (Tables 1 and 4).

For both systems it was generally found that while the values of the actual COP were quite close to the values of the theoretical COP the actual cooling per lb of solution was 5–15 per cent less than the theoretical value.

3. The difference between the theoretical effective cooling and the actual effective cooling depends upon the area of condensing surface provided for a particular rate of heat supply during regeneration. For a condenser provided with stagnant cooling water Table 3 provides a correlation between the over-all heat transfer coefficient in the condenser with the rate of heat supply per lb of solution per sq ft of condensing surface for the NH_3-H_2O system.

4. Where the same vessel serves as both condenser and evaporator the 'available cooling' is less than the actual effective cooling because the vessel has to be cooled at the commencement of the refrigeration stage. This indicates that for larger units the condenser and evaporator will be separated.

5. While the results of this investigation apply specifically to small refrigeration units working on the intermittent absorption cycle, they also indicate the kind of performance which may be expected from larger units. Suitable arrangements incorporating flat-plate solar heat collectors can therefore be expected to operate as intermittent refrigerators with maximum solution temperatures of 200 to 220 F, and values for the COP of about 0.30 for heat abstraction temperatures around 32 F. A small experimental unit of this type with a flat-plate collector 5 ft by 3 ft 6 in. is currently being tested by the author.

6. There does not appear to be much to choose between the merits of the two systems investigated from a thermodynamic viewpoint. With regard to the COP the NH_3-$LiNO_3$ system would seem to be slightly better, while more refrigeration per lb of solution is possible with the NH_3-H_2O combination.

In small units, e.g., portable refrigerators, where NH_3-H_2O has already been used the NH_3-$LiNO_3$ combination can be used with equal advantage. Problems such as absorbent migration which are likely to take place with solid absorbents for NH_3 (e.g., $CaCl_2$) do not arise since NH_3-$LiNO_3$ solution is a liquid. At present however, for large units the refrigerant absorbent combination of NH_3-H_2O appears to be the most promising.

ACKNOWLEDGMENTS

The author acknowledges the help and encouragement of Dr. Harold Heywood, D.Sc., M.I.Mech.E., M.I.Chem.E., under whose supervision this work was carried out. To the Governing Board of Woolwich Polytechnic and Mr. J. Walker, M.Sc., A.M.I.C.E., A.M.I.Mun.E., Head of the Department of Civil and Mechanical Engineering, the author is indebted for facilities abundantly provided, as also to the Laboratory staff, in particular to Mr. F. C. Trotman, for assistance in the construction of the experimental rig.

APPENDIX I

Heat Supplied During the Regeneration Stage for NH_3-$LiNO_3$ System

$$\begin{bmatrix}\text{Heat supplied}\\ \text{during}\\ \text{regeneration, } Q_s\end{bmatrix} = \begin{bmatrix}\text{Heat to solution}\\ \text{before actual dis-}\\ \text{tillation commences}\end{bmatrix} + \begin{bmatrix}\text{Heat to solution}\\ \text{only during}\\ \text{distillation}\end{bmatrix} + \begin{bmatrix}\text{Heat to vapour}\\ \text{only during}\\ \text{distillation}\end{bmatrix}$$

Of the three terms on the right hand side of the equation it is only the second which presents some difficulty in evaluation. The following method was devised to obtain an expression for this second term.

A plot was constructed of the weight (W), temperature (t), and the specific heat (c) against concentration (X_A) for the actual distillation process 3-4 (Fig. 16). The change in the weight of the solution during this

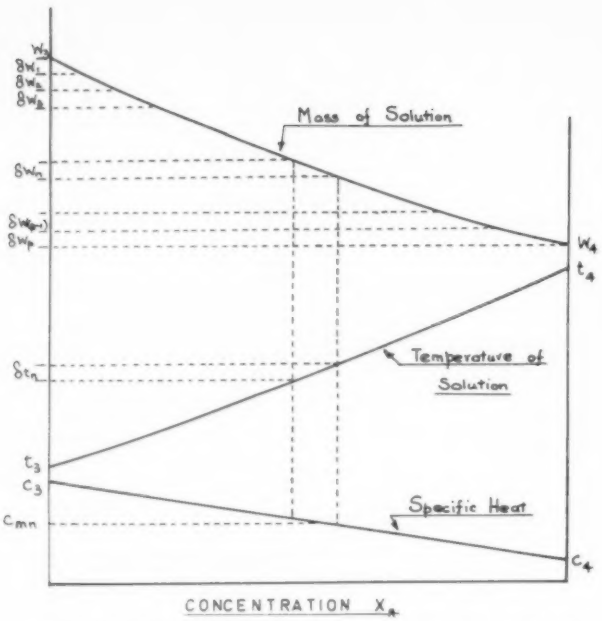

FIG. 16—Plot of Data for the Calculation of Heat Supplied to Solution during Actual Distillation, Process 3–4 (Theoretical Cycle) or Process 7–8 (Actual Cycle).

process, $W_3 - W_4$, (i.e., due to the evaporation of pure ammonia) was divided into a number of equal incremental changes

$$\delta W_1 = \delta W_2 = \cdots = \delta W_n = \cdots = \delta W_{(p-1)} = \delta W_p (= \delta W)$$

The corresponding change in the temperature of the solution during the change δW_n in the weight of solution was δt_n, while the mean specific heat during this change was c_{m_n}.

Hence

Heat to solution during temp rise,

$$\delta t_p = \left(W_4 + \frac{\delta W_p}{2}\right) c_{m_p}\, \delta t_p$$

Heat to solution during temp rise

$$\delta t_{(p-1)} = \left(W_4 + \delta W_p + \frac{\delta W_{(p-1)}}{2}\right) c_{m_{(p-1)}}\, \delta t_{(p-1)}$$

Heat to solution during temp rise

$$\delta t_n = \left(W_4 + \delta W_p + \delta W_{(p-1)} \cdots \frac{\delta W_n}{2}\right) c_{m_n}\, \delta t_n$$

Heat to solution during temp rise

$$\delta t_1 = \left(W_4 + \delta W_p + \delta W_{(p-1)} \cdots \delta W_n \cdots \frac{\delta W_1}{2}\right) c_{m_1}\, \delta t_1$$

Adding and rearranging terms on the right hand side,

Heat to solution during distillation only

$$= \left(W_4 + \frac{\delta W}{2}\right) \sum_{n=1}^{n=p} c_{m_n}\, \delta t_n + \delta W \sum_{r=1}^{r=(p-1)} \sum_{n=1}^{n=r} c_{m_n}\, \delta t_n$$

Therefore for the constant temperature absorption cycle,

$$Q_e = [W_3\, c_3 (t_3 - t_2)] + \left[\left(W_4 + \frac{\delta W}{2}\right) \sum_{n=1}^{n=p} c_{m_n}\, \delta t_n + \delta W \sum_{r=1}^{r=(p-1)} \sum_{n=1}^{n=r} c_{m_n}\, \delta t_n\right] + \left[\sum_{n=1}^{n=p} Ld_{m_n}\, \delta W_n\right] \quad [14]$$

where Ld_{m_n} is the mean differential heat of evaporation during the evaporation of δW_n lb of ammonia.

A similar expression can be framed for the constant pressure absorption cycle (Eq. 3).

When using this expression for the calculation of Q_e in an actual test, it is generally more convenient to divide the change in weight during distillation $(W_8 - W_1)$ into p incremental changes in weight of which $(p-1)$ changes are all equal while the final change in weight (δW_p) is less, i.e.,

$$\delta W_1 = \delta W_2 = \cdots = \delta W_n = \cdots \delta W_{(p-1)} = \delta W > \delta W_p$$

For the constant temperature absorption cycle, Eq. [14] becomes

$$Q_e = [W_3\, c_3 (t_3 - t_2)] + \left[\left(W_4 + \frac{\delta W_p}{2}\right) c_{m_p}\, \delta t_p + \left(W_4 + \delta W_p + \frac{\delta W}{2}\right) \sum_{n=1}^{n=(p-1)} c_{m_n}\, \delta t_n + \delta W \sum_{r=1}^{r=(p-2)} \sum_{n=1}^{n=r} c_{m_n}\, \delta t_n\right] + \left[\sum_{n=1}^{n=(p-1)} Ld_{m_n}\, \delta W_n + Ld_{n_p}\, \delta W_p\right] \quad [15]$$

The second and third terms on the right hand side (each enclosed within square brackets) representing respectively, the heat to solution and to vapour during distillation only, can be evaluated with facility by means of a table constructed from data read off from a plot similar to Fig. 16. This has been done in Table 6 for test number 2 (Table 4) where $X_{A1} = 0.487$, $W_1 = 4.625$ lb, $t_1 = 80$ F, $t_8 = 221.5$ F.

A similar plot to Fig. 16 was made with 6 incremental changes in weight during actual distillation so that

$$\delta W_1 = \delta W_2 = \cdots = \delta W_5 = 0.20 \text{ lb},$$

and $\delta W_6 = 0.03$ lb

The corresponding values of δt and c_m are entered in columns 3 and 4 respectively of Table 6.

The values of Ld_{m_n} corresponding to the mean value of the temperature (column 8) and the concentration (column 9) during each incremental change in weight are entered in column 10.

VOL. 5 1961

TABLE 6.—Calculation of Heat to Solution for Test Number 2 (Table 3), NH_3-$LiNO_3$ System

(1) n	(2) δW_n	(3) δl_n	(4) c_{m_n}	(5) $c_{m_n} \cdot \delta l_n$	(6) Prog. Total $\Sigma c_{m_n} \cdot \delta l_n$	(7) Prog. Total $\Sigma\Sigma c_{m_n} \cdot \delta l_n$	(8) t_{mean}	(9) $X_{A_{mean}}$	(10) L_d	(11) $L_d \cdot \delta W_n$
1	0.2	16	0.716	11.46	11.46	11.46	148	0.498	636	127.2
2	0.2	15	0.698	10.47	21.93	33.39	168	0.521	652	130.4
3	0.2	16	0.677	10.83	32.76	66.15	179.5	0.545	670	134.0
4	0.2	15	0.654	9.81	42.57	108.72	194	0.574	694	138.8
5	0.2	16.5	0.629	10.38	52.95		210	0.605	724	144.8
6	0.03	3	0.613	1.84			220	0.624	740	22.2
										$\sum L_d \cdot \delta W_n = 697.4$

Hence

$$Q_s = [4.625 \times 0.725 \times (140\text{–}80)] + [3.610 \times 1.84 + 3.725 \times 52.95 + 0.2 \times 108.72] + [697.4]$$
$$= 1124.2 \text{ Btu.}$$

APPENDIX II

Extension of Data Charts for NH_3-$LiNO_3$ System

1. *P-t-X Chart.* Dühring's Rule may be stated for NH_3-$LiNO_3$ solutions of constant concentration as

$$t = k_1 t' + k_2 \qquad [16]$$

where

t = Temperature of NH_3-$LiNO_3$ solution
t' = Temperature of pure NH_3 at the same pressure as the solution
k_1 = Dühring constant
k_2 = Constant.

The values of k_1 used by Gensch for the range of concentrations (X_A) from 0.60 to 0.76, and for the range of pressures from 6.27 kg/cm^2 (89.2 psi) to 15.85 kg/cm^2 (225.4 psi) were obtained from Clapeyron's equation (in kg-m-°C units)

$$k_1 = \frac{10^4 \times v \times t}{426 \times L_d} \left(\frac{dP}{dt'}\right) \qquad [17]$$

where

v = Specific volume of superheated vapour
L_d = Differential heat of evaporation

Gensch's values for L_d and t were substituted in this equation together with values for v and dP/dt' obtained from tables and chart for pure ammonia prepared by Kuprianoff[12] and used by Gensch. A suitable equation was sought by the method of least squares to correlate k_1 and X_A, and the following obtained

$$k_1 = 1.352 - 1.673 X_A + 2.0645 X_A^2 \qquad [18]$$

This equation was used to obtain values of k_1 for values of X_A from 0.48 to 0.60.

A Dühring plot was constructed for the range of X_A from 0.48 to 0.68, and for a pressure range from 100 psi to 220 psi, using Gensch's data, the data collected from the present series of tests, and the values of k_1 determined above. Values of t' and t read off from this chart enabled the value of k_2 for various concentrations to be calculated. The values of k_1 and k_2 for various concentrations are given in Table 7. Eq. [16] together with ammonia tables and Table 7 enables the boiling temperature (t) of NH_3-$LiNO_3$ solutions of known concentration and pressure to be determined. Fig. 11 is a composite plot of values obtained from this equation and values from Gensch's chart.

TABLE 7.—Constants in Duhring Equation (NH_3-$LiNO_3$ System)

Concentration X_A	k_1	k_2
0.48	1.025	52.45
0.50	1.032	60.9
0.52	1.040	69.6
0.54	1.051	78.45
0.56	1.063	87.5
0.58	1.076	96.8
0.60	1.091	106.65
0.62	1.108	116.95
0.64	1.127	127.6
0.66	1.147	138.7
0.68	1.169	150.65

2. *L_d vs t Chart.* Clapeyron's equation was employed to obtain the differential heat of evaporation

$$L_d = 0.185 \times v \times t \times \left(\frac{dP}{k_1\, dt}\right) \quad \text{Btu/lb} \qquad [19]$$

t and k_1 were obtained from Eq. [16] and Table 7, and v, the specific volume of superheated vapour of pure NH_3, from the B.S.I. Tables for ammonia.[13]

The relation between saturation pressure (in kg/cm^2) and saturation temperature (in °K) for pure ammonia may be represented by

$$\log_{10} P = 27.39021 - \frac{1914.957}{T} - 8.45983 \log_{10} T + 2.3931 \times 10^{-3} \times T + 2.9552 \times 10^{-6} \times T^2 \qquad [20]$$

whence

$$\frac{dP}{dt} = e^{(2.3026 \log_{10} P)} \times \frac{d(2.3026 \log_{10} P)}{dt} \qquad [21]$$

was obtained from Eq. [20], and after conversion to British units substituted in Eq. [19].

The values of the differential heat of evaporation

obtained for the range of pressures 100 psi to 220 psi are given in Fig. 12.

3. *c vs X Chart.* Gensch has derived the following equation for a solution circuit consisting of a generator, an absorber and a heat exchanger in which 1 lb of NH_3 is evolved in the generator at P_2 and t_2, and 1 lb of NH_3 is absorbed in the absorber at P_1, t_1, for the circulation of an infinitely large quantity of solution

$$\frac{dc}{dX_A} = \frac{1}{X_A}\left[c - \frac{L_{d_2} - L_{d_1} + H_{v_1} - H_{v_2}}{t_1 - t_2}\right] \quad [22]$$

where c = Specific heat of the solution at concentration X_A, and the other symbols have the usual meaning.

Within the limited range of concentration and pressure for which the present charts are plotted it was found that

$$\frac{Dc}{dX_A} \simeq \frac{1}{X_A}[c - 1.124]$$

$$\therefore \quad c_1 = 1.124 - (1.124 - c_2)\frac{X_{A_1}}{X_{A_2}}$$

Substituting Gensch's experimentally determined value for $c = 0.584$ for $X_A = 0.66$,

$$c = 1.124 - 0.818\,X_A \quad [23]$$

Eq. [23] has been plotted in Fig. 13.

4. *Accuracy of the charts.* The accuracy claimed for Gensch's charts is 1–2 per cent. While it is perhaps not possible to claim the same accuracy for these extensions to his charts, reasonably good agreement was obtained between the values for Q_e obtained by the 'direct' and 'indirect methods' (Table 5).

The reliability of the 'indirect method' (heat balance) has been confirmed by earlier tests with NH_3-H_2O. Till such time as better attested data are available, Figs. 11, 12 and 13 are proposed for engineering use.

REFERENCES

1. Trombe, F., and Foex, M. "The Production of Cold by Means of Solar Radiation," *Solar Energy*, **1**-1 (January, 1957), 51.
2. Williams, D. A., Chung, R., Löf, G. O. G., Fester, D. A., and Duffie, J. A. "Intermittent Absorption Cooling Systems with Solar Regeneration," Paper No. 57-A-60, A.S.M.E. (1957).
3. Williams, D. A., Chung, R., Löf, G. O. G., Fester, D. A., and Duffie, J. A. "Cooling Systems based on Solar Regeneration," *Refrig. Eng.* (November, 1958), 33.
4. Andrews, H. I. "Solid Absorption Machine for use on Trains," *Mod Refrig.* (September, 1955), 330.
5. Keith, D. F. "Cooling with Portable Units," *Refrig. Eng.* (December, 1930), 361.
6. Buffington, R. M. "Absorption Refrigeration with Solid Absorbents," *Refrig. Eng.*, **26** (September, 1933), 137.
7. Hulse, G. E. "Freight Car Refrigeration using an Adsorption System," *Refrig. Eng.* (February, 1929), 41.
8. Scatchard, G., Epstein, L. F., Warburton, J., Jr., and Cody, P. J. "Thermodynamic Properties—Saturated Liquid and Vapour of Ammonia-Water Solutions," *Refrig. Eng.*, **53**-5 (1947), 413.
9. Kohloss, F. H., Jr., and Scott, G. L. "Equilibrium Properties of Aqua-ammonia in Chart Form," *Refrig. Eng.*, **58**-10 (1950), 970.
10. Gensch, K. "Lithium-nitratammoniakat als Absorptionsfluessigkeit fuer Kaeltemaschinen," *Zeits. f. d. ges. Kaelte Industrie*, **44**-1 (1937), 1.
11. Berestneff, A. A. "New Absorption System for Low Temperature," *Refrig. Eng.*, **35**-5 (1938), 323.
12. Kuprianoff, I. "Erweiterung der Damptabellen und Diagramme fur Ammoniak bis −76°C," *Zeits. f. d. ges. Kaelte Industrie*, **37**-1 (1930), 1.
13. British Standard 1725:1951 "Thermodynamic Properties of Refrigerants," British Standards Institution.
14. Eisentadt, M. M., Flanigan, F. M., and Farber, E. A. "Solar Air-Conditioning with an Ammonia-Water Absorption Refrigeration System," Paper No. 59-A-276, A.S.M.E. (1959).

VOL. 5 1961

Current Developments in Pyrheliometric Techniques*

By A. J. Drummond

The Eppley Laboratory, Inc., Newport, R. I.

A review is presented of the principal objectives and problems associated with the measurement of the different components of solar radiation. The new universally accepted pyrheliometric standard of reference is discussed as are the more important instrumental requirements for local reproduction, with high precision, of this international standard. Attention is directed towards the accuracy now attainable in integral and spectral wavelength radiation measurements, which is assuming increasing significance in view of the satellite, missile and other upper atmospheric projects currently in focus.

INTRODUCTION

No meteorologist will dispute that the various radiation fluxes to and from the earth's surface constitute some of the most important terms in the heat economy of the earth as a planet and of any individual place at the earth's surface or in the terrestrial atmosphere. In the general geophysical problem we are concerned with such questions as the latitudinal distribution of the different radiation fluxes with time and with altitude.

On the one hand, an adequate knowledge of the solar radiation, of relatively short wavelength, reaching the ground is, perhaps, the most important single requirement for a proper appreciation of physical climatology. On the other hand, the divergence aloft of the difference between the incoming and outgoing fluxes of long-wave atmospheric radiation, or the net radiation as it is usually termed, is directly related to the heating or cooling of the atmosphere.

Another object of radiation research in meteorology is the study of the influence of the atmospheric gases (mainly water vapor, carbon dioxide, and ozone) and the scattering by their molecules and by particulate matter. Our interest in the attenuation of the solar beam in its traverse of the terrestrial atmosphere is wide. For example, the integrated terrestrial reflectance of solar radiation by ground and water surfaces, cloud decks and air, which we call the planetary albedo, is of prime significance since the determination of this characteristic provides us with a picture of the energy-scattering properties of the earth and her atmosphere as a whole, and with an assessment of a major term in the terrestrial thermal budget. Let us consider a different viewpoint. Suppose we attempt to explain the colorations of the twilight sky. We are then immediately concerned with dust which has penetrated into the stratosphere and its distribution; forward scattering by this dust ought to be measurable, through the employment of sufficiently sensitive pyrheliometric techniques. Measurements of this nature will reveal whether real variations in the high level dust exist.

In dynamical meteorology and in weather prediction, at least theoretically, radiation plays a most important role. It has long been recognized that the radiation balance of the atmosphere represents the dynamo without which the atmosphere would come to rest. Only the influx of heat in the tropics and the radiation emission at the poles keep the atmosphere in motion. However, at present, these influences on the temperature field, on the motion processes, and on cloudiness and precipitation are better understood qualitatively than quantitatively, which brings us to the subject of this session, namely, modern instrumentation in radiation meteorology and, in particular, to recent advances in techniques of pyrheliometric measurement.

Until the commencement of the period immediately following the second World War, systematic observation of the radiation fluxes, on any extended basis, had been seriously neglected with the result that in many applications in theoretical and dynamical meteorology, frequent recourse was necessary to assumed rather than measured quantities. At first sight, it is surprising that such should be the position as recently as only 15 years ago, especially when it is recalled that during the first three decades of the 20th century a very large number of radiation measuring instruments had been introduced and the relevant operational techniques elaborated. But, when we examine the philosophy in radiation meteorology, in retrospect, it becomes clear that these early years of enthusiasm were characterized by an optimism which was not always supported by a proper physical concept of what was actually measured. In the course of time, increasing attention began to be paid to the more fundamental difficulties of solar and terrestrial

* This paper was presented at the New York, September 26-30, 1960, meeting of the Instrument Society of America (held jointly with the American Meteorological Society). Acknowledgment is made to these societies for permission to publish the paper.

radiation measurement and to the magnitude of the errors inherent in the results. The first reaction to this was that scepticism arose as to whether data of the requisite reliability could be assembled without the effort involved becoming prohibitively uneconomic. This explains the lessening of interest in radiation measurement in the years immediately preceding the second World War. However, during the last 10 years or so, much attention has been devoted to placing knowledge of the physical principles of the instruments on more secure premises, to deriving better methods for the evaluation and presentation of the radiation data obtained, and to increasing the international co-ordination of these activities. At the same time, a more vigorous effort is being made to apply the results of such studies not only in meteorology but also in other scientific disciplines.

The content of this paper is directed towards summarizing some of the more important recent achievements in the instrumentation of pyrheliometry.

THE STANDARD SCALE OF RADIATION

Towards the end of the last century K. Ångström,[1] in Sweden, introduced the first reliable pyrheliometer intended for the measurement of the intensity of the radiant energy emitted by the sun. About this time, in the United States, the Astrophysical Observatory of the Smithsonian Institution was beginning to concern itself, under the direction of the pioneer astrophysicist Langley, with the study of the solar constant. This work, carried on by Abbot and his collaborators for almost half a century, and aimed at establishing the flux of energy and its possible variations, in free space, at the earth's mean distance from the sun, has become a classic. One of Abbot's most significant contributions,[2] in this respect, was his development of the silver disk pyrheliometer. This instrument and the Ångström electrical compensation pyrheliometer have constituted the basic primary references to date for all pyrheliometric measurement programs.

However, up to the commencement of the third International Geophysical Year, in July 1957, a severe obstacle was imposed upon the presentation of radiation data, in a co-ordinated manner throughout the countries of the world, by the acceptance internationally of the dual pyrheliometric scales each of which was essentially embodied in the respective standard instrument.

The main difficulty in establishing a relationship between the two traditional scales has lain in the inconsistency of their divergence as found by different workers and under varying conditions of exposure. At the International Radiation Conference, held at Davos (Switzerland) in September 1956, an attempt was made to introduce a compromise the basis for which is summarized in Fig. 1. A detailed statement of the evidence (assembled over a period of about 30 years) in support of the new radiation scale has been published.[3, 4]

It is considered, by the International Radiation Commission, that "measurements on the uncorrected Ångström scale increased by 1.5 per cent will almost certainly be within ± 1 per cent and may be within ± 0.5 per cent of the best approximation which can at present be made of the true absolute scale of radiation". This, of course, implies a correction of -2.0 per cent to the Smithsonian 1913 scale which, as mentioned above, has long been the reference standard for pyrheliometry in the United States and in certain other countries.

STANDARD PYRHELIOMETERS

One of the major problems in measuring the direct solar component is the divergence in the observations from pyrheliometers of different construction on account of the circumsolar sky radiation and the geometry of the pyrheliometer tubes. It is clearly impossible to eliminate this sky radiation entirely because of the difficulty, in such an attempt, of defining the effective

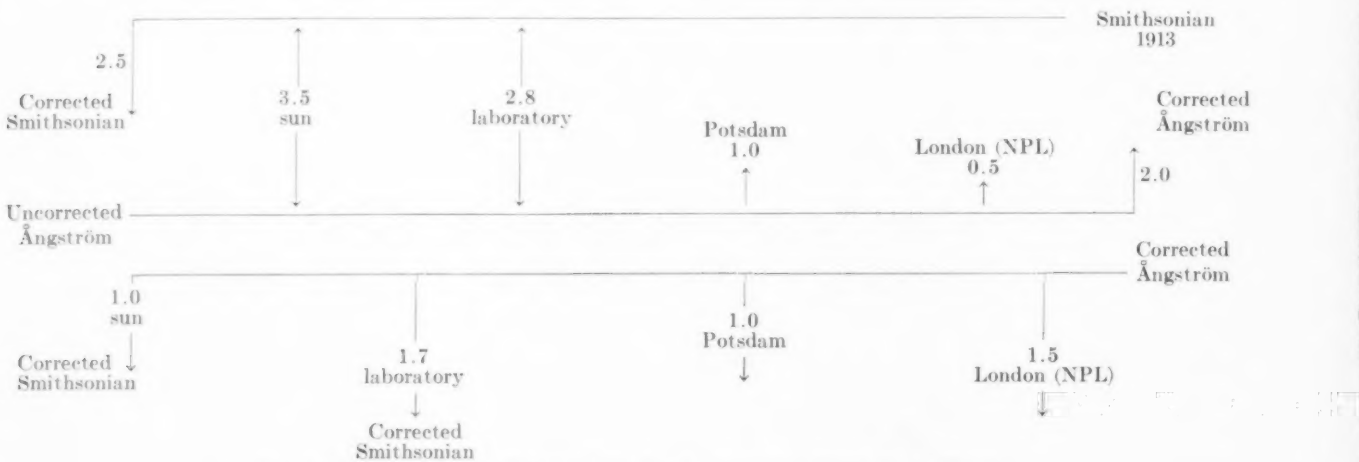

FIG. 1. Diagram Showing Relationship of Pyrheliometric Scales (in per cent).

VOL. 5 1961

solar disk. Computations[5] have shown that the amount of circumsolar sky radiation, which enters the aperture of the pyrheliometers during measurements of solar radiation under average clear atmospheric conditions, is between 2 and 3 per cent in the Smithsonian and Ångström (original model) instruments currently in use, and that the difference between the two types as regards sky radiation and instrument aperture amounts to about 0.5 per cent.

The investigation of this small divergence, which is a function of solar elevation, station altitude and atmospheric turbidity, is of little practical importance in meteorology generally. However, this is not the case when questions arise as to the fixation of the true scale of radiation,[6] with the sun as source, and of the need for the highest realizable accuracy in associated applications such as the determination of the solar radiation fluxes in space and the evaluation of the efficiency of solar energy conversion power units in satellites and outer space vehicles, where marginal limits are significant.

When the engineering aspects of maintaining solar alignment for ground-based observations are considered, it is doubtful whether a pyrheliometer can be constructed, for universal use, which will reduce this circumsolar sky correction to absolute values as low as 0.5 per cent for average cloud-free conditions as observed at normal level sites.

Laboratory investigation of the relationship between the several radiation scales (including that of the U. S. National Bureau of Standards, for low radiant flux density), currently being undertaken at the Eppley Laboratory, should materially assist in the design of improved standard radiometers intended, specifically, for the reproduction of the radiation references under highly controllable conditions indoors.

With regard to the instrumentation for use in natural exposures, the International Radiation Commission has recently attempted to bring a measure of standardization into the geometry of normal incidence pyrheliometers[7] and advocates that "pyrheliometers constructed in future should have an angle of slope not less than 1° and not greater than 2° ($1° \leqq Z_p \leqq 2°$) and a ratio of distance between receiver and limiting aperture to radius of receiver equal to or greater than 15 ($b \geqq 15$). These conditions imply that the opening angle (i.e., half aperture angle) must not be greater than 4° ($Z_0 = \tan^{-1} R/l < 4°$)." In the above, the following normalized parameters specify the aperture conditions of a radiometer:

Z_0 the opening angle $= \tan^{-1} a/b$

Z_p the slope angle $= \tan^{-1} (a - 1)/b$

Z the limit angle $= \tan^{-1} (a + 1)/b$

where $a = R/r$ and $b = l/r$, in which R is the limiting aperture (radius), r the radius of the receiver, and l the distance between R and r.

For the Smithsonian silver disk and the Eppley normal incidence pyrheliometer the appropriate angles are

	Smithsonian	Eppley
Z_0	2.9°	2.9°
Z_p	0.8	2.1
Z	4.9	3.6

The Ångström pyrheliometer (as manufactured in Sweden) has a rectangular aperture with plane angles of 6 and 24° in the original version and about 3.5 and 14° in a recently introduced model.[8] Relevant data for the Eppley pyrheliometer are included here as it has been shown (see below) that a new design of this well-known instrument is as dependable as either of the classical standard pyrheliometers provided that its sensitivity is checked periodically; in addition to being more convenient to use, it can readily be operated continuously.

The Ångström compensation pyrheliometer serves as a means to compare two different heat fluxes, one being produced by the absorption of radiant energy (unknown in magnitude) by an exposed blackened metallic strip, and the other by a known amount of electrical heating in a second similar thin strip. This artificial heating is so regulated that the same temperature effect is produced in both strips, as indicated by a differential thermoelement. It is not the purpose of the present review to criticize the theory of the instrument and the errors inherent mainly on account of internal convection effects.[8, 9] But it should be emphasized that this is the only pyrheliometer presently available, for routine use, which is capable of being employed in an absolute manner,[6] although it is practically always regarded as a secondary relative instrument of extremely high reliability. The principal improvements which have been introduced in recent years have been directed at minimizing the effects caused through inequality in the strip lengths heated naturally and artificially and through associated air convection within the instrument, and also by circumsolar sky radiation: this has been accomplished by increasing the tube length and adjusting the diaphragm system inside the tube. Improvements in the observing technique have been realized through a simplification of the operational electrical circuitry of the pyrheliometer, enabling a more rapid observing sequence to be attained, and provision (by the Eppley Laboratory) of potentiometric controlled auxiliary d.-c. instrumentation for realization, during the actual observing period, of an accuracy of 0.1 per cent in the determination of the electrical compensation current (The radiation intensity is a function of the square of this current).

In the case of the Abbot silver disk pyrheliometer,

which is based on the early instrument of Pouillet, the radiation intensity is derived from a measurement of the rise of temperature of a somewhat massive blackened silver receiver during a specific exposure period, adjusted through the application of certain thermometric corrections relating to stem graduation, mean bulb temperature when the receiver is exposed to radiation, and ambient air temperature. This pyrheliometer cannot be used absolutely; it is calibrated, basically, by reference to a calorimeter (i.e., the Smithsonian water-flow pyrheliometer[10, 11]) with the sun as source. Operation of the silver disk pyrheliometer, even with the aid of an audio timer (e.g., a seconds pendulum), can be very tedious as well as imposing high demands upon personal observational skill. Attempts have therefore been made,[12] in recent years, to incorporate such modifications as (a) an automatic shutter for control of solar exposure of the disk, (b) a simplified heating and cooling timing sequence and (c) an improved method of reading the pyrheliometer thermometer. However, careful comparisons with original type instruments have not indicated any appreciable improvement in the reproducibility of observations obtained with this design of pyrheliometer, either through automatically regulating the exposure or by thermocouple determination of the temperature of the disk.

Tables 1–3 illustrate the precision which is now attainable with working standard pyrheliometers.

TABLE 1.—Comparison of National Working Standard Ångström Pyrheliometers; 18 August 1959, Davos[13]

	Stockholm, Sweden	Davos, Switzerland	Léopoldville, Congo	Newport, U.S.A.	Uccle, Belgium
Pyrheliometer nos.	A.158	A.218	S.I.11	A.162, A.518	S.I.8, A.C.51
Radiation intensity (relative to Stockholm)	1.000	1.006	0.999	1.002	0.999

Pyrheliometers nos. A.158, 162 and 210 are the original Swedish Ångström type; no. 518 is the new long tube instrument; nos. S.I.8 and 11 are specimens of the Smithsonian version of the pyrheliometer; and no. A.C.51 is a secondary thermopile pyrheliometer. The values tabulated represent the mean, in each instance, of five sets of observations over 15-min intervals.

TABLE 2.—Comparison of Abbot Silver Disk Pyrheliometers; 7–13 May 1957, Table Mountain (California)[4]

	Smithsonian		Eppley	U. S. Air Force
Pyrheliometer nos.	S.I.5	S.I.13	S.I.73	S.I.95
Radiation intensity (relative to S.I.5)	1.000	0.997	1.004	0.998

Pyrheliometers nos. S.I.5, 13 and 73 are standard-type instruments; no. 95 incorporates an automatic shutter. The above results refer to means of five sets each of 30-min duration.

TABLE 3.—Comparison of Ångström Pyrheliometers Nos. 162 and 518; 7 July 1960, Newport

	A.162		A.518	
	R strip	L strip	R strip	L strip
(1) 10:39–52 E.D.S.T.				
Mean i (amp)	.2973	.2963	.2878	.2882
	.2968		.2880	
i^2	.0881		.0830	
$I = Ki^2$ (cal cm^{-2} min^{-1})	1.265		1.266	
(2) 10:53–11:33 E.D.S.T.				
Mean i (amp)	.2969	.2956	.2896	.2851
	.2963		.2873	
i^2	.0878		.0826	
$I = Ki^2$ (cal cm^{-2} min^{-1})	1.261		1.259	
Mean A.162/A.518	(1) 0.999 (2) 1.002		1.0005	

General notes: The altitude of the Davos site is approximately 6,000 ft, that of Table Mountain 7,500 and that of Newport close to sea level. The mean radiation intensities during the comparisons reported above were Davos, 1.31; Table Mountain, 1.43; and Newport 1.26 cal cm^{-2} min^{-1}.

TABLE 4.—Temperature Dependence of New Radiometer (Pyranometer) Sensitivity

	Temperature (°C)								
	+50	+40	+30	+20	+10	±0	−10	−20	−30
Radiometer no. 3942									
Deviation of sensitivity from +20 C value (%)	+0.4	+0.3	+0.1	0	−0.2	−0.3	−0.2	+0.2	+0.8
Radiometer no. 3996									
Deviation of sensitivity from +20 C value (%)	0	+0.1	+0.1	0	0	0	+1.0		

SECONDARY PYRHELIOMETERS AND PYRANOMETERS

The principal function of the standard type of pyrheliometer is to provide a pyrheliometric reference, preferably realizable through the maintenance of a group of, say, three or four specimens. For example, at the Eppley Laboratory, the present primary group comprises three Ångström (two original and one with long tube) pyrheliometers and one Abbot pyrheliometer. For the routine calibration of simpler pyrheliometers and pyranometers (i.e., pyrheliometers with a 180° aperture, mainly intended for the measurement of the total radiation from sun and sky received by a horizontal surface) a secondary standard pyrheliometer or pyranometer is frequently employed. Such instruments are the recently improved Eppley normal incidence pyrheliometer and the new high-precision spectral

VOL. 5 1961

radiometer (i.e., a pyranometer for the measurement of solar radiation either wavelength integrally or contained within well-defined spectral regions).[14] Both models utilize a new type of thermopile detector of proven high stability. Very nearly perfect compensation of instrumental sensitivity for variation of ambient temperature over a range of about 80 C is accomplished with the aid of a specially matched thermistor-resistor circuit. The figures in Table 4 demonstrate how the sensitivity-temperature relationship can be normalized. The pyranometer model further incorporates optical compensation of the Lambert cosine error effect, so that the instrument response is practically independent of solar azimuth and elevation.

Calibrations of the new type Eppley pyrheliometer no. 3553 and pyranometer no. 3552, undertaken in March and July 1960 with respective ambient temperatures of 0 C and 25 C, approximately, and solar elevations ranging from about 30 to 70°, confirmed the experimental results quoted above: the agreement of the two pyrheliometer sensitivity determinations was 1.000 ± 0.003 and that of the two pyranometer checks was 1.004 ± 0.004.

This pyranometer is readily adaptable, in a differential arrangement, for the continuous measurement of total solar ultraviolet radiation.[15] It has also been flown at altitudes approaching 50,000 ft, in a Boeing 707 jet aircraft; amongst this series of measurements (18 August 1959) were filter measurements of the incoming and outgoing (reflected) short-wave radiation and of the outgoing long-wave terrestrial radiation (through a transmitting hemispherical envelope of KRS-5).

An important aspect of the research program at the Eppley Laboratory, in recent years, has been an extensive investigation into the characteristics of colored glass filters;[16, 17, 18] the dependence upon ambient temperature of the lower sharp wavelength cutoff and of transmission in the main region of the filters has been studied.

The problems involved in accurate automatic registration of the diffuse sky component of solar radiation have now been largely resolved; techniques employing receivers with shadow bands are better secured as a result of an improved knowledge of the hemispherical distribution of this scattered energy.[19]

In view of the increasing importance of radiation measurements at great altitudes, special attention is currently being devoted, at Newport, to examining the performance characteristics of radiant energy detectors, commercially available, under conditions of temperature, pressure and radiant flux density simulating, in the laboratory, real atmospheres.[20] Of special interest is the development of an empirical equation (valid for all types of thermopile and all pressure levels investigated) enabling any desired response time of a specified detector to be computed from a single measurement made at the pressure level in question.[21] It should be emphasized, in this connection, that the computed values for the periods corresponding to nearly 100 per cent signal are, generally, more accurate than direct measurements.

REFERENCES

1. Ångström, K., *Annalen der Physik und Chemie*, **67,** 633, 1899.
2. Abbot, C. G., *Ann. Astrophys. Obs. Smithson. Inst.* **3,** 47, 1913.
3. *IGY Instruction Manual, Part IV: Radiation Instruments and Measurements*. Pergamon Press, London, 378, 1958.
4. Drummond, A. J. and Greer, H. W., *Sun at Work* (Assoc. App. Solar Energy) **3,** Nos. 2, 3, 1958.
5. Pastiels, R., Inst. Roy. Met. de Belgique, Pub., Ser. A, No. 11, 1959.
6. Drummond, A. J., *Quart. J. R. Met. Soc.*, **82,** 481, 1956.
7. Report of Sub-Commission of IAM (IUGG) submitted to the International Radiation Conference, Davos 1956 (mimeographed).
8. Lindholm, F., *Tellus*, **10,** No. 2, 249, 1958.
9. Ångström, A., *Tellus*, **10,** No. 3, 342, 1958.
10. Hoover, W. H. and Froiland, A. G., *Smithsonian Misc. Coll.*, **122,** No. 5, 1953.
11. Abbot, C. G., Aldrich, L. B., and Froiland, A. G., *Smithsonian Misc. Coll.*, **123,** No. 5, 1954.
12. Foster, N. B. and MacDonald, T. H., *Mon. Weather Rev.*, **83,** No. 2, 33, 1955.
13. Dogniaux, R., Comparison Internationale d'Echelles Pyrheliometriques. Inst. Roy. Met. de Belgique, 1959 (mimeographed).
14. Marchgraber, R. M. and Drummond, A. J., A Precision Radiometer for the Measurement of Total Radiation in Selected Spectral Bands. Contribution to the International Radiation Symposium, Oxford 1959 (mimeographed).
15. Drummond, A. J. and Marchgraber, R. M., New Instrumentation for the Automatic Recording of Solar and Sky Ultraviolet Radiation. Contribution to the International Radiation Symposium. Oxford 1959 (mimeographed).
16. Ångström, A. K. and Drummond, A. J., *J. Opt. Soc. Amer.*, **49,** 1096, 1959.
17. Ångström, A. K. and Drummond, A. J., *Quart. J. R. Met. Soc.*, **85,** 429, 1959.
18. Ångström, A. K. and Drummond, A. J., *J. Opt. Soc. Amer.*, **50,** 974, 1960.
19. Drummond, A. J., *Arch. Met. Geoph. Biokl., Serie B.*, **7,** 413, 1956.
20. Karoli, A. R., Ångström, A. K. and Drummond, A. J., *J. Opt. Soc. Amer.*, **50,** 758, 1960.
21. Drummond, A. J., Karoli, A. R. and Griffiths, J. F., On the Time Constant of Thermopile Radiant Energy Detectors (in press).

Lightweight Solar Concentrator Development

By Roger Gillette, Howard E. Snyder, and Thomas Timar

Boeing Airplane Company, Aero-Space Division, Seattle, Wash.

The objective of the present research program is to develop a lightweight solar concentrator that will provide sufficient solar energy for space vehicle power conversion equipment. Solutions to processing problems such as tooling and parting of the lightweight replica mirror are discussed. Solar test data are furnished for performance evaluation. It was found that a 36 inch diameter mirror weighing 2.9 lb (.410 psf) has the capability of providing sufficient energy for a 15 watt thermionic generator. These developments demonstrate feasibility of supplying highly concentrated solar heat with lightweight concentrators.

INTRODUCTION

Lightweight and accurate solar concentrators are necessary components of some systems for using the solar heat available in space. Although efficient heat-to-electricity converters are also required, the scope of this paper is limited to the solar concentrator. Supporting structure and orientation devices are not discussed.

Theoretical studies[1] point out the importance of optical surface finish and of concentrator accuracy. Practical requirements pose definite questions such as: How much heat can actually be concentrated on a small focal area? How heavy does a mirror have to be to perform properly after being shipped by truck, manhandled, and blasted off by rockets? To answer these questions, a program was initiated to make replica mirrors and to determine their performance by tests. The results obtained in the first six months of the program are reported in this paper.

OBJECTIVE

The concentrator was designed to supply heat at 3140 F to a thermionic generator.[2] The generator has a 0.465 sq in. heat absorber area. It requires 440 watts of heat flux to strike the absorber. A concentrator meeting these requirements would also be more than adequate for operating thermoelectric generators. The following design goals were established:

1. Weight of 0.2 psf. This weight was calculated from knowledge of the properties of aircraft sandwich materials.
2. Mirror concentration efficiency of 70%. This efficiency was considered to be reasonable based on known searchlight mirror efficiency of 75–85%.
3. Area concentration ratio of 1500/1. This concentration seemed readily attainable with paraboloidal mirrors, since searchlight mirrors have concentration ratios as high as 25000/1.
4. Ability to withstand 8 G acceleration. This acceleration synthesizes the loads anticipated during launch conditions.

The objectives were limited to goals attainable with minimum material and process development.

DEVELOPMENT PROGRAM

Fresnel lenses and reflectors, parabolic cylinders, truncated cones, spherical mirrors, and paraboloids of revolution were considered. A paraboloidal mirror was the only shape that could produce the required concentration ratio of 1500 to 1. The optical quality of paraboloidal searchlight mirrors was considered acceptable based on test data, but the mirrors were too heavy. It was decided to make lightweight copies of these reflectors which would have the required accuracy without the weight of the original. The original was a 36 in. diam. Navy searchlight mirror with a $14\frac{5}{16}$ in. focal length. Honeycomb sandwich construction was selected because it is a rigid structure with low unit weight. Short development time was possible because of previous aircraft experience with honeycomb. The finished mirror, developed in six months, is shown in Fig. 1. Inflated and foamed shapes were considered but not used because they cannot be held to precise contours.[3]

A convex tool was made from the original concave mirror. First a parting agent was selected for separating the tool from the mirror. Conventional mold releases and sheet films were tried. "Simonize" auto wax was used as the parting agent for the 36 in. diam specimen reported here. The finished part was cured at 250 F to provide dimensional stability for long-time operation at 150 F. High curing temperature (accelerated aging) was one of the criteria for material selection. The cured materials also had to result in an optically smooth first surface.

The convex tool was "Simonized" and rubbed to a high gloss. A film of epoxy resin was spread onto the tool. The wet resin-coated tool was enclosed in a transparent vacuum bag and smoothed until it was appar-

VOL. 5 1961

FIG. 1—Lightweight Solar Concentrator.

ently uniformly covered with resin as determined by uniformity in color. Thickness was controlled to approximately one-sixteenth of an inch. After the resin was cured and the vacuum bag removed, a 2-mil fiberglass cloth was impregnated with epoxy and placed on the cured film. Honeycomb was laid on this wet fiberglass cloth. A second layer of impregnated fiberglass cloth was placed on top of the honeycomb to form a sandwich. A bag was placed over the assembly and a 3 psi effective pressure applied by partially evacuating the bag. The entire mirror assembly was then cured at 250 F. After curing, the replica was removed from the convex tool.

Research is continuing with vapor-deposited silver-mold release films on mirrors of various diameters. This method was used by Erbe and Haas[4] for a 7-in. diam solid epoxy mirror.

Several 36-in. diam honeycomb sandwich paraboloids were made and the best was selected for efficiency tests. This paraboloid was given a reflective first surface by applying a coat of aluminum in a vacuum chamber. A silicon oxide coating was deposited on the aluminum for protection of the reflective surface. A glass plate was aluminum-coated at the same time for purposes of quality control. Reflectivity of the coated glass was about 90 per cent at three different wavelengths within the visible spectrum.

Three problem areas were explored: surface, shape and weight. About ten per cent of the honeycomb mirror surface was spoiled by waviness due to first surface resin shrinkage. The amplitude of these waves was approximately 0.0001 in. These aberrations followed the honeycomb cell wall pattern.

A second problem was forming the honeycomb over the compound curvature of the tool without crushing the honeycomb. This problem could be solved in any of three ways: (1) contour machining; (2) using honeycomb with corrugated cell walls; and (3) slitting the cell walls of standard honeycomb. Contouring would have been too expensive. Corrugated cell wall honeycomb was too heavy. Slitted standard aluminum honeycomb was used. Three dimensional flexibility was achieved by slitting the honeycomb cell walls. This not only provided flexibility but also reduced the weight by removing material. The slitting operation was performed with the cell walls in a collapsed condition, as shown in Fig. 2. The honeycomb cells were then expanded by a stretching operation. The expanded, slitted honeycomb followed the shape of the convex tool in a satisfactory manner.

The third problem area was the achievement of the 0.2 psf design goal. Actual weights and ultimate goals are shown in Table 1.

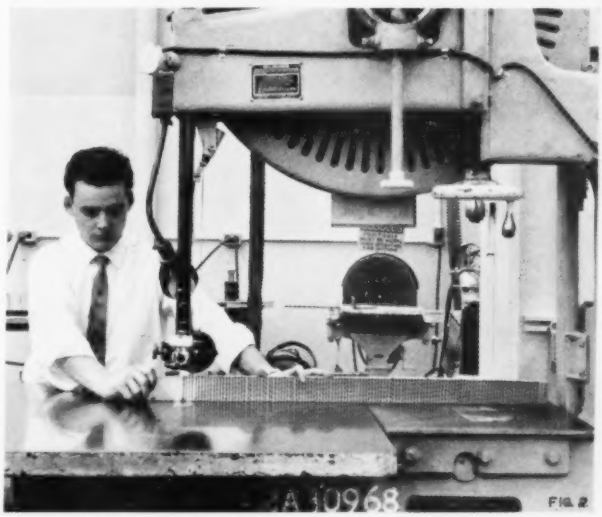

FIG. 2—Preparation of Flexible Honeycomb. Slitting of cell walls with bandsaw.

TABLE 1.—Weight Analysis

Description	Material	Actual Weights psf	Ultimate Goals psf
Films	Al and SiO	Negligible	Negligible
Substrate	Resin	.285	.130
Skin	Fiberglass	.025	.010
Core	Al honeycomb	.080	.050
Skin	Fiberglass	.020	.010
Subtotal without substrate....		.125	.070
		.410	.200psf

The weight of the completed paraboloid shown in Fig. 1, having a $\frac{1}{16}$ in. thick substrate is .410 psf. This mirror has a substrate thicker than necessary. The design objectives of 0.2 psf can be attained by reducing the substrate thickness, enlarging the slits in the honeycomb, and minimizing the amount of bonding resin.

TEST PROGRAM

A program was planned to provide useful engineering data by direct measurement. The colorimeter test setup is shown in Fig. 3. Solar energy intercepted by the mirror was calculated as the product of the effective mirror area times the normal-direct radiation intensity measured by an Eppley pyrheliometer. Masks with four different size holes were employed to vary the effective mirror diameter. The mirror to be tested was installed in an equatorial mount. The mirror was made to track the sun by rotating about the polar axis at a rate of one revolution per 24 hours.

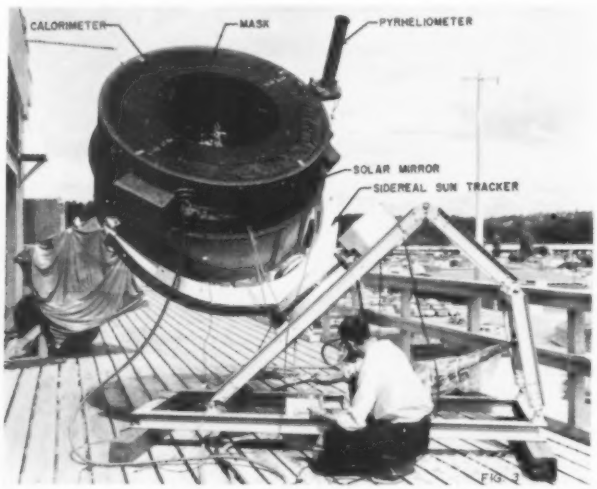

FIG. 3—Calorimeter Test Setup for Evaluating Performance of Solar Concentrators.

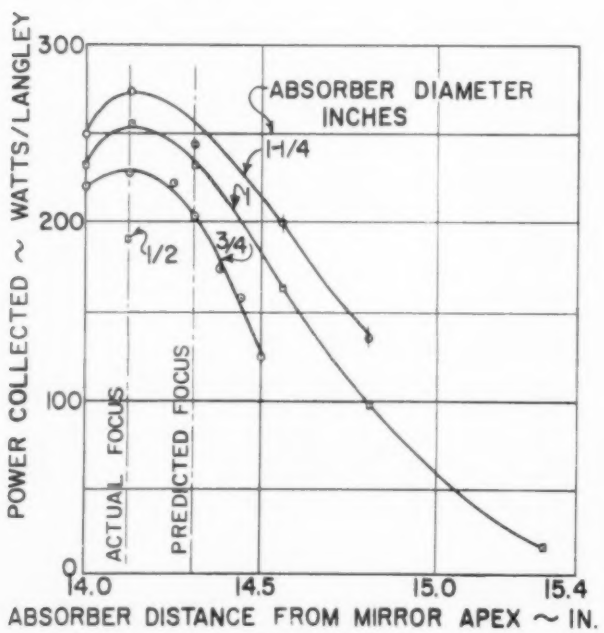

FIG. 4—Location of Focus Along Optical Axis.

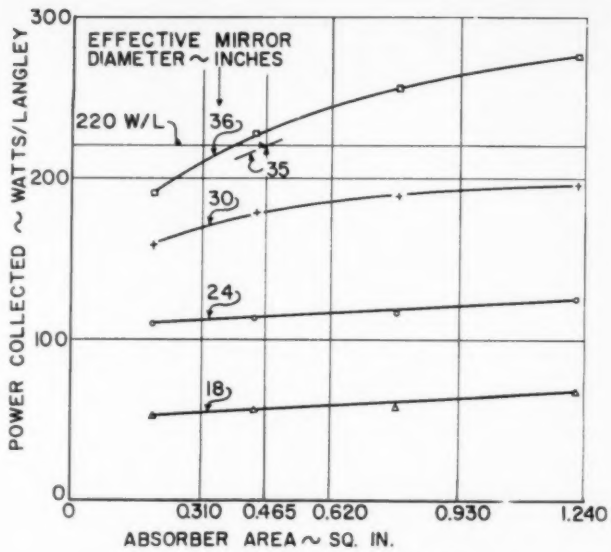

FIG. 5—Solar Power Collected at Focus.

Heat delivered to the focus was measured by the temperature rise of water flowing through a calorimeter. The calorimeter was a cavity type unit described by Glaser.[5] It had double walls, the outer walls protecting the cavity from stray heat inputs. The flow of water through the calorimeter was maintained constant by means of an overflow tank. Iron-constantan thermocouples were used for measuring the water temperature rise. These were calibrated prior to the test. Calorimeter iris openings of $\frac{1}{2}$, $\frac{3}{4}$, $\frac{1}{4}$ and 1P in. in diam were used to vary absorber diameter. Axial distances of the calorimeter from the apex of the paraboloid were measured with a scale placed through a hole in the paraboloid.

During the first series of tests the focus was located by scanning along the optical axis. The scanning produced curves of heat flux versus calorimeter location (Fig. 4). The focus was found at $14\frac{1}{8}$ in. from the apex. This is within $\frac{3}{16}$ in. from the focal length of the original searchlight mirror. All data were standardized to the mean sea level solar radiation intensity of a 45 degree earth latitude, that is, one g-cal per sq cm, per min (one Langley). Solar radiation is twice as intense at satellite altitudes. Therefore in space applications the heat flux values from Fig. 4 must be doubled.

During the next tests, the combined effects of varying mirror diameter and varying absorber area were determined. The calorimeter was located at the focus, $14\frac{1}{8}$ in. from the apex of the paraboloid. The effective mirror diam was varied with masks of 36, 30, 24, and

VOL. 5 1961

18-in. openings. The intercepted radiation varied as shown in Fig. 5. These results can be used directly as illustrated with the following example. A required heat flux of 220 watts per Langley and an absorber area of 0.465 sq in. necessitates a mirror diam of 35 in.

The data can be generalized by expressing them in terms of dimensionless parameters such as collection efficiency and concentration ratio. The collection efficiency is defined as the ratio of heat absorbed to intercepted solar radiation. The concentrator-to-absorber area ratio was also calculated on the basis of actual areas. The effective mirror area was $\pi D^2/4$ less the shadow of the calorimeter and of its supporting structure. The shadow varied from 0.40 to 0.58 sq ft for diam varying from 18 to 36 in. This variation was due to the increased length of the supporting structure. The collection efficiency is plotted on Fig. 6 against concentration ratio. Mirror diam-to-focal length ratios (D/f) are noted on the Figure. Maximum efficiency of 72% occurred at 310 to 1 area ratio and for $D/f = 1.70$. At a concentration ratio of 1500 to 1, typical for thermionic applications, the maximum efficiency was 62%. The reason for lower efficiency at higher concentration ratios is because the calorimeter aperture was smaller than the actual focal area. It is interesting to note that varying mirror diam does not cause a large change in efficiency, indicated by all four curves being close together.

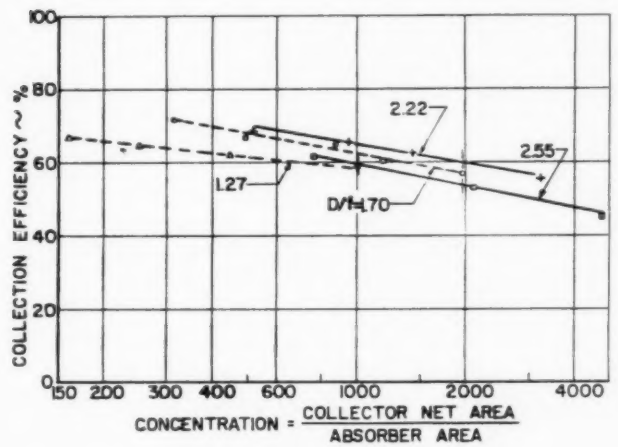

Fig. 6—Solar Concentrator Efficiency.

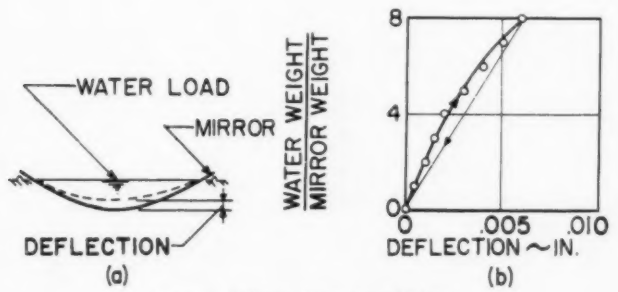

Fig. 7—Mirror Structural Test.

Table 2—Thermal Data

Thermal inertia of mirror substrate surface	0.400 Btu/°F-ft²
Thermal inertia of black surface	0.008 Btu/°F-ft²
Solar absorptivity of mirror surface	10% of black body
Thermal emissivity of mirror surface	2% of black body
Thermal emissivity of black surface	18% of black body
Thermal conductance through ¼" honeycomb	6 Btu/hr-°F-ft

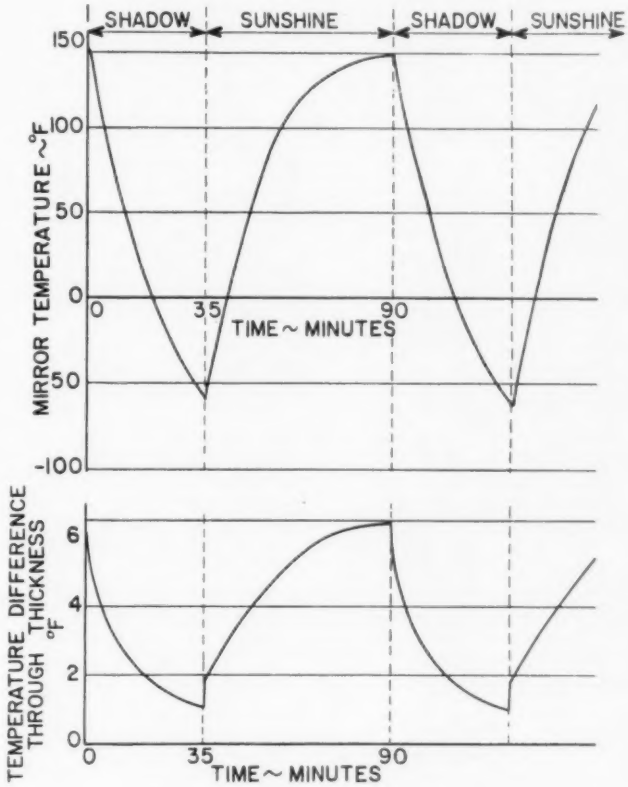

Fig. 8—Mirror Temperatures in Space.

The results are consistent and reproducible within ±2%. Therefore this direct method is satisfactory for testing solar mirrors.

A test was also run to determine residual effects of a simulated launch acceleration load of 8 G on mirror shape. A static load was applied by partially filling the paraboloid with water. The periphery was supported, as shown in Fig. 7a. The deflection was measured and is plotted in Fig. 7b. With the weight of water equal to 8 times the weight of the mirror, the deflection was only 0.006 in. When the water was removed the deflection vanished. This indicated that the load did not exceed elastic limits of the mirror.

ENVIRONMENTAL EFFECTS

The authors performed no environmental tests. Materials in a space environment were evaluated on the

basis of published information. Temperature effects have been studied only by analysis.

Lightweight sandwich mirrors might be expected to have a rather violent thermal behavior in space because of their low thermal inertia. Thermal inertia and other data pertinent to a 0.175 psf mirror are tabulated in Table 2. On any earth satellite, there will be inevitable periods of darkness. Entering earth shadow results in steep temperature drops, as shown in Fig. 8. Calculations indicate that a satellite orbit having 35 min shadow time and 55 min of sunshine causes the mirror temperature to vary between −63 F and +144 F. The maximum temperature difference between front and back was found to be 6.5 F. The focus would move outward 0.14 in. with the 6.5 F temperature differential through the mirror thickness. It would move an additional 0.04 in. under the temperature variations of the mirror surface between −63 F shadow and +144 F sunshine conditions. Approximate compensation for this problem can be made by placing the solar absorber $14\frac{1}{8}$ plus $\frac{3}{16}$ in. from the mirror.

Plastics are somewhat affected by space environment. Preston and Wahl[6] have published the results of experimental studies on the influence of ultraviolet and vacuum on structural plastics. They exposed samples of epoxy resin, "EPON 815", for periods up to 500 hr, to ultraviolet and visible light in the 2000–6000 Angstrom range, to pressures in the order of 1×10^{-6} mm hg and to temperatures up to 319 F. The weight loss by sublimation and evaporation was 0.85%. One half of this occurred in the first 24 hr. The tensile strength in bending dropped from 95,300 psi to 86,300 and the flexural modulus reduced from 3.7 to 3.5×10^6 psi. In this honeycomb mirror design, optical considerations dictated the conservative structural design. Accordingly, strength reduction due to a space environment will not be harmful.

It is estimated[7] that 5 to 10 per cent random degradation of the surface reflectivity will occur as a result of micrometeorites. Smallest size micrometeorites will do the maximum optical damage because of the large number of them. The effect of meteorites of larger size is probably negligible. Optical damage due to solar protons and other cosmic particles will probably be negligible because they effect areas less than one-quarter wave-length in magnitude.

CONCLUSIONS

1. Solar concentrators weighing as little as 0.2 psf that are accurate and yet rugged can be made from aluminum honeycomb sandwich by replica techniques.

2. For efficiency determination, test data rather than analysis is required. The calorimeter method of testing mirrors is suitable.

3. Tests show that a mirror weighing 0.41 psf is capable of 1500 to 1 concentration with 62% efficiency.

4. A 35-in. mirror weighing 2.9 lb is capable of supplying a thermionic generator with adequate heat in space to produce approximately 15 watts.

5. Environmental effects on performance require further analysis.

REFERENCES

1. Boeing document D2-5523, "Collection of Solar Thermal Energy for Space Power Supply Application," January 11, 1960.
2. Oman, Henry, and Street, G. "Experimental Solar Thermionic Converter for Space Use," a paper submitted for presentation at AIEE Pacific General Meeting, August 8–12, 1960, San Diego, California.
3. Boeing document D2-4161, "Mechanisms for Extending Nuclear and Solar APU's from Space Vehicles," June 3, 1959.
4. Bradford, A. P., Erbe, W. W., and Hass, G. "Two-Step Method for Producing Replica Mirrors with Epoxy Resins," *J. Opt. Soc. Am.*, **49**-10 (October, 1959).
5. Glaser, Peter H. "High Radiation Flux Absolute Waterflow Calorimeter," *Rev. Sci. Instr.*, **28**-12 (December, 1957), 1084–1086.
6. Preston, Harold M., and Wahl, Norman E. "Influence of Ultraviolet and Vacuum Environments on Structural Plastics," presented at the Institute of Environmental Sciences National Meeting, April 7–8, 1960, Los Angeles, California.
7. Henderson, R. F., and Stanley, P. "Effect of Micrometeorites on Reflecting Surface," presented at the Institute of Environmental Sciences, April 1960, Los Angeles.

VOL. 5 1961

A Direct Current Motor Integrator for Radiation Measurements

By P. Schoffer* and V. E. Suomi†

A d-c motor integrator amplifier is described in which the motor speed is made proportional to the input signal; accumulated number of revolutions represents the integrated input. Application is made to integration of solar radiation, using an input from an Eppley pyrheliometer.

INTRODUCTION

Solar radiation data are usually reported and used in the form of hourly or daily integrated values. These integrated data are usually obtained by graphical integration of potentiometer-recorder radiation records. These methods are not completely satisfactory and are particularly uncertain on partly cloudy days. They require relatively expensive potentiometer recorders which can, at additional expense, be provided with integrators (usually of the ball-and-disc mechanical type). This paper describes an instrument which can integrate the output of an Eppley pyrheliometer (or other radiation detection device) and record or indicate the integrated radiation at desired time intervals.

Although analog integrators (e.g., wattmeters) have been in use for many years, they are still little used for continuous short-interval integration of natural phenomena. No inexpensive integrator is at this time available on the market; however, several integrators of various designs have been developed for specific purposes.[1, 2] Table 1 gives a survey of some of the possible types of integrators which can be used with low-level electrical input.

Classification of Integrators

The electromechanical systems appear to be the simplest methods, and since wattmeters are being mass-produced and are quite accurate, they seem a logical choice. However, the standard type wattmeter is a high-level long-term integrator-multiplier not directly useable with low-level input from radiation detectors. For short interval use a direct read-out from the rotor disc is needed, and since the torque is low, a photoelectric or equivalent read-out is needed. Further requirements are a regulated a.c. for the current coil and a linear direct-coupled amplifier with reasonably constant output wave-shape. (In mass production the wattmeter would be custom made with the correct coils.)

A d-c wattmeter and a d-c motor with a permanent magnetic field are also useable[2] but they too suffer from a lack of available torque and are expensive. A pure electrical system was also considered whereby a capacitor is charged and discharged at a rate controlled by the input as in analog computers. Here the problem of too much definition (with reasonable capacitor size and loss) makes frequency-divider circuits necessary. Also stable over-all feed back is difficult to obtain.

A d-c motor-amplifier integrator, with rate feedback over the amplifier-motor combination, for 5 mv or higher full-scale input, which can be built with standard components, was chosen for this study.

THEORY OF THE INTEGRATOR

The integrator consists of a conventional chopper-amplifier driving a permanent field d-c motor with half-wave pulses. The other half-wave period is used for sampling the motor emf, and during this period the motor acts as a generator. The generated emf is attenuated and subtracted from the input signal (degenerative feedback). The motor speed is thus made proportional to the input signal, and accumulated number of shaft revolutions represents the integrated input.

Several other types of circuits were considered. With a balancing circuit it is possible to separate the emf from the motor input while the motor is being driven. However, the commutator resistance of a small motor is too variable to permit sufficient accuracy with this technique. A motor and rate feedback generator combination was considered too costly.

Neglecting phase shifts, the following equation can be derived for relationship between motor emf and input voltage of the motor-amplifier arrangement:

$$e = \frac{uG - \mathrm{IR}}{1 + \beta G}$$

Where:

G = open loop gain of the amplifier
e = motor emf
IR = voltage over the internal resistance of the motor
u = the input voltage to the amplifier
β = the feed-back ratio of e

* Solar Energy Laboratory, University of Wisconsin.
† Department of Meteorology, University of Wisconsin.

TABLE 1.—Types of Integrators for Analog Input

Classification	Principle	Example	Integrates	For Low level Electrical Input, Must be Used with:
1. Mechanical, static	a. Variable speed reduction	Ball & disc integr.	Position	Balancing type indicator/recorder
Mechanical, dynamic	b. Switch + adder	Digitizer-summer	Position	Balancing type indicator/recorder
2. Electro-mechanical	a. a-c motor	Wattmeter	Power, I, V	Amplifier
	b. d-c motor	Low torque P.M.-motor	Voltage	Amplifier
3. Electro-Chemical	Electrolytic mass transfer	Electroplating	Current	Amplifier
4. Electrical	Current or voltage storage	R-C network (analog computers)	Voltage, current	Amplifier
5. Thermal	Thermal mass transfer	Distillation	Heat	Amplifier-heater

Then

$$e = u\,\frac{G}{1+\beta G} - \frac{\mathrm{IR}}{1+\beta G}$$

If G is large $G/(1+\beta G)$ will be practically constant and e will be proportional to u except for the second term, which will shift the e-u characteristic off zero. In addition, I is variable because of torque variations with speed, making the e-u curve nonlinear near zero. The second term also varies with G. To eliminate this nonlinear quality in e and thus in n, (assuming the motor speed n is proportional to e) an additive feed-back voltage proportional to the motor current is used. This feedback is α IR (regenerative feed-back):

$$e = u\,\frac{G}{1+\beta G} + \frac{\alpha G\ \mathrm{IR} - \mathrm{IR}}{1+\beta G}$$

The second term will disappear if $\alpha G = 1$ (i.e., if the output resistance is infinitely high). However, G is variable causing drift in zero. To make the second term as small as possible and because there is a limit to d-c feed-back due to instability of the system at high feedback ratios, a-c feed-back is also used:

$$e = \frac{uG - \mathrm{IR} + \alpha G\ \mathrm{IR} - \delta G\ \mathrm{IR}}{1+\beta G+\delta G}$$

where δ = a.c. feed-back ratio. Or, in other words, the a-c open-loop gain is made more constant. There is remaining drift in zero caused by variability of R, which is minimized by the d-c feedback.

DESCRIPTION OF THE CIRCUIT

Figure 1 shows the circuit of the transistorized amplifier which can be driven in both positive and negative directions. The input circuit consists of a 60 cps filter and half-wave chopper and does not use an input transformer. (A conventional input circuit could be used with probable improvement in accuracy and at additional expense.) The amplifier has an a-c feedback which is variable to adjust the gain. The last stage is tuned to 60 cps to remove harmonics and to correct for phase lags in the amplifier. The demodulator consists of compound emitter-follower (npn and pnp) transistor circuits with a 60 cps collector supply.

Feed-back pulses are connected to the emf feed-back network by the second set of contacts of the double-pole chopper. They are peaked by an RC circuit with a large time constant to make the feedback more independent of the chopper cycle and to filter out a-c components. IR feedback is taken from a resistor in series with the motor. Both emf and current feedback are adjustable.

It is necessary to have a zero adjustment because of unsymmetry of the output circuit. The power transistors must be rated for the full transformer peak voltage (35 volts), and they should cut off completely in the "off" phase. The motor emf can be checked during operation with a vacuum tube voltmeter which thus gives a continuous indication proportional to the speed of the motor.

Some selection is necessary for the transistors. For the input transistor X1, a d-c gain of more than 40 is necessary, while for X5 not every 2N169A transistor is useable because of a too low cutoff voltage. (The collector-emitter voltage of X5 can reach 48 volts, which is higher than the rating of a 2N169A.) X7, a pnp transistor, has to be similar in characteristics to X6, and this is more difficult because pnp transistors have in general a much higher I_{cbo} (leakage current). A 2N217, selected for low leakage and matched to a 2N169A, is used. The amplifier and output circuits, as shown on Fig. 1, are built on plug-in etched circuit boards.

The transistorized integrator is adjusted for an input of approximately 2.5 mv at e = 1.4v. The motor is a Haydon Mfg. Co. d-c timing motor with a nominal speed of 8 rpm at 6v and 70 ma. At an emf of 1.4v the motor speed is close to 300 rph ($\frac{1}{2}$ scale point). The over-all open-loop d-c gain of the motor-amplifier, e/u, is approximately 18,000; d-c degenerative feedback, βG, is approximately 30. IR is approximately 1.3v at e = 0.2v. The time constant of the combination is less than $\frac{1}{2}$ sec. The amplifier open-loop gain, E/u, is approximately 100,000 and quite constant between 60 F and 110 F. The temperature range can be changed by

VOL. 5 1961

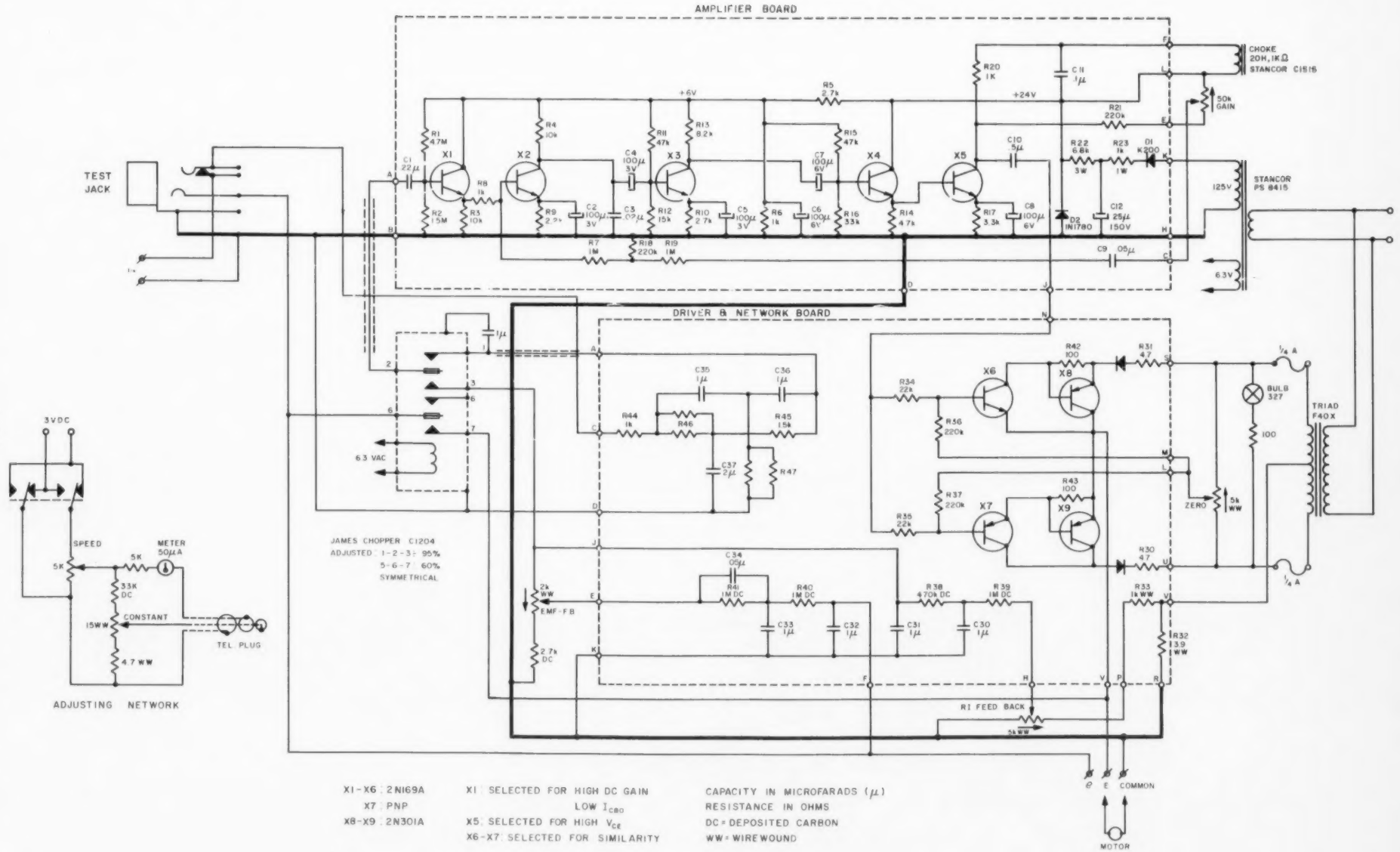
AMPLIFIER BOARD
DRIVER & NETWORK BOARD
TEST JACK
CHOKE 20H, 1K Ω STANCOR C1515
50k GAIN
STANCOR PS 8415
125V
63V
JAMES CHOPPER C1204
ADJUSTED: 1-2-3: 95%
5-6-7: 60%
SYMMETRICAL
63 VAC
3VDC
SPEED
METER 50μA
CONSTANT
TEL PLUG
ADJUSTING NETWORK
EMF-FB
R1 FEED BACK
BULB 327
TRIAD F40X
ZERO
MOTOR
e
E
COMMON
X1-X6: 2N169A
X7: PNP
X8-X9: 2N301A
X1: SELECTED FOR HIGH DC GAIN LOW I_{CBO}
X5: SELECTED FOR HIGH V_{CE}
X6-X7: SELECTED FOR SIMILARITY
CAPACITY IN MICROFARADS (μ)
RESISTANCE IN OHMS
DC = DEPOSITED CARBON
WW = WIREWOUND

Fig. 1
31

changing the base bias of X1. The total power consumption at full speed of the motor is approximately 5w.

ADJUSTMENT OF THE CIRCUIT

Because of the many variables (zero, amplifier gain, positive and negative feedbacks) which have to be adjusted, it is necessary to use a voltage divider network. This adjusting network can either be built into the system or connected externally; it is shown on Fig. 1. The divider is set at a known ratio and its output drives the integrator. The motor emf is now compared with the input voltage of the voltage divider by means of a meter. By varying the input of the voltage divider the whole range of motor speeds can be checked.

The zero control is adjusted for symmetry at positive and negative speeds. The e feedback is adjusted at near full-speed range and the IR feedback at a quarter range. IR and e feedback are interrelated, so it is necessary to readjust them several times.

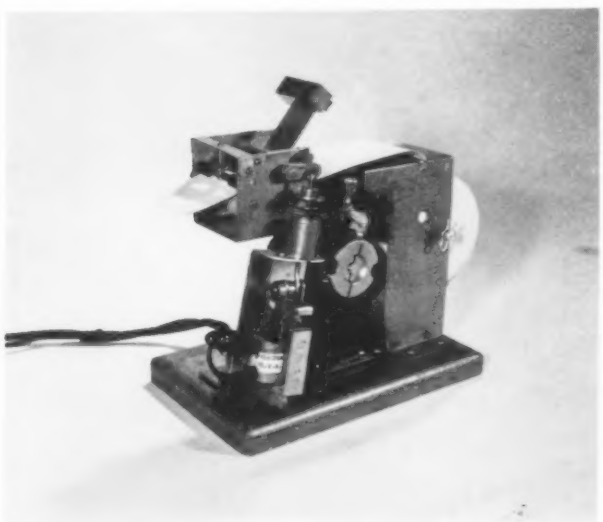

FIG. 2—Photo of Printer Utilizing a Veeder Root Pulse Counter.

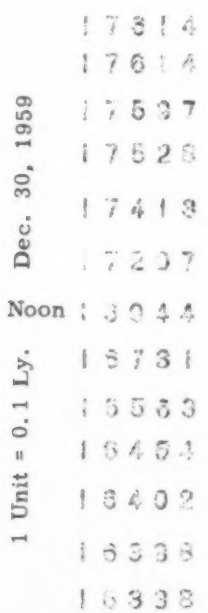

FIG. 3—Sample of Record from the Recorder shown in Figure 2. Registration is Hourly, without Reset; Hourly Values are Obtained by Difference of Successive Numbers.

PRINTING

Display and registration of the integrated values can be accomplished in several ways. The motor can drive a counter directly (necessary for two-way integration, e.g., for net radiometer) or actuate a switch which in turn closes the circuit for a pulse counter. The counters can then be photographed at regular intervals, or they can be provided with number wheels which can print directly on paper. The least expensive printer used in this study is built around a Veeder Root pulse counter. Printing is accomplished by a solenoid-operated hammer; the solenoid also operates the paper advance through a ratchet mechanism and is actuated hourly by a separate timer. An adding machine copying paper is used which does not need ink. A photograph of this printer is shown in Fig. 2; a sample record from it is shown in Fig. 3. It is also possible to use solenoid driven adding machines, computer read-outs, traffic counters with automatic reset, and other similar devices.

EXPERIENCE WITH THE INTEGRATOR

The transistorized integrator described above is a recent development. It has evolved from a series of integrators partially transistorized. The readings of a similar integrator using a vacuum tube amplifier have been compared with clear day solar radiation records, taken from a potentiometer recorder connected to the same Eppley phyheliometer, over a period of six months. (The integrator can be connected to the same circuit as the recorder if the integrator is stable at all times.) The accuracy above 5 per cent of the total range was better than 1.5 per cent of full scale; below that range dissymmetry and other effects decreased reproducibility. The transistorized model discussed above does not exhibit this dissymmetry and has a generally higher accuracy because of improvements in the demodulator circuit.

ACKNOWLEDGMENT

These studies are a part of the Solar Energy Research Program of the University of Wisconsin, and have been supported by the Rockefeller Foundation.

REFERENCES

1. Kassander, A. R., and Knowles, L. L. "An Automatic Printing and Totaling Device for Solar Radiation Measurements," *Trans. Conference on the Use of Solar Energy—The Scientific Basis*, Tuscon, **1** (1955), 48.
2. Blackwell, M. J. "Report on the Automatic Integration of Solar Radiation at Kew Observatory," *G. Brit. Meteor. Res. Comm. M.R.P.* No. 862 (May 12, 1954).

VOL. 5 1961

Solar Abstracts

Prepared by Milton D. Lowenstein, Director, Technical Research Service Center

Abstracts, it may be observed, are useful to the extent that they are readily available at those critical moments in research and development activities when the advancement of a project depends upon objective and well recognized authority.

The Solar Energy Technical Research Service Center is establishing a source of information and a routine for supplying data as soon as they are received and processed. All the material in the library, correspondence on technical metters and research reports are being classified and arranged for quick retrieving of useful information.

As a record of each member's fields of interest is in our file, appropriate data can be expedited to where they may be needed."Uniterm" type and punch card systems and ultimately computers will aid in the retrieving process.

Until the system is fully organized, members will receive, periodically, bibliographies of current literature in the Research Service Center library of AFASE. The most important of these papers will be abstracted for the Journal.

Your suggestions for further improvements will be welcomed by the director of the Technical Research Service Center.

Chapin, D. M. "How to make solar cells." Reprinted from *Radio-Electronics*, March, 1960. Bell Telephone Laboratories, Murray Hill, N. J. 3p. Illus.

The outline below gives an overall picture of the process.

1. The silicon wafers, obtainable from International Rectifier Corp., are lap-ground with 280 mesh carborundum.
2. The cells are lightly etched in a mixture of HNO_3 (nitric acid) and HF (hydrofluoric acid).
3. One surface is painted with a solution of boric acid, boric oxide or commercial grade borax.
4. To diffuse the boron into the surface, wafers are heated in air for about 10 minutes.
5. The untreated side is again lap-ground with carborundum.
6. The cells are treated with HF to remove oxides.
7. Part of the diffused surface is covered with acid-resisting tape.
8. Exposed surfaces are electroplated in electroless nickel-plating solution. (The formula and summary of the process appear later in the article.)
9. Plated surfaces are tinned with solder, and leads are attached.
10. The edges of the wafer are ground with carborundum.
11. HF and HNO_3 etchant is applied to the edges to complete the separation of *p*- and *n*-areas.

Abstracts of American Rocket Society papers relating to solar energy presented at the American Rocket Society Space Power Systems Conference, Santa Monica, California, September 27–30, 1960. (ARS preprint number of each paper is shown in parentheses)

Denney, J. M. "Radiation Damage in Satellite Solar Cell Power Systems", (1295–60).

The performance of satellite power supplies provides a cross comparison of measured radiation intensities in space with experimental radiation damage in solar cells. The results of such comparisons further provide a means of applying displacement theory and data on annealing of point defects in silicon to the formulation of lifetime estimates for solar cells in space. These analyses, using the experimental results presented in a previous paper, show favorable agreement with satellite power supply performance.

* * *

Dowing, R. G. "Electron Bombardment of Silicon Solar Cells", (1294–60).

Silicon solar cells were irradiated with 530 kev electrons to determine the effect of electron radiation similar to that encountered by satellites on the efficiency of solar cells. The experiments show that an integrated flux of about $5 \times 10^{13} e/cm^2$ reduces silicon solar cell efficiency by about 25 per cent. Additional experiments using quartz and glass shielding for radiation protection show the suitability of reducing the radiation damage by this technique. Combining the experimental results with the simple theory, 0.065 inches of quartz or glass are indicated as necessary to provide protection from 800 kev electrons in the trapped radiation bands.

* * *

Eerkens, Jozef William, Reder, Martin C. "Closed-Cycle Monopropellant Fuel Cell System Employing Radiation-Generated or Photochemically Generated Ozone", (1306–60).

A new photochemical/nuclear energy conversion system is described which is based on the following conversion steps. Kinetic energy of photons or nuclear particles (gammas, betas, protons, alphas, fission fragments) is transferred into chemical energy of recombination through the exposure of oxygen to sunlight in the exosphere or through irradiation of oxygen in a nuclear chemogenic reactor or isotopic irradiator, which causes oxygen to recombine (partially) to ozone after photolysis or radiolysis. The efficiency of this chemical energy storage process varies between 10 and 15% depending on the operating conditions. The ozone (mixed with oxygen) is then passed over a specially treated porous electrode of a fuel cell, at which the ozone reacts with the electrolyte according to reaction (1). At the other electrode of the cell, oxygen is liberated according to reaction (2). The over-all reaction (3), is the formation of oxygen from ozone with the liberation of two 0.84 eV electrons.

By recycling the anodic oxygen to the sunlight exposure region, or to the irradiator or reactor, it is converted to ozone again and a closed-cycle system is obtained.

Elliott, James F., Meikleham, Mrs. V. F. "Large Area Solar Cells", (1290–60).

The utility of photovoltaic solar energy converters to supply large amounts of power (i.e., 0.5–100 kw) will probably be determined by the ability of the industry to supply large area solar cells. Theoretical arguments have been advanced which indicate that polycrystalline silicon prepared by thin film techniques and/or by mechanical deformation of ingots into sheets can be used for cell construction. These two approaches to large area cells are being investigated. Both programs have had promising initial success and the experimental results are discussed.

* * *

Finger, Harold B., Schulman, Fred. "Power Requirements of the NASA Space Program", (1333–60).

This paper discusses the overall power requirements for some established space missions, and missions that are still being studied and evaluated. Both auxiliary power and propulsive power missions will be considered.

* * *

Hamilton, Robert C. "Ranger Spacecraft Power System", (1345–60).

Oriented silicon photovoltaic cells provide the basic power source for the Ranger spacecraft. An attitude control system positions the spacecraft so that solar radiation impinges vertically on the solar cell panels. Primary silverzine batteries provide power during the launch phase, prior to sun acquisition, and during guidance maneuvers when the solar radiation incident on the photovoltaic cells is inadequate to power the Ranger spacecraft.

* * *

Hirsch, R. L., Holland, J. W. "Problems Associated with the Development of a Thermionic Conversion Reactor", (1338–60).

This paper describes a conceptual design of a 300 kwe thermionic space power reactor with a subsequent discussion of associated development requirements.

* * *

Kerr, Douglas L. "Thermoelectric Elements in Space Power Systems", (1277–60).

This paper presents a discussion of some of the characteristics, potentialities, and problems encountered in the design of thermoelectric generators for space applications. One means of classifying the basic configurations possible is according to the means of rejecting heat from the cold junction, i.e. whether it is to be a secondary heat transfer fluid which in turn passes through the radiator or whether the generator waste heat is carried directly to the radiating surfaces by thermal conduction from the cold junctions. Presented herein are results of some studies which have been made of the latter case where the generator is integral with the radiator. Two types of construction have been investigated which can be termed the "sandwich" type and the "side fin" type. Estimates of the minimum weight obtainable from each are presented for particular materials properties. Comparison of these indicates that a combination of the two types of construction will result in the least weight.

* * *

Kurnick, S. W., Fitzpatrick, R. L., Leavy, J. F. "High-Temperature Semiconductors for Thermoelectric Conversion", (1274–60).

At the high end of the temperature scale (800°K–1600°K), new semiconductors are receiving emphasis in development. $CeS_{1.33-1.50}$ is such a semiconductor, and at present the material is sufficiently optimized to give zT's of 0.1 and above. The study of this semiconductor (n-type) is implemented by the study of a p-type semiconductor $ThS_{1.71-1.76}$. Progress to date on these materials is discussed. The measurement of the thermal conductivity of Ce-S at high temperatures, usually very difficult to make, is made by a small-area-contact technique developed at General Atomic.

* * *

Miller, R. C., Ure, R. W., Jr. "Thermoelectric Generator Materials", (1273–60).

Some of the best materials known at present which are suitable for use in thermoelectric generators are Bi_2Te_3 and its alloys, PbTe, the III–V compounds, MnTe, GeTe, and CeS. The properties of these materials which are important for their use in thermoelectric generators will be discussed. A theoretical maximum efficiency of 18% would be obtained with these materials working between 30°C and 1030°C, provided that all the design and fabrication problems can be successfully solved.

* * *

Nottingham, Wayne B. "Review of the Physics of Thermionics", (1281–60).

Heat may be converted directly to electrical power by means of either the vacuum or the plasma thermionic diode. The latter holds the greater promise of being valuable for space-power applications. The input heat is delivered to the emitting surface and the excess heat is radiated from the cooler electron collecting surface. The efficiency of a device depends on the use of a low work-function collector and a minimum of unwanted heat losses. The best gas for the plasma seems to be cesium which serves to eliminate space charge and conduct the electric current across the diode. Some of the basic concepts related to the plasma diode are presented.

* * *

Queisser, Hans J., Shockley, William. "Some Theoretical Aspects of the Physics of Solar Cells", (1293–60).

Any theoretical treatment of the photovoltaic effect in semiconductors must be based on a thorough understanding of the current-voltage characteristic of a p-n junction. All previous work used the "ideal rectifier equation", a two parameter formula which correctly describes germanium junctions. In order to account for the experimental values of materials which are of interest for solar energy conversion, the two parameters had to be changed enormously from their predicted values in an entirely arbitrary fashion. This clearly shows the inadequacy of the present theory. In the approach proposed here, emphasis is laid on the hole-electron recombination processes which limit the output voltage of a solar cell. A maximum efficiency may be calculated for the case of minimum recombination which is only the radiative one, as required by statistics. Non-radiative recombination prevents reaching this ultimate efficiency. Proposals are made to predict the current-voltage relationship and the efficiency of a solar cell from first principles with the aid of a theory of recombination processes.

* * *

Snyder, N. W. "Solar Cell Power Systems for Space Vehicles", (1309–60).

On May 3 and 4, 1960 a symposium was held under the sponsorship of the Advanced Research Projects Agency by the Institute of Defense Analyses. Ten programs involving solar cell power systems for current U. S. space vehicles conducted under government sponsorship were discussed by the project engineers who directed these programs. This paper will highlight and summarize the results of that symposium for this session, where possible.

VOL. 5 1961

Thiele, A. W., Coombs, M G. "SNAP Thermoelectric Systems", (1330–60).

In the range of moderate electrical power requirements (approximately 1 kilowatt) thermoelectric power conversion techniques offer many advantages in the design of nuclear auxiliary power units for space application. The current temperature capability of the lead telluride class of thermoelectric materials, in the vicinity of 1100 F, can easily be met with the demonstrated performance of the SNAP reactor systems. Minimum system weights are obtained at Carnot cycle efficiencies of the order of 25%, yielding a total system efficiency of about 3%.

Winkler, Seymour H., Stein, Irving, and Wiener, Paul. "Power Supply for the Tiros I Meteorological Satellite", (1347–60).

It was decided to have no unfolding, latching or extending mechanisms on this early-generation satellite. This meant that the solar-cell power supply had to be part of the fixed skin which covered the vehicle instrumentation. It was also decided that the satellite should be cylindrical in shape and spin-stabilized with a disc-shaped mass distribution, so that it would continue to spin about its figure axis. Furthermore, all thermal control was to be passive and was to be achieved in the design by the selection of proper materials to obtain optimum thermal characteristics for the fixed outer surface, and by the thermal inertia and coupling of the overall system.

VOL.
5
1961

A Solar Energy Pilot Plant for Northern Chile

By Julio G. Hirschmann

Universidad Téchnica Federico Santa María, Valparaiso, Chile

From the point of view of solar energy, the climatic conditions in the deserts of northern Chile are unusually good. Various industrial solar energy plants have been operated in this region. The historical development, present applications, and extensive research being undertaken in this field by various Chilean universities is described. As part of this research program the author also discusses his projected design for a self-supporting solar energy pilot plant which would produce 4,500 gallons of distilled water per day and generate 50 kw of electricity. Such a plant would have many applications in the arid deserts of northern Chile where the river and well water is too salty for irrigation purposes. Finally, the pilot project is compared with a much larger coastal thermal energy plant designed by A. E. Snyder.

The author read Asa E. Snyder's paper[1] about a power and sea water conversion plant with great interest, because this project is quite similar to a pilot plant proposed nearly two years ago for northern Chile.[2] Before discussing the differences between these two projects it may be useful to discuss first the general situation in Chile and then give a description of the pilot plant under consideration.

It is well known that one of the best regions in the world for the utilization of solar energy is the desert of Atacama near Antofagasta in the north of our country. According to publications of the U. S. Weather Bureau[3] the total annual hours of sunshine there reaches an average of 4,000 hours, compared with a theoretical world maximum of 4,383 hours. In that region the conditions are especially good, owing to the fact that the soil is fixed by nitrate salts, which prevent the formation of dust storms such as are prevalent over other deserts.

It is also well known that in the place named Las Salinas, a station on the railway from Antofagasta to Bolivia, a U. S. citizen, Charles Wilson, designed and built the first industrial solar heat collector in the world, as long ago as 1874, and used it for distillation. Nearby, in the Oficina Domeyko mine, a similar solar distillation plant worked successfully for some time.[4] The still of Las Salinas had an area of 4757 m² (51,200 ft²) and produced 22.5 m³/day (6000 gal/day) of distilled water.[5]

FIG. 1.—Present View of the Site of the First Industrial Solar Still.

This solar still was used successfully for more than forty years, and only after the completion of the first fresh water pipe line from the Andes down to Antofagasta was it abolished. Five years ago Maria Telkes published a photograph[6] of this still taken in 1908. Fig. 1 shows a photograph taken recently at the same site during a visit by Prof. John Duffie of the University of Wisconsin. As can be seen, all that remains are some trenches and a great many splinters of glass.

But meanwhile, at Coya, not far from Las Salinas, the nitrate company, Cia. Salitrera Anglo Lautaro, has built ten large solar evaporation ponds. Each of these ponds (Fig. 2) has an area of 44,000 m² (473,600 ft²) and vaporizes 236 m³ (8,336 ft³) per day or an average of 5.34 dm³/m² day (0.1311 gal/ft² day). The quantity of oil saved by this method of evaporation is approximately 158 t/day (3460 cwt/day). Considering that all fuels must be brought to this region from far away, these ten solar evaporaters may be considered very successful, but it should not be forgotten that from a thermodynamic viewpoint their efficiency is very low because the latent heat of evaporation is completely lost.

Francois Desvignes and German Frick[7] took solar

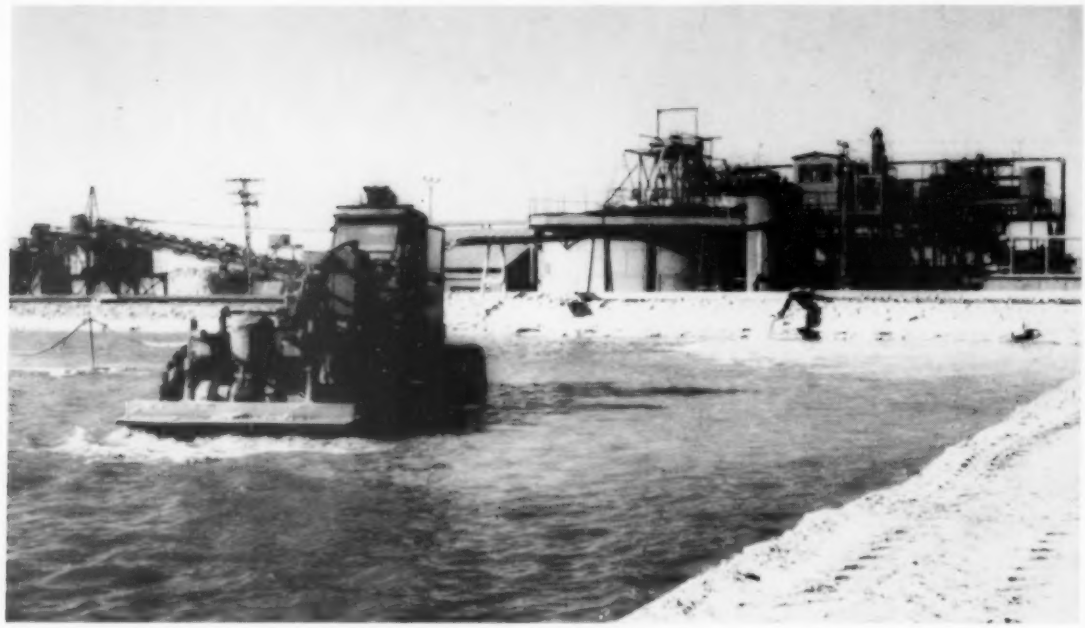

FIG. 2.—Evaporation Pond in Coya, with "Elephant," a Specialized Machine which Removes Crystallization and Pumps Away the Concentrate Once the Evaporation is Finished.

TABLE 1—Solar Evaporation in Coya

Month	Mean Daily Incident Solar Energy E_i		Mean Daily Evaporation*		Mean Daily Vaporization† Heat H_v		Efficiency $\eta = \frac{H_v}{E_i}$
	kcal/m² day	Btu/ft² day	dm³/m² day	US-gal/ft² day	kcal/m² day	Btu/ft² day	
I	7620	2809	7.00	0.1718	4200	1548	0.551
II	7172	2644	5.90	0.1448	3540	1305	0.494
III	6328	2333	5.86	0.1438	3516	1296	0.556
IV	5452	2010	4.54	0.1114	2724	1004	0.550
V	4408	1625	3.71	0.0911	2226	821	0.505
VI	3924	1447	3.48	0.0854	2088	770	0.532
VII	4408	1625	3.82	0.0938	2292	845	0.520
VIII	5452	2010	3.94	0.0967	2364	872	0.434
IX	6328	2333	5.44	0.1335	3264	1203	0.516
X	7172	2644	6.29	0.1544	3774	1391	0.526
XI	7620	2809	6.23	0.1529	3738	1378	0.491
XII	7929	2920	7.91	0.1941	4746	1750	0.599
Mean	6150	2267	5.34‡	0.1311	3204	1182	0.52

* July 1959 to June 1960.
† latent heat of vaporization assumed to be 600 kcal/kg (1080 Btu/lb).
‡ yield of clean water was 4.28 dm³/m² day (0.105 gal/ft² day).

measurements in the desert of Atacama from September 1957 to September 1958. Based on these measurements Victor Bociš[8] established mean monthly curves of solar energy incidence using a monthly average of cloudless days. By planimeter the author obtained from these curves the values of mean daily incident solar energy (E_i) given in the first column of Table 1.

The second part of the table shows the mean daily evaporation measured in the ponds of Coya by the Anglo-Lautaro Nitrate Company and its equivalent vaporization heat (H_v). Finally, the efficiency was calculated as the ratio between this heat and that of the theoretical incident solar energy. In Fig. 3 a graphical representation of both heats is given. As one may see, a well marked relationship exists between the monthly variation of vaporization heat and incident solar energy. Therefore, it must be concluded that the low humidity of air in this region does not have as much influence as has been assumed by some authors. This is also corroborated by the fact that the mean daily evaporation of clean water at the same place is nearly 20 percent less than that of the colored nitrate solution, which the solar-evaporation ponds are used to concentrate.

At the present time, the evaporation ponds of Coya are the only industrial utilization of solar energy of

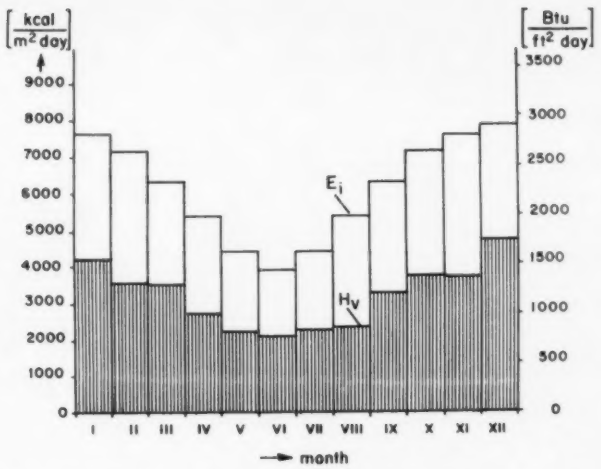

FIG. 3.—Incident Solar Energy E_i and Vaporization Heat H_v of Evaporation Ponds in Coya.

importance in Chile. Nevertheless, there are many projects for other uses of solar energy, and at least three university centers: Research Department for the Northern Zone dependent on the Northern Zone University Centre of the University of Chile (Departamento de Investigaciones de la Zona Norte dependiente del Centro Universitario Zona Norte de la Universidad de Chile), Research Centre for Applied Solar Energy (CIESA) of the University of the North, affiliated with the Catholic University of Valparaiso (Centro de Investigaciones de Energia Solar Aplicada (CIESA) de la Universidad del Norte filial de la Universidad Catolica de Valparaiso), and Engineering School of the Federico Santa Maria Technical University of Valparaiso (Escuela de Ingeniería de la Universidad Técnica Federico Santa María de Valparaiso) are contributing to research in the different fields of applied solar energy.

One of the greatest obstacles to development in the northern provinces of Chile is the scarcity of fresh water. The shortage is so acute that in some places the water needed by miners reaches $15.00 (U.S.) per m³ ($57 per thousand gal). For this reason the engineering school of the Universidad Técnica Federico Santa María has been working for several years on salt water distillation projects utilizing solar energy.

Under the author's direction Victor Bocič developed a project for a pilot plant which uses solar energy to distill salt water and simultaneously generate electric power. Figure 4 shows a scheme of that plant. After heating the salt water in the solar collector (1) up to the desired temperature it passes to the accumulator (2) where air is separated from liquid. The heated salt water leaves the accumulator and enters the vacuum vaporizer (3). In this vaporizer, maintained at low pressure by the vacuum pump (10), part of the water vaporizes, absorbing the necessary heat from the rest of the water. Steam and water leave the vaporizer at the same temperature. The steam passes to the turbine (4) where part of its heat content is transformed into mechanical energy which by means of the reduction gearing (5) and the generator (6) becomes available as electrical energy.

The turbine exhaust steam is condensed (7) and leaves the plant as distilled water. The condensation heat is utilized in part to preheat the salt water which enters the solar collector after passing through the heat exchanger (8). In this heat exchanger the concentrate coming from the vaporizer gives part of its heat to the less concentrated salt water which enters from the river or well (12) via the condenser.

The pumps (9) maintain the circulation of incoming water, concentrate, and distilled water. The valves (11) control the amounts of steam generated and concentrate removed.

Victor Bocič[9] has calculated the best thermodynamic and economic operating conditions for a plant of 50 kw, assuming the temperature of incoming salt water to be 18 C (64.4 F) with a temperature increase to 70 C (158 F) in the solar collector. Under these conditions the plant would produce an average of 9.5 m³ (2,500 gal) per day of distilled water. In this case the proportion between steam produced and salt water heated in the collector is 36 kg per m³ (0.30 lb per gal) of salt water taken into the solar collector. With this proportion each m³ of salt water which enters the collector produces 36 liters of distilled water (one gal of salt water produces 0.036 gal of distilled water).

Salt water enters the condenser at a mean temperature of 18 C (64.4 F) and discharges at 27 C (80.6 F). Only 45 per cent of the water used for cooling the condenser enters the heat exchanger: the other 55 per cent is expelled. The temperature of salt water in the heat exchanger increases to 44 C (111.2 F) and finally reaches 70 C (158 F) in the solar collector. Steam and concentrate leave the vaporizer at a temperature of 50 C (122 F) and in the heat exchanger the concentrate temperature drops to 31 C (87.8 F). The steam temperature was established in accordance with the author's previous thermodynamic investigation[10] of steam-power cycles with vacuum vaporization.

Table 2 gives the heat balance for the total process. It is divided into two sections: one for the primary circuit of salt water and concentrate, and the other for the secondary circuit of steam and condensate. Figure 5 shows the Sankey diagram for the heat balance, based on the heat received by the salt water in the solar collector. It must be observed that differences between certain figures of Table 2 and those indicated in the Sankey diagram are due to the enthalpy of the incoming water which is not included in the values of

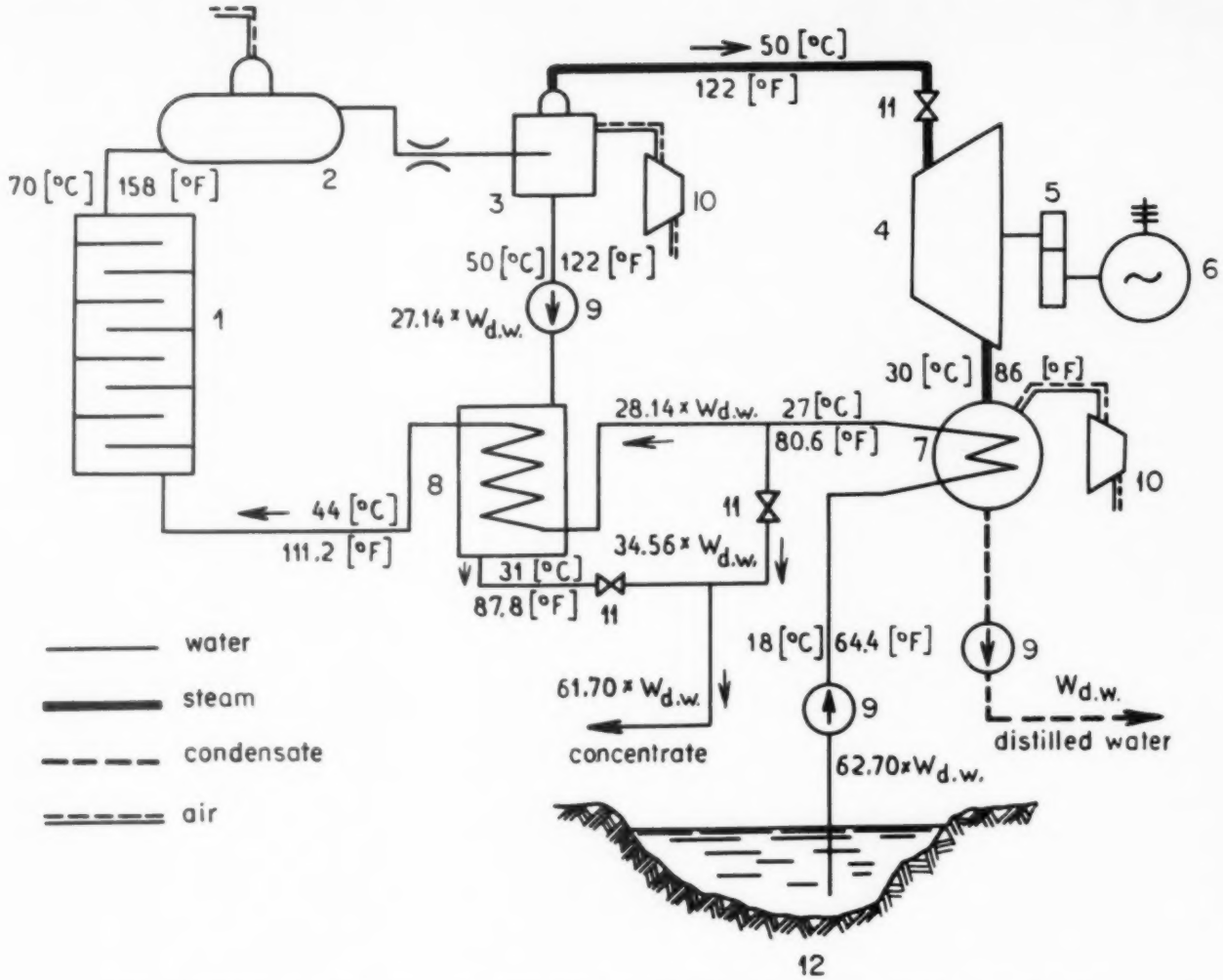

FIG. 4.—Scheme of a Pilot Plant to Distill Salt Water and Generate Electric Power by Solar Energy.

Key to Fig. 4:

(1) Solar collector
(2) Accumulator and air separator
(3) Vacuum Vaporizer
(4) Steam Turbine
(5) Gear
(6) Generator
(7) Condenser
(8) Heat Exchanger
(9) Circulation pump
(10) Vacuum pump
(11) Regulation Valve
(12) River or well

the diagram. The table and diagram are referred to one cubic meter (or one gallon) of distilled water produced by the process.

As may be concluded from the diagram, the heat balance of the cycle is relatively good; nevertheless the rate of solar energy converted into useful mechanical energy by the steam turbine is only 3.4 per cent of the total heat received in the solar collector. However, with reference to the enthalpy of the steam produced by the process the efficiency would be (24,640 × 100)/600,900 or 3.9 per cent, a value which approaches the maximum possible value of the Carnot efficiency which is 6.2 per cent for the given temperature limits, i.e., 50 C (122 F) in the vaporizer and 30 C (86 F) in the condenser. Certainly the mechanical utilization of 3.4 per cent of the solar energy received is acceptable, especially when one considers the simultaneous conversion of salt water into distilled water.

Obviously, academic considerations such as the heat balance do not in themselves justify the cost of building a plant of the size necessary to test the process proposed by the author. Therefore Victor Bocič in his thesis, made a complete calculation of the cost of the plant itself and also of the distilled water and electric energy to be produced. The ratio between prices of water and electricity were assumed to be equal to the ratio existing between present prices in the region of Antofagasta; in other words the price per m^3 of water is assumed to be twice that of a kwhr. The cost estimated by Victor Bocič would be: $0.34 (U.S.) per kwhr and $ 0.68 per m^3 of distilled water (or $2.57 per 1000 gal.) The most expensive item in the plant is the

VOL. 5 1961

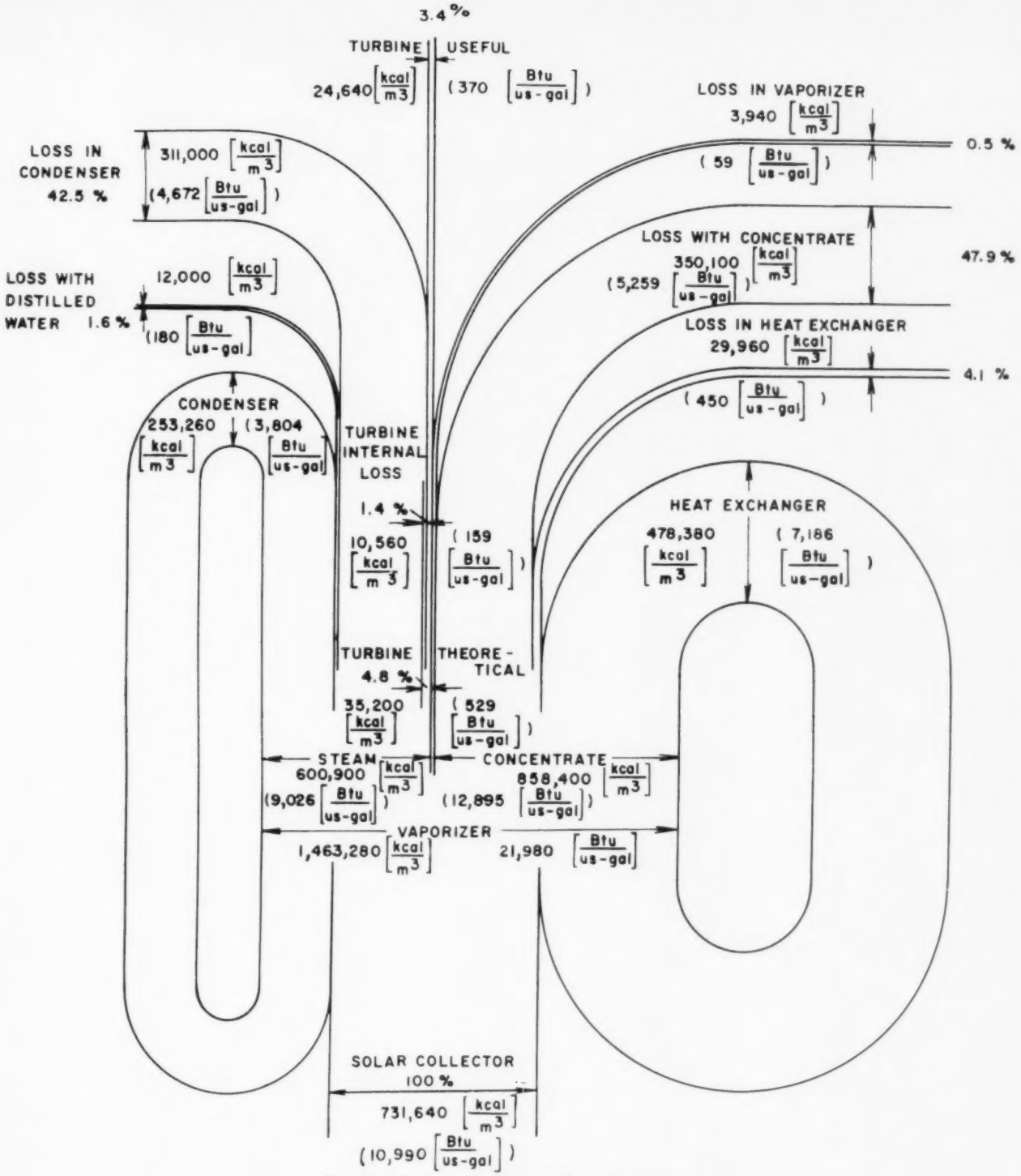

FIG. 5.—Sankey—Diagram of Heat Balance.

solar collector which amounts to nearly 89 per cent of the total investment. Thus any lowering of the cost of the collector would considerably reduce prices of distilled water and electricity. Victor Bocič assumed a plane and inclined collector with copper tubes.

Last August the author had the opportunity to accompany Prof. Farrington Daniels during a visit to the desert of Atacama and to show him the site chosen for building the first pilot plant which will use the process under consideration. Our distinguished guest agreed

TABLE 2—Heat Balance*

Circuit	Place	Enthalpy of Incoming Fluid		Difference of Enthalpy: Heat in		Difference of Enthalpy: Heat cut		Difference of Enthalpy: Loss of heat		Enthalpy of Outgoing Fluid	
		kcal/m³	Btu/gal	kcal/m³	Btu/gal	kcal/m³	Btu/gal	kcal/m³	Btu/gal	kcal/m³	Btu/gal
Primary (Salt water and Concentrated)	Condenser	1,128,600	16,953	+564,260	+8,476					1,692,860	25,429
	Expelled water							−933,120	−14,017		
	Heat Exchanger	759,740	11,412	+478,380	+7,186					1,238,120	18,598
	Solar Collector	1,238,120	18,598	+731,640	+10,990					1,969,760	29,588
	Vaporizer	1,969,760	29,588			−619,000	−9,298	−3,940	−59	1,346,820	20,231
	Heat Exchanger	1,346,820	20,231			−478,380	−7,186	−29,960	−450	838,480	12,595
Secondary (Steam and Condensate)	Vaporizer									619,000	9,298
	Turbine	619,000	9,298			−24,640	−370			594,360	8,928
	Condenser	594,360	8,928			−564,260	−8,476			30,100	452

* The differences between certain figures of Table 2 and those indicated on the Sankey diagram of Fig. 5 are due to the enthalpy of water at 18 C (62.70 F), at which temperature it enters the plant. That enthalpy is 18,100 kcal/m³ (272 Btu/gal).

completely with the choice of location. He kindly suggested a new plastic material which could be useful for the collector. The following description is taken from a paper by Daniels.

> A plastic film basin bottom overlaid with a black fabric mat, is secured at the edges to long concrete curbs. A transparent cover of the same material is joined to the bottom films at the edges also, and secured to the curbs. With a salt water depth of 2 to 5 centimeters and slight air pressure from a small blower the sections become inflated and assume a firm contour.

On the other hand, several factories have developed ditch-diggers for any kind of ground which are now available to commercial purchasers. With modern machinery and new materials it should be possible to lower considerably the cost of the solar collector, but this point requires further study.

But apart from the possibility of developing a cheaper collector, the projected pilot plant already provides a solution for the water problem of the arid zones in northern Chile. Underground water exists in abundance in many parts of the desert, but it is always more or less salty because the soil itself contains various soluble salts. The only river which crosses the desert of Atacama, the river Loa, rises from a spring of pure water, but on arriving at Maria Elena, the place elected for the pilot plant, it contains 4,661 p.p.m. of salts, mostly NaCl. The Research Department for the Northern Zone, established by the Antofagasta Centre of the Universidad de Chile, is currently investigating the possibility of using desert soil for agriculture after washing it, at Salar del Carmen in the desert near Antofagasta. At present, the results of this investigation are highly promising, thus confirming the author's opinion that the projected plant can help to solve one of the agricultural problems of the Northern Zone, because it would utilize the abundant solar energy for pumping salt water as well as converting it into distilled water.

Finally, it seems appropriate to discuss briefly the differences between the author's project and that of Asa E. Snyder. Thanks to Mr. Snyder's gracious help the author is able to point out the following differences: "project A.S." meaning that of Mr. Snyder and "project V.B." that of the author, developed by Victor Bocič.

	"Project A.S."	"Project V.B."
Net power	5,000 kw	50 kw
Distilled water production	1.62×10^6 gal/day	4.46×10^3 gal/day
First cost (estimated)	2,480,000 $ (U.S.)	220,000 $ (U.S.)
Solar collector design	Open trenches covered with asphalt material	Inclined copper tube collector
Price of electrical energy	0.05 $ (U.S.) per kwhr	0.34 $ (U.S.) per kwhr

From the figures given above it is obvious that Asa Snyder's plant is a full-scale industrial power plant while the author's project is a pilot plant. In view of the many practical problems that will be encountered in running such a novel type of power plant, the author considers it desirable to begin with a plant that is just self-supporting.

The reason for the great difference between the quoted prices of electrical energy is, of course, due to the quite distinct types of solar collectors. It is the author's opinion that an open collector would not work under the climatological conditions of the desert at Atacama. Intense solar radiation combined with low humidity would produce such a high rate of evaporation that heating would be impeded. For coastal installations, as proposed by Asa Snyder, the conditions are quite different. In conclusion, it seems advisable to build the proposed pilot plant first and to demon-

VOL. 5 1961

strate that it works. It would then be possible to project larger plants, designed to solve the agricultural problem of the arid zones of Chile with the help of solar energy.

ACKNOWLEDGMENTS

The author wishes to acknowledge and express his sincere thanks to: Engineer Victor Bocič A., the author's assistant; Prof. Luciano Cruz-Coke, Universidad de Chile; Prof. Farrington Daniels, University of Wisconsin; Prof. John Duffie, University of Wisconsin; Prof. German Frick, Universidad de Chile; Prof. Carlos Espinoza, Universidad del Norte; Asa E. Snyder, Executive Vice President of USI Clearing Division of U. S. Industries, Inc.; and to the Anglo-Lautaro Nitrate Company for its valuable information on the solar evaporation ponds of Coya.

REFERENCES

1. Snyder, Asa E., "Design of a Sea Thermal Energy Power Plant," *Solar Energy*, **3**—4 (December 1959), 49–55.
2. Hirschmann R., Julio, "Planta piloto para utilizar la energía solar en producir agua potable de agua salada generando simultaneamente energía electrica," *Scientia* No. 109, Valparaíso (Diciembre 1958).
3. U. S. Department of Commerce, Weather Bureau, Climatological Services Division, *World Sunshine Map*, Washington (1955).
4. Arce R., Isaac, *Narraciones históricas de Antofagasta*, Antofagasta (1930), 250.
5. Harding, Josiah, "Apparatus for Solar Distillation," Paper No. 1933, *Proc. Inst. Civil. Engr.*, No. 73 (1883), 284.
6. Telkes, Maria, "Solar Stills," *Proceedings of the World Symposium on Applied Solar Energy*, Menlo Park, California (1956).
7. Desvignes, F, et Frick, G., "Mesures solarimetriques dans le Nord du Chili," *Acta Electronica*, **3**—2, Paris (1959).
8. Bocič A., Victor, "*Memoria para optar al titulo de ingeniero mecánico*, Valparaiso, Chile (1958), 173.
9. Reference 8, 125 ff.
10. Hirschmann R., Julio, "Sobre las posibilidades de aprovechar la energía geotermica en Chile, *Scientia* **21**—1 Valparaíso (marzo 1954).

Photochemical Systems for Solar Energy Conversion—Nitrosyl Chloride*

By Rudolph J. Marcus and Henry C. Wohlers

Chemistry Department, Stanford Research Institute, Menlo Park, California

The desirable properties of a photochemical conversion reaction are discussed and a number of possible reactions are listed and rated. This list should be added to by additional work in this field.

Studies of one of these reactions, the photolysis of nitrosyl chloride, are reported. The solar furnace was used as a light source for these studies. All available physical, photochemical, and thermochemical data on nitrosyl chloride, chlorine, and nitric oxide have been gathered.

Modern society has an insatiable hunger for energy. This need for energy will continue to increase as the newly developing countries become more industrialized and as the mature nations increase their scope of mechanization. To satisfy this need, vast quantities of coal and petroleum products have been exhumed. More recently, the advent of nuclear energy has added vast quantities for future needs.

There is no doubt that the supply of natural resources will be depleted eventually on earth. At this point we will have arrived at a time when mankind will have to utilize Aristotle's four elements— the sea, the rocks, the air, and the sun (fire) — as energy sources.[64]

Brown, Bonner, and Weir[14] have estimated the energy input pattern for a world population of seven billion inhabitants around 2000 A.D. Their data, presented in Table 1, show that at that time the supply of natural petroleum products and coal will have been exhausted. The major sources of energy then, according to these data, will be nuclear energy accounting for 65%, and solar energy accounting for 22% of the estimated energy needs.

Although sunlight is the energy source for the production of food, the diluteness and unpredictability of the light energy lessens its usefulness as a prime energy source unless efficient methods of conversion and storage are available. The supply of energy available in the sun by the conversion of hydrogen to heavier elements will last on the order of 13×10^{10} years,[1] but research must be undertaken to provide means of converting this energy into a more usable form.

In this paper we concentrate on one aspect of the development of the utilization of the sun for power purposes, that of photochemistry. In particular, we wish to discuss the effect of light collected at the focus of a solar furnace on various chemical systems, including the photochemical decomposition of nitrosyl chloride.

PHOTOCHEMISTRY

Many authors, among them Farrington Daniels,[20] have stated that photochemistry is the key to mankind's utilization of solar energy. The research goal in photochemistry is to find a suitable reaction which can be induced by sunlight, and then to allow this reaction to reverse itself upon demand, with the evolution of energy. Light is thus used to bring about a reaction which would not occur otherwise; the energy involved should be in the range of 40 to 100 kcal/mole. This is the amount of energy which is necessary to excite a molecule electronically and is the energy equivalent of ultraviolet or visible light. Infrared radiation (wavelengths greater than 8000 Å) merely excites the vibration or the rotation of molecules. Such forms of energy are not storable with presently known techniques, because the time in which they occur and in which they can be reversed is so small. For photochemical conversion on earth, the lower limit of absorption of light is 3000 Å, which is the lower cut-off limit of the earth's atmosphere.[55] For space technology, however, the lower wave length is about 1000 Å.

There is as yet no practical system for solar energy conversion except that of photosynthesis.[16, 19, 20, 21, 51, 53] Since at the present time there is no synthetic chemical reaction which is ideal for the photochemical conversion of solar energy, it is desirable to discuss first the principles involved, the ideal requirements for the reaction, and suitability of various reactions for this purpose.

Primary Photochemical Processes

Prior to a consideration of the requirements of an ideal chemical reaction for solar energy conversion,

* This work was supported by the U. S. Air Force Research Center under contract AF 19(604)-7302.

VOL. 5 1961

TABLE 1—Asymptotic Yearly Energy Input Pattern for Seven Billion People
(After Brown, Bonner, and Weir)

Source	Equivalent Metric Tons of Coal (billions)	Equivalent Heat Energy	
		10^{15} Btu	10^{3} Megawatt Years
Solar energy (for ⅔ of space heating)	15.6	0.42	140
Hydroelectricity	4.2	0.10	38
Wood for lumber and paper	2.7	0.07	24
Wood for conversion to liquid fuels and chemicals	2.3	0.06	21
Liquid fuels and "petro" chemicals produced via nuclear energy	10.0	0.27	90
Nuclear energy	35.2	0.96	320
Total	70.0	1.88	633

it is instructive to review briefly various possible primary photochemical processes. The primary photochemical process is usually characterized by molecular change, and such processes define the broad scope of the methods available for radiant energy utilization. Rosenberg[53] lists the following primary photochemical processes which might result in the conversion and storage of solar energy:

a. bond rupture, free radical formation,

$$Br_2 \overset{h\nu}{\rightleftharpoons} 2Br \qquad [1]$$

or

$$H_2 + Cl_2 \xrightarrow{h\nu} 2HCl \qquad [2]$$

b. intramolecular rearrangement to stable products

$$CH_3CHO \xrightarrow{h\nu} CH_4 + CO \qquad [3]$$

c. photoisomerization

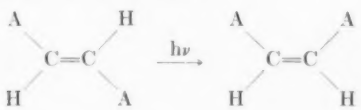

[4]

d. photoionization

$$Cs \xrightarrow{h\nu} Cs^+ + e \qquad [5]$$

e. electron transfer

$$Fe^{++}(H_2O)_n \xrightarrow{h\nu} Fe^{+++}(H_2O)^-(H_2O)_{n-1} \qquad [6]$$

f. photoconduction in solids

$$H_2O + \tfrac{1}{2}\,O_2 \xrightarrow[ZnO]{h\nu} H_2O_2 \qquad [7]$$

g. photosensitized decomposition of unexcited molecule

$$2CCl_3Br + O_2 \xrightarrow{h\nu} 2COCl_2 + Br_2 + Cl_2 \qquad [8]$$

h. photophysical processes (fluorescence, phosphorescence, etc.).

Careful evaluation indicates that two of these eight primary photochemical conversion processes have the greatest chance of being useful for the conversion of solar energy. One of these is electron transfer and the other is the formation of free radicals. For present purposes, the intramolecular rearrangement to stable products was discarded because such reactions are usually not reversible; photoisomerization and photoionization were ruled out because the former is usually a low energy process and the latter a high energy process; photoconduction in solids, because we are interested principally in solution reactions; and photophysical processes, because the absorbed energy is immediately dissipated as thermal energy. Photosensitized decomposition of unexcited molecules could be useful for either electron transfer or bond rupture with consequent free radical formation.

Electron Transfer Spectra

Storage of energy by electron transfer reactions may be briefly described as a transfer of an electron from one compound to another against the gradient of chemical potential.[36] Such reactions may consist of photooxidations or photoreductions. The energy requirement for an electron transfer reaction against the gradient of chemical potential is faithfully reflected in some region of the absorption spectrum of the species concerned. Two general ways of identifying electron transfer spectra are: (a) the light-absorbing material has a very high extinction coefficient (of the order of 10^4), and (b) the absorption peaks for a series of compounds vary as does some electronic characteristic of the compounds (ionization energy, electron affinity, etc.) of that series.

Electron transfer reactions occur most frequently in the ultraviolet region of the spectrum. Thus this type of reaction will be of greatest value for space technology, since in space the 1000–3000 Å spectral region is available. The photochemistry of the cerous-ceric electron transfer reaction is a case in point. The reduction step,

$$Ce^{+4} + \tfrac{1}{2}\,H_2O \xrightarrow[HClO_4]{h\nu} Ce^{+3} + H^+ + \tfrac{1}{4}\,O_2, \qquad [9]$$

proceeds with a reasonable rate on the earth's surface at wavelengths greater than 3000 Å.[27, 37] The corresponding photooxidation,

$$Ce^{+3} + H_2O \xrightarrow[HClO_4]{h\nu} Ce^{+4} + OH^- + \tfrac{1}{2}\,H_2, \qquad [10]$$

is feasible with light of 2537 Å,[28] but is extremely slow or inefficient with any sunlight to be found on the earth's surface.[39] For instance, we have shown that the production of hydrogen by this reaction in sunlight which has been concentrated 8,000 times is negligible for all practical purposes at the earth's surface (i.e., at wavelengths greater than 3000 Å).[39]

We have now come to the conclusion that this kind of result is to be expected of all electron transfer reactions occurring in aqueous solutions. The reasoning which has led us to this conclusion proceeds as

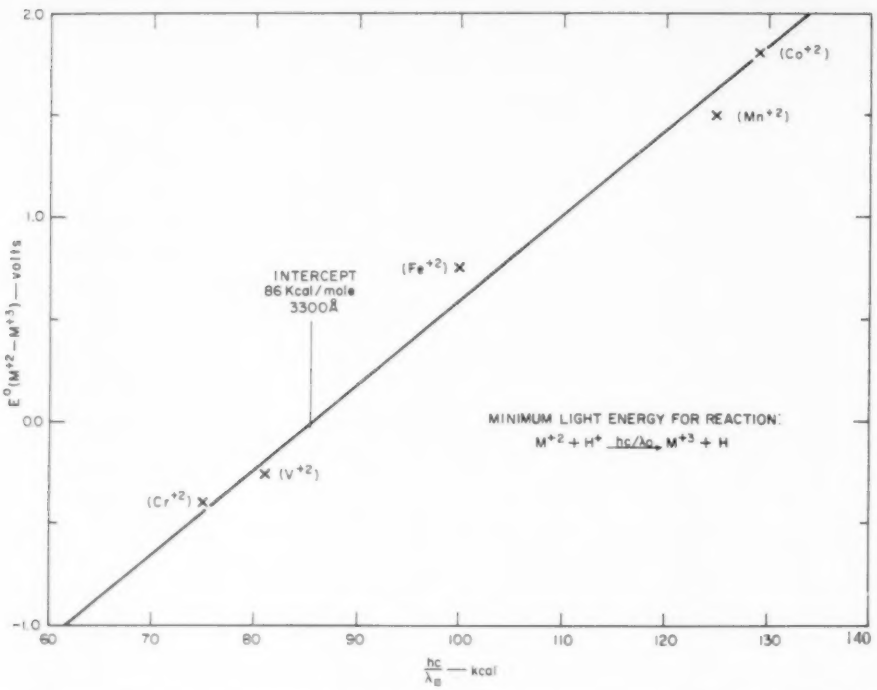

FIG. 1—Edge of the Electron Transfer Spectrum (λ_0) as a Function of the Oxidation-Reduction Potential (E^0) of the M^{+2}—M^{+3} Couple for a Number of Metal Ions, M^{+2}. (Wavelengths from Dainton and James. Potentials from Latimer).

VOL. 5 1961

follows: each of these reactions needs to have at least one photooxidation step. The only photooxidation reaction which has been found for all electron transfer systems in aqueous solutions is one which involves the reduction of hydrogen ions,

$$M^{+2}\,(aq) + H^+ \xrightarrow{h\nu} M^{+3}\,(aq) + \tfrac{1}{2}\,H_2 \qquad [11]$$

Dainton and James[13] have determined the minimum light energy required for reaction [11] as a function of the half-cell potential of the metal ions involved. A graph of these data (Fig. 1) shows that the minimum light energy required at an oxidation-reduction potential of zero is 86 kcal/mole. This light energy corresponds to a wavelength of about 3300 Å. This is the amount of energy required to make the reaction go when no energy is stored.

At first glance such a high activation energy sounds unreasonable but a closer look at Eq. [11] convinces one that the energy of formation of a hydrogen atom from a hydrogen ion is included in that number. This energy amounts to about 48 kcal/mole. If this value, as well as that for the oxidation-reduction potential for the metal ion couple, is subtracted from the observed minimum light energy required for reaction [11], the remaining energy is the same for a number of metal ions (Table 2), indicating that all of these reactions appear to proceed by the same mechanism. One concludes that reactions like Eq. [11] will always limit electron transfer reactions to space uses where ultraviolet light of such wavelengths is available. A subsidiary conclusion to be drawn from this reasoning is that no amount of photosensitization is going to push the limit for effectiveness of this reaction any further into the visible than the limit of 3300 Å. For these reasons, electron transfer reactions involving a hydrogen ion as the primary acceptor are unlikely to be of much use for energy conversion and storage on the surface of the earth.

TABLE 2—Activation Energy for Photooxidation of Some Metal Ions

Species	λ_{edge} (mμ)	$\frac{hc}{\lambda_{edge}}$ (kcal/mole)	E^0 (kcal/mole)	Ionization Potential (volts)	$E^\ddagger$ (kcal/mole)
Co^{+2}	220	129	42	33.49	39
Ni^{+2}	220	129	—	—	—
Mn^{+2}	225	125	35	(32)	42
Fe^{+2}	285	100	18	43.43	34
V^{+2}	350	81	−6	26.4	39
Cr^{+2}	380	75	−9	29.8	36

$$E^\ddagger = \frac{hc}{\lambda_{edge}} - E^0_{M^{++} - M^{+++}} - E^0_{H - H^+}$$

Under these conditions, how is it possible for chlorophyll to transfer electrons with light of much longer wavelength, up to 6700 Å? Undoubtedly, the primary acceptor in photosynthesis is not a free hydrogen ion; thus the energy calculations which we have just presented do not apply in this case.

Photohomolysis or Free Radical Formation

We have just discussed reactions in which the electron pair comprising the broken bond stays with one of the products. We would now like to consider reactions in which bond rupture results in the formation of two free radicals, that is, the electron pair is split and one electron goes with each of the two products. Since this kind of bond rupture is usually referred to as homolysis, a bond ruptured photochemically in this manner can properly be said to have been broken by photohomolysis. Two commonly proposed reactions for the storage of solar energy fall into this category. These are the photolysis of nitrosyl chloride[46] and of nitrogen dioxide.[49] In both of these reactions, the effective spectral response extends to much longer wavelengths than any electron transfer reactions reported before.

One reason for considering photohomolytic reactions as an alternative to the more frequently considered electron transfer reactions is that the activation energy calculated in the previous section, which includes at least 48 kcal/mole for the formation of a hydrogen atom from a hydrogen ion, is not likely to be that high for photohomolysis. In particular, these 48 kcal/mole are not going to be needed for photohomolysis.

While the spectral response is going to be much better in the case of photohomolytic reactions, there are other problems which have to be seriously considered. One of these is a problem of the separation of the photoproducts. There are a number of reasons why the photoproducts will recombine quite quickly. The first reason is that the products are free radicals. It is well known that the activation energy for the combination of free radicals is quite low. Furthermore, if the photohomolysis takes place in solution, the recombination of the photoproducts will be strongly affected by the solvent cage in which they are enclosed. One mechanism, which has been suggested by Neuwirth[46] for the quick separation of the photoproducts, is to carry out these irradiations in a solution, such that one of the photoproducts is insoluble in the solvent and will escape to the gas phase while the other one remains dissolved.

Criteria for Suitable Photochemical Reactions

We have shown in the preceding sections of this paper that electron transfer reactions seem to offer the best spectral response for photochemical conversion of sunlight for space technology purposes. For use on earth, however, free radical reactions seem to offer the best chance of success.

In addition to the spectral response already discussed, other chemical and physical criteria need to be considered in assessing photochemical energy conversion reactions.[21, 53] Some of these criteria are listed below.

a. The photochemical reaction must be endothermic and reversible. That the reaction must be endothermic is obvious, for the absorbed light must bring about a reaction which would otherwise not occur. The energy involved should be in the range of 40 to 100 kcal/mole as discussed earlier.

It is not necessary that the reactants absorb the light directly. The solution of the problem of energy conversion and storage could also be found in the method of sensitizing the system for visible and, if possible, also for the near infrared light by appropriate dyes. Examples of such sensitizers are the various dyes used in photographic film to make the silver bromide sensitive to orange or red light as well as to blue, violet, and ultraviolet light.

Not only must the reaction be reversible but the rate of the reverse reaction should not be so fast that the photostationary state is far to the left. This would indicate a small degree of decomposition of the light-absorbing compound. Yet the rate of the reverse reaction must be sufficiently fast to be practical in answering the energy demand.

b. The products of the photochemical reaction must be separable and storable until such time as the energy is required. In some cases the products can remain together, provided that the reverse reaction is not initiated without a specific stimulus.

The photodecomposition of nitrosyl chloride illustrates the need for storable products. This compound is easily decomposed into nitric oxide and chlorine. Various authors[6, 46] have suggested solvents to dissolve the chlorine; in this manner nitric oxide in the gas phase would have been separated from the chlorine dissolved in the liquid phase. Unfortunately nitric oxide is not completely insoluble in the solvents suggested, such as carbon tetrachloride, and the recombination of nitric oxide and chlorine is fast enough to prevent the effective escape of nitric oxide into the gas phase.[4, 5, 6, 65]

The photoproducts may remain mixed as long as they remain inactive. The reverse reaction may be initiated by a spark or by raising the temperature. This is the kind of situation which is found in the hydrogen-oxygen system. The problem of the photochemical conversion or storage of energy is not so much to raise the electrons to a higher potential as it is to keep them there until the energy of recombination is needed.

c. The temperature of the photochemical reaction should be greater rather than lower than ambient temperature. In the solar energy research, of course, any reaction which proceeds at any reasonable temperature should be investigated. For practical purposes,

TABLE 3—Photochemical Reactions for Energy Conversion and Storage (Photohomolysis)

Over-all Reaction	Reference	Maximum Effective Wavelength, Å	ΔF°_{298} kcal./mole	ΔH°_{298} kcal./mole	Rating of Reaction	Reasons* for Rating of Reaction
1. $\frac{3}{2}\ O_2 \rightarrow O_3$	16	2537	39.1	34.0	Poor	a
2. $CO_2 \rightarrow CO + \frac{1}{2}\ O_2$	16	1692	61.5	67.7	Poor	a
3. $HBr \rightarrow \frac{1}{2}\ Br_2 + \frac{1}{2}\ H_2$	16	2537	12.7	8.7	Poor	a, i
4. $SO_3 \rightarrow \frac{1}{2}\ O_2 + SO_2$	16	2760	16.7	23.5	Poor	a
5. $COCl_2 \rightarrow CO + Cl_2$	16	2750	17.5	26.9	Poor	a
6. $NO_3^- \rightarrow NO_2^- + \frac{1}{2}\ O_2$ (in H_2O)	16	2800	18.1	24.9	Poor	a, d
7. $NO_2 \rightarrow NO + \frac{1}{2}\ O_2$ (in CCl_4)	16	4350	8.3	13.5	Fair	e, i
8. $NOCl \rightarrow NO + \frac{1}{2}\ Cl_2$ (in CCl_4)	16	6370	4.8	9.0	Fair	e, i
9. $AgCl(s) \rightarrow Ag(s) + \frac{1}{2}\ Cl_2$	16	4050	26.2	30.4	Poor	c
10. $AgBr(s) \rightarrow Ag(s) \rightarrow \frac{1}{2}\ Br_2$	16	4600	22.9	23.8	Poor	c
11. $AgI(s) \rightarrow Ag(s) + \frac{1}{2}\ I_2$	16	4400	15.9	14.9	Poor	c, i
12. $NH_3 \rightarrow \frac{1}{2}\ N_2 + \frac{3}{2}\ H_2$	19	2537	4.0	11.0	Poor	a, i
13. $HF \rightarrow \frac{1}{2}\ H_2 + \frac{1}{2}\ F_2$	51	2800	64.7	64.2	Poor	a
14. $2Fe(CO)_5 \rightarrow CO + Fe_2(CO)_9$ (in C_6H_{14})	49	4400			Poor	h
15. $Ni(CO)_4 \rightarrow Ni + 4CO$ (in CCl_4)	49	3660			Poor	c
16. $BiOCl(s) \rightarrow BiO(s) + \frac{1}{2}\ Cl_2$	49	Visible	33.5	37.4	Poor	g
17. $Hg(NO_3)_2 \rightarrow HgO + 2NO_2 + \frac{1}{2}\ O_2$	49	Ultraviolet	24.2	52.3	Poor	a, e, d
18. $Hg_2(NO_3)_2 \rightarrow 2HgO + 2NO_2$	49	Ultraviolet		31.2	Poor	a, e, d
19. $SO_2Cl_2 \rightarrow SO_2 + Cl_2$	49	3000	1.8		Poor	a, e, i

*a—Wavelength of exciting light is less than 3000 Å and thus reaction cannot be used in earth's atmosphere. Reaction might proceed in outer space, or on earth if sensitizing agent could be found.
b—Reaction is not reversible and hence cannot be used without "refueling."
c—Precipitate is formed. The settling and caking of the precipitate slows the rate of reverse reaction.
d—The possibility exists that side reaction products may be formed. Hence, reaction cannot be used without "refueling."
e—Back reaction is fast. The photostationary state is far to the left.
f—It was claimed that the reaction takes place in the gas phase. Solution of chemical showed essentially no absorption greater than 3000 Å.
g—Compound is insoluble in most simple solvents.
h—Insufficient data available.
i—Small amount of energy storage

however, a cooling system might well require more energy than is obtained by the photochemical reaction. Further, the added weight of a refrigeration system would be a serious disadvantage in some instances. Temperature control in photochemical conversion reactions can be obtained by the addition of dyes or of carbon black to the reaction solution. If quartz is used for the reaction vessels, a maximum reaction temperature of 1,200° C will be possible.

d. Inorganic reactions are to be preferred over organic reactions. Most promising organic reactions have a serious drawback: the occurrence of side reactions vitiates their usefulness. The occurrence of side reactions means that the system is not truly reversible and hence that the light-absorbing compound will be consumed slowly.

The most promising inorganic reactions from the point of view of energy conversion are oxidation-reduction reactions. It is somewhat harder to find inorganic molecules which will form free radicals upon light absorption, but it will be noted that both of the examples previously mentioned, nitrosyl chloride and nitrogen dioxide, are inorganic compounds.

e. In addition to the previous remarks, several minor points might also be considered. The reactants (either alone or in solution) should be liquid at room temperature. The vapor pressure of this solution should be low and the solution should be both noncorrosive and nonhazardous. The original reactants may be decomposed either into a gas or into a solute, but the formation of a precipitate had best be avoided.

PHOTOCHEMICAL REACTIONS

The types of reaction which were considered suitable for the photochemical conversion of solar energy and some required chemical and physical criteria of such reactions have been described. A large number of equations were reviewed, attempting to determine new and useful reactions for this purpose or attempting to see if any order could be discerned among the equations or compounds examined. The equations are listed in Tables 3–5. These tables form a convenient listing of reactions which might be studied for possible photochemical conversion of solar energy.

Of the equations listed in these tables, only three were rated as "Fair"—the remainder were rated "Poor." Of the three "Fair" reactions the photolysis of nitrogen dioxide

$$NO_2 \xrightarrow[CCl_4]{h\nu} NO + \tfrac{1}{2}\ O_2, \qquad [12]$$

has a slow recombination reaction.[49] Furthermore, the quantum yield of nitrogen dioxide decomposition in carbon tetrachloride solution is relatively low.[16, 30]

VOL. 5 1961

TABLE 4—Photochemical Reactions for Energy Conversion and Storage
(Electron Transfer)

Over-all Reaction	Reference	Maximum Effective Wavelength, Å	ΔF°_{298} kcal/mole	ΔH°_{298} kcal/mole	Rating of Reaction	Reasons* for Rating of Reaction
1. $H_2O \rightarrow H_2 + \frac{1}{2} O_2$	16	1800	54.6	57.8	Poor	a
2. $2Fe^{+2} + I_3^- \rightarrow 2Fe^{+3} + 3I^-$ (in H_2O)	16	5460	10.7	−8.6	Poor	h, i
3. $I_2 + NO_2^- + H_2O \rightarrow NO_3^- + 2HF$ (in H_2O)	16	5790	11.0	7.0	Poor	h, i
4. $Fe^{+2} + H_2O \rightarrow \frac{1}{2} H_2 + Fe^{+3} + OH^-$ (in H_2O)	16	2960	34.2	12.4	Poor	a
5. $Fe^{+2} + H^+ \rightarrow Fe^{+3} + \frac{1}{2} H_2$ (in $HClO_4$)	16	2537	17.8	9.6	Poor	a, i
6. $AgCl + \frac{1}{2} H_2O \rightarrow Ag + HCl + \frac{1}{4} O_2$ (in H_2O)	16	4050	22.1	19.3	Poor	e
7. $H_2O + \frac{1}{2} O_2 \xrightarrow{ZnO} H_2O_2$	16	4000	23.1	12.1	Poor	e
8. $RbI \rightarrow Rb + \frac{1}{2} I_2$	49	3700	92.0	87.8	Poor	e, f
9. $CrCl_3 \rightarrow CrCl_2 + \frac{1}{2} Cl_2$			32.8	40.1	Poor	a, h
10. $FeCl_3 \rightarrow FeCl_2 + \frac{1}{2} Cl_2$			8.2	15.3	Poor	a, h
11. $HClO_4 \rightarrow HClO_3 + \frac{1}{2} O_2$			2.0	7.9	Poor	h, i
12. $2Ce^{+4} + H_2O \rightarrow 2Ce^{+3} + 2H^+ + \frac{1}{2} O_2$	20	4000		−3.8	Fair	b
13. $Ce^{+3} + H^+ \rightarrow Ce^{+4} + \frac{1}{2} H_2$	20	2537		37.9	Poor	a

* See footnote to Table 3.

TABLE 5—Photochemical Reactions for Energy Conversion and Storage
(Miscellaneous)

Over-all Reaction	Reference	Maximum Effective Wavelength, Å	ΔF°_{298} kcal/mole	ΔH°_{298} kcal/mole	Rating of Reaction	Reasons* for Rating of Reaction
1. $CO + H_2 \rightarrow CH_2O$	16	1470	6.5	−1.3	Poor	a, i
2. $NH_3 \rightarrow \frac{1}{2} N_2H_4 + \frac{1}{2} H_2$	16	2138		17.1	Poor	a,d
3. $CH_4 \rightarrow \frac{1}{2} H_2 + \frac{1}{2} C_2H_6$	16	1450	8.1	7.8	Poor	a,d,i
4. Anthracene → Dianthracene	16	3800		15.6	Poor	d
5. $C_2H_2 + Br_2 \rightarrow C_2H_2Br_2$	19	5790			Poor	b
6. $H_2O + \frac{1}{2} Br_2 \rightarrow HBrO + \frac{1}{2} H_2$	20		34.7		Poor	b, d

* See footnote to Table 3.

The remaining two reactions,

$$2Ce^{+4} + H_2O \xrightarrow[HClO_4]{h\nu} 2Ce^{+3} + 2H^+ + \tfrac{1}{2} O_2 \quad [9]$$

and

$$2NOCl \xrightarrow[CCl_4]{h\nu} 2NO + Cl_2, \quad [13]$$

have been studied by the authors at the focus of a solar furnace. The concept of the use of the solar furnace as a light concentrator for photochemical reactions will be discussed while reviewing the experimental data on the ceric-cerous reaction. Following this, the nitrosyl chloride reaction will be discussed in detail.

SOLAR FURNACE AS A LIGHT SOURCE

The cerous-ceric reaction has been studied in the laboratory, using the usual ultraviolet and visible light sources.[20, 27, 28] Another light source which has been used for this reaction is the solar furnace. Since this is a new technique, a short description of it might not be out of place.

The solar furnace is a radiation concentrator. When a black body absorber is placed at its focus, the expected black body temperature of 3200° C is obtained. When a nonblack body, for instance a solution of ceric perchlorate, is placed at the focus, parts of the concentrated radiation are absorbed and others leave the solution unaffected. Of the concentrated radiation, the part absorbed by water (the infrared part) appears as heat; this amounts to less than $\frac{1}{3}$ of the total sunlight. The part absorbed by ceric ions (3000–4000 Å) however, acts just as light of this wavelength from any emitter would, except that it appears as a point source inside the solution. We have, then, in the solar furnace a new, cool, concentrated light source.[37, 38]

We first studied the photoreduction of ceric perchlorate at the focus of a 5-foot rear-silvered paraboloid. We found that this reaction was just as clean in the solar furnace as it was under more ordinary conditions. The photochemical production of oxygen according to Eq. [9] is of little value for the conversion of solar energy without the concomitant formation of a reducing substance which will react with oxygen and thereby produce either heat or electricity. As a rear-silvered glass surface effectively cuts off radiation below 3500 Å,[58] we repeated these experiments with a 2-foot front-surfaced furnace which reflected 60 to 70% of the light down to 3000 Å.[39] The purpose of these experiments was to determine if hydrogen could be produced at this wavelength according to the reaction:

$$Ce^{+3} + H_2O \xrightarrow[HClO_4]{h\nu} Ce^{+4} + OH^- + \tfrac{1}{2}H_2 \quad [14]$$

These experiments showed that the mass balance for Eq. [9] obtained with the 2-foot front-surfaced furnace was better than that obtained with the 5-foot rear-silvered furnace. The rate of oxygen evolution with the small furnace was 10-fold faster, based upon equal volumes and concentrations; this increase in rate was due to the additional light energy in the 3000–3500 Å region. No hydrogen was found according to Eq. [14]. Any hydrogen which may have been formed during a 2-hour exposure was less than 2.5×10^{-6} moles, which was the sensitivity limit of our mass spectrometer.

Thus the ceric-cerous perchlorate reaction, as here tested, seems to be of little value for the conversion of solar energy on the earth's surface. Of the reactions listed in Tables 3–5, we have yet to consider the photodecomposition of nitrosyl chloride.

PHOTODECOMPOSITION OF NITROSYL CHLORIDE

The photodecomposition of nitrosyl chloride has been suggested by Daniels[19] as one possible system of utilizing solar energy. Thermodynamically the photodissociation of nitrosyl chloride is endergonic by 4.5 kcal/mole. The efficiency, Q, of conversion of radiant energy to chemical energy as defined by Calvert[16] is 21.8%.

The free energy stored in the products of this reaction,

$$2NOCl \xrightarrow[CCl_4]{h\nu} 2NO + Cl_2 \qquad [13]$$

is available upon demand by recombination of the nitric oxide and chlorine to form the original nitrosyl chloride. In order to prevent recombination of the product gases and concomitant waste of absorbed light, the reaction should take place in a solvent in which only one of the products, chlorine, is soluble. In this manner, the gases could be stored and later recombined to give the original nitrosyl chloride and to release the solar energy consumed in the decomposition.

We have completed a preliminary examination of the photodecomposition of nitrosyl chloride in both a static system and a flow system using the 2-foot solar furnace described previously.[39] In these experiments, using the static system, less than 2% of the initial nitrosyl chloride content was decomposed.[40] This low yield, which may be of the order of the experimental error, was the result of recombination of the products prior to the end of the experiment.

In order to minimize this back reaction, crude experiments were undertaken with a gravity feed flow system in order to minimize or prevent the accumulation of the products, nitric oxide and chlorine.[40] The tests with the flow system will be continued, using a direct pumping system to feed the reactant quickly into the furnace.

Prior to the continued research on flow systems for nitrosyl chloride, it was considered expedient to evaluate carefully the chemical and physical data of the reactants and products which might be relevant to the problem.

CHEMICAL AND PHYSICAL PROPERTIES

Nitrosyl Chloride

Excellent reviews of the chemistry of nitrosyl chloride were published by Beckham, et al.[8] and McGonigle.[41] Physical data for nitrosyl chloride are shown in Table 6.[8, 41, 43]

Nitrosyl chloride, in vapor form, has an orange-red color; it forms a dark red liquid and a red solid, which in thin layers is yellowish. The nitrosyl chloride molecule has a nitrogen-oxygen bond distance of 1.14 Å, a nitrogen-chlorine bond distance of 1.95 Å, and a bond angle of 116°.[8] The molecule is a resonance hybrid between the normal covalent structure, O=N=Cl, and the ionic form, Cl^-NO^+. The nitrosyl and chloride ions are colorless.

Nitrosyl chloride is soluble in various aliphatic chlorides such as chloroform, carbon tetrachloride, and methylene chloride, and in many inorganic compounds such as sulfur monochloride, nitric acid, liquid sulfur dioxide, and silicon tetrachloride. Although nitrosyl chloride shows appreciable solubility in many organic compounds, it reacts slowly with compounds such as liquid alkanes, benzene, acetic acid, acetic anhydride, ether, and dioxane; it reacts quickly with alcohols and ketones. Liquid nitrosyl chloride also forms inorganic adducts such as $AlCl_3 \cdot NOCl$, $FeCl_3 \cdot NOCl$, and $SbCl_3 \cdot NOCl$.

Nitrosyl chloride reacts rapidly with water to form nitrous and hydrochloric acids:

$$NOCl + H_2O = HNO_2 + HCl. \qquad [15]$$

Both wet and dry nitrosyl chloride react with most metals. Nickel, lead, tantalum, platinum, or Inconel may be used with dry nitrosyl chloride; tantalum may be used with moist nitrosyl chloride.

Nitric Oxide

Physical data for nitric oxide are presented in Table 6.[43, 50, 52, 56, 66] Nitric oxide as a solid and liquid has a bluish tint, but it is a colorless gas at room temperature. The molecule contains an odd number of electrons and is paramagnetic. Pauling[50] has postulated resonance between the following structures:

$$\dot{:}\ddot{N}: :\ddot{O}: \quad \text{and} \quad {}^{-}:\ddot{N}: :\dot{O}:^{+}$$

The nitrogen and oxygen atoms are said to be connected by two electron-pair bonds and one three-

VOL. 5 1961

TABLE 6—Physical Properties of Nitrosyl Chloride, Nitric Oxide and Chlorine

	Nitrosyl Chloride[5, 41, 42]	Nitric Oxide[42, 50, 52, 58, 66]	Chlorine[42, 44, 52, 57]
Molecular weight	65.47	30.01	70.91
Melting point, °C	−61.5	−163.51	−102.4
Boiling point, °C	−5.8	−151.74	−34.0
Critical temperature, °C	167.	−94.	144.0
Critical pressure, atm	90.	65.	76.1
Critic density, g/ml	0.47		0.57
ΔH°_{298} (formation), kcal/mole	12.57	21.600	0.
ΔH°_{298} (dissociation), kcal/mole	9.03		58.02 ($Cl_2 \rightarrow 2Cl$)
ΔF°_{298} (formation), kcal/mole	15.86	20.719	0.
ΔF°_{298}(dissociation), kcal/mole	4.86		50.38 ($Cl_2 \rightarrow 2Cl$)
$\Delta H_{b.p.}$ (vaporization), kcal/mole	5.960	3.2926	4.680
$\Delta H_{f.p.}$ (fusion), kcal/mole	1.439	0.5495	1.531
S°_{298}, cal/deg mole	63.	50.	53.32
ΔC_p, gas, cal/deg mole	3.47–2.26 (0–100°C)	7.14 7.28 (−45°C to −80°C)	8.28–8.56 (−70°C–178°C)
ΔC_v, gas, cal/deg mole		5.15–5.29 (−45°C to −80°C)	5.97–6.32 (0°C–100°C)
Density			
liquid, gm/ml	−45°C 1.550 0°C 1.349 −40°C 1.446 10°C 1.325 −30°C 1.422 20°C 1.300 −20°C 1.398 30°C 1.276 −10°C 1.373 40°C 1.221	1.269 (151.74°C)	−70°C 1.6552 80°C 1.1991 −35°C 1.5649 100°C 1.1099 0°C 1.4680 120°C 0.9962 20°C 1.4085 140°C 0.7921 40°C 1.3456 141°C 0.5672 60°C 1.2760
gas, gm/l	0°C 2.972 75°C 2.309 25°C 2.710 100°C 2.152 50°C 2.492	1.3402 (NTP)	3.063 (0°C, 725 mm) 2.896 (15°C, 725 mm)
Vapor pressure			
solid	$\log p(mm) = -\frac{1660}{T} + 9.37$	$\log p(cm) = -\frac{867}{T} + 0.00076T + 9.05125$	$\log p(mm) = -\frac{1530}{T} + 9.950$
liquid	$\log p(mm) = -\frac{1347}{T} + 7.922$ (−97°C to −7°C)	$\log p(cm) = -\frac{776}{T} - 0.002364T + 8.562128$	$\log p(mm) = -\frac{1160}{T} + 7.773$
Viscosity, poises			
liquid	−20°C 0.00547 −29.5°C 0.00604 −25°C 0.00567 −33.3°C 0.00642		0.00729 (−76.5°C) 0.00488 (−33.8°C)
gas	15°C 1139 × 10^{-7} 100°C 1504 × 10^{-7} 50°C 1303 × 10^{-7} 200°C 1920 × 10^{-7}	0°C 1645 × 10^{-7} 20°C 1800 × 10^{-7}	20°C 1327 × 10^{-7} 100°C 1679 × 10^{-7} 50°C 1469 × 10^{-7} 200°C 2085 × 10^{-7}
Surface tension, dynes/cm			
liquid	−33 °C 34.5 −22 °C 32.7 −5.5°C 30.3		−72 °C 33.65 −35.3 26.55 −61.5°C 31.61 −28.7 25.33 −49.5°C 29.28
Dipole moment (in CCl_4), e.s.u.	1.83–2.19 × 10^{-18}	0.18 × 10^{-18}	
Dielectric constant			
liquid	18.2 (12°C)		
gas		1.00044(NTP)	1.00152(NTP)
Magnetic susceptibility per unit mass		+0.04 × 10^{-6} (16°C, 760 mm)	−0.50 × 10^{-6}
Molecular velocity, cm/sec		43,900	30,700
Molecular diameter, cm		16 26 × 10^{-9}	96 × 10^{-9}
Mean free path, cm		903 × 10^{-8}	2.9 × 10^{-8}
Ionization potential, volts		9–9.4	8.2
Molecular polarizability, cc			4.61 × 10^{-24}
Atomic radius, Å			1.07 (Crystal)
Ionic radius, Å			1.81
Moment of inertia of gas molecule, $gcm^2 \times 10^{40}$			113.7
Internuclear distance, Å	1.14 (N—O) 1.95 (N—Cl)	1.14	1.98 (gas)
Degree of thermal dissociation, %	784°C 5.54 968°C 39.19 815°C 10.64 985°C 41.85	700°C 0.5 1200°C 60 900°C 1.0 1690°C 100	0.035 (1000°K) 52. (2000°K)
Electron affinity, kcal/mole			86.5 ($Cl + e \rightarrow Cl^-$)
Free energy, kcal/mole			−115.8 ($Cl_2 + 2e \rightarrow 2Cl^-$)
Normal potential, volts			−1.36 (18°C—hydrogen electrode)
Heat of hydration, kcal/mole			96.9 (negative ion)
Electrolytic mobility of the negative ion at infinite dilution			66.3 (18°C)

electron bond. The N—O distance is 1.14 Å, between the double and triple bond distances. With this structure, the nitric oxide molecule is capable of entering into chemical combination in one of the following ways: (a) by losing the odd electron to form a positive ion NO^+, or (b) by gaining an electron to form the negative ion NO^-.

Nitric oxide is but slightly soluble in water as well as in most solvents; it does, however, undergo a number of addition reactions with compounds such as ferrous sulfate and copper sulfate. Carbon tetrachloride, at 8.8° C, dissolves 0.339 volumes nitric oxide per volume; at 34° C, 0.374 volumes of nitric oxide dissolve per volume CCl_4.[54]

Nitric oxide is easily oxidized; as soon as it comes into contact with air it forms brown fumes as a result of oxidation to the dioxide. The oxide is reactive with both chlorine and bromine, forming the corresponding nitrosyl halides. Nitric oxide can enter as a neutral constituent into many metallic salts. At low temperatures a dimer, N_2O_2, may be formed. Nitric oxide does not support combustion unless activated; glowing carbon or boron will burn in nitric oxide as in free oxygen.

Chlorine

The physical data for chlorine are listed in Table 6.[42, 44, 52, 57] Chlorine is greenish-yellow as a solid, liquid, or gas. The bond distance between chlorine atoms is 1.98 Å.

The solubility of chlorine in water is between that of the slightly soluble gases, such as oxygen and hydrogen, and the exceedingly soluble gases, such as HCl or NH_3. Chlorine is quite soluble in carbon tetrachloride. Seidell[54] mentions that at 0° C, 0.156 g chlorine are soluble per gram of carbon tetrachloride; at 40° C the chlorine solubility is reduced to 0.0433 g/g CCl_4.

Chlorine can combine with both electronegative and electropositive elements. In compounds with electronegative elements, chlorine can exhibit valences of seven, five, four, three, and unity; the most extreme valence states are generally the most stable, i.e., negative univalent and positive hepta-valent. There are no simple salts in which a positively charged chlorine exists; rather the positively charged halogen usually is combined with oxygen or with other halogens. In its normal chemical reactions, chlorine acts as an electron acceptor.

PHOTOCHEMICAL PROPERTIES

Nitrosyl Chloride

The consensus of a number of authors[7, 13, 26, 31, 32, 45, 59] is that the mechanism of the photodecomposition of nitrosyl chloride proceeds as follows.

$$NOCl \xrightarrow{h\nu} NO + Cl \qquad [16]$$

$$Cl + NOCl \rightarrow NO + Cl_2 \qquad [17]$$

$$2NOCl \rightarrow 2NO + Cl_2 \qquad [18]$$

This reaction has been reinvestigated because of its possible potential use for the conversion and storage of solar energy.[6, 40, 46, 51, 53]

Atwood and Rollefson[6] determined that the quantum yield for the photodecomposition of nitrosyl chloride in carbon tetrachloride (oxygen present) was 0.7 at 3650 Å and 0.5 at 5790 Å, compared with about 2 in the gas phase.[13] Neuwirth,[46] using a 500-watt projection lamp as a source of light, found quantum yields ranging from 0.7 to 1.1 for the initial reaction of decomposition of nitrosyl chloride in carbon tetrachloride but that these values dropped to 0.05 to 0.1 when a steady state was reached.

Atwood and Rollefson found no measurable decomposition during the illumination of a solution of nitrosyl chloride in carbon tetrachloride with their thick-walled capillary arc light source. These authors showed that the back reaction is so fast that the photostationary state which could be set up by their light source was not measurable. This condition was eliminated by adding oxygen to form NO_2 or by using hexane as a solvent to react with the chlorine. Neuwirth, on the other hand, suggested that the best way to reduce the effect of the back reaction was to use a dynamic system in which the carbon tetrachloride solution of nitrosyl chloride is continuously removed from the reaction vessel.

The absorption curve of nitrosyl chloride as a gas[26] or in carbon tetrachloride solution[40] is shown in Fig. 2; also included in this figure is the absorption curve for gaseous chlorine. It is interesting to note that both NOCl and Cl_2 show one absorption maximum at about 3340 Å and another at about 6000–6400 Å. The curve for NOCl also shows a maximum at about 4785 Å, the convergence limit for chlorine.

Nitric Oxide

The calculated value for the molal heat of dissociation of nitric oxide is 121.95 kcal, equivalent to a light wavelength of about 2300 Å. This was proved by Leifson[34] who found an intense banded absorption beginning at 2264 Å. MacDonald[35] found that the decomposition produced by irradiating nitric oxide gas at wavelengths of 1860–1990 Å followed two courses: (a) ninety percent of the decomposition yielded nitrogen and oxygen, and (b) ten percent followed the equation,

$$3NO \rightarrow N_2O + NO_2. \qquad [19]$$

Thus the photodissociation of nitric oxide will not occur on the surface of the earth where the limiting wavelength of light is 3000 Å. There is, therefore,

VOL. 5 1961

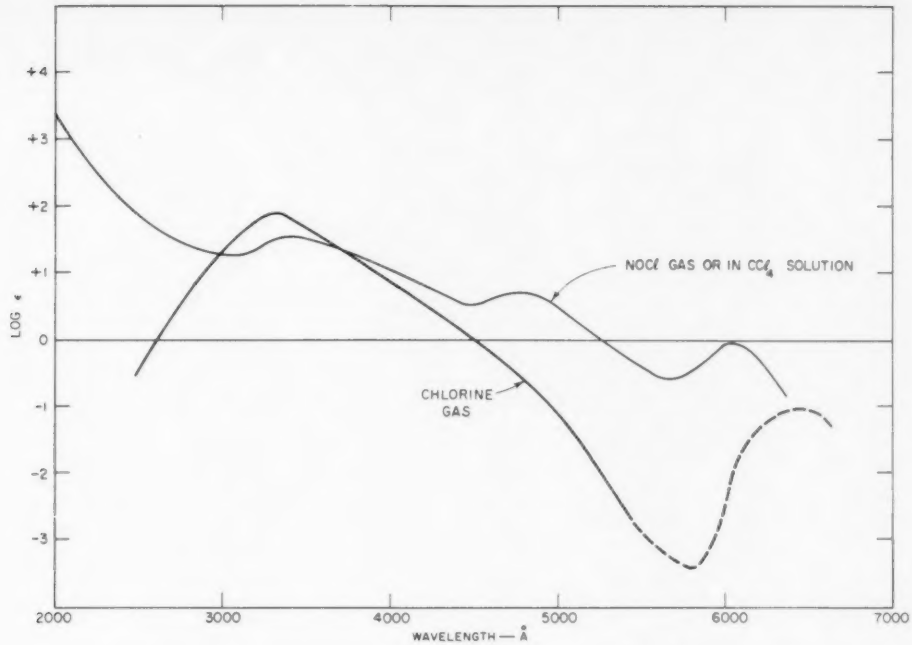

FIG. 2—Absorption Spectra of Gaseous Nitrosyl Chloride and Chlorine.

no reaction of nitric oxide with light during the photodecomposition of nitrosyl chloride on the surface of the earth. However, the data presented show that any photochemical reaction involving nitric oxide either as a reactant or product cannot take place in space at wavelengths less than 2300 Å. At wavelengths less than 2300 Å, the nitric oxide formed from the photochemical decomposition of nitrosyl chloride will decompose to nitrogen, oxygen, nitrous oxide, and nitrogen dioxide; the products cannot then again be recombined to form nitrosyl chloride.

As expected, Bernstein and Herzberg[10] found only a weak absorption band system for gaseous nitric oxide in the wavelength region 3500–2300 Å. For liquid nitric oxide, however, these authors found one strong continuous absorption starting at 4000 Å, extending to shorter wavelengths, and one at 5600 Å, extending to longer wavelengths. The maximum transmission occurred around 4600 Å.

Chlorine

Halban and Siedentopf[62] determined the absorption spectra of gaseous chlorine (Fig. 2). Chlorine absorbs in two broad regions. The first extends from about 6430 Å to about 2500 Å, with a maximum at 3340 Å. The spectrum at longer wavelengths is banded and the absorption coefficients have low values.[33] The second absorption region extends from about 1900 Å to 1560 Å and is entirely continuous, according to Cordes and Sponer.[17] Absorption in the lower wavelength region corresponds to a dissociation similar to that produced by absorption in the region of longer wavelengths, except that the atoms produced are endowed with greater kinetic energies. The convergence limit for chlorine is 4785 Å, at which point the molecule dissociates into a normal and an excited atom:

$$Cl_2 \rightarrow Cl + Cl^* \qquad [20]$$

This production of chlorine atoms in both the gaseous and liquid phases is perhaps the prime reason why the photoproducts will recombine quite quickly. As has been previously mentioned, the activation energy for the combination of free radicals is quite low.

Chlorine shows a Budde effect,[15] that is, an expansion upon illumination. Budde found that this expansion was the result of a temperature rise, an observation confirmed by Bevan.[11] Such a temperature rise is not surprising in view of the fact that the chlorine atoms which are produced must recombine to form chlorine molecules, with the evolution of heat. The Budde effect is mentioned briefly, for it is possible that the effect observed by the authors,[40] Neuwirth,[46] and others could be attributed to this phenomenon.

THERMAL DISSOCIATION

Nitrosyl Chloride

The extent of the thermal dissociation of nitrosyl chloride under various conditions has been calculated

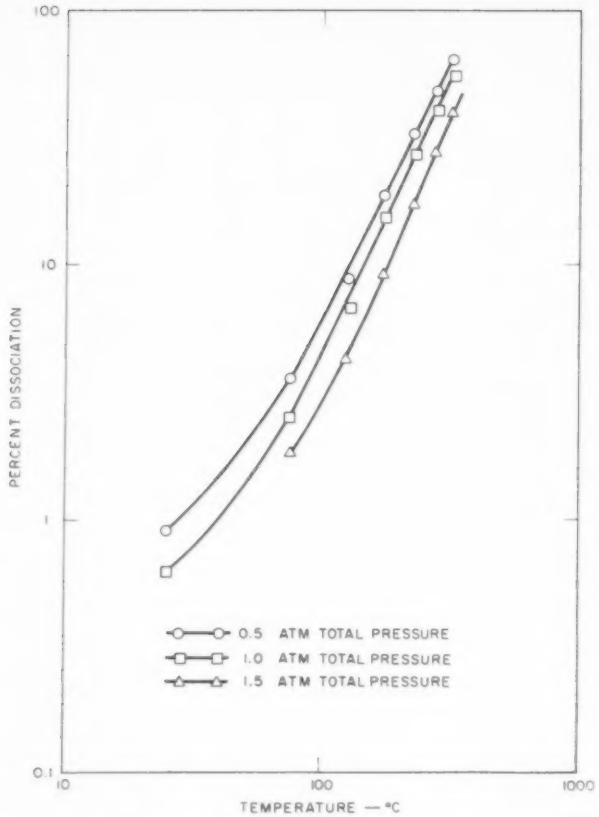

FIG. 3—Thermal Dissociation of Nitrosyl Chloride (after McGonigle).

by McGonigle,[41] based on an equation of Beeson and Yost[9] for the equilibrium,

$$\log_{10} K_p(\text{cm Hg}) = -2.808 - \frac{3591.0}{T} + 4.1457 \log_{10} T - 0.0023406\ T + 0.52915 \times 10^{-5}\ T^2 \pm 0.02. \quad [21]$$

These data, presented in Fig. 3, show that the percent dissociation increases with increasing temperature and decreasing pressure. On this basis, the photochemical dissociation could be increased by raising the temperature and lowering the pressure of the reaction.

Much study has been devoted to the kinetics of the NOCl system. The thermal decomposition of nitrosyl chloride is second order and the formation of nitrosyl chloride represents one of the rare cases of a homogeneous reaction of the third order. Welinsky and Taylor[65] have critically discussed much of the work on kinetics.

Ashmore and associates[2–5] have described the mechanism of both the decomposition and the formation of nitrosyl chloride in the gaseous phase. Ashmore and Spencer[5] established that reaction paths involving chlorine atoms occur in parallel with molecular reactions and that some of the chlorine atom reactions occur on the wall of the vessel; the following reactions were considered.

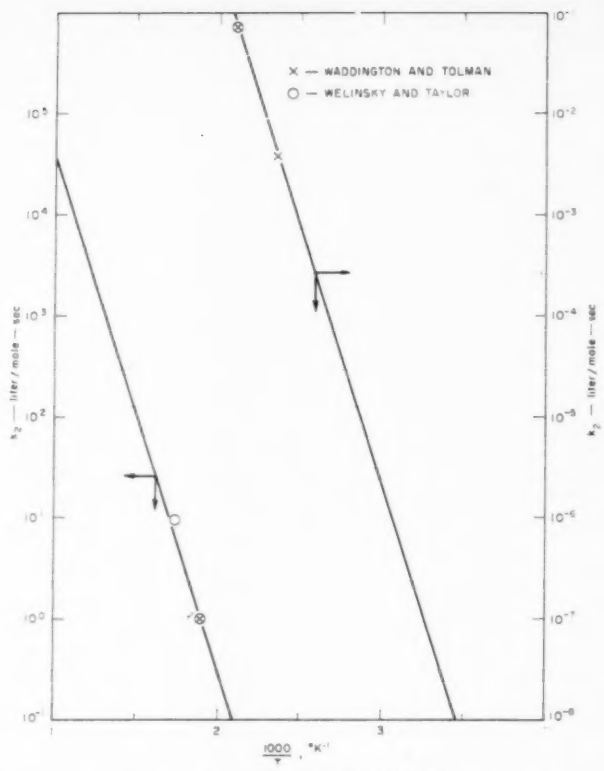

FIG. 4—Equilibrium Constant $K_E = \frac{(NO)^2(Cl_2)}{(NOCl)^2}$ (after Ashmore and Chanmugam).

$$2NOCl \underset{k_2}{\overset{k_1}{\rightleftharpoons}} 2NO + Cl_2 \quad [22]$$

$$NOCl + M \underset{k_4}{\overset{k_3}{\rightleftharpoons}} NO + Cl + M \quad [23]$$

(M represents any gas present)

$$NO + Cl_2 \underset{k_5}{\overset{k_5}{\rightleftharpoons}} NOCl + Cl \quad [24]$$

$$NOCl + \text{wall} \underset{k_8}{\overset{k_7}{\rightleftharpoons}} NO + Cl_w \quad [25]$$

$$Cl_w \underset{k_{10}}{\overset{k_9}{\rightleftharpoons}} Cl + \text{wall} \quad [26]$$

$$NOCl + Cl_w \underset{k_{12}}{\overset{k_{11}}{\rightleftharpoons}} NO + Cl_2 + \text{wall} \quad [27]$$

The same authors stated that in parallel with the accepted molecular mechanisms (Eq. 22), there are mechanisms (Eqs. 23 and 24) which contribute about 60% of the total rate of decomposition at 300° C, and about 95% of the initial rate of formation of nitrosyl chloride in a typical mixture of 12 mm of nitric oxide and 50 mm of chlorine at 200° C; these proportions increase as the temperature increases. Rate constants for several of these reactions (Eqs. 22–27) were determined.

VOL. 5 1961

The equilibrium constant based partly on Dixon's data[22] has been presented by Ashmore and Chanmugam;[4] these results, shown in Fig. 4, were confirmed by Waddington and Tolman.[63] At 25° C, the equilibrium constant is 4.0×10^{-9} moles/liter, which decreases to 3.6×10^{-2} moles/liter at 400° C.

The rate constants for the decomposition of nitrosyl chloride are presented in Fig. 5;[63, 65] the rate constants for the formation of nitrosyl chloride are presented in Fig. 6.[5, 65] The half life for the decomposition and formation of nitrosyl chloride was calculated based upon the data of Figs. 5 and 6. At a concentration of 1 mole/liter and 25° C, 3.0×10^7 seconds are required for half of the original nitrosyl chloride to decompose thermally and 0.13 seconds are required for the formation of nitrosyl chloride (Table 7). There is little doubt that the rate of thermal formation is more rapid than that of the thermal decomposition.

Trautz and Gerwig[60] noted that the kinetics of the liquid phase reaction were about what might have been expected from extrapolation of gas phase data. Noyes[48] found that the reaction between nitric oxide and liquid chlorine, or chlorine dissolved in carbon tetrachloride, was rapid at −80° C and that the rate was still appreciable at −150° C. These fast rates were also observed by Boubnoff and Guye.[12] Further, Kiss[31] showed that the recombination took place in the dark.

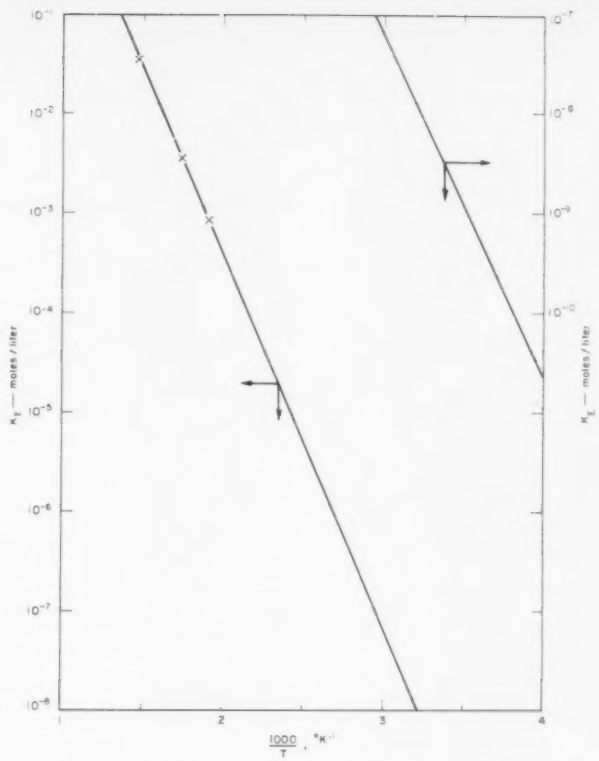

FIG. 5—Reaction Rate for Thermal Decomposition $2NOCl \xrightarrow{k_2} 2NO + Cl_2$.

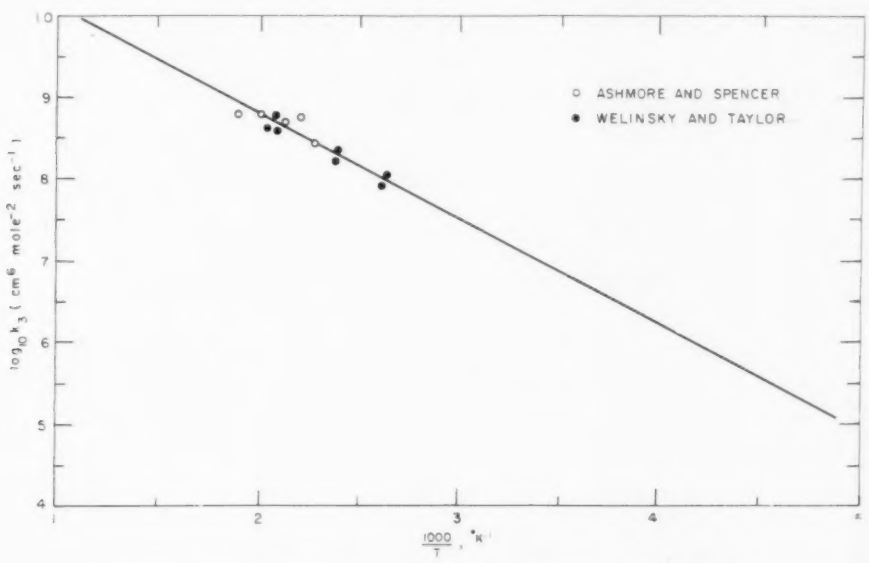

FIG. 6—Reaction Rate for Thermal Formation $2NO + Cl_2 \xrightarrow{k_3} 2NOCl$

Nitric Oxide

As has been mentioned, nitric oxide reacts with oxygen to form the brownish-red gas nitrogen dioxide. This reaction

$$NO + \tfrac{1}{2} O_2 = NO_2 \qquad [28]$$

is reversible; at room temperature the equilibrium lies almost completely to the right but at about 750° C the equilibrium constant

$$K_{atm} = \frac{P_{NO} P_{O_2}^{\frac{1}{2}}}{P_{NO_2}} \qquad [29]$$

is approximately unity.[66]

TABLE 7—Half-Life for the Decomposition and Formation of Nitrosyl Chloride (in seconds)

Temperature (°C)	Concentration (moles/liter)			
	2	1	0.50	0.25
	Decomposition			
−50	7.1×10^{12}	1.4×10^{13}	2.9×10^{13}	5.7×10^{13}
25	1.5×10^{7}	3.0×10^{7}	5.9×10^{7}	1.2×10^{8}
200	6.6	13.	26.	53.
	Formation			
−50	1.06	4.23	16.9	67.7
25	0.033	0.130	0.521	2.08
200	0.008	0.003	0.013	0.051

The maximum absorption of nitrogen dioxide is at about 4500 Å. If oxygen were added during the photolysis of nitrosyl chloride, would the formed NO_2 be able to reverse itself to reform the nitric oxide and oxygen? Unfortunately, as has been mentioned, the quantum yields of the reaction

$$NO_2 \xrightarrow[CCl_4]{h\nu} NO + \tfrac{1}{2}O_2 \qquad [12]$$

are small. Norrish[47] determined that the quantum yield was zero at 5760 Å, 5460 Å, and 4360 Å; 0.37 at 4050 Å; 1.05 at 3650 Å; and 1.04 for the range 3160–2650 Å.

Thermally the decomposition of nitrogen dioxide is perceptible at 150° C and is complete at 620° C. The decomposition at various temperatures is as follows.[23]

Temperature, °C	130	184	279	494	620
Decomposition, %	0	5	13	57	100

Nitric oxide has a strong thermodynamic tendency to decompose into its elements at room temperature; the heat of formation of nitric oxide is negative. That nitric oxide is nevertheless capable of existence at ordinary temperature is due to the fact that its rate of decomposition is practically zero at room temperature: it is metastable.

The nature of the decomposition may be judged by the free energy equation of Giauque and Kemp:[24]

$$\Delta F_T^\circ = 21{,}600 - 2.50\ T. \qquad [30]$$

On this basis (equation 30), $\Delta F^\circ = 0$ at 8650°K. In the process of manufacture, air is passed through an electric arc at 3500°; by rapidly cooling the heated equilibrium mixture (the rate of decomposition of NO is slow even at 1500°), a mixture of air containing only 2% or 3% nitric oxide is obtained.

The equilibrium constants at various temperatures for the reaction

$$\tfrac{1}{2}\ N_2(g) + \tfrac{1}{2}\ O_2(g) = NO(g) \qquad [31]$$

are shown in Table 8.[66]

TABLE 8—Equilibrium Constants for the Reaction $\frac{1}{2}\ N_2(g) + \frac{1}{2}\ O_2(g) = NO(g)$

Temperature (°K)	K (calc.)	K (obs.)
298.1	7.26×10^{-16}	—
1000	8.86×10^{-5}	—
1500	3.30×10^{-3}	—
1811	1.14×10^{-2}	0.93×10^{-2}
2033	2.21×10^{-2}	1.6×10^{-2}
2675	7.98×10^{-2}	5.8×10^{-2}
3000	1.24×10^{-1}	—
3500	2.09×10^{-1}	—
4000	3.07×10^{-1}	—
5000	5.26×10^{-1}	—

TABLE 9—Equilibrium Constants for the Reaction $Cl_2(g) \rightarrow 2Cl(g)$

Temperature (°K)	K_p (atm)
298.1	1.95×10^{-37}
500.	2.70×10^{-20}
1000.	1.71×10^{-7}
1500.	3.68×10^{-5}
2000.	5.69×10^{-4}
2500.	11.99
3000.	92.21

Chlorine

Trautz and Staeckel[61] determined the degree of thermal dissociation of chlorine at one atmosphere to be 1.5% at 1200° C, 2.10% at 1240° C and 3.05% at 1280° C. At lower pressure (10^{-3} atm), Henglein[29] found the degree of dissociation to be 18% at 712° C and 60% at 878° C. Giauque and Overstreet[25] later derived more precise values for the equilibrium constant, K_p, based upon spectroscopic data. These data are given in Table 9.

REFERENCES

1. Abetti, G. *The Sun*. Translated by J. B. Sidgwick. The MacMillan Company, New York, 1957.
2. Ashmore, P. G., and J. Chanmugam. *Trans. Faraday Soc.* **49,** 254 (1953).
3. Ashmore, P. G., and J. Chanmugam. *Trans. Faraday Soc.* **49,** 265 (1953).
4. Ashmore, P. G., and J. Chanmugam. *Trans. Faraday Soc.* **49,** 270 (1953).
5. Ashmore, P. G., and M. S. Spencer. *Trans. Faraday Soc.* **55,** 1868 (1959).
6. Atwood, K., and G. K. Rollefson. *J. Chem. Phys.* **9,** 506 (1941).
7. Bailey, C. R., and A. B. D. Cassie. *Proc. Roy. Soc.* (London) **A145,** 336 (1934).
8. Beckham, L. J., W. A. Fessler, and M. A. Kise. *Chem. Rev.* **48,** 319 (1951).
9. Beeson, C. M., and D. M. Yost. *J. Chem. Phys.* **7,** 44 (1939).
10. Bernstein, H. J., and G. Herzberg. *J. Chem. Phys.* **15,** 77 (1947).
11. Bevan, P. V. *Phil. Trans.* **202,** 90 (1904).
12. Boubnoff, N., and P. A. Guye. *J. chim. phys.* **9,** 290 (1911).
13. Bowen, E. J., and J. F. Sharp. *J. Chem. Soc.* **127,** 1026 (1925).
14. Brown, H., J. Bonner, and J. Weir. *The Next Hundred Years*. The Viking Press, New York, 1957.
15. Budde, E. *J. prakt. Chem.* **7,** 376 (1873).
16. Calvert, J. G. *Ohio J. Sci.* **53,** 293 (1953).
17. Cordes, H., and H. Sponer. *Z. Physik.* **63,** 334 (1930).
18. Dainton, F. S., and D. G. L. James. *J. chim. phys.* **48,** No. 9/10, C17 (1951).

VOL. 5 1961

19. Daniels, F. *J. Phys. Chem.* **42,** 713 (1938).
20. Daniels, F., and J. A. Duffie, (ed.). *Solar Energy Research.* Univ. of Wisconsin Press, Madison, Wisc., 1955.
21. Daniels, F., L. J. Heidt, R. S. Livingston, and E. Rabinowitch. *Photochemistry in the Liquid and Solid States.* John Wiley and Sons, Inc., New York, 1960.
22. Dixon, J. K. *Z. physik. Chem.* (Bodenstein Festband), 1931, 679.
23. Ephraim, F. *Inorganic Chemistry.* by P. C. L. Thorne and E. R. Roberts. Nordeman Publishing Co., New York, 1943.
24. Giauque, W. F., and J. D. Kemp. *J. Chem. Phys.* **6,** 40 (1938).
25. Giauque, W. F., and R. Overstreet. *J. Am. Chem. Soc.* **54,** 1731 (1932).
26. Goodeve, C. F., and S. Katz. *Proc. Roy. Soc.* (London) **A172,** 432 (1939).
27. Heidt, L. J., and A. F. MacMillan. *Science* **117,** 75 (1953).
28. Heidt, L. J., and M. E. Smith. *J. Am. Chem. Soc.* **70,** 2476 (1948).
29. Henglein, F. A. *Z. anorg. Chem.* **123,** 137 (1922).
30. Holmes, H. H., and F. Daniels. *J. Am. Chem. Soc.* **56,** 630 (1934).
31. Kiss, A., *Rec. trav. chim.* **42,** 665 (1923).
32. Kistiakowsky, G. B. *J. Am. Chem. Soc.* **52,** 102 (1930).
33. Kuhn, H. *Z. Physik.* **39,** 77 (1926).
34. Leifson, S. W. *Astrophys. J.* **63,** 73 (1926).
35. MacDonald, J. Y. *J. Chem. Soc.*, 1 (1928).
36. Marcus, R. J. *Science* **123,** 399 (1956).
37. Marcus, R. J., and H. C. Wohlers. *Ind. Eng. Chem.* **51,** 1335 (1959).
38. Marcus, R. J., and H. C. Wohlers. *Ind. Eng. Chem.* **52,** 377 (1960).
39. Marcus, R. J., and H. C. Wohlers. *Ind. Eng. Chem.* **52,** 825 (1960).
40. Marcus, R. J., and H. C. Wohlers. *Solar Energy.* **4(2),** 1 (1960).
41. McGonigle, T. J. *Properties and Reactions of Nitrosyl Chloride.* Solvay Process Division, Allied Chemical Corp., New York, 1949.
42. Mellor, J. W. *Inorganic and Theoretical Chemistry.* Vol. II. Longmans, Green and Co., New York, 1946.
43. Mellor, J. W. *Inorganic and Theoretical Chemistry.* Vol. VIII. Longmans, Green and Co., New York, 1947.
44. Mellor, J. W. *Inorganic and Theoretical Chemistry.* Supplement II, Part I, Longmans, Green and Co., New York, 1956.
45. Natanson, G. L. *Acta Physicochim. USSR* **11,** 521 (1939).
46. Neuwirth, O. *J. Phys. Chem.* **63,** 17 (1959).
47. Norrish, R. W. G. *J. Chem. Soc.* 1158, 1604, 1611 (1929).
48. Noyes, W. A. *J. Am. Chem. Soc.* **53,** 2137 (1931).
49. Noyes, W. A., and P. A. Leighton. *The Photochemistry of Gases.* Reinhold Publishing Corp., New York, 1941.
50. Pauling, L. *The Nature of the Chemical Bond.* Cornell Univ. Press, Ithaca, New York, 1940.
51. Pitts, J. N., J. D. Margerum, and W. E. McKee. "Photochemistry and Space Power Generation." Presented at American Rocket Society Meeting, May 1960.
52. Remy, H. *Treatise on Inorganic Chemistry.* Translated by J. S. Anderson, edited by J. Kleinberg. Elsevier Publishing Co., New York, 1956.
53. Rosenberg, N. "Photochemical processes and their utilization for solar energy." In *Proceedings of a Seminar on Advanced Energy Sources and Conversion Techniques,* Vol. I, 139 (1958) ASTIA No. AD 209301.
54. Seidell, A. *Solubility of Inorganic and Organic Compounds.* Vol. I. D. Van Nostrand Co., New York, 1940.
55. Shaw, J. H. *Ohio J. Sci.* **53,** 258 (1953).
56. Sneed, M. C., and R. C. Brasted. *Comprehensive Inorganic Chemistry.* Vol. V. D. Van Nostrand Co., New York, 1956.
57. Sneed, M. C., J. L. Maynard, and R. C. Brasted. *Comprehensive Inorganic Chemistry.* Vol. III. D. Van Nostrand Co., New York, 1954.
58. Stewart, D. C. "Light absorption of solutions of the trivalent ions of the lanthanide and actinide rare earths." AECD-2389.
59. Taylor, H. S. *J. Phys. Chem.* **34,** 2049 (1930).
60. Trautz, M., and W. Gerwig. *Z. anorg. allgem. Chem.* **146,** 1 (1925).
61. Trautz, M., and W. Staeckel. *Z. anorg. Chem.* **122,** 82 (1922).
62. V. Halban, H., and K. Siedentopf. *Z. physik. Chem.* **103,** 71 (1922).
63. Waddington, G., and R. C. Tolman. *J. Am. Chem. Soc.* **57,** 689 (1935).
64. Weinberg, A. M. *Physics Today* **12,** 18 (1959).
65. Welinsky, I., and H. A. Taylor. *J. Chem. Phys.* **6,** 466 (1938).
66. Yost, D. M., and H. Russel. *Systematic Inorganic Chemistry.* Prentice-Hall, Inc., New York, 1944.

Some Considerations Relative to a Solar-Powered Savery Water Pump

By James R. Jenness, Jr.

HRB-Singer Research Laboratories, State College, Pa.

No small inexpensive steam engine of piston or turbine type is now available, and the precision required in the manufacture of parts for such mechanisms makes such a development unlikely. The primitive Savery steam engine should be adaptable to mass production at low unit cost, so that in spite of its low efficiency it may be useful as a solar-powered low-lift water pump.

INTRODUCTION

Since abundant solar power is available to all who might use it, operating efficiency is not the most important characteristic of solar-powered devices. In some cases, a beneficial flow of solar energy into the economies of nonindustrial regions is held back only by the high cost of solar-powered equipment. Therefore, the cost of the equipment is a prime consideration.

In the development of technology, the refinement of crude devices to achieve increased efficiency is a recurring theme. Watt considered his pistons and cylinders well matched if a small coin fit tightly between them. Later developments in machine tools made possible improved accuracies in steam engine construction which in turn brought about more efficient engine operation to pay the expense of employing greater skills in the fabrication of engine components. Thus, the steam engine evolved into a machine of high precision; no small inexpensive steam engine of a type adaptable to solar power was developed.

For satisfactory operation of devices such as high-

VOL. 5 1961

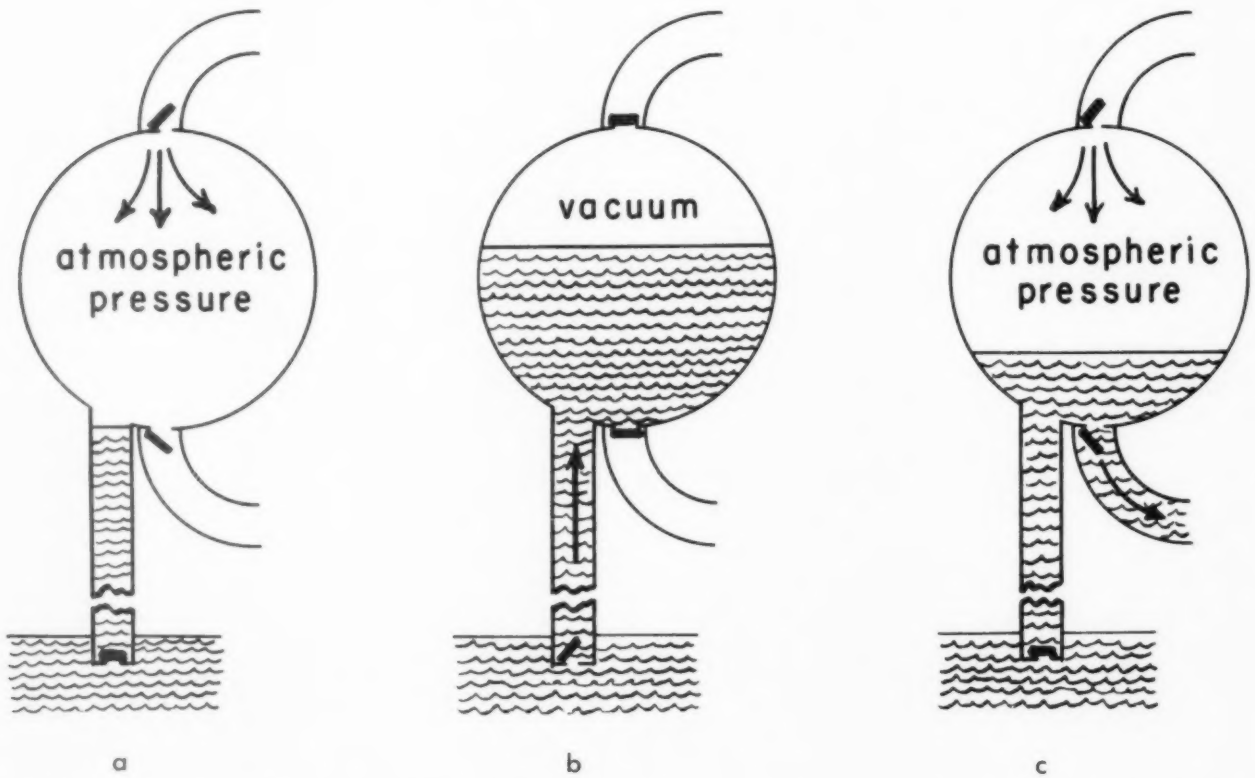

FIG. 1. Operating cycle of the Savery pump: a. tank filled with saturated steam b. steam condenses, drawing water into tank c. water drains from tank, drawing in new charge of steam

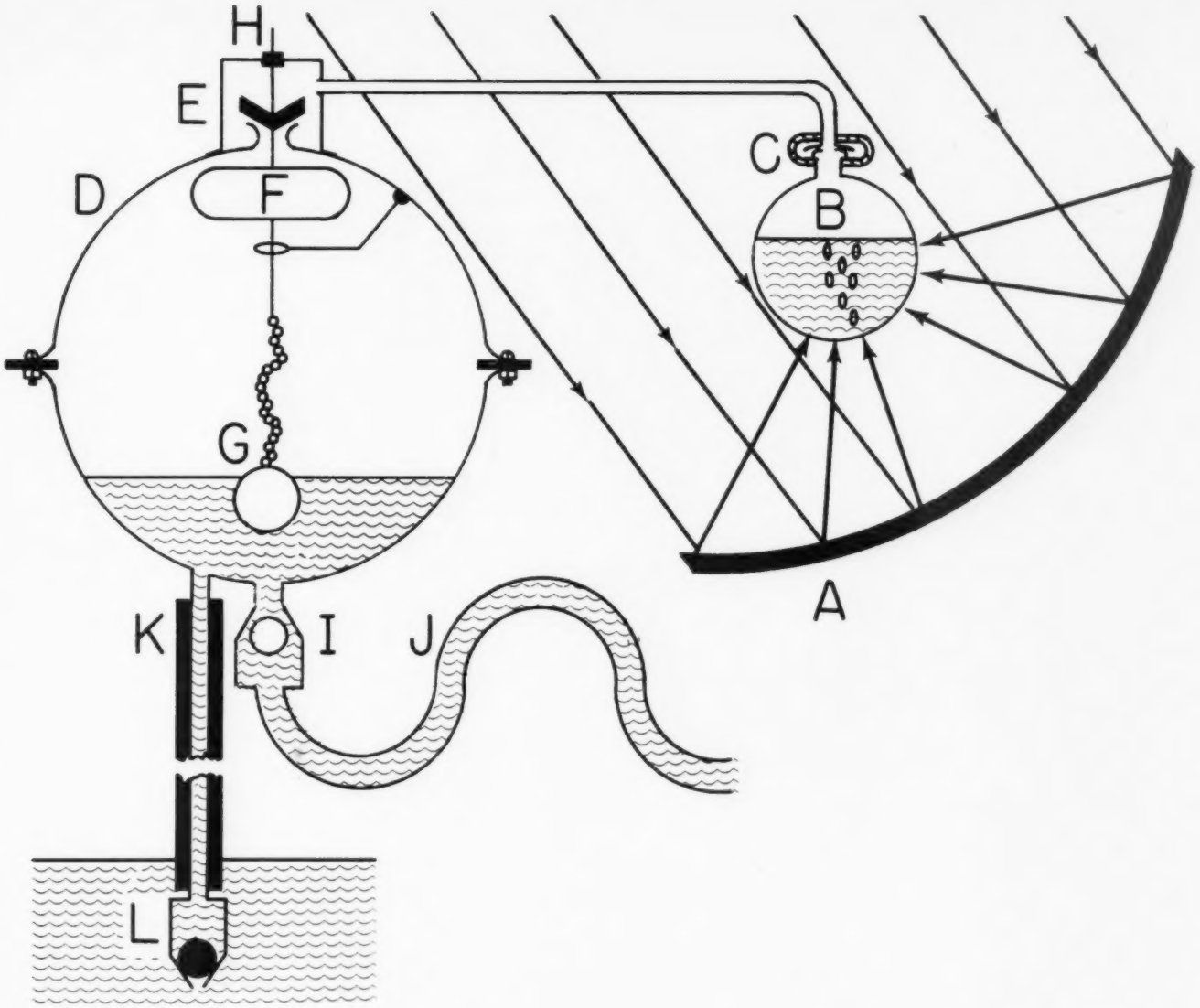

FIG. 2. Schematic of an automatic solar-powered Savery pump: Reflector *A* concentrates solar radiation on boiler *B*. Boiler refill and steam tube retaining cap *C* also serves as safety valve. Steam enters tank *D* through valve *E* which is raised and opened by float *F* when water rises to top of tank. When water level descends to bottom of tank, float *G* hanging from chain pulls steam inlet valve shut. Friction of steam valve rod in grommet *H* prevents downward motion of valve so long as *G* is afloat and prevents upward motion until *F* is afloat. Floating-ball valve *I* prevents reversal of flow in outlet pipe *J* when steam condensation creates vacuum in tank. Pipe *J* forms trap to keep valve *I* filled with water at all times. Vacuum resulting from condensation of steam in tank draws well water up through hose *K*. Sinking-ball valve *L* prevents flow of water back into well when tank is at atmospheric pressure.

pressure piston engines and turbines, concentrated power sources are required. Therefore, in considering the feasibility of developing a small solar-powered steam engine, other mechanisms must be investigated. The Savery water pump is of interest since its simplicity of construction may offset its low operating efficiency. It may prove economically feasible to employ solar-powered Savery engines for such applications as raising irrigation water from shallow wells or up river banks.

THE SAVERY ENGINE

Thomas Savery, a military engineer, received a British patent in 1698 for the first practical steam-powered lift pump.[1] In the early eighteenth century Savery engines came into considerable use for low-lift water pumping until they were superseded by the more efficient Newcomen engines. The Savery steam-powered lift pump has no large moving parts, so it might have competed successfully with the piston engine if sim-

plicity of construction had been more important than economy of fuel consumption.

The principle of operation of the Savery engine is illustrated in Fig. 1. First, the steam inlet valve and water outlet valve are opened to fill the tank with saturated steam at atmospheric pressure as shown in Fig. 1a. Next, the steam inlet valve and water outlet valve are closed and the steam cools. This operation causes it to condense and lower the pressure in the tank, opening the water inlet valve (Fig. 1b) and drawing water into the tank. The incoming water accelerates the condensation of steam. When the tank is filled with water, the water inlet valve is closed and the steam inlet and water outlet valves are opened, draining out the water and admitting saturated steam to the tank (Fig. 1c) after which the cycle is repeated.

Figure 2 indicates how a solar-powered Savery pump with automatically operated valves might be contrived. It is shown in the "water out, steam in" step of its cycle, corresponding to Fig. 1c. Since the differential pressures involved are only of the order of one atmosphere, relatively lightweight construction is adequate. The tank might be stamped from sheet metal or fabricated of plastic in two hemispherical halves by laminating or by vacuum drawing from flat sheets. The other pump components could also be mass produced at low cost. It should be possible for the average handyman to assemble such a device from a do-it-yourself kit, using only a few simple hand tools.

The maximum efficiency possible for such a pump is Dgh/dH, where D is the density of water, g is gravitational acceleration, h is the distance the water is lifted, d is the density of 100 C saturated steam at atmospheric pressure, and H is the heat of vaporization of water at 100 C. The maximum value h can have (at sea level) is 1.03 (10^3) cm., so the theoretical efficiency of the Savery pump is found to be 7.5%. Most of the heat consumed in vaporizing water in the boiler goes to warm the water drawn into the tank during condensation of the steam. This is an inherent inefficiency of any heat engine operating above ambient temperature, adding heat to and subsequently removing heat from the working substance.

The actual efficiency will of course be less than the theoretical. The chief loss to be anticipated is condensation of steam during intake after the tank has been cooled by newly raised water. A spherical aluminum shell of 20-cm diam (approximately one gal capacity) with a wall thickness of 0.15 mm (38-gauge sheet metal) will require approximately 850 cal to raise the temperature from 20 C to 100 C. Therefore, this amount of heat must be added to the 1350 cal required to produce this volume of saturated steam at atmospheric pressure. Since only about 100 cal per cycle are converted to useful work, the efficiency is $100/(1350 + 850) = 4.5\%$.

Principles whereby inexpensive paraboloidal reflectors might be fabricated have been discussed in an earlier paper.[2] Such a reflector of one m² area could supply 300 w to a boiler at its focus on a sunny day. A transparent or translucent water container should be an efficient boiler if a dark nonvolatile water-soluble dye is added to the water. If the assembly is adjusted to set the focus in the darkened water inside, the solar radiation is converted to heat within the water and the walls of the container need not be heated above 100 C. It might be possible to boil water in a cheap plastic container by this technique. A cylindrical parabolic reflector may require less frequent focusing adjustments than a paraboloid, so this type of radiation collector may be preferable for use in a solar boiler. Archibald[3] has suggested techniques for making inexpensive cylindrical reflectors.

If steam is generated at a rate of 300 w by a solar boiler and fed to a Savery pump of 4.5% efficiency, water could be pumped at a rate of 2.2 gpm. Assuming solar power is available to sustain an average pumping rate of 1.5 gpm for 10 hr per day, the irrigation rate on a $\frac{1}{10}$ acre garden plot is approximately $\frac{1}{3}$ in. per day, which Blaney and Criddle[4] consider quite adequate for most plants in a climate of negligible rainfall.

CONCLUSIONS

A small portable Savery engine with a one-gal pumping tank powered by a solar boiler with a collecting reflector of one m² area could raise water at a rate sufficient to irrigate a family-sized vegetable garden. The low efficiency of the Savery pump is of relatively little importance when its power is derived from solar radiation, since solar power is most abundant at times when irrigation requirements are high. Since the mechanism is simple, it should lend itself to low-cost manufacture for sale at a retail price within the means of small farmers in nonindustrial regions.

REFERENCES

1. Singer, C., Holmyard, E. J., Hall, A. R., and Williams, T. I.(eds.). *A History of Technology*, Vol. 4, page 172. New York and London: Oxford University Press, 1958.
2. Jenness, Jr., James R. "Recommendations and Suggested Techniques for the Manufacture of Inexpensive Solar Cookers," *Solar Energy* **4**—3 (July 1960), 22.
3. Archibald, Paul B., "A Stationary Solar Energy Converter," *Solar Energy* **3**—4 (December 1959), 65.
4. Blaney, Harry F., and Criddle, Wayne D., U. S. Department of Agriculture, Soil Conservation Service Technical Paper 96 (1950).

VOL. 5 1961

Theoretical Concentrations for Solar Furnaces

By M. H. Cobble*

University of Delaware, Newark, Delaware

The concentration for a paraboloid of revolution mirror and for a parabolic cylinder mirror are derived as a function of relative aperture for several target geometries. The expression for optimum concentration for each target-mirror combination is developed, and the equation for the ideal target shape for a target of a parabolic cylinder mirror having a relative aperture of 4 is obtained.

THEORETICAL CONCENTRATIONS FOR SOLAR FURNACES

Several relationships are derived for determining the concentration of solar furnaces, using either a single-curved or a double-curved mirror, for several types of targets.

The derivations are based on the following assumptions: (1) all the energy reflected by an ideal mirror is used; (2) the target area is small compared to the mirror area, and so it is assumed that the target does not shield the mirror; (3) all the radiation is parallel to the axis of the mirror.

NOMENCLATURE

A = constant
A_{nm} = area of mirror normal to radiation, ft²
A_t = area of target, ft²
a = vertex ot triangle
b = vertex of triangle
C = concentration $\dfrac{\text{Btu(target)}}{\text{hr ft}^2} \Big/ \dfrac{\text{Btu(mirror)}}{\text{hr ft}^2}$
c = vertex of a triangle
D = mirror aperture, ft
d = targer width, ft
d_1, d_1', d_a, d_b, d_c = target geometry, ft (See Figures)
dc/dn = rate of change of concentration with respect to relative aperture, dimensionless
ds = differential of arc length, ft
f = focal length of mirror, ft
l = distance from point on mirror to focus, ft
l_m = maximum distance from point on mirror to focus, ft
n = relative aperture $\left(n = \dfrac{D}{f}\right)$, dimensionless
Q = radiation rate, $\dfrac{\text{Btu}}{\text{hr}}$
Q_m = radiation rate to mirror, $\dfrac{\text{Btu}}{\text{hr}}$
Q_t = radiation rate to target, $\dfrac{\text{Btu}}{\text{hr}}$
R_{es} = distance from the earth to the sun, $(92.9 \times 10^6$ mi)
$r = \dfrac{d}{2}$, ft
S = arc length, ft
S_d = diameter of sun, 8.66×10^5 mi
S_r = radius of sun, 4.33×10^5 mi
x = rectangular coordinate, ft
x_m = maximum rectangular coordinate, ft
y = rectangular coordinate, ft
y_m = maximum rectangular coordinate, ft
α = angle subtended by the sun, dimensionless
β = angle of deflection that a ray makes when hitting mirror, dimensionless
$\gamma_1 = \left(90° - \dfrac{\alpha}{2}\right)$, dimensionless
$\gamma_2 = \left(90° + \dfrac{\alpha}{2}\right)$, dimensionless
δ = angle, dimensionless
ρ = polar radius, ft

INTRODUCTION—DEFINITION OF CONCENTRATION

Assuming an ideal mirror, the radiation rate falling on the mirror is equal to the radiation rate going through the target area, so that

$$Q_m = Q_t \qquad [1]$$

Multiplying the left side numerator and denominator by the normal area of the mirror, and multiplying the right side numerator and denominator by the area of the target results in

$$\frac{Q_m A_{nm}}{A_{nm}} = \frac{Q_t A_t}{A_t} \qquad [2]$$

* Associate Professor of Mechanical Engineering.

Rearranging yields the concentration

$$\frac{\frac{Q_t}{A_t}}{\frac{Q_m}{A_{nm}}} = \frac{A_{nm}}{A_t} = C \qquad [3]$$

This concentration (C) will be used in the following derivations:

I. Concentration for a parabolic cylinder having a small relative aperture

The concentration is given from the introduction as

$$C = \frac{A_{nm}}{A_t} \qquad [1]$$

From the geometry of Fig. 1, it is seen that

$$C = \frac{D \times L}{d \times L} = \frac{D}{d} \qquad [2]$$

The definition of relative aperture (n) is

$$n = \frac{D}{f} \qquad [3]$$

thus

$$D = nf \qquad [4]$$

The tangent of the solar half-angle is

$$\tan \frac{\alpha}{2} = \frac{d/2}{f} = \frac{d}{2f} \qquad [5]$$

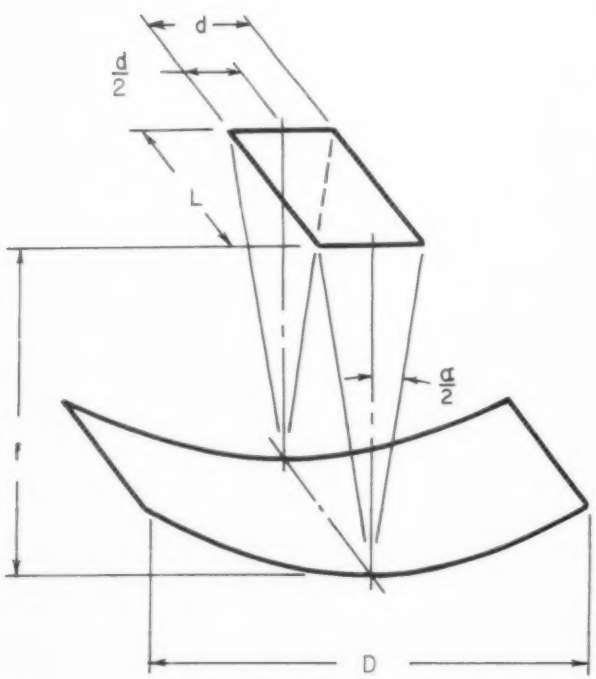

FIG. 1. Parabolic cylinder mirror with small relative aperture

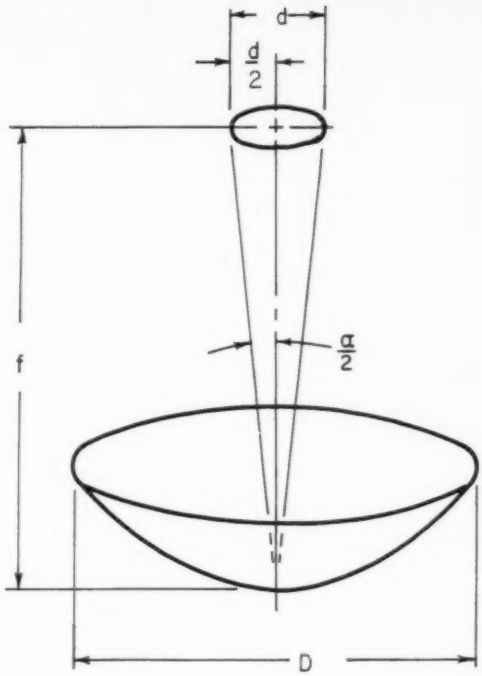

FIG. 2. Paraboloid of revolution with small relative aperture

so

$$d = f\left(2 \tan \frac{\alpha}{2}\right) \qquad [6]$$

The concentration then follows

$$C = \frac{D}{d} = \frac{nf}{f\left(2 \tan \frac{\alpha}{2}\right)} \qquad [7]$$

$$C = \frac{n}{2 \tan \alpha/2} \qquad [8]$$

$$C \leqq 107.3n \qquad [9]$$

Equations [8] and [9] are good approximations for $n < .5$, becoming more accurate as $n \to 0$.

II. Concentration for a paraboloid of revolution having a small relative aperture

The concentration is

$$C = \frac{A_{nm}}{A_t} \qquad [1]$$

As seen from Fig. 2 this is equivalent to

$$C = \frac{\frac{\pi D^2}{4}}{\frac{\pi d^2}{4}} = \frac{D^2}{d^2} \qquad [2]$$

VOL. 5 1961

Equation I-[4] states

$$D = nf \qquad [3]$$

From Fig. 2

$$\tan \frac{\alpha}{2} = \frac{d/2}{f} = \frac{d}{2f} \qquad [4]$$

Thus as above

$$d = f\left(2 \tan \frac{\alpha}{2}\right) \qquad [5]$$

Using the results of Eqs. [3] and [5] in [2] results in

$$C = \frac{D^2}{d^2} = \frac{(nf)^2}{\left[f\left(2 \tan \frac{\alpha}{2}\right)\right]^2} = \frac{n^2 f^2}{f^2\left(2 \tan \frac{\alpha}{2}\right)^2} = \frac{n^2}{\left(2 \tan \frac{\alpha}{2}\right)^2} \qquad [6]$$

or

$$C \leqq (107.3)^2\, n^2 \leqq 11{,}550\, n^2 \qquad [7]$$

Equations [6] and [7] are good approximations for small n.

III. Concentration for a parabolic cylinder having a circular cylinder target

It is evident from the geometry of the problem, as shown in Fig. 3, that the diameter of the target that will just receive all the radiation is determined by the rays reflected from the extremity of the mirror (assuming the mirror is symmetric). Thus the concentration is

$$C = \frac{A_{am}}{A_t} \qquad [1]$$

From Fig. 3 it is obvious that if the target and mirror are of length L, Eq. [1] becomes

$$C = \frac{D \times L}{\pi d L} = \frac{D}{\pi d} \qquad [2]$$

Using Eq. I-[4]

$$D = nf \qquad [3]$$

From Fig. 4

$$\sin \frac{\alpha}{2} = \frac{d/2}{l_m} = \frac{d}{2l_m} \qquad [4]$$

or rearranged

$$d = l_m\left(2 \sin \frac{\alpha}{2}\right) \qquad [5]$$

From Fig. 3

$$l_m = \sqrt{(f - y_m)^2 + x_m^2} \qquad [6]$$

The equation of the parabola with vertex at the origin is

$$y = \frac{x^2}{4f} \qquad [7]$$

or

$$x^2 = 4fy \qquad [8]$$

At the maximum position this becomes

$$x_m^2 = 4fy_m \qquad [9]$$

Substitution in Eq. [6] yields

$$l_m = \sqrt{(f - y_m)^2 + 4fy_m} \qquad [10]$$

this becomes with rearrangement

$$l_m = \sqrt{(f + y_m)^2} \qquad [11]$$

or

$$l_m = f + y_m \qquad [12]$$

But

$$y_m = \frac{x_m^2}{4f} \qquad [13]$$

and

$$n = \frac{D}{f} = \frac{2x_m}{f} \qquad [14]$$

or

$$x_m = \frac{nf}{2} \qquad [15]$$

Thus substitution of Eq. [13] and [15] in Eq. [12] gives

$$l_m = f + y_m = f + \frac{x_m^2}{4f} = f + \frac{1}{4f}\left(\frac{nf}{2}\right)^2 = f + \frac{n^2 f}{16} = f\left(1 + \frac{n^2}{16}\right) \qquad [16]$$

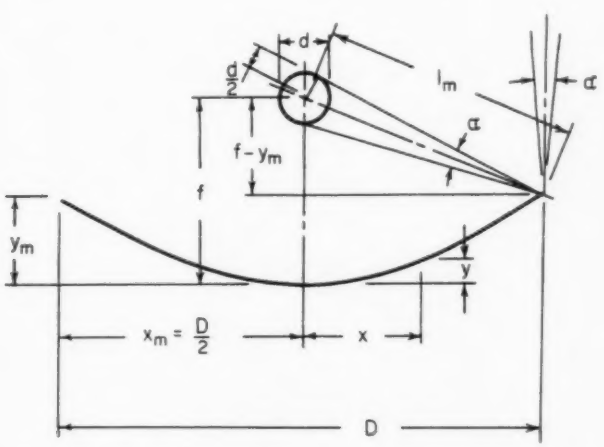

FIG. 3. Parabolic cylinder mirror with circular cylinder target

Therefore using Eq. [3] and [16] in Eq. [2] yields

$$C = \frac{D}{\pi d} = \frac{nf}{\pi\left[l_m\left(2\sin\frac{\alpha}{2}\right)\right]}$$

$$= \frac{nf}{\pi\left[f\left(1+\frac{n^2}{16}\right)\left(2\sin\frac{\alpha}{2}\right)\right]} \qquad [17]$$

$$C = \frac{n}{\pi\left(1+\frac{n^2}{16}\right)\left(2\sin\frac{\alpha}{2}\right)}$$

or

$$C \cong \frac{107.3n}{\pi\left(1+\frac{n^2}{16}\right)} \qquad [18]$$

When $n \ll 1$, Eq. [18] simplifies to

$$C \leqq \frac{107.3n}{\pi} \leqq 34.2n \qquad [19]$$

This relation is good for $n < \frac{1}{2}$

IV. Maximum concentration for a parabolic cylinder having a circular cylinder target

The expression for concentration, Eq. III-[17] is

$$C = \frac{n}{\pi\left(1+\frac{n^2}{16}\right)\left(2\sin\frac{\alpha}{2}\right)} = \frac{An}{\left(1+\frac{n^2}{16}\right)} \qquad [1]$$

where the constant A is given by

$$A = \frac{1}{\pi\left(2\sin\frac{\alpha}{2}\right)} \qquad [2]$$

The maximum concentration is determined by setting the derivative $\left(\frac{dC}{dn}\right)$ equal to zero, and solving the resulting equation, which is

$$\frac{dC}{dn} = 0 = A\left[\frac{1}{1+\frac{n^2}{16}} + \frac{(-1)n\left(\frac{2n}{16}\right)}{\left(1+\frac{n^2}{16}\right)^2}\right] \qquad [3]$$

rearranging gives

$$0 = 1 + \frac{n^2}{16} - \frac{2n^2}{16} \qquad [4]$$

or

$$n^2 - 16 = 0 \qquad [5]$$

thus

$$n = \pm 4 \qquad [6]$$

The solution of $n = -4$ has no meaning. Substitution of $n = 4$ into Eq. III-[17] gives the maximum concentration.

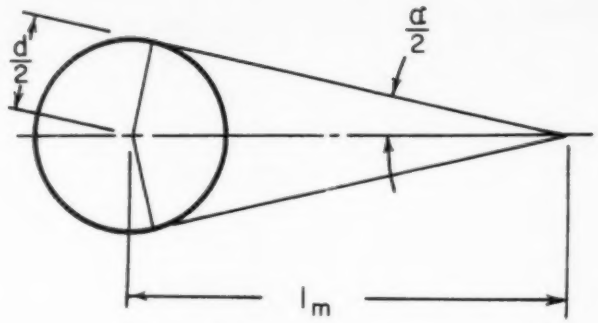

FIG. 4. Cylinder target geometry

$$C = \frac{n}{\pi\left(1+\frac{n^2}{16}\right)\left(2\sin\frac{\alpha}{2}\right)} \qquad [7]$$

$$= \frac{4}{\pi\left(1+\frac{n^2}{16}\right)\left(2\sin\frac{\alpha}{2}\right)}$$

$$C = \frac{2}{\pi\left(2\sin\frac{\alpha}{2}\right)} \leqq \frac{2\times 107.3}{\pi} \qquad [8]$$

or

$$C \leqq 68.3 \qquad [9]$$

V. Concentration for a paraboloid of revolution having a spherical target

Referring to Fig. 3, the diameter of the sphere that will just receive all the radiation is determined by the rays reflected from the extremity of the mirror. Thus the concentration is

$$C = \frac{A_{nm}}{A_t} \qquad [1]$$

Looking at Fig. 3, and evaluating for a sphere of diameter d, Eq. [1] becomes

$$C = \frac{\frac{\pi D^2}{4}}{\pi d^2} = \frac{D^2}{4d^2} \qquad [2]$$

Using Eq. I-[4]

$$D = nf \qquad [3]$$

From Fig. 4

$$\sin\frac{\alpha}{2} = \frac{d/2}{l_m} = \frac{d}{2l_m} \qquad [4]$$

solving for d yields

$$d = l_m\left(2\sin\frac{\alpha}{2}\right) \qquad [5]$$

VOL. 5 1961

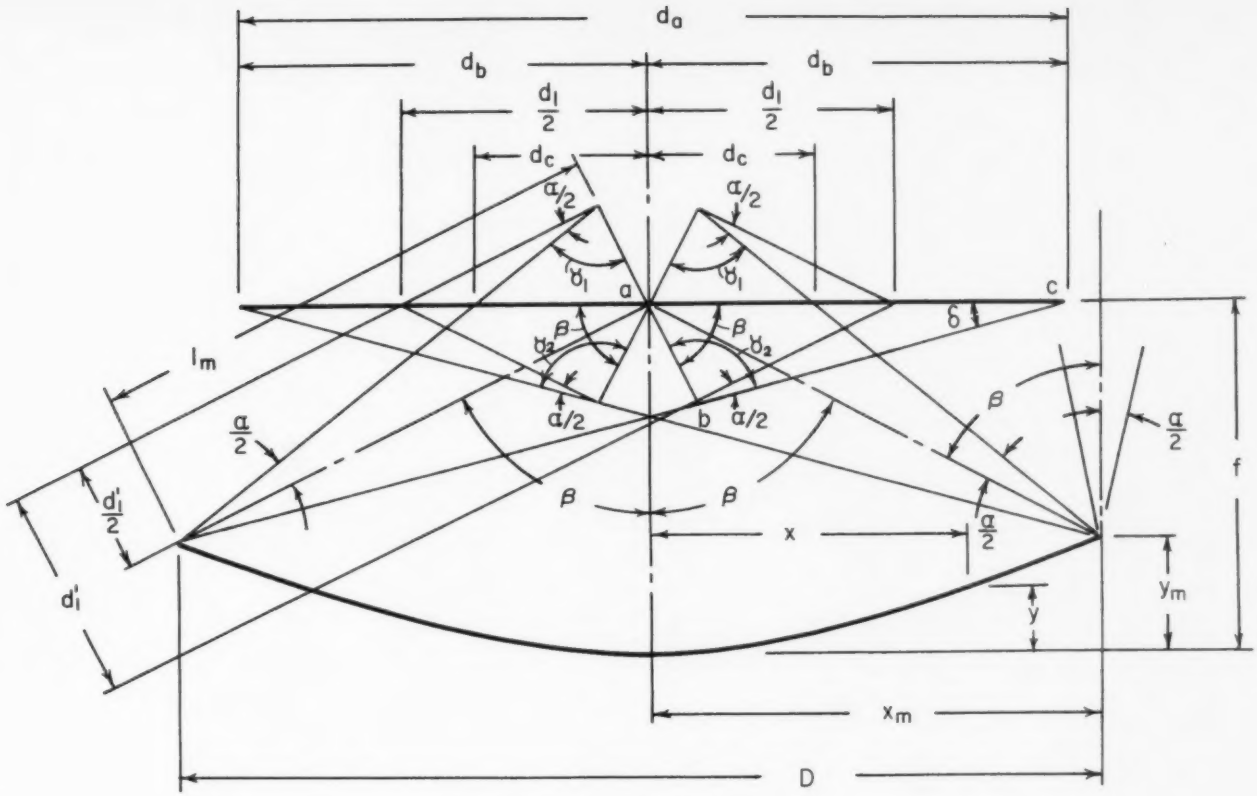

FIG. 5. Flat plate target geometry

Using Eq. III-[16]

$$l_m = f\left(1 + \frac{n^2}{16}\right) \qquad [6]$$

Substitution of Eqs. [3], [5] and [6] in (2) gives

$$C = \frac{D^2}{4d^2} = \frac{(nf)^2}{4\left[f\left(1 + \frac{n^2}{16}\right)\left(2 \sin \frac{\alpha}{2}\right)\right]^2} \qquad [7]$$

$$C = \frac{n^2}{4\left(1 + \frac{n^2}{16}\right)^2\left(2 \sin \frac{\alpha}{2}\right)^2} \qquad [8]$$

or

$$C \leqq \frac{(107.3)^2 n^2}{4\left(1 + \frac{n^2}{16}\right)^2} \leqq \frac{11{,}550n^2}{4\left(1 + \frac{n^2}{16}\right)^2} \qquad [9]$$

When $n \ll 1$, Eq. [9] may be given as

$$C \leqq \frac{11{,}550n^2}{4} \leqq 2890n^2 \qquad [10]$$

VI. Maximum concentration for a paraboloid of revolution having a spherical target

The expression for concentration is

$$C = \frac{n^2}{4\left(1 + \frac{n^2}{16}\right)^2\left(2 \sin \frac{\alpha}{2}\right)^2} = \frac{An^2}{\left(1 + \frac{n^2}{16}\right)^2} \qquad [1]$$

Where the constant A is given by

$$A = \frac{1}{4\left(2 \sin \frac{\alpha}{2}\right)^2} \qquad [2]$$

Setting $\left(\frac{dC}{dn}\right)$ equal to zero and solving the resulting equation yields

$$\frac{dC}{dn} = 0 = A\left[\frac{2n}{\left(1 + \frac{n^2}{16}\right)^2} + \frac{(-2)n^2\left(\frac{2n}{16}\right)}{\left(1 + \frac{n^2}{16}\right)^3}\right] \qquad [3]$$

rearranging gives

$$0 = 2n\left(1 + \frac{n^2}{16}\right) - \frac{4n^3}{16} \qquad [4]$$

or

$$2n^3 = 32n \qquad [5]$$

$$n = \pm 4$$

As before, the solution $n = -4$ has no meaning. Substitution of $n = +4$ into Eq. V-[8], gives the maximum concentration

$$C = \frac{n^2}{4\left(1 + \frac{n^2}{16}\right)^2 \left(2 \sin \frac{\alpha}{2}\right)^2} = \frac{4^2}{4\left(1 + \frac{4^2}{16}\right)\left(2 \sin \frac{\alpha}{2}\right)^2} \quad [6]$$

$$C = \frac{1}{\left(2 \sin \frac{\alpha}{2}\right)^2} \quad [7]$$

or

$$C \leqq 11{,}550 \quad [8]$$

VII. Concentration for a parabolic cylinder having a flat plate target

The starting point for the concentration is

$$C = \frac{A_{nm}}{A_t} \quad [1]$$

From Fig. 5 it is seen that for a mirror and target of length L,

$$C = \frac{D \times L}{d_a \times L} = \frac{D}{d_a} \quad [2]$$

From Fig. 5 it is also apparent that

$$\tan \frac{\alpha}{2} = \frac{d_1'/2}{l_m} = \frac{d_1'}{2 \times l_m} \quad [3]$$

thus, upon rearranging this becomes

$$d_1' = l_m \left(2 \tan \frac{\alpha}{2}\right) \quad [4]$$

Using the law of sines on triangle abc, Fig. 5

$$\frac{d_b}{\sin \gamma_2} = \frac{d_1'/2}{\sin \delta} \quad [5]$$

rearranging yields

$$d_b = \frac{d_1' \sin \gamma_2}{2 \sin \delta} \quad [6]$$

substitution of

$$\gamma_2 = 90^\circ + \frac{\alpha}{2} \quad [7]$$

and

$$\delta = 180^\circ - \gamma_2 - \beta = 180 - \left(90^\circ + \frac{\alpha}{2}\right) - \beta = 90^\circ - \frac{\alpha}{2} - \beta \quad [8]$$

in Eq. [6] gives

$$d_b = \frac{d_1' \sin \left(90^\circ + \frac{\alpha}{2}\right)}{2 \sin \left(90^\circ - \frac{\alpha}{2} - \beta\right)} \quad [9]$$

$$d_b = \frac{d_1' \left(\sin 90^\circ \cos \frac{\alpha}{2} + \cos 90^\circ \sin \frac{\alpha}{2}\right)}{2\left[\sin \left(90^\circ - \frac{\alpha}{2}\right) \cos \beta - \cos \left(90^\circ - \frac{\alpha}{2}\right) \sin \beta\right]},$$

$$d_b = \frac{d_1' \cos \frac{\alpha}{2}}{2\left[\left(\sin 90^\circ \cos \frac{\alpha}{2} - \cos 90^\circ \sin \frac{\alpha}{2}\right) \cos \beta - \left(\cos 90^\circ \cos \frac{\alpha}{2} + \sin 90^\circ \sin \frac{\alpha}{2}\right) \sin \beta\right]},$$

$$d_b = \frac{d_1' \cos \frac{\alpha}{2}}{2\left[\cos \frac{\alpha}{2} \cos \beta - \sin \frac{\alpha}{2} \sin \beta\right]} \quad [10]$$

But since

$$\cos \frac{\alpha}{2} = 1.0000 \quad [11]$$

and

$$\sin \frac{\alpha}{2} = .00467 \quad [12]$$

Eq. [10] may be written with good approximation for all values of β except those approaching 90° as

$$d_b = \frac{d_1'}{2 \cos \beta} \quad [13]$$

The value on the right of Eq. [13] is equal to $\frac{d_1}{2}$ as seen from Fig. 5. By symmetry it is seen that the largest image dimension

$$d_a = 2d_b \quad [14]$$

Further it is seen that

$$\tan \frac{\alpha}{2} = \frac{d_1'/2}{l_m} \quad [15]$$

or

$$d_1' = l_m \left(2 \tan \frac{\alpha}{2}\right) = f \left(1 + \frac{n^2}{16}\right)\left(2 \tan \frac{\alpha}{2}\right) \quad [16]$$

Dealing with the angle β, it can be seen from Fig. 5 that

$$\cos \beta = \frac{f - y}{l} \quad [17]$$

or

$$\cos \beta_m = \frac{f - y_m}{l_m} = \frac{f - y_m}{f + y_m} \quad [18]$$

From Eq. III-[13],

$$y_m = \frac{x_m^2}{4f} \quad [19]$$

or

$$y_m = \left(\frac{nf}{2}\right)^2 \frac{1}{4f} = \frac{n^2 f}{16} \quad [20]$$

VOL. 5 1961

Substitution in Eq. [18] gives

$$\cos \beta_m = \frac{f - \frac{n^2 f}{16}}{f + \frac{n^2 f}{16}} = \frac{1 - \frac{n^2}{16}}{1 + \frac{n^2}{16}} \qquad [21]$$

Using Eq. [14] in [13] used at the mirror extremity gives

$$d_a = \frac{d_1'}{\cos \beta_m} = \frac{f\left(1 + \frac{n^2}{16}\right)\left(2 \tan \frac{\alpha}{2}\right)}{\frac{\left(1 - \frac{n^2}{16}\right)}{\left(1 + \frac{n^2}{16}\right)}} \qquad [22]$$

or

$$d_a \leqq \frac{f\left(1 + \frac{n^2}{16}\right)^2 \left(2 \tan \frac{\alpha}{2}\right)}{\left(1 - \frac{n^2}{16}\right)} \qquad [23]$$

As before

$$D = nf \qquad [24]$$

Substitution of Eq. [23] and [24] in Eq. [2] yields

$$C = \frac{nf}{\frac{f\left(1 + \frac{n^2}{16}\right)^2 \left(2 \tan \frac{\alpha}{2}\right)}{\left(1 - \frac{n^2}{16}\right)}}$$

or

$$C = \frac{n\left(1 - \frac{n^2}{16}\right)}{\left(1 + \frac{n^2}{16}\right)^2 \left(2 \tan \frac{\alpha}{2}\right)} \qquad [25]$$

or

$$C = \frac{107.3n\left(1 - \frac{n^2}{16}\right)}{\left(1 + \frac{n^2}{16}\right)^2} \qquad [26]$$

For $n \ll 1$

$$C \leqq \frac{n}{2 \tan \frac{\alpha}{2}} = 107.3n \qquad [27]$$

which is Eq. I-[9].

VIII. Maximum concentration for a parabolic cylinder having a flat plate target

The expression for concentration Eq. VII-(25) is

$$C = \frac{n\left(1 - \frac{n^2}{16}\right)}{\left(1 + \frac{n^2}{16}\right)^2 \left(2 \tan \frac{\alpha}{2}\right)} = \frac{An\left(1 - \frac{n^2}{16}\right)}{\left(1 + \frac{n^2}{16}\right)^2} \qquad [1]$$

where the constant A is given by

$$A = \frac{1}{2 \tan \frac{\alpha}{2}} \qquad [2]$$

The maximum concentration is determined by setting $\left(\frac{dC}{dn}\right)$ equal to zero, and solving the resulting equation for n. Thus

$$\frac{dC}{dn} = 0 = A\left[\left(1 - \frac{n^2}{16}\right)\left(1 + \frac{n^2}{16}\right)^{-2} + n\left(1 + \frac{n^2}{16}\right)^{-2}\left(-\frac{2n}{16}\right) + (-2)n\left(1 - \frac{n^2}{16}\right)\left(1 + \frac{n^2}{16}\right)^{-3}\left(\frac{2n}{16}\right)\right] \qquad [3]$$

after some rearranging this results in

$$n^4 - 96n^2 + 256 = 0 \qquad [4]$$

which in turn yields

$$n = \pm 4\sqrt{3 \pm \sqrt{8}} \qquad [5]$$

Rejecting negative relative apertures, this gives

$$n = 4\sqrt{3 \pm \sqrt{8}} \qquad [6]$$

and

$$n \leqq 1.65 \qquad [7]$$

$$n \leqq 9.64 \qquad [8]$$

Putting the solution [7] in Eq. VII-[25] gives the value

$$C = \frac{n\left(1 - \frac{n^2}{16}\right)}{\left(1 + \frac{n^2}{16}\right)^2 \left(2 \tan \frac{\alpha}{2}\right)} \qquad [1]$$

$$C \leqq \frac{1}{\left(2 \tan \frac{\alpha}{2}\right)} \qquad [9]$$

or

$$C \leqq 107.3 \qquad [10]$$

The value $n = 9.64$ is thrown out because it gives a negative concentration.

IX. Concentration for a paraboloid of revolution having a flat plate target

As before the starting point is

$$C = \frac{A_{nm}}{A_t} \qquad [1]$$

From Fig. 5 the target geometry is determined by the largest image thrown on the plate from the extremities of the mirror. Due to symmetry this image will be a

circle. Thus

$$C = \frac{\frac{\pi D^2}{4}}{\frac{\pi d_a^2}{4}} = \frac{D^2}{d_a^2} \qquad [2]$$

From Eq. III-[3]

$$D = nf \qquad [3]$$

and from Eq. VII-[23]

$$d_a \cong \frac{f\left(1 + \frac{n^2}{16}\right)^2\left(2 \tan \frac{\alpha}{2}\right)}{\left(1 - \frac{n^2}{16}\right)} \qquad [4]$$

Substitution of Eq. [3] and [4] in Eq. [2] gives

$$C \cong \frac{(nf)^2}{\left[f\left(1 + \frac{n^2}{16}\right)^2\left(2 \tan \frac{\alpha}{2}\right)\right]^2} \qquad [5]$$
$$\left(1 - \frac{n^2}{16}\right)^2$$

or

$$C \cong \frac{n^2\left(1 - \frac{n^2}{16}\right)^2}{\left[\left(1 + \frac{n^2}{16}\right)^2\left(2 \tan \frac{\alpha}{2}\right)\right]^2} \qquad [6]$$

or

$$C \cong \frac{11{,}550\, n^2\left(1 - \frac{n^2}{16}\right)^2}{\left(1 + \frac{n^2}{16}\right)^4} \qquad [7]$$

When $n \ll 1$, Eq. [6] reduces to

$$C \cong \frac{n^2}{\left(2 \tan \frac{\alpha}{2}\right)^2}$$

or

$$C \cong 11{,}550\, n^2 \qquad [8]$$

These are the same as Equations II-[6] and II-[7] respectively.

X. Maximum concentration for a paraboloid of revolution having a flat plate target

The expression for concentration is

$$C = \frac{n^2\left(1 - \frac{n^2}{16}\right)^2}{\left(1 + \frac{n^2}{16}\right)^4\left(2 \tan \frac{\alpha}{2}\right)^2} = \frac{An^2\left(1 - \frac{n^2}{16}\right)^2}{\left(1 + \frac{n^2}{16}\right)^4} \qquad [1]$$

Where the constant A is given by

$$A = \frac{1}{\left(2 \tan \frac{\alpha}{2}\right)^2} \qquad [2]$$

The maximum concentration is determined by setting $\left(\frac{dC}{dn}\right)$ equal to zero and solving the resulting equation for n. Thus

$$\frac{dC}{dn} = 0 = A\left[2n\left(1 - \frac{n^2}{16}\right)^2\left(1 + \frac{n^2}{16}\right)^{-4} + 2n^2\left(1 - \frac{n^2}{16}\right)\left(\frac{-2n}{16}\right)\left(1 + \frac{n^2}{16}\right)^{-4} + (-4)n^2\left(\frac{1 - n^2}{16}\right)^2\left(1 + \frac{n^2}{16}\right)^{-5}\left(\frac{2n}{16}\right)\right] \qquad [3]$$

this results after some rearranging in

$$n^4 - 96n^2 + 256 = 0 \qquad [4]$$

which in turn yields

$$n = \pm 4\sqrt{3 \pm \sqrt{8}} \qquad [5]$$

finally

$$n = +4\sqrt{3 \pm \sqrt{8}} \qquad [6]$$

with the applicable result

$$n = +4\sqrt{3 - \sqrt{8}} \cong 1.65 \qquad [7]$$

Using this value of n in Eq. [1] yields

$$C = \frac{n^2\left(1 - \frac{n^2}{16}\right)^2}{\left(1 + \frac{n^2}{16}\right)^4\left(2 \tan \frac{\alpha}{2}\right)^2} \qquad [1]$$

or

$$C = \frac{1}{\left(2 \tan \frac{\alpha}{2}\right)^2} \qquad [8]$$

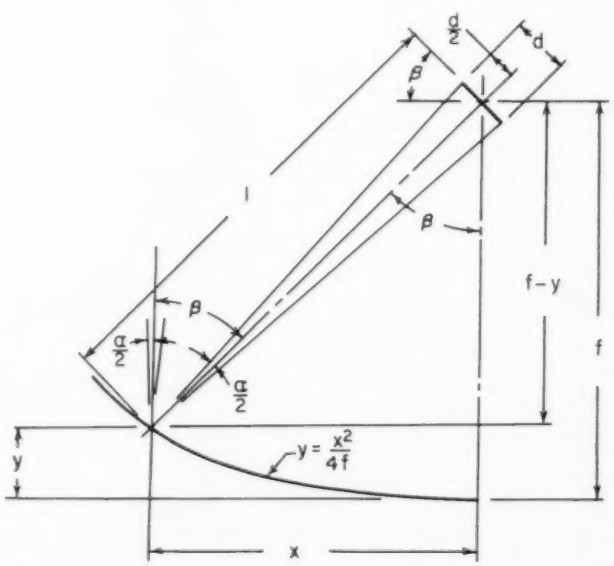

FIG. 6. Mirror geometry for optimum target shape for a parabolic mirror having a relative aperture of 4.

VOL. 5 1961

and finally

$$C \leqq 11{,}550 \qquad [9]$$

XI. Optimum target shape for a parabolic mirror having a relative aperture of 4

The target should provide a cross section just wide enough to intercept each beam from every point on the mirror. The development follows. From Fig. 6 it is seen that

$$\tan \frac{\alpha}{2} = \frac{d/2}{l} = \frac{d}{2 \times l} \qquad [1]$$

thus

$$d = l\left(2 \tan \frac{\alpha}{2}\right) \qquad [2]$$

From a previous development

$$l = f + y \qquad [3]$$

On the mirror

$$y = \frac{x^2}{4f} \qquad [4]$$

and

$$n = \frac{D}{f} = \frac{2x}{f} \qquad [5]$$

thus

$$x = \frac{nf}{2} \qquad [6]$$

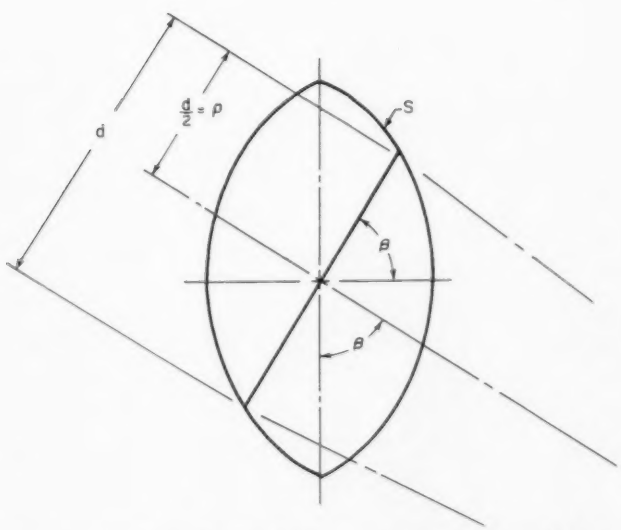

FIG. 7. Target geometry for optimum target shape with a parabolic mirror having a relative aperture of 4.

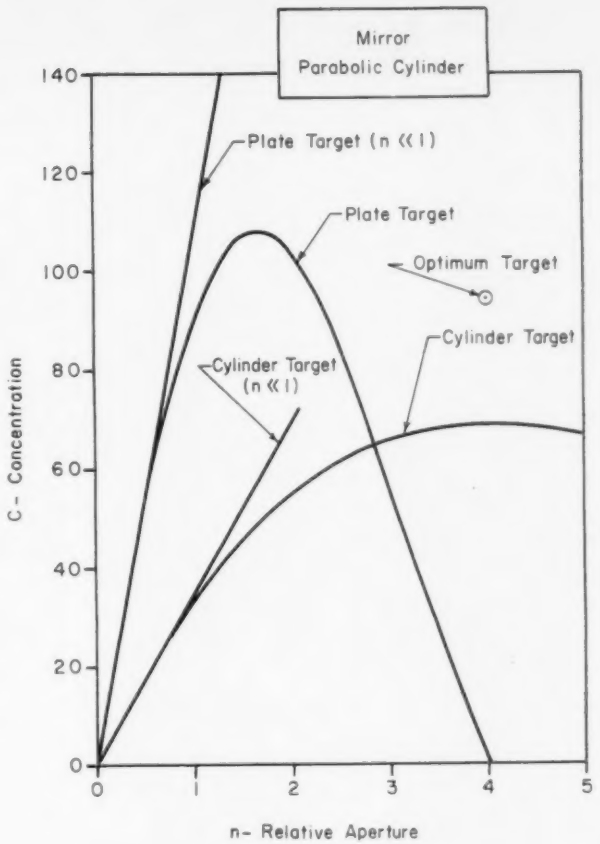

FIG. 8

From Fig. 6 also

$$\text{cotan } \beta = \frac{f - y}{x} = \frac{f}{x} - \frac{y}{x} = \frac{f}{x} - \frac{x^2}{4fx}$$

$$= f\left(\frac{2}{nf}\right) - \left(\frac{nf}{2}\right)\frac{l}{4f}$$

$$\text{cotan } \beta = \frac{2}{n} - \frac{n}{8} \qquad [7]$$

multiplying through by $8n$ gives

$$8n \text{ cotan } \beta = 16 - n^2$$

or

$$n^2 + 8n \text{ cotan} - 16 = 0 \qquad [8]$$

solving for n yields, finally

$$n = 4 (\csc \beta - \cot \beta)$$

or

$$n = 4 \tan \frac{\beta}{2}. \qquad [9]$$

Eq. [9] is a convenient relation between n and β. Sub-

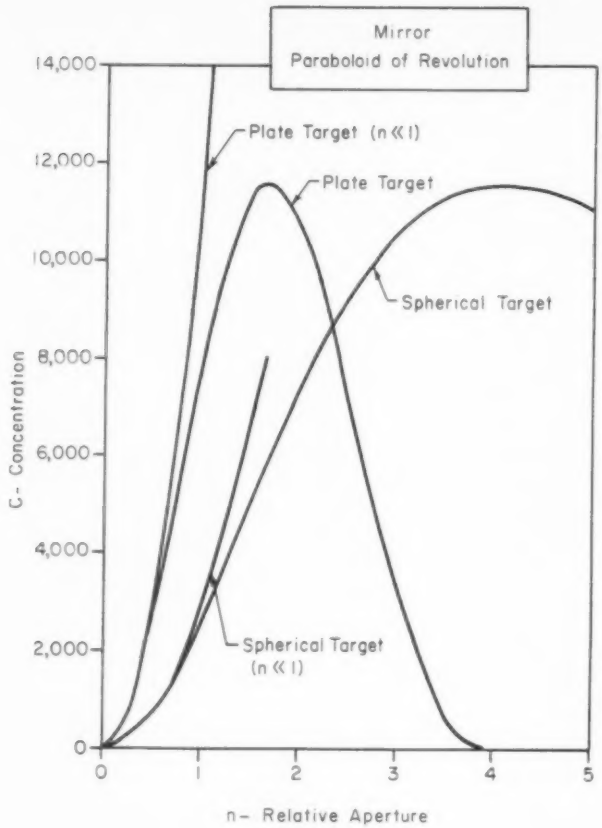

FIG. 9

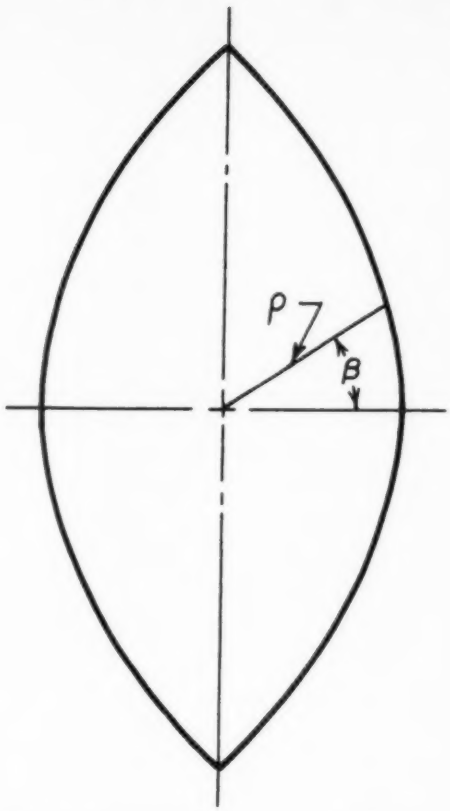

FIG. 10. Ideal target cross section for a parabolic mirror with a relative aperture of 4.

stitution in Eq. [2] yields

$$d = l\left(2\tan\frac{\alpha}{2}\right) = (f+y)\left(2\tan\frac{\alpha}{2}\right)$$

$$= \left(f + \frac{x^2}{4f}\right)\left(2\tan\frac{\alpha}{2}\right)$$

$$d = f\left(1 + \frac{x^2}{4f^2}\right)\left(2\tan\frac{\alpha}{2}\right)$$

$$= f\left[1 + \left(\frac{nf}{2}\right)^2\frac{1}{4f^2}\right]\left(2\tan\frac{\alpha}{2}\right)$$

or

$$d = f\left(1 + \frac{n^2}{16}\right)\left(2\tan\frac{\alpha}{2}\right) \qquad [10]$$

From Fig. 7

$$\rho = \frac{d}{2} = \frac{f}{2}\left(1 + \frac{n^2}{16}\right)\left(2\tan\frac{\alpha}{2}\right)$$

$$\rho = \frac{f}{2}\left[1 + \frac{\left(4\tan\frac{\beta}{2}\right)^2}{16}\right]\left(2\tan\frac{\alpha}{2}\right)$$

$$\rho = \frac{f}{2}\left[1 + \tan^2\frac{\beta}{2}\right]\left(2\tan\frac{\alpha}{2}\right)$$

finally

$$\rho = \frac{f}{2}\left(\sec^2\frac{\beta}{2}\right)\left(2\tan\frac{\alpha}{2}\right)$$

The length of arc S of Fig. 7 is given by

$$S = \int dS = \int_{\beta_1}^{\beta_2} \sqrt{\rho^2 + \rho'^2}\, d\beta \qquad [12]$$

By symmetry

$$S = 4\int_0^{\pi/2} \sqrt{\rho^2 + \rho'^2}\, d\beta \qquad [13]$$

Where

$$\rho = A\sec^2\frac{\beta}{2} \qquad [14]$$

and the constant A is given by

$$A = \frac{f}{2}\left(2\tan\frac{\alpha}{2}\right) \qquad [15]$$

and ρ' is

$$\rho' = \frac{A\sin\frac{\beta}{2}}{\cos^3\frac{\beta}{2}} \qquad [16]$$

VOL. 5 1961

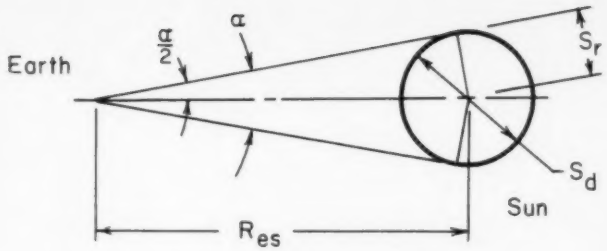

FIG. 11. Geometry of earth and sun

Thus continuing

$$S = 4\int_0^{\pi/2} \sqrt{\left(\frac{A}{\cos^2\frac{\beta}{2}}\right)^2 + \left(\frac{A\tan\frac{\beta}{2}}{\cos^2\frac{\beta}{2}}\right)^2}\, d\beta$$

$$S = 4\int_0^{\pi/2} \frac{A}{\cos^2\frac{\beta}{2}} \sqrt{1 + \tan^2\frac{\beta}{2}}\, d\beta$$

$$S = 4A\int_0^{\pi/2} \frac{\sec\frac{\beta}{2}}{\cos^2\frac{\beta}{2}}\, d\beta = 4A\int_0^{\pi/2} \frac{d\beta}{\cos^3\frac{\beta}{2}} \qquad [17]$$

$$= 8A\int_0^{\pi/2} \frac{d\beta/2}{\cos^3\frac{\beta}{2}}$$

integration yields

$$S = 8A\left[\frac{1}{2}\frac{\sin\frac{\beta}{2}}{\cos^2\frac{\beta}{2}} + \frac{1}{2}\ln\left|\tan\left(\frac{\pi}{4}+\frac{\beta}{4}\right)\right|\right]_0^{\pi/2}$$

$$S = 4A\left[\frac{\sin\frac{\pi}{4}}{\cos^2\frac{\pi}{4}} + \ln\left|\tan\left(\frac{\pi}{4}+\frac{\pi}{8}\right)\right| - \frac{\sin 0}{\cos^2 0} + \ln\left|\tan\left(\frac{\pi}{4}+0\right)\right|\right]$$

$$S = 4A\left[\frac{\frac{1}{2}\sqrt{2}}{(\frac{1}{2}\sqrt{2})^2} + \ln\tan\frac{3\pi}{8}\right] \qquad [18]$$

$$S \leqq 4A\left[\frac{1}{.7071} + \ln 2.42\right] = 4A[1.414 + .885]$$

$$S \cong 4A[2.299] \cong 4\left[\frac{f}{2}\left(2\tan\frac{\alpha}{2}\right)\right][2.299]$$

$$S \cong 4.598f\left(2\tan\frac{\alpha}{2}\right)$$

The concentration then, for a mirror and target of length L, is

$$C = \frac{A_{n\,m}}{A_t} = \frac{D\times L}{S\times L} = \frac{D}{S} \qquad [19]$$

$$C \leqq \frac{nf}{4.598f\left(2\tan\frac{\alpha}{2}\right)} = \frac{n}{4.598\left(2\tan\frac{\alpha}{2}\right)} \qquad [20]$$

Since $n = 4$, the concentration is

$$C \leqq \frac{4\times 107.3}{4.598} \qquad [21]$$

$$C \leqq 93.8$$

This compares to the value of $C = 68.3$ for a circular pipe that will receive all the radiation.

To obtain the equation of the target in rectangular coordinates let

$$x = \rho\cos\beta \qquad [22]$$

and

$$y = \rho\sin\beta \qquad [23]$$

The equation for ρ is

$$\rho = A\sec^2\frac{\beta}{2} = \frac{A}{\cos^2\frac{\beta}{2}} = \frac{2A}{1+\cos\beta} \qquad [24]$$

but also

$$\rho = \sqrt{x^2+y^2} \qquad [25]$$

and

$$\cos\beta = \frac{x}{\rho} = \frac{x}{\sqrt{x^2+y^2}} \qquad [26]$$

setting $\rho = \rho$, and rearranging

$$\frac{2A}{1+\cos\beta} = \sqrt{x^2+y^2}$$

$$\frac{2A}{1+\frac{x}{\sqrt{x^2+y^2}}} = \sqrt{x^2+y^2}$$

$$\frac{2A\sqrt{x^2+y^2}}{\sqrt{x^2+y^2}+x} = \sqrt{x^2+y^2}$$

finally

$$\sqrt{x^2+y^2} + x = 2A \qquad [27]$$

this can be modified to

$$\sqrt{x^2+y^2} = 2A - x$$

$$x^2+y^2 = 4A^2 - 4Ax + x^2$$

$$y^2 = 4A^2 - 4Ax = 4A^2\left(1-\frac{x}{A}\right) \qquad [28]$$

$$y = \pm 2A\sqrt{1-\frac{x}{A}}$$

Substitution of the value of A gives

$$y = \pm 2\left[f\left(2\tan\frac{\alpha}{2}\right)\right]\sqrt{1 - \frac{x}{f\left(2\tan\frac{\alpha}{2}\right)}}, \quad [29]$$

the equation for one-half of the surface when

$$\left[0 \leq x \leq f\left(2\tan\frac{\alpha}{2}\right)\right]$$

The equation for the other half of the target is

$$y = \pm 2\left[f\left(2\tan\frac{\alpha}{2}\right)\right]\sqrt{1 + \frac{x}{f\left(2\tan\frac{\alpha}{2}\right)}} \quad [30]$$

$$\cdot\left[-f\left(2\tan\frac{\alpha}{2}\right) \leq x \leq 0\right]$$

The slope is given by

$$y' = \pm 2A\left(\frac{1}{2}\right)\left(1 - \frac{x}{A}\right)^{-1/2}\left(-\frac{1}{A}\right)$$

$$y' = \frac{\pm 1}{\sqrt{1 - \frac{x}{A}}}$$

$$y' = \pm\frac{1}{\sqrt{1 - \frac{x}{f\left(2\tan\frac{\alpha}{2}\right)}}}$$

$$\left[0 \leq x \leq f\left(2\tan\frac{\alpha}{2}\right)\right]$$

The points of interest are at $x = f\left(2\tan\frac{\alpha}{2}\right)$, and $x = 0$.

For the first the slope is

$$y' = \pm\infty.$$

For $x = 0$, the slope is

$$y' = \pm 1$$

APPENDIX I

From Fig. 1

$$\sin\frac{\alpha}{2} = \frac{S_r}{R_{cs}} \quad [1]$$

but since $\frac{S_d}{2} = S_r$,

$$\sin\frac{\alpha}{2} = \frac{S_d}{2R_{cs}} \leqq \frac{8.66 \times 10^5}{2 \times 92.9 \times 10^6} \quad [3a]$$

$$\leqq .00467 \leqq \frac{1}{214.6}$$

also

$$2\sin\frac{\alpha}{2} \leqq \frac{1}{107.3} \quad [3b]$$

The following trigonometric series are useful in solar furnace relationships

$$\sin x = x - \frac{x^3}{3!} + \frac{x^5}{5!} - \frac{x^7}{7!} + \cdots \qquad [x^2 < \infty] \quad [4]$$

$$\tan x = x + \frac{x^3}{3} + \frac{2x^5}{15} + \frac{17x^7}{315} + \frac{62x^9}{2835} + \cdots \quad [5]$$

$$\left[x^2 < \frac{\pi^2}{4}\right]$$

Thus when α is a small angle, it is true that

$$\sin\frac{\alpha}{2} \cong \tan\frac{\alpha}{2} \leqq \frac{\alpha}{2} \quad [6a]$$

and

$$2\sin\frac{\alpha}{2} \cong 2\tan\frac{\alpha}{2} \cong \alpha \quad [6b]$$

On the earth, the solar half angle is

$$\frac{\alpha}{2} = \sin^{-1}(.00467) \quad [7]$$

Since

$$\sin^{-1}x = x + \frac{x^3}{2\cdot 3} + \frac{1\cdot 3x^5}{2\cdot 4\cdot 5} + \frac{1\cdot 3\cdot 5\,x^7}{2\cdot 4\cdot 6\cdot 7} + \cdots \quad [8]$$

$$\left[x^2 < 1, -\frac{\pi}{2} < \sin^{-1}x < \frac{\pi}{2}\right]$$

Thus

$$\frac{\alpha}{2} \cong .00467 \text{ radians} \cong .2675 \text{ degrees} \cong 16.08 \text{ minutes.} \quad [9]$$

It follows then that the solar angle is

$$\cong 32.16 \text{ minutes.} \quad [10]$$

VOL. 5 1961

Solar Abstracts

By Milton D. Lowenstein
Director, Technical Research Service Center

Included in the growing volume of documents which the Technical Research Service Center will process through our storage and retrieving system, are papers from Russia. The interest of U. S. scientists and engineers in the technological achievements of the U.S.S.R. has also prompted several of our government departments to begin the task of translating Russian journals. The Technical Research Service Center receives all the material bearing upon the subject of our interests in solar energy.

Titles of many of our Russian acquisitions have been compiled into a bibliography which has already been distributed to our membership. The extent of the translation was indicated for each title. Additional copies of the bibliography are available.

All the material is being arranged according to the categories of solar energy interests devised by the Research Service Center for the convenience of A.F.A.S.E. members.

The following abstracts of papers are among those that have been completely translated:

Evaporative Processes

Brdlik, P. M., "Testing and Designing Solar Desalination Installations." 22 p. Illus. Translation.

Solar desalinators of the "hot box" type. Solar desalinators with rotating concentrators of radiant energy. Thermal calculation of solar desalinators with rotating reflectors.

* * *

Ismailova, A. A., "The possibilities of Using Solar Energy for Drying Fruits and Vegetables." 22 p. Illus. Translation.

In the present work the following tasks were set: investigating the special operational features of various designs of helio driers, determining their optimum operating conditions, determining the basic technical characteristics and parameters of drying; an analysis of the special operational features of air heaters and calculating their basic technical characteristics and parameters.

* * *

Shceegolev, D. M., "Heating Buildings by Solar Radiation." 17 p. Illus. Translation.

The best system of solar heating is the complex utilization of helio installations in the summer for desalinating water, obtaining ice, cooling buildings, etc., and in the fall-winter period for heating buildings.

* * *

Space, Water Heating, and Absorptive Collectors

Markov, G. I. and Rekant, N. B., "Tests on Solar Water Heaters in Tashkent in 1952–1953." 10 p. Illus. Translation.

Of a number of solar water heaters, the tubular-type water heaters designed by B. V. Petukhov is the most widely used in the USSR. Pan-type water heaters are not widely used, although they are sufficiently simple in design and in some cases can prove more economical than tubular ones. In 1952 at the experimental station in Tashkent, comparative tests were conducted on water heaters of the two indicated designs. The purpose of the test was to determine the average daily efficiency and its change in relation to the temperature of the hot water obtained. In 1953 tubular-type water heaters were tested to determine the effect of the numbers of panes on the efficiency of the installation and its productivity.

* * *

Petukhov, B. V., "Method for Calculating Solar Water Heaters." 35 p. Illus. Translation.

Design principle of solar water heaters of the "hot box" type. Data necessary for the calculation of a solar water heater. The position of a solar water heater. Heat balance of a solar water heater. Determining the amount of solar energy falling on the water heater. Computing the coefficient of entry of direct solar radiation into a water heater. Passage of solar energy by the panes. Determining the coefficient of entry into the water heater of diffused radiation. Determining heat losses by a solar water heater to the ambient medium. Determining the amount of heat necessary for the initial heating of the solar water heater. Heat transmission. Selecting a glass cover for the water heater. Determining the productivity of a solar water heater.

* * *

Cooling Processes: Refrigeration and Heat Rejection Systems

Brdlik, P. M., "Testing a Solar Refrigerator." 8 p. Illus. Translation.

The efficiency of a solar refrigerator can be considerably increased by: better utilization of the heat from the warming steam in the generator. This can be attained by increasing the heating surface of the generator; decreasing the lag of the system by decreasing the dimensions and weight of some of its parts and the employment of a less heat-absorbing insulation; supplying the boiler of the helio installation with condensate from the generator of the absorption refrigerator and finally, placing the generator of the refrigerator directly in the focal plane of the solar installation.

Solar Furnaces

Aparisi, R. R., Baum, V. A., Garf, B. A., "High Power Solar Installations." 19 p. Illus. Translation.

During the last few years, a system has been developed in the helio-laboratory for a solar station whose capacity can attain 10·10⁶ kilo-calories per hour and more, which is 40–80 times greater than the possible unit capacity of a paraboloid unit and 20–40 times the capacity of a unit with flat mirrors and an immovable boiler, illuminated from below. This station is designed to produce steam at a pressure of 30–35 atm. abs. Solar rays, gathered from a 19,395 m² area, are reflected by means of 1293 individual, flat, standard-type reflectors, onto a steam boiler rotating around its axis. This boiler is located in the focus of the optical system formed by these reflectors. Each of these individual reflectors with an area of 15 m² (3 × 5 m) consists of 28 flat mirrors, mounted on a standard metal chassis, placed on a trolley. The 1293 trolleys are broken down into 23 separate trains, moving with the same angular velocity along concentric tracks, around the boiler which is placed on a tower 40 m high. Thus is accomplished the azimuthal movement of mirrors for focussing reflected rays in the boiler. The zenithal movement is accomplished by rotating the chassis by means of an electric motor around an axis close to the horizontal.

* * *

Aparisi, R. R., "An Experimental Installation for the Receipt of High Temperatures." 15 p. Illus. Translation.

To conduct experimental tests in the area of high temperatures, an experimental installation was erected on the grounds of the Power Institute, USSR Academy of Sciences, in Tashkent. It has a precision-cast mirror with a diameter of 2.05 m and with automatic control. To it was attached a kinematic system of azimuthal and zenithal rotation with two mutually perpendicular axes of rotation: horizontal GG′ and vertical VV′.

* * *

Garf, B. A., "A Small Solar Cooker." 12 p. Illus. Translation.

The present article contains calculations of the MSK-1 cooker and the results of its tests. Experimental operation under field conditions has an average productivity of 5 liters of boiling water per hour with an efficiency of the unit of $\eta = 0.5$. Under normal conditions in the Central Asian Republics, the MSK-1 fully provides for the preparation of food for a family of 3–4 persons. Handling it is simple. Its cost, with mass production, will not exceed 250–300 rubles. By saving fuel, the unit pays for itself in 2½ years. The MSK-1 can be recommended for everyday use in regions with intense solar radiation and insufficient fuel resources.

* * *

Garf, B. A., Borozdina, M. S., Rekant, N. B., "Investigating the Reflecting Surfaces of Solar Installations." 19 p. Illus. Translation.

Tests and experience in the operation of solar units with mirrors, both in the Soviet Union and abroad, indicate that at the present time, sheet glass with a silver or aluminum reflecting coating and metallic sheets with an electrically polished mirror surface satisfy the enumerated requirements.

* * *

Kozlov, B. K., Boganov, F. F., Kolos, ya. G., Markov, G. I., "Thermotechnical Tests of a Solar Paraboloid Installation for the Production of Steam." 10 p. Illus. Translation.

The installation consists of a solar steam boiler, a mirror reflector with a counterweight, a rotating mechanism, a column and a base. The reflector is made in the form of a thin, reinforced-concrete casing, shaped as a paraboloid of rotation, 10 m in diameter. Mirrors made of window glass, glued to the casing, serve as the reflecting surface. The casing is rigidly connected with a counterweight in the form of a metal rod having removable concrete blocks at its end. The mechanism of daily rotation provides for the turning of the casing around an inclined axis, placed on a meridional plane at an angle to the horizon equal to the geographical latitude of the location of the installation. Rotation takes place at a constant speed and is effected by an electric motor of 0.25 kw capacity; the reducer has a total gear ratio of about 2 million. The position of the casing is changed, in relation to the change in the declination of the sun, by means of a special yearly declination screw, rotated by hand, one turn once a day.

* * *

Markov, G. I., "Special Technological Features in the Manufacture of Reinforced Concrete Paraboloid Mirror Reflectors for Solar Installations and Some Indexes of Their Operation." 14 p. Illus. Translation.

The method of creating huge reinforced-concrete paraboloid reflectors, set forth in this article, is sufficiently simple, and is accessible for any construction organization; it provides a reflector accuracy completely adequate to effect, in the focal plane, a heat liberation of about 300,000 kcal/m² hour.

* * *

Photoelectric: Photovoltaic, Photogalvanic, Piezoelectric

Petukhov, B. V., "Devices for Direct Conversion of Solar Energy into Electrical Energy." *Utilization of Solar Energy*, Series IV, No. 14, 1958. 4 p. Translation.

A general discussion on the various means for directly converting solar into electrical energy, e.g., photoelectric and thermoelectric types of conversion; and the materials used and their efficiency.

* * *

Vavilov, V. S., Malovetskaya, V. M., Galkin, G. N., Landsman, A. P., "Silicon Solar Batteries as Sources of Electrical Power for Artificial Earth Satellites." *Uspekhi Fizicheskikh Nauk*, Vol. 63, 1. Sept. 1957, 13 p. Translation.

The authors discuss the design, construction, operation, and theoretical and experimental characteristics of photoelements employing silicon $p - n$ junctions to transform solar radiation into electrical energy.

* * *

Radiation Mechanics: Insolation, Spectroscopy, Spectral Distribution

Krat, V. A., "Photographic Method Used in Solar Spectrography." *J. Sci. Appl. Phot. Cinemat.*, USSR. 9 p. Translation.

The paper discusses the variety of problems arising out of attempts to use photographic methods in solar spectrography. Nevertheless, when spectra of separate solar details are desired within a wide range of wavelengths, the photoelectric method can not compete with the photographic method. The evaluation of solar spectrograms at present consists chiefly of careful photometry of spectral lines. Two somewhat con-

VOL. 5 1961

tradictory qualities are required of the emulsion of the photographic plate. The emulsion must be as fast as possible and have fine grain. Coarse grains are a serious handicap on the spectrogram in the accurate photometry of lines and especially in the narrow lines of Fraunhofer's spectrum. A high speed of the photographic emulsion is needed in order that very short exposure times may be made. At the same time it is important that the emulsions have a maximum speed at exposures of 0.1–0.5 second. A photographic material which would be four times faster than that now available is necessary for working with light fluxes obtainable with a telescope equipped with a mirror having twice the area of the telescope mirror used now. Often the problem of increasing the size of the mirror is insoluble. Increasing the speed of photographic materials is the most important goal of technical photography at the present time. Without solving this problem, no serious improvement can be expected in the application of photography to astronomy.

* * *

Yaroslavtsev, I. N., "Fluctuations in the Amount of Heat from the Radiation of the Sun and Sky and the Distribution of the Energy from that Radiation in Daytime, for Tashkent." *Symposium on Utilization of Solar Energy.* 10 p. Translation.

Common specific problems, not related to any particular solar unit or method of using solar energy, are discussed.

* * *

Economic, Social, Cultural Parameters of Solar Energy

Baum, V. A., "Possibilities of the Utilization of Solar Energy." *Symposium on Utilization of Solar Energy.* 24 p. Translation.

This article familiarizes the reader with the status of the practical use of solar energy and its potentialities to date. Some projects dealing with the utilization of solar energy in the USSR. The use of "hot box"-type installations. The use of mirror installations. The utilization of solar energy to heat apartments. Investigations in the field of creating large solar heating stations. Trends in projects abroad. Status of the practical use of solar energy and its potential prospects.

* * *

Poyarkov, S. G., "Technical and Economic Indicators of Solar Installations." 23 p. Translation.

The growing needs of the USSR national economy make it necessary to expand the production of energy. One of the possible supplementary sources of energy could be solar radiation, the use of which was shown by several experimental and computational investigations to be profitable in satisfying some of the power needs of the population of our southern republics. With large-scale use of solar radiation, a great amount of fuel could be freed for other purposes—in the chemical, the metallurgical industries, etc.

* * *

Accessories: Batteries, Tracking and Control Systems

Garf, B. A., "Rotation Mechanisms for Portable Solar Units." 29 p. Illus. Translation.

Common specific problems, not related to any particular solar unit or method of using solar energy, are discussed.

* * *

Garf, B. A. and Khuntsariya, R. K., "A Parabolic-Cylindrical Installation with a Productivity of 40 Liters of Boiling Water per Hour." 7 p. Illus. Translation.

According to rough calculations, the cost of the installation, with series production, is estimated to be 3500 rubles and can be lowered by simplifying the rotation mechanism.

* * *

Materials and Production

Nechayev, Yu., "The Development of Jet Engines," *Soviet Aviation*, No. 293, Dec. 16, 1958. 1p. Translation.

Analyzing the development of jet engines, described in foreign press, the author mentions that the engines may increase their efficiency at the expense of new sources of energy, i.e., by utilizing the nuclear and solar energy. Light-weight gases, ionized matter and the energy of light should be the working elements (exhaust products) of those respective engines.

* * *

Veynberg, B. V., "The Spectral Characteristics of Solar Radiation." 12 p. Illus. Translation.

Using coatings for heating surfaces, as well as the usual glass, virtually does not reflect long-wave radiation emitted by the heating surfaces and elements of transparent insulation in solar units. There apparently exist ways of decreasing heat loss. For this, it is necessary to study the heating surfaces and insulation glass of solar heating units.

* * *

Geophysical and Meteorological: Weather, Climate, Sundials, Telescopes, Magnetism, and Gravity

Gnevyshev, M. N., Gnevsheva, R. S., "Contribution to the Question of the Solar Corona and Prominences," *Doklady Akademii Nauk* SSSR, Vol. 94, No. 4, 1954. 6 p. Translation.

It may be that the appearance of prominences is connected with brief intensifications of the magnetic field in an active region. These intensifications are due to surges of great masses of matter from the chromosphere, which either describe trajectories along the lines of force, or are dissipated when the electromagnetic fields weaken. The great density in these surges is the cause of the fact that with respect to radiation their properties remain characteristic for the chromosphere.

VOL.
5
1961

Photosynthesis of Hydrogen Peroxide by Crystal Phosphors

V. A. Garten and K. Eppinger

Commonwealth Scientific and Industrial Research Organization, Melbourne, Australia

The photosynthesis of hydrogen peroxide in the presence of zinc oxide, cadmium sulphide or basic zinc carbonate, as a means of storing solar energy, is re-examined. It is shown that with due allowance for losses of incident energy by the processes of reflection and luminescence, a maximum quantum yield of 0.5 can be obtained when no nonluminous transitions are incurred. Of the two quanta required to produce one equivalent of hydrogen peroxide, one is consumed to excite an electron whilst the other is, most likely, used to release a negatively charged oxygen or water molecule from the surface of the solid catalyst.

The central problem in the recovery of hydrogen peroxide from these systems lies in the efficient removal of hydroxyl free radicals which are produced in concentrations equivalent to ·OOH or H·, the precursors of hydrogen peroxide. As the expenditure of chemical potential required to take care of ·OH is greater than the gain in free energy due to the generation of H_2O_2, these processes, and others based on the same electronic processes, must be considered thermodynamically unsound.

INTRODUCTION

Photolysis of water, catalytic reduction of oxygen in light and, more generally, photochemical reactions with appreciable positive changes in free energy have in the past been suggested as potential methods of converting solar energy.[1, 2, 3, 4]

It has also been generally realised that the efficiency of such chemical systems is controlled mainly by (1) the change in free energy, (2) the quantum yield, (3) the spectral range of absorption.

The present paper deals with the particular problem of the photosynthesis of hydrogen peroxide by various crystal phosphors, viz., zinc oxides, cadmium sulphides, and basic zinc carbonates. The physical characteristics of the semiconductor-catalysts, viz., luminescence, reflection, and photoconductivity and its quenching by oxygen will be discussed and the basic limitations of a typically "non-structured" system, i.e., suspension of a catalyst in the reaction medium, will be briefly outlined with particular attention to the electron transfer mechanisms and the role of so-called "inhibitors" or "additives".

THE PHOTOCHEMICAL ACTIVITY OF ZnO AND CdS AS A FUNCTION OF LUMINESCENCE, PHOTOCONDUCTIVITY AND OXYGEN QUENCHING

All previous work on the photochemical activity of zinc oxide and cadmium sulphide appears to have been performed with materials of either varying commercial origins or materials obtained in the laboratory by precipitation methods, irrespective of the degree of purity despite its unique importance in semiconductor physics. Materials used in the present work were zinc oxide analar (ex B.D.H.) which was submitted to different temperatures in mildly oxidizing and reducing atmospheres respectively, in order to induce various degrees of self-activity, and cadmium sulphide, luminescent pure (ex Avonmouth Smelting) which was activated in a similar fashion.

Figure 1 shows the effect of reduction at increasing temperatures on the excitation spectra of zinc oxide with an excitation maximum at 380–385 mμ that grows more pronounced the higher the temperature of reduction becomes. Excitation in the range of 300–400 mμ invariably results in the well-known yellowish-green emission with a broad maximum at 505 mμ with no indication of spectral shifts. Figure 1 has been constructed on the basis of an energy yield of 19.5% with 365 mμ excitation, as given by Schleede,[5] with the necessary corrections for the spectral variation in the emission intensity of the tungsten excitation source, the variation in the spectral response of the 931 A photocell and the transmission of the exciting radiation by Kodak Filter No. 4. It may be noted in passing that the observed excitation peak coincides with the additional emission by zinc oxide under cathode ray bombardment. Conversely, the character of emission of cadmium sulphide changes markedly with the degree of reduction; beginning with two distinct bands, green and red, at 500 C and proceeding towards the infrared end of the

spectrum with the simultaneous loss of the green band on reduction at higher temperatures (Fig. 2).

In order to relate the number of electrons available for chemical reaction to photoconductivity and fluorescence we used monochromatic excitation of the zinc oxides with the 365 mμ line of a mercury discharge lamp with Jena filters UG2 (2 mm) and BG12 (4 mm). Let the photochemical yield Q_λ be defined as the equivalents of hydrogen peroxide produced per litre and second by a radiation of $\lambda = 365$ mμ incident on 1 cm² of area of the solid catalyst. The catalyst was suspended in water in such a concentration and stirred so as to produce a maximum yield of hydrogen peroxide. Usually, 200–400 mg catalyst/25 cc were found sufficient for this purpose. It was assumed that under these conditions no transmission of the excitation light occurred. Then we would expect the relation:

$$Q_\lambda = \tfrac{1}{2} \cdot E_{\text{abs.}} \cdot C_{O_2} \qquad [1]$$

Furthermore:

$$E_{\text{abs.}} = E_{\text{total}} - E_{\text{fl.}} - E_{\text{refl.}} \qquad [2]$$

where E_{total} is the number of einsteins incident on 1 cm² of the exposed area of the catalyst per second,

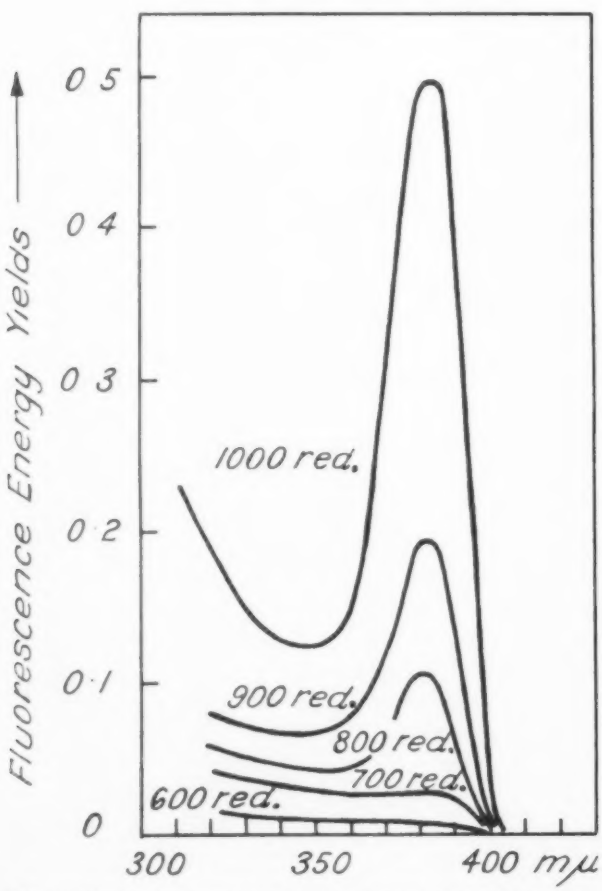

FIG. 1—Excitation spectra of self-activated zinc oxides (activated in the region of 600–1000 C).

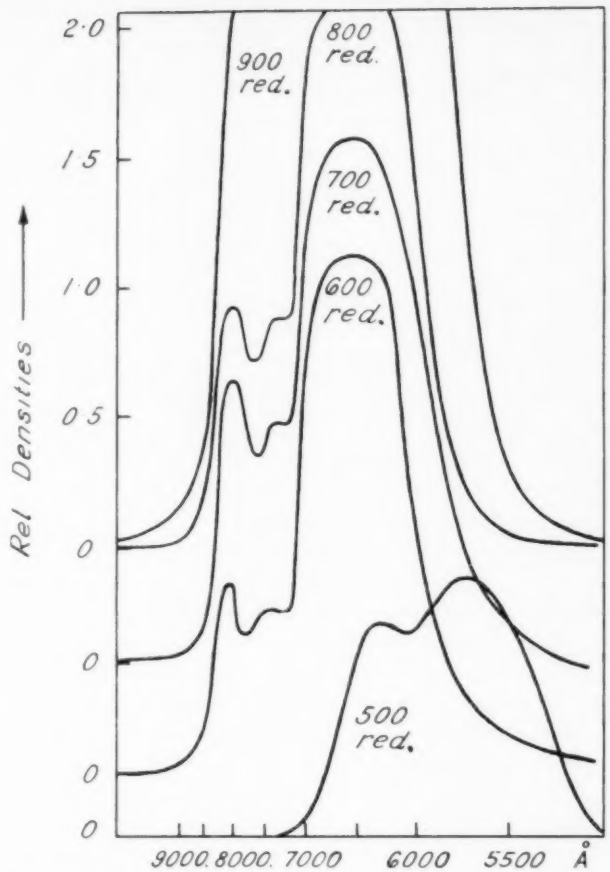

FIG. 2—Luminescence emission of self-activated cadmium sulphides (activated in the region of 500–900 C).

$E_{\text{abs.}}$ that absorbed by 1 cm² of catalyst area per second, $E_{\text{fl.}}$ and $E_{\text{refl.}}$ those parts re-emitted either in the form of fluorescence or reflection. C_{O_2} is the coefficient of oxygen quenching of the photoconductivity, representing that fraction of photoconductivity attributable to surface electrons only. In most zinc oxides this coefficient is only slightly smaller than unity. Conversely, water vapour seems to increase the photoconductivity of zinc oxide, as we observed repeatedly. (The photoconductivity and the degree of its quenching by oxygen were determined on powdered samples in contact with a silver grid of 2 mm spacings which was attached to the front window of a silica cell and which was biased with 10 v at 50 c.) The factor ½ in Eq. [1] is based on the assumption that two einsteins are required to produce one equivalent of O_2^-, the first one being used to raise electrons into the conduction band, where they can be quenched by oxygen, the second one to desorb O_2^-. This concept is in agreement with a quantum yield of nearly 0.5, as observed by previous workers.[6] The total number of quanta of $\lambda = 365$ mμ incident on 1 cm² of exposed catalyst area, in einsteins per second, was obtained actinometrically by the potassium-ferric-oxalate

VOL. 5 1961

TABLE 1—Photochemical Yields of H_2O_2 with ZnO-Catalysis

Sample	Analar	$600_{red.}$	$700_{red.}$	$800_{red.}$	$900_{red.}$	$1000_{red.}$	$600_{ox.}$	$1000_{ox.}$	ZnO(Mn) $1000_{red.}$
$E_{fl.}$	0	0.05×10^{-8}	0.14×10^{-8}	0.28×10^{-8}	0.55×10^{-8}	1.10×10^{-8}	0	0	0
$E_{refl.}$	0.55×10^{-8}	0.53×10^{-8}	0.59×10^{-8}	0.99×10^{-8}	1.49×10^{-8}	2.04×10^{-8}	0.66×10^{-8}	1.15×10^{-8}	0.72×10^{-8}
$E_{abs.}$	4.95×10^{-8}	4.92×10^{-8}	4.77×10^{-8}	4.23×10^{-8}	3.46×10^{-8}	2.36×10^{-8}	4.8×10^{-8}	4.35×10^{-8}	4.78×10^{-8}
C_{O_2}	0.997	0.998	0.995	0.992	0.976	0.922	0.998	0.993	0.903
Q_λ (calc.)	2.47×10^{-8}	2.46×10^{-8}	2.38×10^{-8}	2.10×10^{-8}	1.69×10^{-8}	1.09×10^{-8}	2.42×10^{-8}	2.16×10^{-8}	2.16×10^{-8}
Q_λ (exp.)	2.55×10^{-8}	1.76×10^{-8}	1.74×10^{-8}	1.48×10^{-8}	1.30×10^{-8}	1.09×10^{-8}	2.03×10^{-8}	0.95×10^{-8}	0.34×10^{-8}
Φ	*0.52*	0.36	0.36	0.35	0.39	*0.50*	0.42	0.22	0.08

TABLE 2—Photochemical Yields of H_2O_2 with CdS Catalysis

Sample	$400_{red.}$	$500_{red.}$	$600_{red.}$	$700_{red.}$	$800_{red.}$	$900_{red.}$
$E_{refl.}$ (einsteins/sec.)	0.84×10^{-8}	0.84×10^{-8}	1.15×10^{-8}	1.69×10^{-8}	1.80×10^{-8}	1.79×10^{-8}
$E_{fl.}$ (einsteins/sec.)	0	0	0.04×10^{-8}	0.04×10^{-8}	0.04×10^{-8}	0.05×10^{-8}
$E_{abs.}$ (einsteins/sec.)	2.66×10^{-3}	2.66×10^{-8}	2.41×10^{-8}	1.87×10^{-8}	1.76×10^{-8}	1.76×10^{-8}
C_{O_2}	approx. 1	approx. 1	approx. 1	approx. 1	?	?
Q_λ (calc. from [1])	1.33×10^{-8}	1.33×10^{-8}	1.20×10^{-8}	0.94×10^{-8}	0.88×10^{-8}	0.88×10^{-8}
Q_λ (exp.)	0.61×10^{-8}	0.45×10^{-8}	1.30×10^{-8}	1.00×10^{-8}	0.97×10^{-8}	1.10×10^{-8}
Φ	0.23	0.17	0.54	0.53	0.55	0.62

method[7] to:

$$E_{total} = 5.50 \times 10^{-8} \text{ einsteins/cm}^2\text{-sec}$$

The values $E_{abs.}$ in Table 1 were calculated from the fluorescence energy yields shown in the excitation spectra of zinc oxide in Fig. 1 and determinations of reflection losses based on the MgO standard with 95% reflection of the 365 mμ line.

Zinc oxide (Analar) and the same specimen after being heated in a mildly reducing atmosphere at 1000 C to produce maximum fluorescence (ZnO, $1000_{red.}$), both show very good agreement with the theoretical yield of 0.5, when energy losses due to reflection and fluorescence are taken into consideration, whereas all other specimens do not (Table 1). We note the particularly great discrepancy of the zinc oxide that has been doped with manganous ions before being heated in a mildly reducing atmosphere at 1000 C (ZnO(Mn)). This material also shows very little photoconductivity as compared with ZnO Analar or ZnO, $1000_{red.}$. It is suggested, therefore, that here a considerable amount of the absorbed energy is degraded into lattice vibrations, since the incident energy is not balanced by those parts lost by reflection and the production of conducting electrons as represented in the photochemical yield. The same reasoning would apply to the rest of the samples showing quantum yields markedly smaller than 0.5. It is reasonable to assume that with increased heating in an inert, or mildly oxidizing atmosphere the degree of crystallization will increase and thus facilitate nonluminous transitions. On the other hand, there is good evidence for the mechanism suggested by equations [1] and [2] in those instances where the expenditure of the incident energy can be quantitatively accounted for.

In the experiments with cadmium sulphide, fluorescence yields were obtained by integration of the fluorescence spectra shown in Fig. 2, based on a 19.5% fluorescence yield of ZnO (activated in a mildly reducing atmosphere at 1000 C) on excitation with 365 mμ as a secondary standard.

Markham, et al.,[8] have shown that cadmium sulphide, on exposure to U.V. is rapidly oxidized to cadmium sulphate. Thus, the photochemical production of hydrogen peroxide in the presence of cadmium sulphide is not entirely catalytic, the semiconductor being gradually decomposed with concurrent loss in activity. It appears from the present work that this is due to the combined action of ·OH free radicals produced by

$$CdS^+ + OH^- \rightarrow CdS + \cdot OH,$$

followed possibly by some reaction of hydrogen peroxide with both CdS and H_2S and intermediately formed sulphite ions. Since the stoichiometry of these reactions is still open to doubt no accurate predictions of quantum yields can be made on the basis of chemical mechanism. In any case, the loss of activity of CdS through conversion to $CdSO_4$, coupled with the removal of hydrogen peroxide by reaction with CdS, H_2S, and SO_3'' would suggest quantum yields smaller than 0.5.

Results given in Table 2 show that in the relatively short runs of 30 min that were used in the experiments of photochemical production of hydrogen peroxide by cadmium sulphide with 365 mμ excitation, the catalytic activity of cadmium sulphide is fully maintained, giving quantum yields of approximately 0.5 with the CdS specimens activated at 600–700 C. A remarkable feature of CdS 800 and CdS 900 is that in these instances oxygen did not exert quenching but rather activation of photoconductivity despite the fact that point contact rectification experiments indicated an *n*-type semiconductor.

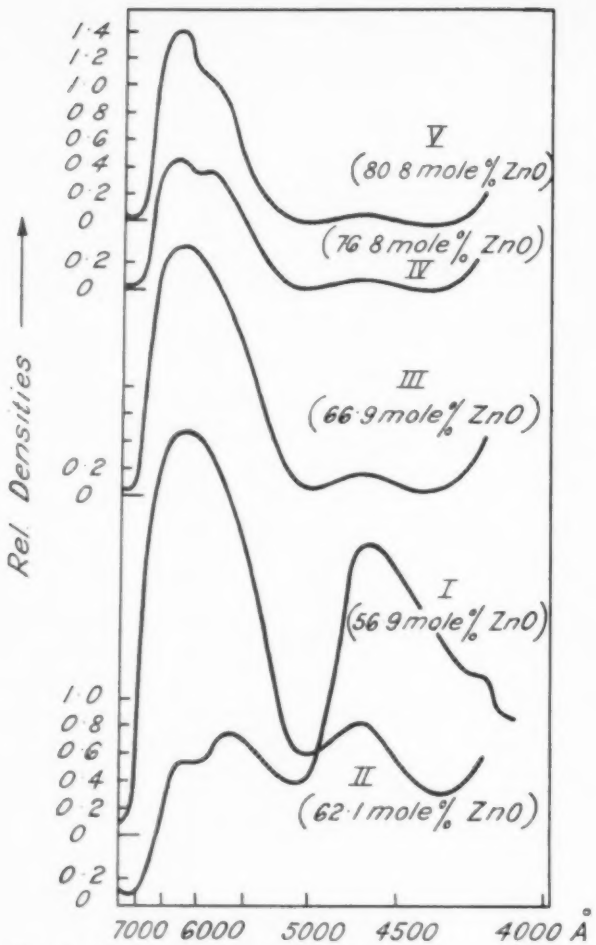

FIG. 3—Luminescence emission of basic zinc carbonates.

THE PHOTOCHEMICAL ACTIVITY OF BASIC ZINC CARBONATE AND ITS RELATION TO PHOTO-EMF AND RATE OF WATER ABSORPTION

In 1944, Chari and Qureshi[9] found that zinc carbonate is a solid catalyst at least as efficient as zinc oxide for the photosynthesis of hydrogen peroxide.

In the present study, zinc carbonate (laboratory reagent ex B.D.H.), which is, in effect, basic zinc carbonate of the approximate composition $ZnO \cdot 2ZnCO_3$ hydr., has been decomposed stepwise by continued heating in air at 210 C. The effect of this treatment on the phosphorescent spectral emission is shown in Fig. 3. The phosphorescence emission changes from a strong bright blue (with weak yellow and orange-red bands) to a strong orange-red with the simultaneous loss of the original blue band on prolonged heating. Phosphorescence energy yields have again been obtained by standardization with ZnO ($1000_{red.}$). The electrical conductivity in air of basic zinc carbonate is extremely weak in the dark and shows only very little response to radiation. Neither can oxygen quenching be studied unambiguously with this material as it cannot be exposed to vacuum. The results in Table 3 are given in terms of energy yields

$$Q'_\lambda = \frac{\Delta F}{E'_{abs.}} \qquad [3]$$

where $E'_{abs.}$ is the energy absorbed by 1 cm² of exposed area of the catalyst in kcal/sec. and ΔF is the corresponding increase in free energy of the system due to the formation of H_2O_2. In the experiments with basic zinc carbonates unfiltered U.V. was used as an excitation source, the energy of which was calibrated with a thermopile. The energy yield is seen to pass through a broad maximum at 65–75 mole % ZnO content of the basic carbonate.

The strong oxygen quenching of the photoconductivity of zinc oxide and cadmium sulphide suggests that electron transfer to oxygen rather than to water is the primary step. Conversely, the rates of water adsorption by basic zinc carbonates, shown in Fig. 4, might be taken as an indication that here the electron transfer proceeds directly into water, producing hydroxyl ions and atomic hydrogen.

The magnitude of photo-emf imposed on a bright, O_2-saturated, platinum electrode coated with zinc, carbonate on gelatin shows close analogy to photochemical activity as is also seen in Fig. 4. Its observed reversibility in the dark can reasonably be assumed to indicate an increase in the ionization of adsorbed water under the effect of radiation. This phenomenon would thus be somewhat akin to the so-called "suspension pH" of hydrated zinc oxide which was found to be much greater than that of $Zn(OH)_2$.

In the self-activated zinc oxides and cadmium sulphides the interstitial metal is generally considered to provide defects of the electron-donor type. In zinc carbonate defects are more likely to be due to vacancies produced by the removal of CO_2.

MECHANISMS

With a change in the standard free energy of approximately 25 kcal/mole and a quantum yield of nearly 0.5 for radiation of $\lambda < 400$ mμ, the reaction

$$H_2O + \tfrac{1}{2}O_2 \rightarrow H_2O_2 \qquad [4]$$

has been considered as one of the most promising for the photochemical conversion and storage of solar energy, provided that the useful spectral range could be expanded, e.g., by the adsorption of suitable organic dyes on the surface of the solid catalyst.[4]

Whether hydrogen peroxide is produced by the primary transfer of an electron from the photo-excited catalyst to oxygen

$$\begin{gathered} h\nu + ZnO + O_2 \rightarrow ZnO^+ + O_2^- \\ O_2^- + H^+ + OH^- \rightarrow \cdot OOH + OH^- \\ ZnO^+ + OH^- \rightarrow ZnO + \cdot OH \end{gathered} \qquad [5]$$

VOL. 5 1961

TABLE 3—Photochemical Activity of Basic Zinc Carbonates

Sample	I	II	III	IV	V	VI	VII
Mole % ZnO	56.9	62.1	66.9	76.8	80.8	99.0	99.1
$(E'_{refl.} + E'_{fl.})$ (kcal/cm²-sec)	404×10^{-7}	292×10^{-7}	150×10^{-7}	120×10^{-7}	98×10^{-7}	94×10^{-7}	91×10^{-7}
$E'_{abs.}$ (kcal/cm²-sec)	26×10^{-7}	138×10^{-7}	280×10^{-7}	310×10^{-7}	332×10^{-7}	336×10^{-7}	339×10^{-7}
ΔF	1.25×10^{-8}	5.25×10^{-8}	26.0×10^{-8}	28.3×10^{-8}	25.0×10^{-8}	20.5×10^{-8}	23.1×10^{-8}
Q_λ' (calc. from [3])	0.005	0.004	0.009	0.009	0.008	0.006	0.007

as suggested, e.g., by Calvert et al.,[10] or to water

$$h\nu + ZnO + H_2O \rightarrow ZnO^+ + \cdot H + OH^-$$
$$\cdot H + O_2 \rightarrow \cdot OOH \qquad [6]$$
$$ZnO^+ + OH^- \rightarrow ZnO + .OH$$

as proposed earlier, e.g., by Markham and Laidler[11] appears, prima facie, not so important as the eventual fate of the hydroxyl free radical, which invariably forms as a result of the regeneration of the catalyst. It has been well established that the presence of both oxygen and an organic "additive" is essential for the formation of hydrogen peroxide in irradiated suspensions of zinc oxide.[6] Occasional statements to the contrary[11, 12] can well be explained by the great difficulty of quantitatively displacing oxygen by another gas or by evacuation at room temperature[13] and by the equally great difficulty of completely excluding impurities that would react with ·OH.

From the fact that H_2O_2, when added to the system ZnO-H_2O-additive at low supplies of oxygen is rapidly decomposed, Rubin et al.,[6] deduced that the "additive" does not perform the function of a "stabilizer" for hydrogen peroxide, and they preferred to formulate the overall reaction, e.g., in the presence of oxalate ion as the "additive," as:

$$O_2 + 2H_2O + C_2O_4^= \rightarrow H_2O_2 + 2HCO_3^- \qquad [7]$$

expressing the action of ZnO as that of a catalyst for the occurrence of a normally exothermic reaction, viz., the formation of hydrogen peroxide as a byproduct of the catalytic oxidation of oxalate ion by oxygen.

With oxalate ion as the organic substrate in the system $h\nu \rightarrow$ (ZnO-H_2O-O_2), we confirmed that the formation of hydrogen peroxide and the disappearance of oxalate ion are nearly equivalent, as is shown in Table 4 for various zinc oxides. The function of oxalate ion is obviously that of a scavenger for hydroxyl free radicals, which would otherwise interfere with the production of hydrogen peroxide by interacting with ·OOH:

$$.OOH + \cdot OH \rightarrow H_2O + O_2 \qquad [8]$$

In the presence of more effective free radical scavengers, e.g., hydroquinone or 3,4,5-tripropoxy-benzoic acid, hydrogen peroxide yields were reduced, probably due to a reaction of the scavenger not only with ·OH but also with ·OOH. When ·OH is effectively removed, the formation of hydrogen becomes possible by the disproportionation:

$$2 \cdot OOH \rightarrow HOOH + O_2 \qquad [9]$$

It appears, then, that the photochemical production of hydrogen peroxide on *n*-type semiconductor surfaces is strictly dependent on the effective removal of hydroxyl free radicals. This would require the presence of some

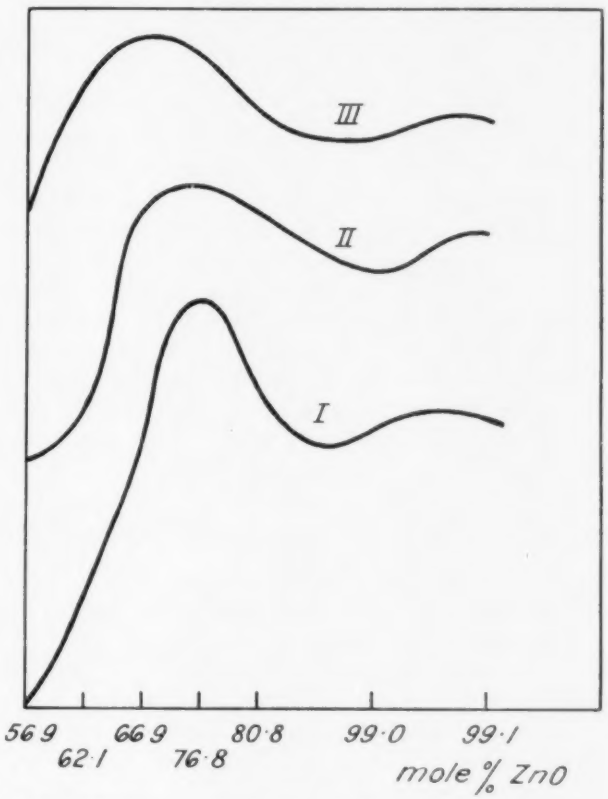

FIG. 4—Relative reactivities of basic zinc carbonates:
I. Photo-emf.
II. Photosynthesis of H_2O_2.
III. Rates of hydration.

TABLE 4—Equivalence of H_2O_2 Production and Substrate Consumption

Sample	C_2O_4 consumed (moles/l) = a	H_2O_2 formed (moles/l) = b	a/b
ZnO Analar	0.00112	0.000927	1.20
ex B.D.H.	0.00112	0.000907	1.23
ZnO 1000 R.	0.000513	0.000453	1.13
	0.000478	0.000418	1.14
ZnO(Mn)	0.000284	0.000234	1.21
	0.000274	0.000224	1.22

cheap organic "additive" in a concentration equivalent to the hydrogen peroxide formed.

With a quantum yield of 0.5, 1 mole H_2O_2 formed would involve the absorption of 2.4×10^{24} quanta of $\lambda = 385$ mμ, being the maximum excitation line as shown above; this is equivalent to the absorption of 300 kcal/mole. Conversely, 1 mole of H_2O_2 formed represents an increase in Standard Free Energy ΔF°_{298} of 25 kcal. This would, at first sight, suggest an energy yield of 8.3%. However, the removal of ·OH by reaction with a scavenger, e.g., benzene, according to

$$2 \cdot H + \text{benzene} \rightarrow \text{phenol} + H_2O \qquad [10]$$

involves a further unavoidable expenditure of energy, i.e., chemical energy of 40 kcal/mole, in addition to the adsorbed radiation energy of 300 kcal/mole, in order to recover 25 kcal/mole in the form of hydrogen peroxide. This demonstrates the intrinsic difficulties of the photochemical synthesis of hydrogen peroxide as a solar energy converting device. The same reasoning would rule out possibilities of alternative reactions involving the transfer of electrons from illuminated zinc oxide, or other *n*-type semiconductors, to suitable electron acceptors, as envisaged by some workers in the past,[2] and also the use of sensitizing dyes on e.g., zinc oxide, suggested more recently,[4] since these would soon be destroyed by ·OH.

CONCLUSIONS

In all instances considered in this paper, luminescence, short or long-lived, visible or infrared, has been found to result in a loss of photochemical efficiency of a solid catalyst. Conversely, surface photoconductivity which is accessible to oxygen quenching, represents the activated state essential for the photosynthesis of hydrogen peroxide via O_2^- in both zinc oxide and cadmium sulphide. The nature of the electrons produced by excitation of basic zinc carbonate, which can be utilized chemically, is more difficult to envisage at present. These electrons do not appear to be of either the luminescent or the conductive types. The study of photo-emf and rate of H_2O-adsorption suggests that it is water that acts as an electron acceptor in basic zinc carbonate. However, in zinc oxide, neither water held randomly by physical forces nor that forming distinct chemical bonds with the matrix in the form of hydroxyl groups, appears to be photoelectrically active. Thus, Hoja[14] found that small amounts of water of hydration are necessary for the photoelectric sensitivity of zinc oxide. Conversely, zinc hydroxide is photochemically quite inactive. We would, therefore, suggest that in basic zinc carbonate also, water of co-ordination is involved in the electron transfer mechanism.

The formulation of the over-all reaction as involving the participation of a solid catalyst implies that the photochemical reduction of oxygen, or water, does not result in the permanent oxidation of the catalyst, but rather allows its eventual return to the original neutral state, which can only be achieved by the simultaneous oxidation of some suitable substrate. Since the second half of the reaction cycle requires the expenditure of chemical potential greater than that obtained by the gain in free energy of the system by the synthesis of hydrogen peroxide, it seems a fallacy to consider the photosynthesis of hydrogen peroxide by crystal phosphors as a means of converting solar energy. In bulk reactions, such as those considered in the present study, and others characterized by the absence of structural elements, an efficient generation of a reduction equivalent is not likely to succeed as this will always tend to react with the simultaneously produced oxidation equivalent. In the photosynthesis of hydrogen peroxide, ·OH is the oxidation equivalent, whereas ·OOH must be regarded as the reduction equivalent. Their interaction can be prevented by the thermodynamically expensive use of a scavenger for ·OH. In systems where oxygen is the oxidation equivalent, the problem is reduced to an elimination of oxygen not by chemical means but rather by its spatial separation from the reduction equivalent. This, it seems, could practically be achieved only by the use of catalysts in the form of laminated structures with all the complexities and costs involved in their preparation.

REFERENCES

1. Heidt, L. J. and Smith, M. E., *J. Am. Chem. Soc.* **70,** 2476, 1948.
2. Stephens, R. E., Bacon Ke, and Dan Trivich, *J. Phys. Chem.* **59,** 966, 1955.
3. Calvert, J. G., *Ohio J. Sci.* **53,** 293, 1953.
4. Levine, S., Halter, H. and Mannis, F., *Solar Energy* **2,** 11, 1958.
5. Schleede, A., München 1943 in: P. Pringsheim, Fluorescence and Phosphorescence, *Interscience Publ.*, New York 1949, p. 584.
6. Rubin, T. R., Calvert, J. G., Rankin, R. T. and MacNevin, W., *J. Am. Chem. Soc.* **75,** 2850, 1953.
7. Hatchard, C. G. and Parker, C. A., *Proc. Roy. Soc.* **A235,** 518, 1956.
8. Markham, M. C., Barry, J., Iava, M., Haddad, J., *J. Phys. Chem.* **61,** 1665, 1957.
9. Chari, C. N. and Qureshi, M., *J. Indian Chem. Soc.* **21,** 297, 1944.
10. Calvert, J. C., Theurer, J., Rankin, G. T. and MacNevin, W., *J. Am. Chem. Soc.* **76,** 2575, 1954.
11. Markham, M. C. and Laidler, J. J., *J. Phys. Chem.* **57,** 363, 1953.
12. Yamagudi, K., Nishioeda, M. and Imagawa, H., *Biochem. J.* **301,** 404, 1939.
13. Mjasnikov, I. A. and Pscheschetzkyi, S. Ya., Problems of Kineties and Catalysis, Vol. VIII. *Publ. Acad. Nauk. S.S.S.R.*, Moskow, 1955.
14. Hoja, E., *Z. phys. Chem.* **B40,** 263, 1938.

VOL. 5 1961

The Present State-Of-The-Art of Photovoltaic Solar Energy Conversion*

M. Wolf

Heliotek Corporation, Sylmar, California

The present state-of-the-art in photovoltaic solar energy conversion, in particular, as applied for space vehicle power supplies is summarized. Past and future development goals are: lower weight-to-power and cost-to-power ratios, higher reliability, and increased useful lifetimes. Difficulties with photovoltaic solar energy converting devices were encountered in their classification based on exact determination of the power output and efficiency in "standard" sunlight, and by a reduction of their useful life expectancy due to radiation damage encountered in the Van Allen belts and in solar flares. Remedial actions in progress are outlined. Recent improvements introduced on the present standard device, namely, the silicon solar cell are discussed. They include application of metallic grids for the reduction of series resistance and change of the p-layer thickness for improved spectral response. Further, attempts to develop methods for preparing large area and thin film silicon solar devices are reviewed, and finally a survey is given of the progress made in the application of other semiconductor materials to solar photovoltaic energy conversion. Here the work on cadmium sulphide solar cells stands out due to the achievement of solar conversion efficiencies of up to 4½% on thin film cells.

INTRODUCTION

Since photovoltaic solar energy conversion is the mechanism for obtaining electrical power utilized on all major space programs undertaken in the past, presently underway or contemplated for the next few years, it appears to be a timely task to summarize the present state-of-the-art in this field. The major goals of the development work undertaken on devices based on this mechanism were: lower weight-to-power and cost-to-power ratios, higher reliability, and increased useful lifetimes. It is interesting to review in the light of the experience gained the difficulties encountered with these devices, and the corrective measures undertaken. This will be followed by a discussion of the improvements introduced on the present standard device, namely, the silicon solar cell. Further attempts to develop methods for preparing large area and thin film silicon solar devices will be reviewed, and finally a survey will be given of the progress made in the application of other semiconductor materials to solar photovoltaic energy conversion.

Essential contributions to the analysis of the photovoltaic effect or of the device operation have not been made during the last year, with the exception of a new explanation for the operation of the cadmium sulfide solar cell.[1] In view of the length of this paper, only references to previous publications will be given for the whole complex of the device analysis.[2, 3, 4, 5, 6]

DIFFICULTIES EXPERIENCED WITH THE SILICON SOLAR CELL AND CORRECTIVE MEASURES UNDERTAKEN

The difficulties experienced with the silicon solar cells during the last year were of a twofold nature. The first of these problems is the measurements problem, which was encountered because of the introduction of insufficient sunlight simulation for the performance determination of silicon solar cells, coupled with a variation in the spectral response of these devices. The second problem is due to the presence of intense nuclear radiation fields in the space surrounding the earth, causing a very substantial decrease in the useful lifetime of silicon solar cells in certain orbits. Without this radiation, the lifetime would be much longer than needed for any practical purpose.

The Problem of Performance Measurements on Solar Cells

Since the prime objective of the solar cell is to convert solar energy into useful electrical energy, the basic performance measurement has to be connected with the solar radiation. The standard instrument used for the determination of the energy content in the solar radiation received is the pyrheliometer. The principle of the measurement is to obtain the electrical output of the solar cells in sunlight using the pyrheliometer as the calibration instrument. Difficulties are already encoun-

* This paper was prepared and presented at the 1961 Winter Convention on Military Electronics while employed with Hoffman Electronics Corporation, Semiconductor Division, El Monte, California.

tered at this point. The pyrheliometer measurement is dependent on the ambient temperature as well as on the tilt of the device. A few other unknown variables also seem to afflict the measurements, besides variations found in the basic calibration of the instrument. The result is an uncertainty in the pyrheliometer readings of several per cent for the 90% confidence level. Another bigger problem area is the variation of the spectral distribution of the sunlight. Variations in the intensity of the sunlight as received on the earth's surface are due to various amounts of attenuation in the atmosphere. Since the atmosphere is not a neutral attenuator, the intensity variations are always connected with changes in the spectral distribution, and even various spectral distributions with the same integrated light intensity are not infrequently found. Since the pyrheliometer is a relatively flat receiver, while the solar cell is a selective receiver, discrepancies in the solar cell output measurements are normal. Such discrepancies have been observed to reach as much as ±10% between different measurements performed on the same cell.

Since measurements as described above are too dependent on weather conditions to be useful for production and regular inspection purposes, a measurement method capable of being performed at all times in the laboratory had to be devised. Tungsten light sources have been found in the past to be the most suitable artificial sources because of their superior stability in short as well as in long term respect. The spectral distribution of this light source can readily be maintained constant by measurement of the color temperature and by regulation of the input power. The desired light intensity is then obtained by varying the distance between the source and the object. Repeatability of solar cell measurements with such tungsten light sources within ±1% over periods in the order of a day and within ±2% in long term with respect to the 90% confidence level has been achieved. The color temperature of these tungsten light sources is now normally set to 2800° ± 50°K, while the intensity is adjusted by means of so-called standard cells which have been calibrated in sunlight, as described above. The parameter used on the standard cells for this light intensity transfer is the short circuit current.

If all solar cells would have exactly the same spectral response, then such a transfer from one source with a specific spectral distribution to another with a completely different spectral distribution would be perfectly valid.

Figure 1 shows, for comparison purposes, a normalized spectral distribution of sunlight as it is received outside the earth's atmosphere,[7] and the spectral distribution of a tungsten light source with a color temperature of 2800° K. It further presents the spectral distribution of the same tungsten light after passage through a water layer of 3 cm thickness.[8]

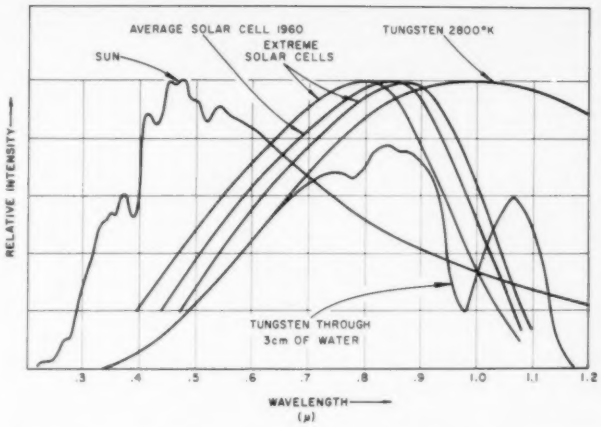

FIG. 1—Normalized spectral distributions of sunlight as received outside the earth's atmosphere and of light from a tungsten filament lamp of 2800°K color temperature, direct and through a 3 cm thick layer of water. Also the average spectral response determined from 400 Hoffman silicon solar cells type 120 CG of the 9–13% efficiency classifications, together with the extreme spectral response curves found in this group.

It has been found, however, that a considerable spread exists in spectral response between various production cells. This spread causes some uncertainty in a measurement method involving a variation of the source spectrum. Figure 1 also shows the average spectral response of the typical silicon solar cell as produced throughout the year 1960. This average response curve was determined from a sample of 400 production cells, having efficiencies between 9 and 13%. Two other curves show the extremes of the spectral responses found in the same study. If one chooses for the preparation of the standard cells, however, to use cells having a spectral response very close to the average of the production spread, then the average measurement should be proper with a symmetrical deviation for the production spread.

It has, however, been found recently that the average spectral response of the production solar cells can fluctuate with time. The result of this is that improper measurements can be obtained at certain times for the whole production by use of the tungsten system. Such a difficulty has been experienced recently. Since the selection, preparation and calibration of standard cells is a very tedious and time consuming process, it appears impractical to prepare standard cells whenever a fluctuation of the production spectral distribution is experienced.

The ideal solution to the afore-mentioned problem is the creation of a "sunlight simulator." With this name, a light source is meant which exhibits the same spectral distribution and intensity as observed in the solar radiation. Such light sources which have to meet

VOL. 5 1961

the conditions of extremely close resemblance to the spectral distribution of the solar radiation, and of being capable of very good short and long term stability, are under development at various organizations. The best candidates at the present time appear to be: carbon arcs, if efforts to obtain the needed stability will be successful; a plasma jet system developed by Mt. Vernon Research Laboratories; and the application of xenon high pressure arc sources combined with filters as under development at the present time separately by General Electric Company, Spectrolab, Inc., and the Hoffman Semiconductor Division. Prototypes of some of these sources are already finding limited application.

These efforts of finding the proper light source are paralleled by meetings between representatives of the interested industries, with the objective of standardizing methods and tolerances, and of resolving the problem encountered.

The Radiation Damage Problem

The second major problem encountered during the last year with silicon solar cells in their application as power sources for space vehicles is due to nuclear radiation. Such radiation has been found to be continuously present in the space surrounding the earth in the Van Allen belts, and also to occur from time to time in the space outside these belts as the result of solar flares.

The Van Allen belts consist of charged particles trapped in the geomagnetic field. The belts contain an inner zone with its heart near 10,000 km geocentric radius and an outer zone having its highest intensity at a geocentric radius of 25,000 km, both measured near the equatorial plane. The inner zone extends in the equatorial plane from an altitude of 600 km above the earth's surface to an altitude of about 10,000 km. It consists of electrons which reach in the energy range of 20 keV to 1 MeV an omnidirectional flux intensity of 10^{10} electrons/cm^2 sec, and of protons which reach in energy up to about 1,000 MeV, and which reach in the heart of the inner zone an omnidirectional flux intensity of $2 \cdot 10^4$ protons/cm^2 sec for the energy range above 30 MeV. The outer zone extends from an altitude of about 15,000 km in the equatorial plane to about 70,000 km above the earth's surface. It comprises chiefly electrons in the energy range of 50 to 5,000 keV and some protons with energies less than 1 MeV. The omnidirectional flux intensity for electrons with energies greater than 20 keV reaches 10^{11} electrons/cm^2 sec in the maximum intensity regions.[9]

Due to the nature of the Van Allen belts, the intensity distribution of the charged particles follows quite well the lines of the geomagnetic field, as shown in Fig. 2.[10] This figure also shows measurement points obtained with a scintillation counter mounted on the earth Satellite Explorer VI. Many measurements of

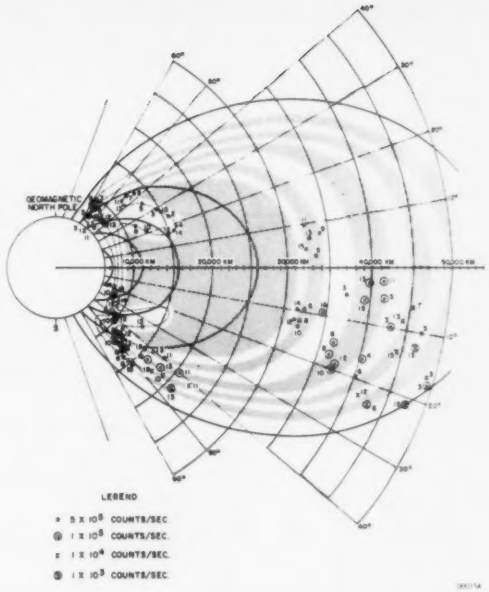

REPRODUCED FROM: A. ROSEN, T. A. FARLEY AND C. P. SONETT, "SOFT RADIATION MEASUREMENTS ON EXPLORER VI EARTH SATELLITE"

FIG. 2—Isointensity contours as observed by a scintillation counter on the Explorer VI satellite.

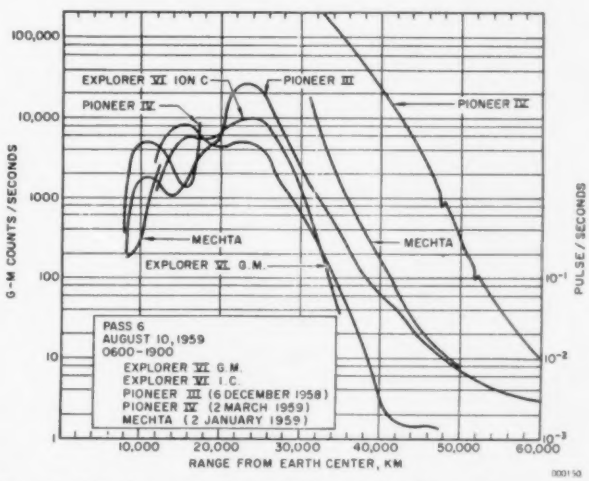

FIG. 3—Relative particle radiation intensities observed at different times by instruments traversing the outer regions of the trapped particle radiation zones. All measurements are taken by Geiger-Mueller tubes, except those for one curve, which was obtained using an ionization chamber on Explorer VI satellite.

this sort have been carried out on various space vehicles with the different types of measurement instruments, like scintillation counters, Geiger tubes, photographic emulsions, and others. Figure 3, reproduced from reference[9], shows a compilation of measurements obtained with different earth satellites. These data were obtained from Geiger counters on the listed satellites, except one curve obtained with an Explorer VI ionization chamber. The differences in the trajectories of the different vehicles were not sufficient to account for the

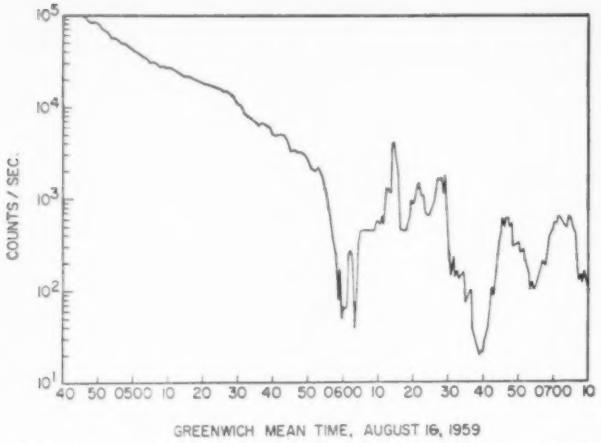

FIG. 4—Rapid fluctuations of particle count rates of a scintillation counter on Explorer VI satellite during a geomagnetic storm.

differences in the observed radiation intensities. It is, however, felt by the original author of the figure that the differences between the individual curves are attributable to temporal variations of the radiation intensity in the outer zone rather than to uncertainties of the measurement systems.

The second type of radiation found is particles emanating from the solar flares, which consist predominantly of protons in the energy range of 30 MeV to 20 BeV. In a typically large event which may occur as often as once per year, peak proton intensities of $1.5 \cdot 10^5$ protons/cm² sec with energies over 30 MeV have been observed. The integrated flux over one day measured in such a flare was $5 \cdot 10^9$ protons/cm² with energies above 30 MeV. Besides these relatively few events with highly intense proton showers, a larger number of smaller flares do occur, which give rise to a total yearly integrated flux intensity from solar flares of 10^{10} protons/cm² with energies above 30 MeV, as deduced from measurements carried out on the polar caps, where the geomagnetic field does not prevent the incidence of these particles. Figure 4[11] shows the very rapid and heavy fluctuations of the particle intensity in the outer Van Allen zone during a geomagnetic storm, as they are connected with the solar flares.

The effect of such charged particle radiation on solar cells and other semiconductor devices can be estimated from experiments carried out in various laboratories. Such experiments have been carried out with different types of particle accelerators using electrons and protons. Results of such radiation damage experiments are shown in Fig. 5[12] which presents the current-voltage characteristics of originally 11% efficient silicon solar cells of standard type, as they were found to be before irradiation and after three different levels of bombardment intensities with 750 keV electrons. The result of irradiation is mainly a reduction of the short circuit current, and a lesser decrease of the open circuit voltage, which largely corresponds to the reduction in short circuit current, similar to that occurring with a reduction of light level. Figure 6[12] shows that this radiation damage and decrease in short circuit current is accompanied by a change of the spectral response. Since all the curves are normalized, a possible difference in the total amplitude of the curves cannot be obtained from this set of information. It is, however, very evident that the long wavelength response of the solar cell gets successively lost with increasing amounts of bombardment. Figure 7 presents the absorption coefficient as a function of wavelength of the incident radiation. It shows that at the longer wavelengths a large number of photons will penetrate deeply into the crystal. This means that in order to obtain high collection efficiency at the long wavelengths, large minority carrier lifetimes and corre-

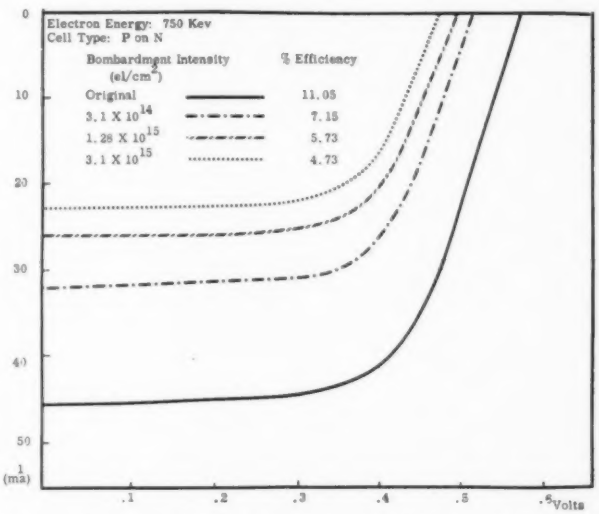

FIG. 5—Current-voltage characteristics of a "p on n" silicon solar cell initially and after various irradiation dosages with 750 keV electrons.

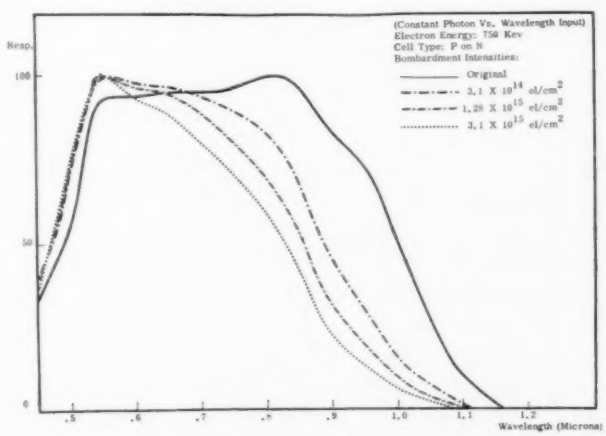

FIG. 6—Relative spectral response of a "p on n" silicon solar cell initially and after various irradiation dosages with 750 keV electrons.

VOL. 5 1961

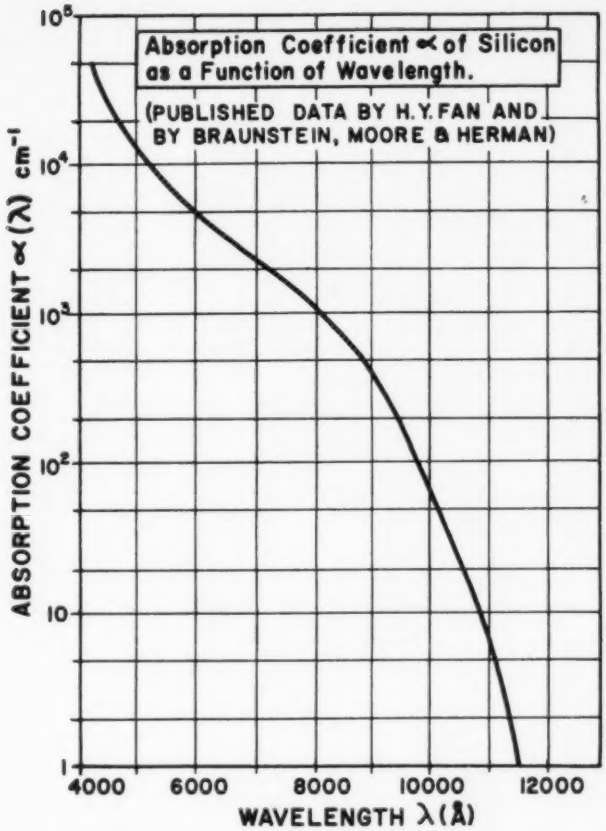
Absorption Coefficient ∝ of Silicon as a Function of Wavelength.
(PUBLISHED DATA BY H.Y. FAN AND BY BRAUNSTEIN, MOORE & HERMAN)
ABSORPTION COEFFICIENT ∝(λ) cm⁻¹
WAVELENGTH λ(Å)

FIG. 7—Absorption coefficient $\alpha(\lambda)$ of silicon as a function of wavelength.

spondingly large diffusion lengths are necessary. This also means that the long wavelength response is predominantly a response from the n-layer, while the short wavelength response with large absorption coefficients is based on contributions from the p-layer. Comparing now Fig. 6 with Fig. 8 which shows the collection efficiency (or spectral response for constant number of photons) as a function of wavelength,[4, 5, 6] including its p- and n-layer contributions, it becomes evident that the major change is encountered in the n-layer, and that the minority carrier lifetime and the related diffusion length must have been affected by the production of defects in the single crystal through the particle radiation.

It is now generally accepted that the result of high energy electron bombardment on single crystal structures is the production of localized defects, while high energy proton radiation causes the destruction of nuclei and resultant generation of large defect clusters. Figure 9[13] shows the transition from Rutherford type scattering of relatively low energy protons and the resultant production of localized defects to spallation at proton energies above 200 MeV. The result of this high energy spallation process is a much larger contribution to the defect production by high energy protons, than would be expected from the older theories.

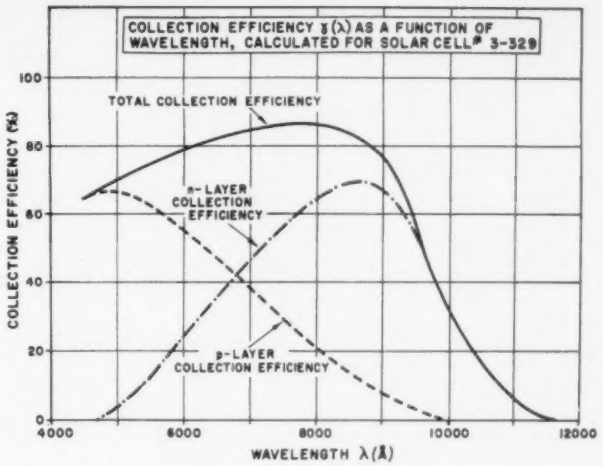
COLLECTION EFFICIENCY η(λ) AS A FUNCTION OF WAVELENGTH, CALCULATED FOR SOLAR CELL # 3-329
TOTAL COLLECTION EFFICIENCY
n-LAYER COLLECTION EFFICIENCY
p-LAYER COLLECTION EFFICIENCY
COLLECTION EFFICIENCY (%)
WAVELENGTH λ(Å)

FIG. 8—Collection efficiency $\eta(\lambda)$ as a function of wavelength, calculated for solar cell no. 3-329.

Defect Production as a Function of Proton Energy

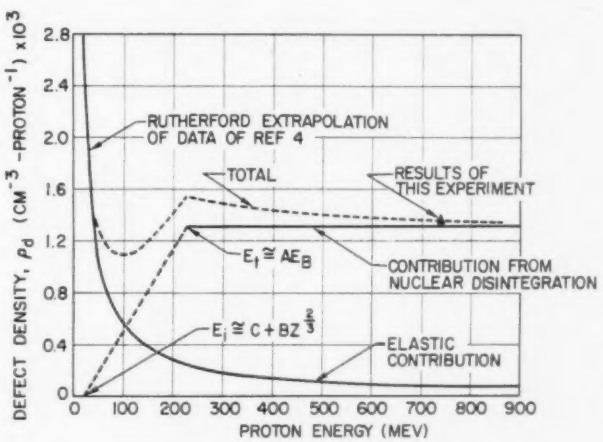

FIG. 9—Energy dependence of the defect production in silicon using extrapolation from the Loferski and Rappaport data (ref. 14) by the Rutherford reciprocal energy relation at low energy levels and superposition of the spallation model at higher energy levels for proton irradiation.

It has generally been found[14, 13, 12] that proton flux with energies above 10 MeV and a total integrated dosage of 10^{10} to 10^{11} protons/cm^2, or a total integrated electron dosage of 10^{14} to 10^{15} electrons/cm^2 having energies above 200 keV will cause a 25% degradation of the power output of p$^+$n type silicon solar cells. Such doses may be accumulated by solar cells mounted on space vehicles in equatorial orbits through the heart of the inner Van Allen belt in a matter of 10 to 20 days. Since, however, as shown in Fig. 2, the intensity distribution in the Van Allen belts is highly dependent on latitude as well as on altitude, it may be possible to find for many missions orbits in which the radiation level is sufficiently low as to assure long useful lifetimes of the solar cell power supplies.

Space probes may be launched so as to exit over the polar regions, or pass through other minima of the Van Allen belt particle distribution so that a minimum of radiation damage will be obtained during the early lifetime of the vehicle.

High energy proton damage due to solar flares, however, may not be avoidable. These flares occur in a random pattern, and highly intense ones could cause considerable radiation damage in a matter of days. Fortunately, they do occur even at times of high solar flare activity only a few times per year. The solar flare activity has a periodic pattern, and a time of high activity is just passing, so that major flares may not pose any problems for the next few years.

Two approaches to the overcoming of at least part of the effects of nuclear radiation on space vehicle solar power systems are being pursued. It is possible to shield against electron radiation up to 1 MeV by using transparent covers over the silicon solar cells. These covers have to meet the conditions of absorbing the radiation without generation of color centers in sufficient number as to impede light transmission. Certain types of quartz have been found to be especially suitable for these purposes when used in thicknesses of about .060 to .070 inches. It is also known that the presence of quartz or glass cover plates of practical thicknesses is not sufficient to shield effectively against high energy protons, and it is expected that rather to the contrary spallation effects taking place in these covers at very high energy proton bombardment will increase the resulting damage to the silicon solar cells. More recently experiments were directed towards the application of organic films having a large content of hydrogen atoms, which have a high electron absorption cross section. These films also show only negligible transmission loss due to radiation damage.

Another approach to the reduction of radiation damage has resulted from the work of Mandelkorn and coworkers[15] who prepared solar cells by phosphorus diffusion into boron doped p-type base material. It has been found that these n^+p cells are somewhat less susceptible to radiation damage than the standard cell having a boron diffused layer on arsenic doped base material. The exact magnitude of this improvement is not known at this time, but a factor of two at least seems to have been observed in all experiments. There is evidence that p-type material, and especially boron doped material is less susceptible to the generation of defects by nuclear radiation than n-type material is. Since the effect of radiation damage will be noticed first on deep lying material, as outlined above, it is important to choose material of a resistant type for the base. The high impurity concentrations present in the very thin diffused layer cause a low minority carrier lifetime in this layer, with the result that larger defect concentrations generated by particle bombardment can be tolerated without observable effects on the minority carrier lifetime if compared to higher resistivity and lifetime material. The drift field normally existing in the shallow diffused layer due to the impurity gradient, also contributes to the tolerance of larger radiation dosages by the diffused layer in comparison to the base layer.

Annealing and defect clustering appear to be of importance in the complicated processes connected with radiation damage and defect generation which to some extent still elude conclusive explanations. The complication of these processes is the reason for the observed strong effects, which the very small concentrations of electrically active as well as of electrically inactive impurities have on the course of the processes. It is clear, however, that more work has to be performed in this field in order to arrive at solar cells showing optimum performance and lifetime for power supplies in the space environment.

IMPROVEMENTS ON THE SILICON SOLAR CELL DURING 1960

Two significant improvements have been made on the silicon solar cell during the past year. The first one, already available on production cells, was the introduction of the gridding method. The second one, on which the development stage is just completed, consists in a shift of the spectral response in order to obtain improved efficiency in sunlight, and especially in free space sunlight. This shift was made possible only through the introduction of the gridding method.

Gridded Cell

It has been found that in actual silicon solar cells the internal series resistance is large enough to cause a deviation of the current-voltage characteristic from its ideal curve. With the best methods presently known, the impurity concentration of the diffused p-layer cannot be made sufficiently high in order to keep the series resistance of the p-layer negligibly small for p-layer thicknesses as small as desirable for obtaining highest collection efficiency. In the present silicon solar cell a compromise is obtained between p-layer thicknesses and p-layer series resistance in order to obtain the highest possible over-all efficiency.[3]

A substantial decrease of the total p-layer series resistance can be achieved by applying metallic grids over the p-layer. Fig. 10 shows silicon solar cells of different sizes with such grids applied. These grids reduce the resistance of the p-layer by lowering the length of the current path through this layer to the next collecting metallic line having low resistance. This effect is so great that despite the loss of part of the active area due to coverage by these grid lines, the efficiency of gridded solar cells of 1×2 cm size has been found to be in the

VOL. 5 1961

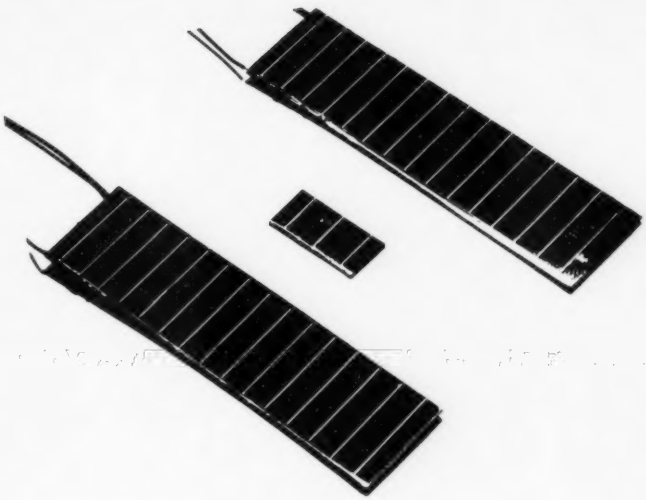

FIG. 10—Photograph of a 1 x 2 cm gridded silicon solar cell (center) and of two 2 x 7.5 cm gridded silicon solar cells.

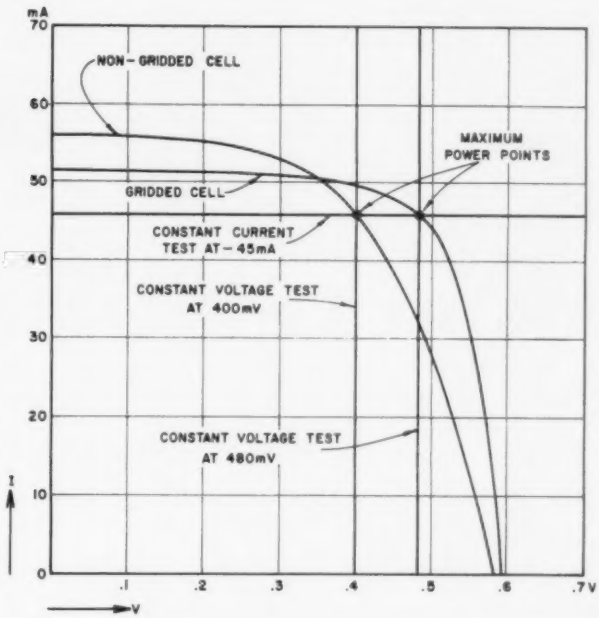

FIG. 11—Current-voltage characteristics with maximum power points indicated and constant voltage and constant current test method for typical silicon solar cells, 1 x 2 cm size gridded and nongridded, taken at 25°C.

average 1.5% higher than that of nongridded, but otherwise identical cells. This efficiency calculation is based on the total exposed area of the cell in a series shingle, counting the area covered by grid lines as exposed area. The introduction of such grids permits also freedom from considerations on size and shape of solar cells as were previously necessary for optimum performance. Solar cells of 2 × 7.5 cm size with grids have now been made with better than 12% efficiency. The two large cells shown in Fig. 10 are of this size.

The reduction of the series resistance causes a change in the current-voltage characteristic, as indicated in Fig. 11, for a gridded and a nongridded cell. The open circuit voltage should be identical, and the difference in short circuit current due to the coverage of part of the active area by grid lines is also normally not as large as appearing in this figure. The major feature is however clearly indicated: the characteristic is more "squared," resulting in a higher voltage for the maximum power point, which occurs at the same current value so that a higher output power results. Consequently, on a power panel having to meet a certain load voltage, fewer cells can be connected in series in order to reach this voltage, which leads either to a reduction in the total panel area for equal power output, or to an increase in power output by adding additional series strings to fill the original panel area.

Spectral Response Modification for Improved Sunlight Performance

It had been shown previously[4, 5, 6] that the long wavelength part of the spectral response curve of silicon solar cells is mainly affected by the minority carrier lifetime of the base material, which usually is an n-region, and that the short wavelength part of the spectral response is influenced by the minority carrier diffusion length and the thickness of the diffused layer, which normally is a p-type layer. These theoretical considerations have been verified by the recent developments.

First, strides were made toward improved minority carrier lifetimes in the base region, which resulted in an increase of the spectral response toward the long wavelength side as shown in Fig. 12-a. This improvement was accomplished during 1959, and it led to the difficulties with the measurement methods as explained in an earlier section. At that time, an increase in the base minority carrier lifetime was the only possible approach to an improvement, as before the advent of the gridding technique a change of the thickness or the minority carrier diffusion length of the p-layer could not lead to better efficiencies. This had its reason in the previous optimization of impurity concentration and the p-layer thickness in such a way as to give the best compromise between short circuit current and series resistance. After the gridding method was introduced, efforts could be undertaken toward reaching a new compromise of p-layer thickness and minority carrier diffusion length by modification of the diffusion parameters. The interesting feature is that modifications of either the short wavelength or the long wavelength part of the spectral response curve can be achieved without affecting the other part.

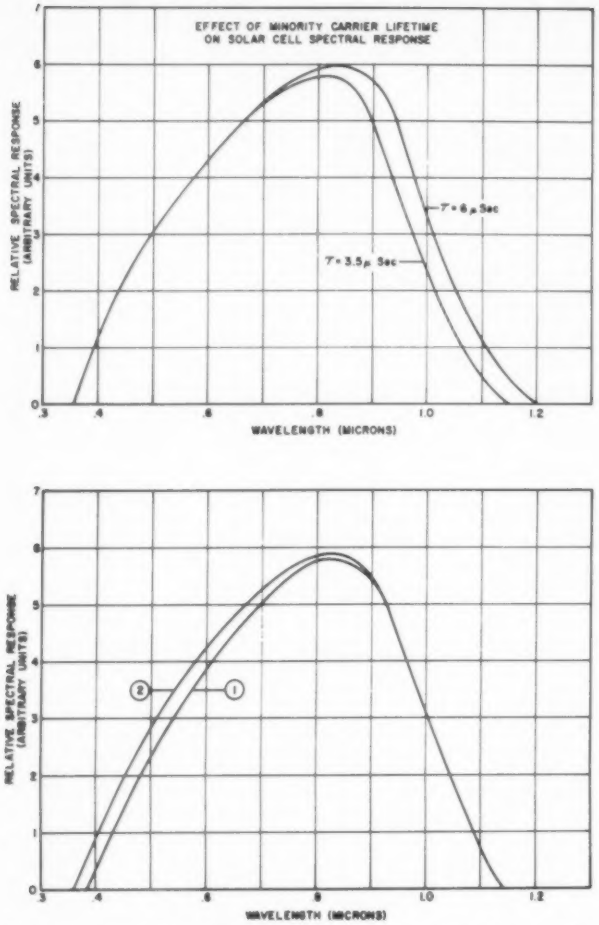
EFFECT OF MINORITY CARRIER LIFETIME
ON SOLAR CELL SPECTRAL RESPONSE
RELATIVE SPECTRAL RESPONSE (ARBITRARY UNITS)
τ = 6 μ Sec
τ = 3.5 μ Sec
WAVELENGTH (MICRONS)
RELATIVE SPECTRAL RESPONSE (ARBITRARY UNITS)
WAVELENGTH (MICRONS)

FIG. 12—Top: The effect of minority carrier lifetime on the spectral response of an otherwise identical solar cell. Bottom: The effect of a variation in the p-layer thickness on the spectral response of an otherwise identical solar cell. Curve 2 has the smaller p-layer thickness.

Fig. 12-b shows the spectral response curves of two silicon solar cells which were prepared with identical parameters except for some diffusion modification. The cell represented by curve 1 has been fabricated with the same diffusion parameters as were used before the introduction of the gridding technique. Curve 2 represents a cell with the modified diffusion parameters. Both cells have the same base material minority carrier lifetime, and therefore the same long wavelength response.

The short circuit current of a solar cell is proportional to the integral under a curve which is obtained by multiplying the cell spectral response curve point for point with the spectral distribution of the light source. Since tungsten light (2800 K) contains only a small amount of energy in the short wavelength part of the spectrum, the modification of the spectral response curve as indicated in Fig. 12-b will result in a hardly noticeable difference of the short circuit current, if measurements are performed under tungsten light sources. This is indicated in Fig. 13-a, which shows curves for the two cells 1 and 2 of Fig. 12-b. These curves are labelled 1 and 2 for the two cells respectively and were obtained by the explained spectral response-spectral distribution multiplication method. Fig. 13-b shows a corresponding set of curves for the same cells, but this time using the spectral distribution of sunlight as received outside of the earth's atmosphere. Here the difference in spectral response between the two cells results in a marked difference in the two curves, leading to a ratio of the integrated areas under the curves of 1.09, as compared to a ratio of 1.02 for the two curves of Fig. 13-a. The interesting result of this modification therefore is that cells are obtained which show under tungsten light a performance comparable to that of the cells prepared with the previously used parameters, but that the same cells will produce a nearly 10% higher short circuit

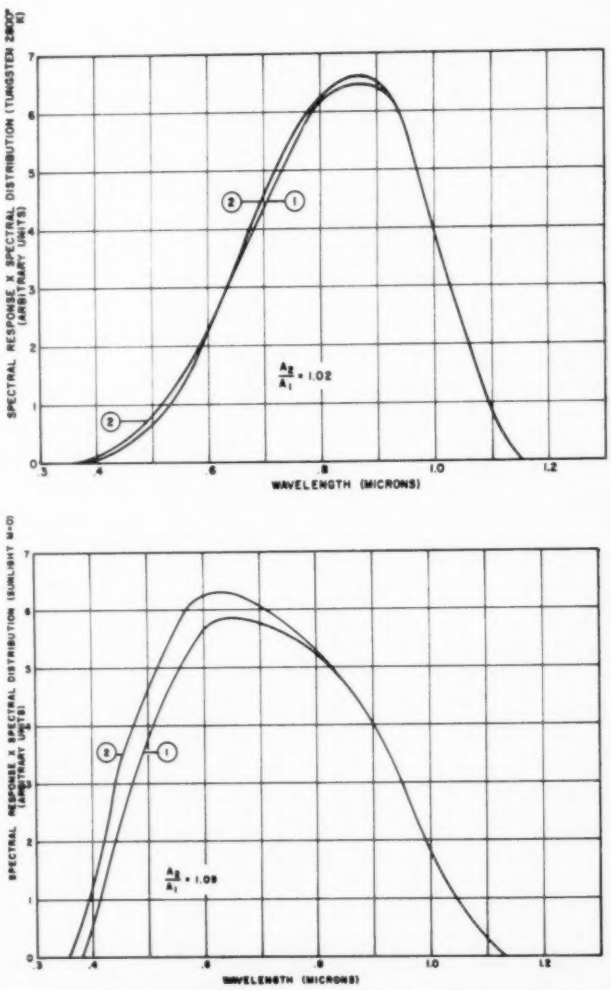
SPECTRAL RESPONSE X SPECTRAL DISTRIBUTION (TUNGSTEN 2800°K) (ARBITRARY UNITS)
A2/A1 = 1.02
WAVELENGTH (MICRONS)
SPECTRAL RESPONSE X SPECTRAL DISTRIBUTION (SUNLIGHT M=0) (ARBITRARY UNITS)
A2/A1 = 1.09
WAVELENGTH (MICRONS)

FIG. 13—Top: Spectral response multiplied by the spectral distribution of light from a tungsten filament lamp at 2800°K color temperature for the cells labeled 1 and 2 of Fig. 12, bottom. The ratio of the areas under the curves 2 and 1 of this figure is given by A_2/A_1. Bottom: Same as the top curves, except that the spectral distribution of sunlight as received outside the earth's atmosphere has been used.

VOL. 5 1961

current and correspondingly higher power output in sunlight in free space than the older cells. This development was carried out with support from the Air Materiel Command.[16]

NEW CONFIGURATIONS AND APPROACHES ON SILICON SOLAR CELLS

Large Area Single Crystal Cells

The advent of the gridding technique permits for the first time complete freedom from geometrical considerations for the design of solar cells. Since diffusions can be controlled with sufficient uniformity, the size of the cells is determined only by limitations in crystal growing and cutting techniques. Future developments probably will retain the rectangular configuration due to its advantage of better area utilization. Cells as large as $2 \times 7\frac{1}{2}$ cm have been prepared with efficiencies as good as those obtained in the smaller types. Preparation of these cells is possible since single crystals of silicon with over 2 in. dia and more than 4 in. length having good crystalline properties are readily available now. Essential difficulties are not expected to be encountered by going to still larger sizes, and 10×2 cm is anticipated as the next step.

These larger area cells have the advantages of lower cost per unit power due to decreased handling time in preparation as well as in application of the cells, and of higher reliability due to the reduction in the number of contacts to be made. While the mentioned approach uses standard methods, it would be very desirable to obtain large area single crystalline wafers without the presently used cutting process in which about 50% of the valuable raw material is lost. A method successfully applied to germanium by Bösenberg[17] consists in casting the material in a mold and successive gradient cooling after attachment of a seed crystal. This method is, however, not applicable to silicon due to the high reactivity of this element with every known material which could be used for a mold. Another approach with the same objective has recently been pursued by W. R. Grace and Co. on an ARPA-Contract.[18] Here molten silicon was floated on molten lead and then gradient cooled after attachment of a seed crystal. This method was expected to be workable since lead was supposed to have a very small solubility in silicon and to act not as an electrically active impurity. Experience showed, however, these assumptions not to be correct. Beyond this, difficulties were encountered in the preparation of thinner wafers as surface tension caused formation of a lens shaped molten silicon mass rather than a flat thin layer.

Another approach not resulting in large wafers but possibly in long strips of solar cells is pursued by the Westinghouse Electric Corporation on a WADD contract.[19] This approach consists in the application of the dendritic growth method to silicon and the preparation of solar cells from these dendritic crystals. This growth method was very successfully used with germanium, and diodes and transistors were prepared from this material. Although not much information is available about the progress of this project, it appears that difficulties encountered earlier in the growing of the dendritic crystals or ribbons of silicon are being worked out. Some solar cells have been prepared from such dendritically grown crystals, and achievement of efficiencies as high as those obtained in solar cells prepared from single crystals grown by the Czochralski method have been reported.[20]

Another line of attack is the preparation of thin film solar cells. The obvious advantages of such an approach are the most conservative use of the costly silicon raw material, the possibility of readily preparing large area devices, and the possibility of obtaining flexible cells which should be capable of relieving some of the storage, transportation and deployment problems of extremely large area energy converters. There are, however, obvious difficulties connected with this approach, and it is questionable whether sufficiently large efficiencies can be obtained in order to make this approach competitive with the one pursued presently.

Thin Film Solar Cells

A thin film solar cell has a basic physical performance limit given by its thickness. This is due to the magnitude of the absorption coefficient which in silicon varies strongly with wavelength over the range of interest for solar energy conversion, as was shown in Fig. 7 of this paper. Since rather small absorption coefficients are found towards the longer wavelengths, only a small portion of the incident energy will be absorbed in thin films in these wavelength regions. Figure 14 shows that portion of the energy available in sunlight at wavelengths up to 1.1 μ, which can be absorbed in films of different

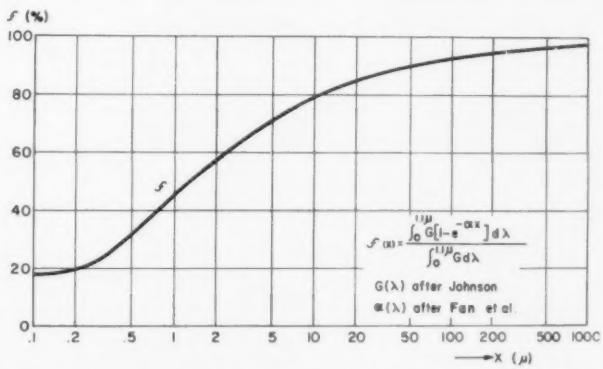

FIG. 14—Portion of the photons with energies greater than 1.1 eV which can be absorbed in silicon films of variable thickness x, based on the spectral distribution of sunlight outside the earth's atmosphere as described by Johnson, F. S., *Jour. Meteorology* **11**, pp. 431–439 (1954), and on the absorption coefficient of Fig. 7 of this paper.

thicknesses. The calculations leading to this curve were based on the spectral distribution of sunlight as received in free space[21] and on Fig. 7 of this paper.

Appropriate factors obtained from Fig. 14 have to be applied to the limit conversion efficiency as well as to the actually obtainable conversion efficiencies for silicon solar cells, if these are to be made from thin films. These data therefore give valuable design information for the thin film solar cell development.

Another limitation of yet unknown severity is to be found in the crystallinity of the thin films. It is most improbable that any reasonable degree of conversion can be obtained in solar cells of the p-n junction type prepared from amorphous films or films of very small crystal size. It should however be possible to utilize so-called surface barriers or metal to semiconductor junctions in order to obtain a certain amount of conversion. Another approach would be to obtain large crystals or even single crystalline thin films. Epitaxial growth and gradient cooling with seed attachment after melting or near melting of the film are two different approaches investigated for this purpose. Success has been met with certain epitaxial growth experiments using freshly etched silicon as a substrate.

Three different methods for the deposition of the silicon for the formation of the thin films have been or are presently under investigation. These three methods are: (1) vacuum deposition, (2) electrolytic plating, and (3) pyrolytic decomposition. Of these methods, only the latter one has met with reasonable success in the past. The major problem in the vacuum deposition method was again found in the high reactivity of the silicon with practically all known materials, which led to a contamination of the evaporation source by the crucible. A further problem was found in the contamination of the film from residual gases in the high vacuum. This problem could be partially overcome by a rapid deposition which, however, is not conducive to good crystal growth. Silicon carbide or carbon crucibles with silicon carbide surface layers were found to give reasonably good results for the deposition of very thin films. Good p-n junction devices could however not be formed by this method.

The electrolytic plating method did not lead to usable silicon films due to contamination from the solution. Best success was met with in the pyrolytic deposition of thin films. One frequently used pyrolytic process consists of the decomposition of silane on heated substrates in a hydrogen atmosphere. Large crystallites could be deposited on various substrates, and single crystal films were grown on single crystal silicon substrates. P-n junctions exhibiting good diode characteristics were formed by this method, and photovoltaic conversion was observed. Elliott from the General Electric Company reports[22] on work performed in his laboratory on deposition of thin films for the preparation of solar cells as performed under an ARPA contract.

The Composite Sphere Cell

A quite different approach has been conceived and pursued at the Hoffman Semiconductor Division[23] and is presently being continued under an ARPA contract.[24] It consists in the preparation of an array of silicon spheres each containing a p-n junction (Fig. 15). These p-n junctions are formed by a diffusion process performed on a large number of spheres simultaneously. The spheres are imbedded in a transparent plastic substrate and are connected by deposited metal films. These metal films form the ohmic contacts to the cells as well as provide a conductive path between the individual spheres. The process is quite intricate, but would lend itself readily to automation. The advantages of the method are seen in a possibility for the use of small particles of silicon obtained without the costly crystal growing and cutting processes, and in its potential for obtaining large-area and possibly mechanically flexible systems. The capability of the method has well been demonstrated, with 10% conversion efficiency achieved based on the total exposed area of the device. A major problem in the present approach is, however, the economical preparation of small silicon spheres.

PROGRESS ON SOLAR CELLS USING MATERIALS OTHER THAN SILICON

Various other approaches to the development of either highly efficient or more economical photovoltaic energy conversion devices have been pursued and have achieved mixed results.

The Gallium Arsenide Cell

Some work on the gallium arsenide cell has been performed by the RCA Laboratories[25] on a Signal Corps Contract, but major progress on this device cannot be reported, except for an improved understanding for the material problems. It appears now that the very short minority carrier lifetimes observed on gallium arsenide

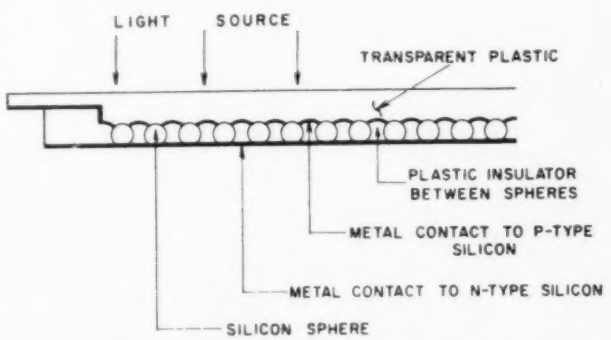

FIG. 15—Cross-sectional view of large-area solar cell composed of silicon spheres.

VOL. 5 1961

devices are not due to recombination centers which one has not been able to eliminate, but are rather due to a high level of direct radiative recombination present in this material.[26] These very small minority carrier lifetimes had earlier been found to be the limiting parameter in the performance of the gallium arsenide solar cells.

The Integrally Composed Variable Energy Gap Solar Cell

For the theoretical consideration governing the performance of the integrally composed variable energy gap photovolatic solar energy converter, reference shall be made to a previous publication.[6] The experimental work carried out at the Eagle Picher Research Laboratories on a Signal Corps contract[27] is basically an extension of the GaAs work, except for the addition of a wider energy gap layer to the active surface of the GaAs device, thus obtaining a variable energy gap in the transition region between pure GaP and pure GaAs. The p-n junction is formed in a separate diffusion process and can be located anywhere within or outside of this graded energy gap region. Different device characteristics have been obtained, depending upon the location of this p-n junction. Either larger open circuit voltages with relatively small short circuit currents were found with junction locations in the large energy gap region, or larger short circuit currents with open circuit voltages corresponding to those of a GaAs solar cell were obtained with p-n junctions located at the narrow energy gap side of the graded region. The latter approach is a sensible one for GaAs with its rapid increase of the absorption coefficient near the absorption edge, and with its extremely short minority carrier lifetimes leading to low collection efficiencies. Adding the wide energy gap layer causes deeper penetration of the photons and thus helps to obtain more generation of carriers within a diffusion length of the p-n junction. The results of the experimental work reported in Eagle Picher's Final Technical Summary Report are in agreement with the theoretical considerations outlined in ref. 6.

The Stacked Variable Energy Gap Solar Cell

Electro-Optical Systems, Inc. carried a research program on the stacked variable energy gap photovoltaic solar energy converter under Signal Corps sponsorship.[28] After earlier work utilizing the transmission of the longer wavelength radiation through a larger energy gap first cell and obtaining conversion of this longer wavelength radiation in a second cell of narrower energy gap mounted behind the first cell, the more recent approach at Electro-Optical Systems, Inc. used a dichroic mirror for splitting the incoming radiation into a long wavelength and a short wavelength component. The two components are separately incident on two solar cells having different energy gaps. The first approach was found by the Electro-Optical Systems, Inc. researchers to be rather disappointing, although some investigations carried out at the Semiconductor Division of Hoffman Electronics Corporation on the transmission of infrared radiation through silicon wafers with and without p-n junctions, and on a silicon-germanium stacked variable energy gap solar cell indicated that some feasibility of this approach may be shown. The latest work of Electro-Optical Systems, Inc. applying dichroic mirrors also did not lead to an improvement of the conversion efficiency above that obtained on silicon solar cells alone.

Thv Gallium Telluride Solar Cell

Efforts by the Armour Research Foundation carried out on a Signal Corps contract[29] with the objective of preparing single crystal gallium telluride material and of fabricating solar cells from this material has not progressed to the point where performing solar cells could be prepared.

The Cadmium Sulfide Solar Cell

The Harshaw Chemical Company performed extensive research on cadmium sulfide solar cells under Air Force sponsorship.[30] The art of growing single crystals of cadmium sulfide and of preparing solar cells from these crystals have been further perfected by these efforts. Solar cells with efficiencies in the 5 to 7% efficiency range have been repeatedly prepared. Simultaneously with these fabrication efforts, more insight has been gained into the very complicated and varied processes of photo-generation and of trapping of carriers, as they take place in cadmium sulfide crystals in dependence on variations of the contact materials and of the types of crystal impurities.

Beyond the single crystal effort, the research workers of the Harshaw Chemical Company prepared a number of 20 cm^2-large thin film cadmium sulfide solar cells.[31] They are presently in the process of perfecting the methods used for fabricating these film type cells. Overall efficiencies of 2 to 2.5% have been obtained on these films, but smaller areas showed efficiencies as high as 4.5%. It will be of great interest to follow the further progress of this work, which can possibly lead to a highly economical large area solar energy converter.

CONCLUSION

A review of the work performed on photovoltaic solar energy conversion shows that certain problem areas have been encountered, but that efforts of overcoming the difficulties are well under way. Beyond this, further improvements of the performance of the silicon solar cells have been achieved, which make better solar power panels feasible with 11% conversion efficiency in free space based on the total panel area. Work on other materials and new approaches resulted in some interesting

insights, but did not yet lead to any improvement of performance or economy.

REFERENCES

1. Williams, Richard and Bube, Richard H., "Photoemission in the Photovoltaic Effect in Cadmium Sulfide Crystals," *J. Appl. Phys.*, **31,** 968–978, June 1960.
2. Loferski, J. J., "Theoretical Considerations Governing the Choice of the Optimum Semiconductor for Photovoltaic Solar Energy Conversion," *Jour. Appl. Phys.*, **27,** 777–784, July 1956.
3. Prince, M. B., "Silicon Solar Energy Converters," *Jour. Appl. Phys.* **26,** 534–540, May 1955.
4. Wolf, M. and Prince, M. B., "New Developments in Silicon Photovoltaic Devices and Their Application in Electronics," published in "Solid State Physics in Electronics and Telecommunications," *Proceedings* of an International Conference held in Brussels, Belgium, June 2–7, 1958, **2,** 1180–1196, Academic Press, London and New York, 1960.
5. Prince, M. B. and Wolf, M., "New Developments in Silicon Photovoltaic Devices," *Jour. of the British Inst. of Radio Eng.*, **18,** 583–595, October 1958.
6. Wolf, M., "Limitations and Possibilities for Improvement of Photovoltaic Solar Energy Converters. Part I.," *Proc. IRE*, **48,** 1246–1263, July 1960.
7. F. S. Johnson, "The Solar Constant," *J. of Meteorology*, **11,** 431–439, December 1954.
8. Rauschenbach, Hans, "Understanding Solar Measurements, Part II," *Hoffman Semiconductor Product Application News* May–June, 1960, pp. 6–9, Hoffman Electronics Corporation, Semiconductor Division, El Monte, California.
9. Alan Rosen, "The Radiation Environment In The Interior Of A Space Vehicle," *Technical Report #STL/TN-60-0000-02196*, Space Technology Laboratories, Los Angeles 45, California.
10. A. Rosen, T. A. Farley, and C. P. Sonett, "Soft Radiation Measurements on Explorer VI Earth Satellite." Published in: "Space Research," *Proc. of the 1st International Space Science Symposium*, Nice, France, January 1960, Holland Publ. Company.
11. T. A. Farley and A. Rosen, "Charged-Particle Variations in the Outer Van Allen Zone during a Geomagnetic Storm," *Jour. of Geophysical Research*, **65,** 3494–3496, October 1960.
12. Paul Berman, "Radiation Damage In Silicon Solar Cells Using 750 keV and 2 MeV Electrons," delivered at meeting on "Radiation Damage to Semiconductors by High Energy Protons," Washington, D. C., October 1960, sponsored by NASA.
13. J. M. Denney, R. G. Downing, and A. Grenall, "High Energy Proton Damage," Internal Report, Space Technology Laboratories, Los Angeles, Calif., presented at the meeting on "Radiation Damage to Semiconductors by High Energy Protons," Washington, D. C., October 1960, sponsored by NASA.
14. J. J. Loferski and P. Rappaport, "The Effect of Radiation on Silicon Solar-Energy Converters," *RCA Review*, **19,** 536–554, December 1958.
15. Mandelkorn, J., Kesperis, J., McAfee, C., Pharo, W. and Schwartz, L., "Comparison of p-n and n-p Silicon Solar Cells," *Proc. 14th Annual Power Sources Conference*, 42–45, May 17–19, 1960; Power Sources Div., U. S. Army Signal Res. and Dev. Lab., Ft. Monmouth, N. J.
16. Contract #33(600)-40497: "Improvement of Silicon Solar Cell Efficiency," from Air Materiel Command, Manufacturing Methods Division, Electronics Branch, Wright-Patterson Air Force Base, Dayton, Ohio, to Hoffman Electronics Corp., Semiconductor Division, El Monte, Cal.
17. Bösenberg, Wolfram, "Kokillen Guss von duennen einkristallinen Germanium Platten," *Z.f. Angew. Phys. einschl. Nukleonik*, **9** (7), 347–349, 1957.
18. Contract No. DA 36-039 SC-85242, dtd 8-31-59, from the U. S. Army Signal Res. and Dev. Lab., Ft. Monmouth, N. J., to W. R. Grace and Co., Res. Div., Clarksville, Md.
19. Contract No. AF 33(616)-6612 from Wright Air Dev. Div., Dayton, Ohio, to Westinghouse Electric Corporation, Pittsburgh, Penn.
20. Private communication, R. K. Riel, Westinghouse Electric Co., Youngwood, Pa.
21. Johnson, F. S., "The Solar Constant," *Jour. Meteorology* **11,** 431–439, (1954).
22. Elliott, J. F. and Meikleham, Mrs. V. F., "Large Area Solar Cells," Paper presented at the Space Power Systems Conference of the American Rocket Society, Santa Monica, Calif., Sept. 27–30, 1960. Proceedings to be published.
23. Prince, M. B., "Large Area Silicon Solar Cells," *Proc. 14th Annual Power Sources Conference*, pp. 26–27, May 17–19, 1960; Power Sources Div., U. S. Army Signal Res. and Dev. Lab., Ft. Monmouth, N. J.
24. Contract No. DA 36-039 SC-85243 from U. S. Army Signal Res. and Dev. Lab., Ft. Monmouth, N. J., to Hoffman Electronics Corp., Semiconductor Div., El Monte, Calif.
25. J. J. Wysocki, J. J. Loferski, P. Rappaport and R. Williams, "High-Temperature, Improved Efficiency, Photovoltaic Solar Energy Converter," Contract No. DA 36-039 SC-78184, *RCA Sixth Triannual Report*, July 1960.
26. S. Mayburg, "Direct Recombination in GaAs and Some Consequences in Transistor Design," Presented at the Electro Chemical Soc. Meeting in Houston, Texas, October 9–13, 1960.
27. L. E. Stone, J. E. Powderly, W. E. Medcalf, "Investigation of Integrally Composed Variable Energy Gap Photovoltaic Solar Energy Converter," Contract DA 36-039 SC-85246, Final Technical Summary Report, October 10, 1960.
28. Second Semiannual Progress Report, Contract DA 36-039 SC-85244, "Investigation of Composite or Stacked Variable Energy Gap Photovoltaic Solar Energy Converter," from U. S. Army Signal Research and Development Laboratory, to Electro-Optical Systems, Inc., Pasadena, California.
29. ARF Final Report 1155-15, Contract DA 36-039 SC-85247, "Investigation of Single Energy Gap Solar Cell Material," from U. S. Army Signal Research and Development Laboratory, Ft. Monmouth, New Jersey, to Armour Research Foundation, Chicago, Illinois.
30. Fred A. Shirland, " Photovoltaic Cadmium Sulfide," The Harshall Chemical Company, *ARL Technical Report #62 93*, August 1960, Contract AF 33(616)-3466, Project #7116, Aeronautical Res. Lab., Air Force Res. Div., Air Res. and Dev. Command, Wright-Patterson AFB, Ohio.
31. Middleton, A. E., Gorski, D. A., and Shirland, F. A., "Evaporated CdS Film Photovoltaic Cells for Solar Energy Conversion," Paper #1291-60, presented at the American Rocket Soc. Space Power System Conference. Santa Monica, September 27–30, 1960.

VOL. 5 1961

Solar Radiation at the Earth's Surface

H. E. Landsberg

Office of Climatology, U. S. Weather Bureau

Longer records of annual solar radiation intensity on the horizontal surface are now available from over 300 locations. These have been incorporated into a new generalized world map of average solar energy received at the earth's surface. Greatest uncertainty exists over the oceans. Highest intensity centers are located around 22° latitude north and south on most continents. In North America the energy center of 35° N has the greatest poleward displacement.

The exploitation of solar radiation at the earth's surface has become more than a utopian dream. Devices to transform this energy into usable form are increasing in number and efficiency.

Strangely enough information on the energy income from this source is not readily obtained. Meteorological services have usually been content to measure the duration of sunshine. Cost of equipment to record the intensity of solar radiation and the expert care needed for this equipment have retarded progress in this field for many years. From the few meteorological stations where both radiation and duration of sunshine were recorded, statistical relations between these two variables were obtained. This permitted an estimate of solar intensity, in first approximation. In some areas not even this method could be used. Instead the duration of sunshine had first to be inferred from cloudiness observations, which were the only available indication of insolation. This was, and still is, particularly true for ocean areas.

It may seem quite surprising that solar radiation found such relatively little emphasis among meteorologists, who otherwise are known to be among the most prodigious data collectors. It might have seemed logical that they would concentrate their observational zeal on the quantities that energize the atmospheric movements. However, dynamic and kinematic principles gained an early foothold in this science and energetic concepts are only gradually being incorporated into the theory of atmospheric mechanisms and motions.

General climatological considerations and specific applications in agriculture and housing technology paved the way for more intensive study of solar energy at the earth's surface. The most comprehensive effort in recent years has been that of Budyko and his collaborators to chart, on a world-wide basis, the elements of the earth's heat balance.[5, 6] This resulted in an Atlas which appeared in 1955. Much of the information in this valuable work had to be based on indirect data and on calculations. In conjunction with the UNESCO Arid Zone Program, Black[4] (1956) had also prepared generalized world maps of radiation based on sunshine data.

In the last decade, however, in part stimulated by the desire to use solar energy in countries poor in other sources of power, measurements of solar radiation have multiplied. Another powerful impetus was given by the International Geophysical Year (IGY) and its subsequent cooperative world efforts in geophysics. One of the principal aims of the IGY was to learn more about the relations of our planet to the sun. The meteorological programs in all parts of the world were reinforced with solar radiation measurements. The data were collected under a uniform system arranged by the World Meteorological Organization[35] (WMO) and collected centrally.

This new information, in conjunction with the fewer but long-established series of observations permitted a new attempt to depict the radiation climate of the earth. This was aided by the fact that local radiation maps, based on new analyses of the available data appeared for several regions (U. S., U. S. S. R., Japan, North and South Africa, India). New summarizations of cloud cover over the major ocean areas of the world also appeared (U. S. Navy, 1955–1959).[31]

After making some reductions of shorter series to longer records and adjusting for different periods of record it seemed possible to draw a generalized map of radiation received at the earth's surface. At this time the attempt had still to be restricted to depict the sum of solar and diffuse sky radiation on a horizontal surface. This is the only element for which a sufficiently large number of measurements were available. Well over 300 stations record this element, but they are unfortunately far from evenly distributed. Some countries have much denser networks than others. Much as a compilation would have been desirable, the seasonal variation still remains quite uncertain in many places. Two to five

GENERALIZED ISOLINES OF GLOBAL RADIATION, SURFACE

kg. cal. / cm.^{2} / yr.

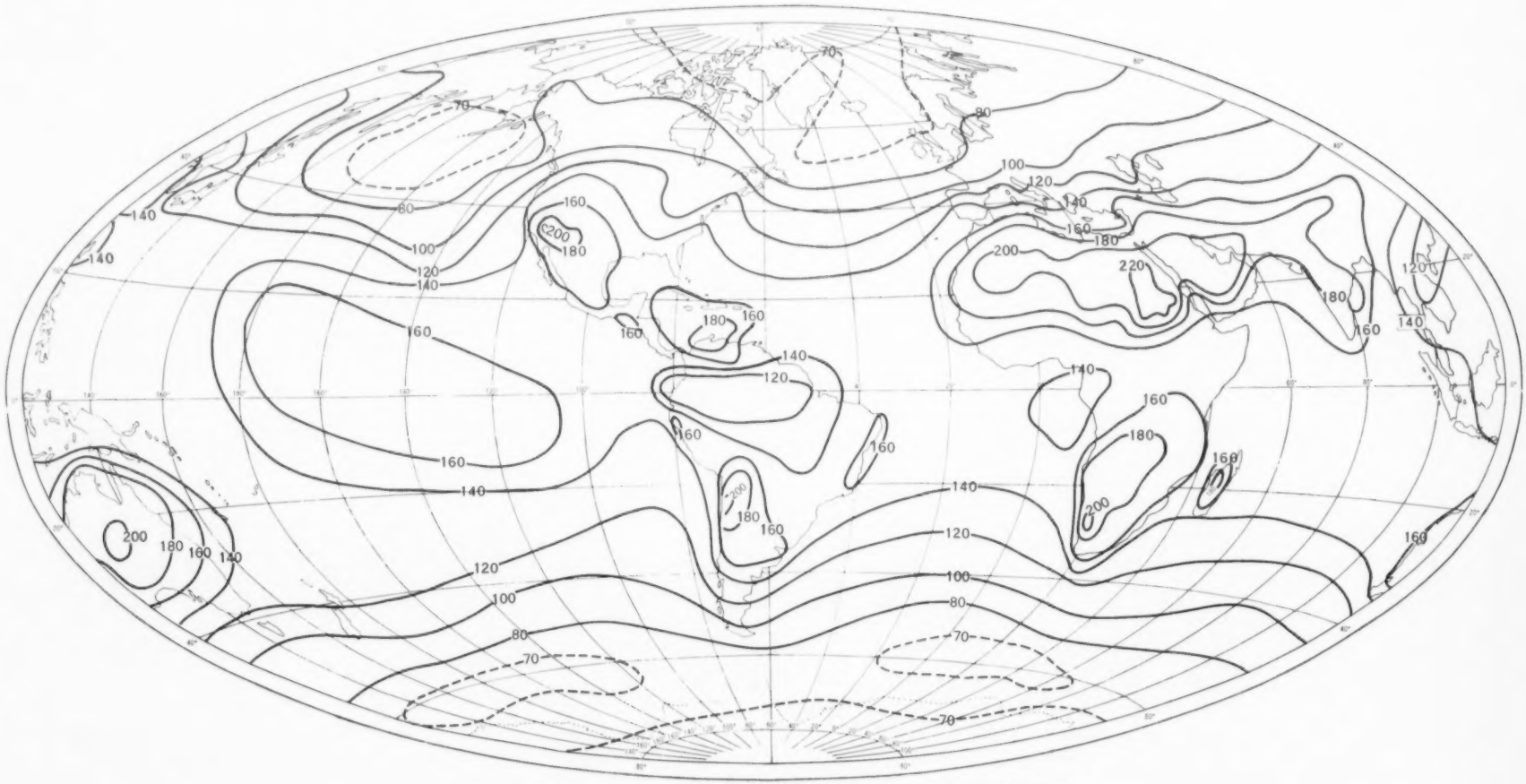

FIG. 1—Generalized isolines of global radiation, surface (kcal/cm²/yr)

TABLE 1—Latitudinal Distribution of Solar Energy Received on a Horizontal Surface at the Earth's Surface, According to Various Authors, in kcal/cm²/year

Latitude Zone	Budyko, et al., (1954)	Black (1956)	Landsberg (1961)	
			Mean	Range
N 90–80	—	—	65	?
80–70	—	—	70	68–72
70–60	—	—	72	68–85
60–50	91	83	85	68–110
50–40	114	111	117	68–140
40–30	146	139	135	90–200
30–20	163	157	159	115–220
20–10	163	158	152	120–220
10–0	149	149	148	120–170
S 0–10	150	148	145	120–180
10–20	156	152	150	130–190
20–30	152	147	145	120–200
30–40	130	123	123	110–170
40–50	104	92	100	80–135
50–60	83	63?	76	65–95
60–70	—	—	70	65–75
70–80	—	—	72	?
80–90	—	—	70	?

TABLE 2—Approximate Total Annual Heat Received in each Latitudinal Zone in 10^{18} kcal/yr.

	90–80	80–70	70–60	60–50	50–40	40–30	30–20	20–10	10–0
N	2.5	8.1	13.6	21.8	36.9	49.2	63.9	65.0	65.2
S	2.7	8.3	13.2	19.5	31.5	44.8	56.5	64.2	63.9

years of observations cannot yet be considered adequate for monthly averages. But the world pattern over land, on an annual basis, seems to be emerging now.

The results—approximately adjusted to the 1951–1960 decade—are shown in Fig. 1. The quantity shown is kcal/cm² (klangleys) per year. The primary interval is 20 units. All continents in the latitudes between 20 and 30 degrees show centers of high surface intensities of radiation. The extraordinarily extended field of energy reception, extending from the west coast of Africa through Arabia into India, is one of the earth's primary heat sources. The North American heat center in the southwestern U. S. appears to be the most poleward located major radiation center.

Budyko, Berlyand and Zubenock[6] (1954) gave a broad view of the latitudinal distribution of energy received at the surface of the earth between latitudes 60 north and south. Burdecki[7] (1958) contrasted this with data from Black[4] (1956). From our compilation a new set of values from pole to pole were derived. All these estimates are shown in Table 1. The reliability of the column derived from Fig. 1 and its underlying data is, however, probably not better than about ±5 units. The range for each latitudinal zone is also given.

The current data are generally lower than Budyko's but not much beyond the estimated level of reliability. The discrepancies are primarily caused by different estimates of oceanic cloudiness. These are still very conjectural but this problem will be solved when consistent and complete observations from satellites become available. The systematically lower values for the southern hemisphere compared with corresponding northern latitudes is also partly attributable to lack of precise oceanic information. However, there is enough evidence to consider it a reality, even though the precise magnitude of the difference between the two hemispheres is uncertain.

These zonal variations give only the grossest picture of the energy distribution. Even on an annual scale, there remains considerable topographically and orographically induced variation. The areas within the 160 kcal/cm²/yr line seem to be the ones where solar energy is important in the earth's heat balance. Even though some of them show seasonally low values, they are also the regions where exploitation of solar energy would be most practical.

From a meteorological point of view it is interesting to note the total radiation received at the surface for each zone. This quantity is shown in Table 2. This is as yet a quantity unmodified by the surface albedo. It gives nevertheless a good measure of the enormous heat transactions that go on at the earth's surface.

The asymmetry of the two hemispheres is quite apparent. Also very notable is the high value in the subtropical belt of the Northern Hemisphere (20–30°N). This almost matches the energy received in the equatorial zone, even though the total area of this higher latitude zone is less.

REFERENCES AND SOURCES OF INFORMATION

1. Albrecht, F., "Jahreskarten des Wärme- und Wasserhaushaltes der Ozeane," *Ber. d. deut. Wetterdienstes* **9**(66), 1800 (1960).
2. Barashkova, E. P., "Certain Regularities in the Regime of Total Radiation, Leningrad," *Glav. Geofiz. Obs. Voeik. Trudy* **80,** 51–69 (1959), Translation by I. A. Donehoo, U.S.W.B. Washington, D. C., 21 p.
3. Berliand, T. G., and Efimova, N. A., "Mesiachnye karti summarnoi solechnoi radiatsii i radiatsionogo balansa territorii Sovietskogo soinza," *Glavnia Obs. im. Voeikova Trudy* **50,** 40–82 (1955).
4. Black, J. N., "The Distribution of Solar Radiation Over the Earth's Surface," *Arch. Met. Geophys. Biokl. B,* **7,** 165–189, (1956). also: "Wind and Solar Energy," UNESCO, Arid Zone Research VII, 138–140.
5. Budyko, M. I., "Atlas Teplovogo Balantsa," *Leningrad Glav. Geofi. Obs. im. Voeikova* (1955).
6. Budyko, M. I., Berlyand, T. G., and Zubenok, L. I., "The Heat Balance of the Earth's Surface," *Izvest. Akad. Nauk. S.S.S.R., Ser. Geog.* No. 3, 17–41 (1954).
7. Burdecki, F., "Remarks on the Distribution of Solar Radiation Over the Surface of the Earth," *Arch. Met. Geophys. Biokl. B* **8,** 326–335 (1958).
8. Bossolasco, M., and Castagnoli, B., "La Radiazione Globale a Genova," *Geofis. e Meteorol.* **4**(6) (1956), 6 p.
9. Chagnon, Jr., S. A., "Summary of Weather Conditions at Champaign-Urbana, Illinois," *Bull. 447 Ill. State Water Survey,* (1959), 95 p.
10. Drummond, A. J., and Vowinkel, E., "The Distribution of Solar Radiation Throughout Southern Africa," *J. Meteorol.* **14,** 343–353 (1957).
11. Dubief, J., *Le Climat du Sahara,* Univ. d'Alger, Inst. Recherches Sahariennes, Vol. I. (1959), 312 p.

12. Dupont, G., and Schüepp, W., "Le rayonnement Solaire à Leopoldville," *Publ. Serv. Met. du Congo Belge No. 3* (1952), Bruxelles.
13. Fleischer, R., "Vier Jahre Strahlungsbilanz-Registrierungen am Meteorologischen Observatorium Hamburg," *Ber. d. deut. Wetterdienstes* **7**(51), 9–13 (1959).
14. Hinzpeter, H., "Studium zum Strahlungsklima von Potsdam," *Veröff. Met. Dienst. d. deut. dem. Republ.* No. 10, (1953) Berlin.
15. Lebedev, A. N., "Klimat SSSR, Vyp. I. Evro peiskaia Territoriia SSSR, Leningrad 368 p. (1958) (see p. 24).
16. Lindholm, F., "Die Globalstrahlung in Stockholm," *Arch. Met. Geophys. Biokl.* **9**, 292–301 (1958).
17. Lippmann, H. S., "Means of Daily Solar Radiation for United States Stations," *Weekly Weather and Crop Bull.* **46**(7), 7–8 (1959).
18. Mateer, C. L., "A Preliminary Estimate of the Average Insolation in Canada," *Canad. Journ. Ag. Sci.* **35**, 579–594 (1955).
19. McQuigg, J. D., and Decker, W. L., Solar Energy, A Summary of Records at Columbia, Missouri, Ag. Exp. Sta., *U. of Missouri Res. Bull.* 671, (1958) 27 p.
20. Morais, J. C. de, "Radiacao Global e Insolacao em Coimbra," *Publ. U. de Coimbra*, (1959) 12 p.
21. Nicolet, M. and Dogniaux, R., "Etude de la radiation global du soleil," *Mem. Inst. R. Met. Belg.* 48 (1951).
22. Nelson, C. E., and Domingo, C. E., Data on Weather from 1924–1957 at the Irrigation Experiment Station near Prosser, Washington, *Wash. Ag. Exp. Sta. Bull.* 593, (1958) p. 19.
23. Noffsinger, T. L. and Nunns, F. K., Water Requirement of Field Crops Estimated from Total Solar Radiation, *Bull. Am. Meteorol. Soc.* **41**, 403–405 (1960).
24. Prohaska, F., "Die Globalstrahlung in Davos," *Gerl. Beitr. z. Geophys.* **59**, 247–275 (1943).
25. Ramdas, L. A., and Yegnanarayanan, S., Solar Energy in India, "Wind and Solar Energy," *UNESCO Arid Zone Research VII*, 188–195 (1956).
26. Rusin, N. P., "Radiatsionnyi balans snezhnoi poverkhnosti v. antarktide," *Bull. Antarkt. Eksped. No. 2*, 25–30 (1958).
27. Schüepp, W., Le rayonnement solaire a Stanleyville, *Serv. Met. du Congo Belge, Publ. No. 6* (1955).
28. Tarnishewskii, B. V., "Kadastr Pyranoi Solnechnoi Radiatsii Chetbirkh Punktov Turkmenistana," *Ak. Nauk Turkmen Trudii (Fis. & Geofis)* **4**, 33–49 (1958).
29. Uchijima, Z., "A Physico-Climatological Study of the Water Temperature in the Paddy Field," *Bull. Nat'l. Inst. Ag. Sci. (Japan), Ser. A. No. 7*, 131–181 (1959).
30. Verle, E. K., and Svinukhov, G. V. (1960), "Radiation balance in the Primorskiy Kray Region, *Leningrad Trudy Daln. Nauch.-Issl. Gidromet. Inst.* **6**, 30–43 (1960). transl. by I. E. Donehoo, U.S.W.B. Washington, D. C.
31. U. S. Navy; Marine Climatic Atlas of the World:
    Vol. I NAVAER 50-1C-528 (1955)
    Vol. II NAVAER 50-1C-529 (1956)
    Vol. III NAVAER 50-1C-530 (1957)
    Vol. IV NAVAER 50-1C-531 (1958)
    Vol. V NAVAER 50-1C-532 (1959)
32. Austral. Commonwealth Bureau of Meteorology, Australian Radiation Records.
33. Institut pour la recherche scientifique en Afrique Central —Rayonnement Solaire AGI.
34. Institut R. de Belgique, Station Uccle, Rayonnement au cours de l'AGI et au cours de la CGI.
35. WMO records of solar radiation for IGY and IGC.

VOL.
5
1961

Plastic-Replica Mirror Segments for a Solar Furnace

J. Bolin, C. J. Tenukest and C. J. Milner

School of Physics, The University of New South Wales, Sydney, Australia

A paraboloidal mirror, 12 ft in diam and of focal length 47 in., is built up from 162 segments arranged in six concentric zones. Segments for each zone are cast in epoxy resin, using as matrix one of six glass plates optically worked to convex off-axis paraboloidal form. In order to avoid distortion and wrinkling of the final surface, due to shrinkage and other causes, three successive coatings of resin, each using a different filler and curing schedule, are applied to a stout cast-aluminum backing plate. To part the casting from the matrix (which is especially difficult because of the accuracy of copying that is attained) a silicone release agent is used, which is effective when applied as an extremely thin film. The final casting is front-surface-aluminized by vacuum evaporation.

A parallel beam of light formed by one such segment (approx. 12 in. × 10 in.) may be refocussed by another segment, suitably placed, to an image less than $\frac{1}{20}$ in. in diam. The surfaces formed by this process are hard and permanent, and numerous optical and mechanical uses are foreseen.

INTRODUCTION

In a solar furnace, light and heat from the sun are concentrated by an optical system to such an extent that the temperature of any object placed at the focus is raised to a temperature comparable with the sun's surface temperature. Many workers have employed disused searchlight mirrors for this purpose; but the attainment of extreme temperatures, say about 3000 C, requires a mirror, or other concentrating system, both larger in diam and more perfect in form than that used in searchlights, or indeed in any large system other than the great astronomical telescopes. While the optical perfection of astronomical mirrors is far beyond what is required in a solar furnace, still in the latter a large numerical aperture is also very desirable, certainly much larger than the values encountered in astronomical instruments.

Several large solar furnaces, which are larger than searchlight size and not limited by the imperfections of searchlight mirrors, have recently been constructed. In all of these furnaces, the concentrating system has used a number of segments. Details of several furnaces are given in Table 1.

While planning a large solar furnace[1] now in course of construction at Kensington, Sydney (Table 1) the present authors and colleagues decided to employ a replica method to produce all the sectors of each zone of the paraboloid. Prolonged efforts were devoted to preparing a single set of accurate "matrix" plates, and at the same time various techniques were explored that might enable accurate copies of these negatives (negative in the sense that concave replicas were made from convex matrices) to be made with reasonable ease, reliability, and safety to the matrices.

The production of matrix plates and replicas is further described below; this introduction will conclude with a review of the requirements for accuracy in the optical system of the solar furnace in general, and in the paraboloid segments in particular.

The sun subtends an angle of $\frac{1}{115}$ radian or almost exactly 0.5°; the sun's image formed by the paraxial part of a single concave mirror therefore has a diam of f/115, where f is the focal length. Maximum heating will obtain only over the smaller circle within which the images of the sun produced by all mirror elements overlap. To ensure that this overlap circle is little smaller than the paraxial image circle, it has been determined that the combined effect of the several errors of alignment must be kept less than three minutes of angle ($\frac{1}{10}$ of the image diam). In particular, the aim throughout the present development work has been that each portion of the surface of each replica segment shall produce reflected rays parallel to those from an ideal paraboloid segment within one to two minutes of angle.

PREPARATION OF MATRICES

Experimental work was essential to ascertain the possibilities of making the master plates or matrices envisaged by the design. It was attempted in complete absence of any literature on the subject. Known figuring techniques for making off-axis sections of paraboloid are practicable only as long as the sections are near the axis. In our case the sagittal values required for the final curve were beyond the reach of local correction by polishing. For example, the component for the outermost zone, 10 in. in radial width, commences 62 in. from the paraboloid axis: the curvature radius in the "radial"

TABLE 1—Details of Certain Large Solar Furnaces

Location	Concentrator		Segments	
	Over-all diam (ft)	Angle subtended at focus (degrees)	Number	Type
California Institute of Technology	c.7	c.90	19	Optically-worked glass lenses
Montlouis, France	c.33	c.90	c.4000	Bent metallized glass
Bouzareah, Algeria	27	120	144	Moulded and electro-polished aluminum
Kensington, Sydney	12	150	162	Plastic replicas of optically-worked glass

plane containing the axis has to vary from 188.0 to 166.2 in., and that in the "transversal" plane, at right angles to the radial, from 118.3 to 113.5 in.

The first trial convex surface was ground, figured and polished entirely by hand. However, this work evaluated certain possibilities for use of machines specially constructed for the purpose. The image formed by reflection from this surface through the polished plane back of the plate was found satisfactory even when examined with the 40 mm orthoscopic eyepiece. Further to assess the chances of satisfying the design tolerances, a concave surface of the same zone was completed. This also produced a sharp image of the sun, of size very close to the theoretical value. With this encouragement, work was commenced on master plates for each of the six zones into which the paraboloid was divided (144 in. rim diam, with 18 in. central hole).

Sets of precision glass templates had been made and used for verifying the first convex surface, but these were replaced by a precision 6-in. cylindrometer with dial gauge reading to 0.0001 in. The computed elements of each zone were converted into sagittal values at intervals of 0.5 in. Cylindrometer readings were taken by two workers independently. The mean readings, plotted for comparison with curves of the required values, formed the sole means of assessing the generated radii during grinding and figuring.

Pyrex of suitable quality and thickness was not available. Very careful consideration was given to the manner of supporting the glass plates used, which were 14 × 14 in. and only 1 in. thick. Although, with precautions, these dimensions were acceptable for the tolerances involved, it is obvious that use of low-expansion glass of greater thickness would result in better surfaces.

For rough grinding, conventional machines were used, with grooved glass tools. Systematic reversal of the surfaces during grinding assisted the smooth fit of the curves. For converting the spherical surface to toric form, special adaptations of existing machines were made. Speed was reduced.

Figuring was done by handwork alone. Adjustable tools were made by cementing small glass squares (0.4 × 0.4 × 0.15 in.) with a layer of rosin of uniform thickness and controlled viscosity to a steel base plate machined to a curvature roughly concentric with the worked surface. Hot pressing was repeated until the glass facets all attained contact with the workpiece. The spells of figuring were often reduced to only one minute, after which hot pressings were repeated. This not only prevented gross deformations through unequal wear but also enabled adjustment of the tool for changes developing in the corresponding area of the job.

The final smoothing was also manual, machine work presenting too many dangers of flattening the figured curves. Rosin laps and finely-washed abrasives assisted detection of high and low spots. Contact cylindrometer testing was indispensable, thousands of readings being taken on each plate. Precautions against zero errors due to wear of the ball points, etc, were necessary.

The polishing in general followed a pattern suggested by the experience of figuring and smoothing the particular plate. Machine action was unavoidable because local work and general blending required at least 40 hours per plate. To reduce the fine pattern of "hairlines" the policy of changing the laps and the superimposition of strokes was strictly observed. A hand-worked lap, nearly dry, usually completed the final retouching.

SELECTION OF PLASTIC TECHNIQUE

In selecting a technique for making plastic replicas from glass matrices, three processes were considered. They were hot pressing, hot casting and cold casting.

Hot pressing

Two materials, polystyrene and methyl methacrylate, seemed to be suitable. As the former was not available in Australia, the latter was used for trials. Temperatures of 120–130 C were found necessary to soften this material suitably. At these temperatures, glass plates used as trial matrices sometimes cracked and blistering of the plastic surface occurred. These difficulties were not overcome and as the required accuracy was not achieved this process was abandoned.

Hot casting

The high temperatures necessary in this process cause distortion due to thermal expansion and endanger the glass matrices. As plastic materials, which polymerize at room temperatures, were available this process was not further considered.

Cold casting

Polymerization of methyl methacrylate monomer on the glass matrices was tried. The surfaces so produced were excessively rippled, and this material was therefore

VOL. 5 1961

abandoned. Finally epoxy resin was tried which provided a satisfactory solution. It has the advantages of availability, cold cure, low polymerization shrinkage ($2\frac{1}{2}\%$ as compared with 12–30% for other resins), and high luster; and it can be vacuum coated. No expensive or complicated equipment is required for processing, and much information was available from the manufacturers.

DEVELOPMENT OF EPOXY-RESIN CASTING PROCESS

The main difficulties encountered were in producing reliable release in conjunction with high luster and freedom from ripples and distortion. As the surface actually copied is that of the release agent, it must be very uniform in thickness if the replicas are to be accurate copies of the matrix. This means in practice that it must be very thin and completely reliable in release if the matrix is to be preserved intact.

During an investigation extending over a period of two years many substances were tested as release agents with only partial success. None of them provided reliable release when applied in sufficiently thin layers. Substances tested included waxes, petroleum jelly, cellulose acetate, methyl methacrylate, soap, glycerine, oils, lanolin, stearic acid and molybdenum disulphide, as well as many industrial releasers.

A method due to Hass and Erbe[2] was then tried. This requires the matrix to be coated with silver, silicon monoxide, and aluminum, in that order, by evaporation in vacuum. The resin, with filler added to reduce shrinkage, is cast on this surface in a single layer. Release takes place at the plane of the silver layer, part of which may remain on the matrix and part on the replica. Residual silver is removed with acid and leaves an aluminum coating protected by silicon monoxide. This process, which showed considerable promise, was given an extensive trial. In the authors' experience with this and other epoxy-resin processes, use of a suitable filler was essential in order to secure a tolerably small large-scale distortion; however, the free surface of a coating made with filled resin was generally found to be, or to become, covered with small-scale ripples of a wavelength comparable with the filler grain size. Coatings of pure resin were reasonably free of ripples, but distortion of figure was relatively severe, presumably due to shrinkage in setting of the resin, which, even with thin layers, is capable of distorting even robust backing plates.

In this dilemma attention was turned to the possibilities of multiple coats using a thick heavily-filled initial coat and a thin unfilled final coat. Consequently work with the Hass process, which essentially provides for only a single coat, was discontinued. In the further investigation which was undertaken, dimethyl-dichloro-silane, a substance which forms a silicone with the free water usually present on the surface of glass, was tried as a release agent and a satisfactory process[3] was evolved based on its use.

Supplies of pure dimethyl-dichloro-silane were not available in Australia and an I.C.I. product, "Silicone liquid M441," which contains some unhydrolyzed methyl-chloro-silanes, had to be used. A suitable technique for its use was developed. The coating so produced on the matrix gives 100% effective release and is virtually unwettable. It is so thin that it cannot be detected by either visual or optical means. This technique made a multiple coat process feasible, and a three coat process was finally developed which gave results well in excess of the minimum requirements. The luster is such that the reflectance of the aluminum coated surface is only some 3% lower than that of similarly coated glass.

PREPARATION OF CASTINGS

In order to provide for fittings for aligning and adjusting the finished segments, and to save work in the casting process, cast aluminum backing plates strengthened with ribs were used. The inner surface of the pattern was given a spherical curvature approximating that of the segment, in order to keep the thickness of the resin coat as even as possible. Castings were thoroughly cleaned before use.

The matrix was thoroughly cleaned and given a coat of release agent (I.C.I. M441 10% in acetone) with a cotton wool swab. A jig, placed over the coated matrix, held accurately in place a "model", made accurately to the dimensions of the final segment and around which were formed walls of plastic strip $\frac{1}{16}$ in. thick held in place by a wooden frame and sealed with beeswax. The "model" was then removed and replaced by the backing plate. A mixture of resin and filler ("Mix A" of Table 2) was now poured onto the surface of the matrix and the backing plate lowered into it, care being taken to avoid trapping bubbles. It was then secured in position by a jig.

After standing overnight the casting had hardened. The jigs and mould walls were removed from the casting and the casting removed from the matrix. The casting was baked in an oven (8 hr at 80 C) to stabilize it.

The stabilized casting was then cleaned and roughened on the front surface, and placed face up in a jig. The edges were coated with wax to prevent resin from subsequent coats from sticking. The matrix was cleaned and coated as before, but was afterwards allowed to stand 2–3 min and then washed down with mineral turps and allowed to dry.

Sufficient of "Mix B" (Table 2) was placed in the center of the casting, care being taken not to trap any bubbles, and the matrix carefully lowered, face down, into the pool of "Mix B." A single drop of "Mix B" placed on the center of the matrix helps to prevent

TABLE 2

Mix A

100 parts resin (Shell "Epikote 815")
166 parts marble dust (300 mesh)
25 parts curing agent (Shell "Epicure U")

Mix thoroughly and allow to stand until free of large and medium bubbles.

Thickness of first layer 2–5 mm

Mix B

100 parts resin as above
50 parts lamp black (particle size 1–5 microns)
15 parts curing agent (Shell "Epicure U")
3 parts curing agent (Shell "Epicure A")

Mix the lamp black thoroughly with the resin and allow to stand until free of bubbles. Heating may help.

Add the curing agent and mix thoroughly without introducing bubbles.

Thickness of second layer about 0.5 mm

Mix C

100 parts resine as above
17 parts curing agent (Shell "Epicure U")
3 parts curing agent (Shell "Epicure A")

Allow ingredients to stand until free of bubbles. Pour curing agent into resin carefully avoiding bubbles. Mix thoroughly without introducing bubbles.

Thickness of final layer about 0.05 mm.

bubbles being trapped. The matrix was allowed to rest on the thin layer of "Mix B", being kept in place by a jig. The surplus resin was allowed to run over the edges. The coating was allowed to cure overnight and then treated as the first coat, except for the walls.

The matrix was again cleaned and coated with release agent as before, except that it was washed after coating first with mineral turps and then with detergent and water, and rinsed with water. Any drops of water remaining were carefully removed with blotting paper. This removed the surplus release agent and ensures that the surface is clean and that the final surface of the casting is of a high luster.

The final coat of "Mix C" (Table 2) was then cast in the same manner as the second coat, except that the matrix and the casting were heated to 45–50 C before coating. When removed from the matrix the castings were rinsed with water, all remaining drops being carefully removed with blotting paper. They were then placed, without further cleaning, in the vacuum chamber. All work was carried out at a room temperature of 20–22 C maintained by air conditioning.

METALLIZING AND TESTING

The surface of the casting is given an opaque coating of aluminum in vacuum in the normal way. The surface is very clean and very little discharge cleaning is required; this is kept to a minimum to prevent surface heating. After metallizing, the edges of the segments are cleaned up and the segment tested optically by an autocollimation method for satisfactory performance. The segments are placed in a jig which holds them accurately in the correct position. Light passing through a small aperture in a screen at the focal point, falls upon the paraboloidal mirror segment and is converted to a parallel beam. A plane mirror placed in the path of the parallel beam, reflects it back on to the same screen, forming an image of the aperture a little to one side. This is a critical test and is necessary if the segments in each zone are to be interchangeable and to align correctly when assembled.

CONCLUSION

Production of mirrors for the Kensington solar furnace is now complete. Tests over the past 18 months have shown that, with careful washing when necessary to remove accumulated dirt, reflectance is well maintained at about 80%. The surfaces appear to be both permanent and sufficiently hard for at least light wear.

It has been fully established that high-grade mirrors of off-axis paraboloidal or other aspheric form can be made by repetitive casting from optically-worked glass, in sizes up to at least 10 or 12 in. square and in number up to at least 50. (The glass master plates are still serviceable if not quite unmarked after production of up to this number of replicas.) Where the original preparation of such a surface, whether as a master plate or for direct use, may cost hundreds of pounds, the provision of replication facilities, also costing hundreds of pounds, will enable replicas to be made at a repetition cost of only tens of pounds each.

The present process for replicating surfaces should therefore be economically attractive in several fields where amounts of this order are expended on producing single surfaces. In particular, it might be usefully considered in relation to engineers' surface plates, perhaps even lathe beds, etc, as well as for large optical components particularly for infrared use.

ACKNOWLEDGMENT

The authors wish to thank most warmly Mr. R. Urquhart for constant skilled assistance in both the optical and plastic work here described.

REFERENCES

1. Giutronich, J. E., Milner, C. J., and Symonds, R., (to be published)
2. Hass, G., and Erbe, W. W., *J. Opt. Soc. Amer.* **44** (9) 669, (1954).
3. The patent rights for this process are held by Unisearch Limited, a company established by The University of New South Wales to undertake research for industry and to exploit patents arising out of the work of the University.

VOL. 5 1961

Atmospheric Radiation Near the Surface of the Ground: A Summary for Engineers*

Raymond W. Bliss, Jr.

Solar Energy Laboratory, Institute of Atmospheric Physics, The University of Arizona, Tucson, Arizona

A procedure for estimating the intensity of atmospheric radiation upon horizontal surfaces is presented in detail, together with results of the calculations for typical atmospheric conditions. Hottel's values for water-vapor emissivity, together with an extrapolation by the author, are used as a starting point for the calculations. Resulting values of atmospheric radiation are found to be a little higher than those usually found by meteorologists. The procedure is considered adequate for most engineering problems requiring an estimate of the intensity of atmospheric radiation upon horizontal surfaces near ground level.

PRINCIPAL SYMBOLS USED†

A Intensity of radiation from atmospheric gases incident upon a horizontal plane near ground level, mly/min.

f_p Pressure correction factor, dimensionless.

I_λ Spectral intensity of radiation per unit of wavelength, mly/min-cm.

K Exponential absorption coefficient, sq cm/g.

L Path length, cm.

m Density-length product ρL, g/sq cm.

M Molecular weight, g/mol.

P Pressure, atmospheres.

q Radiation intensity incident on or emitted by a surface, mly/min.

- q_b emitted by a black body in solid angle 2π steradians
- q_g intensity of gas radiation upon a surface.
- $q_{\Delta\lambda}$ intensity in a finite range of wavelengths of width $\Delta\lambda$.
- q_{sun} intensity of sunshine upon a horizontal surface.

R Net radiation exchange between atmospheric gases and an exposed thermally black horizontal surface at air temperature, mly/min.

t, T Temperature, °C or °K.

Z Height, cm.

β, γ Exponential coefficients, sq cm/g or cm^{-1} as indicated in text.

ϵ Emissivity, dimensionless

- ϵ_a apparent emissivity of the atmosphere.
- ϵ_s emissivity of a slab.
- ϵ_λ spectral emissivity.
- $\epsilon_{\Delta\lambda}$ weighted average spectral emissivity over a finite wavelength range.

θ, ϕ Angles, radians.

λ Wavelength, cm.

ρ Density, g/cc.

σ Stefan-Boltzmann constant = 8.13×10^{-8} mly/min − $°K^4$.

ω Solid angle, steradians.

INTRODUCTION

A clear sky seems "colder" than the air temperature near the ground. Farmers, air-conditioning engineers, and designers of solar heat collectors are well aware of this. The farmer, noting frosts which occur on a clear night even though the air temperature remains well above the freezing point, rightly ascribes these frosts to the "cold" sky. The air-conditioning engineer knows that the temperatures of roofs and other surfaces exposed to the sky fall below prevailing air temperatures at night, and he sometimes takes this effect into consideration in calculations and in building design.

The designer of solar heat collectors is aware that this "cold sky" effect exists in the daytime also. It causes his collectors to have a higher-than-expected loss rate, particularly when they are set near horizontal and operating at or near prevailing air temperature.

This situation is illustrated schematically in Fig. 1. An idealized thermally black collector surface near ground level and at the temperature of the surrounding air is receiving and absorbing solar energy (direct and diffuse) at the rate q_{sun} per unit area of the surface. By a thermally "black" surface we mean a surface whose emissivity and absorptivity are unity for all wave-

* This work was supported in part by The National Science Foundation (Grant #G-6293) and in part by the State of Arizona.

† The unit of heat transfer per unit time and area used in this article is the milli-langley/minute, abbreviated mly/min. A langley is defined as equal to one gram-calorie/sq cm. Consequently 1 mly/min = 1 milligram-calorie/sq cm-min. The conversion to English units is 1 mly/min = 0.221 Btu/sq ft-hr.

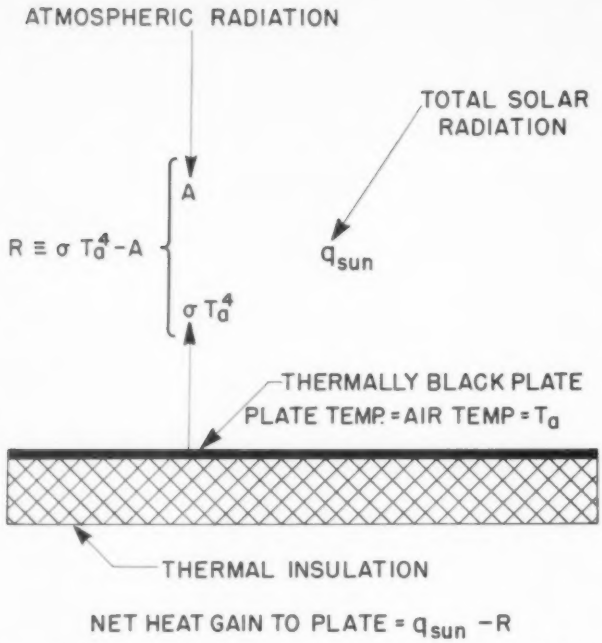

FIG. 1—Radiant energy exchanges between the sky and an exposed thermally black plate at air temperature.

lengths. Because it is at the same temperature as the surrounding air the surface does not lose heat by convection to the air; nevertheless it exhibits a radiation loss rate R in the far infrared. This loss rate R is actually the difference between the black-body radiation σT_a^4 emitted by the surface and the incoming longwave atmospheric radiation A which is striking the plate.

Under clear sky conditions this loss rate R—that is, the net longwave radiation exchange between a horizontal thermally black surface and the sky when the surface is at air temperature—is typically in the range of 100 to 150 mly/min (about 20 to 30 Btu/sq ft-hr). Since the intensity of solar radiation striking a solar heat collector is seldom greater than 1500 mly/min, and often more like 1000 mly/min, it is evident that this loss rate R is large enough to merit consideration and understanding in problems of solar heat collector design.

In order to determine R, one must know the magnitude of A, the intensity of atmospheric radiation upon a horizontal surface near ground level. It is the purpose of this article to discuss this facet of atmospheric radiation, to explain in reasonable detail the procedures for calculating its magnitude, and to present the results of the calculations in a form convenient for use by heat-transfer engineers concerned with the design of solar heat collectors or by others who may have need for a good engineering approximation of the intensity of atmospheric radiation under given conditions. Attention will be centered chiefly upon atmospheric radiation from cloudless skies, although the effects of clouds will be mentioned briefly.

It is believed that the methods and results presented are adequate for the intended purpose, but it should be emphasized that this article is essentially an engineering simplification of what is in fact an extremely complicated problem in radiative heat transfer.

GENERAL NATURE OF ATMOSPHERIC RADIATION

Atmospheric radiation originates from gases in the air, some of which absorb and emit radiation in the far infrared range. This range we will arbitrarily define as encompassing wavelengths between 3 and 100 microns.

Since the atmosphere as a whole is composed of about 99% (by volume) oxygen and nitrogen, one might guess that the bulk of atmospheric radiation originates from these gases. However, this guess would be quite wrong. Oxygen and nitrogen, and other symmetrical gas molecules, do not absorb or emit radiation in the far infrared; they seem to be completely transparent to such radiation. Atmospheric radiation originates from water vapor, carbon dioxide, ozone, and other asymmetrical molecules which occur in the atmosphere.

Insofar as atmospheric radiation at ground level is concerned, only radiation from water vapor and carbon dioxide is of any importance, with that from water vapor being much the more important of the two. At ground level the proportion of water vapor in the air ranges from about 0.2% to 2% by volume, depending upon the relative humidity and temperature, and this proportion usually decreases with increasing altitude. The proportion of carbon dioxide in the atmosphere is about 0.03% by volume, and this proportion is relatively constant throughout most of the atmosphere. It is interesting to note that it is only the presence of the small amounts of these two gases which prevents the atmosphere from being completely transparent in the far infrared. If the air were completely dry and completely free of carbon dioxide, the mean radiant temperature of the sky at night would be very near the absolute zero of outer space, or about 290 centigrade degrees below typical air temperature at ground level. As we shall see, the presence of these two gases and their radiation effects causes the actual mean radiant temperature of a clear night sky to be usually only about 10 to 25 centigrade degrees lower than the prevailing ground air temperature.

Our problem in determining radiation from the atmosphere to a surface near ground level is essentially that of determining the radiation to be expected from the gaseous mixture of water vapor, carbon dioxide and nonradiating gas overlying the ground. Matters are complicated by the fact that the composition, temperature, and pressure of this mixture vary with height above the ground.

VOL. 5 1961

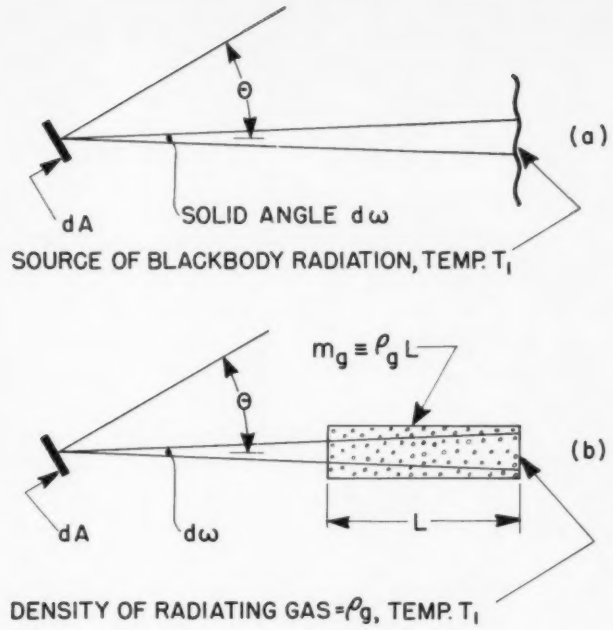

FIG. 2—Radiation from column of gas.

As a prelude to attacking the problem, we review some basic concepts and definitions.

BASIC CONCEPTS OF GAS EMISSIVITY

In defining the emissivity of a body of gas one must specify, among other things, the shape of the gas body under consideration. The emissivities of three shapes are of interest in our problem:

1. The emissivity ϵ_1 of a column of gas, measured along the axis of the column.
2. The emissivity ϵ_2 of a hemisphere of gas, measured at the center of the flat base of the hemisphere.
3. The emissivity ϵ_s of an infinite slab of gas, measured at a point on one boundary plane.

As will be shown shortly, column emissivity ϵ_1 and hemispherical emissivity ϵ_2 have the same value.

The emissivity of a column of gas may be defined, albeit rather loosely, as the ratio between the total energy emitted by the base of the column in a direction closely parallel to the axis of the column and the total energy which would be radiated in the same direction by a black body at gas temperature placed at the base of the column.

A more explicit definition is desirable, both for the sake of definiteness and as a step in showing the equivalence of column emissivity to hemispherical emissivity. For this more explicit definition first consider Fig. 2a. A small plane area dA is receiving radiation through a small solid angle $d\omega$ from a black-body source whose temperature is T_1. The solid angle $d\omega$ makes an angle θ with the normal to dA. The area dA is sufficiently small that neither $d\omega$ nor θ vary appreciably over the surface of dA (the relative size of dA is exaggerated in the figure).

As can be determined from most heat transfer texts, for example,[1a, 2a, 3a] the radiant heat flow (per unit area of dA) received by dA from the black-body surface will then be:

$$dq_b = \frac{q_b}{\pi} \cos\theta \, d\omega \qquad [1]$$

in which q_b is the total radiant heat flow emitted by a black body at temperature T_1.

Now consider Fig. 2b. Here the black-body radiating surface has been replaced by a column of radiating gas of length L, density ρ_g, and temperature T_1. We again consider the area dA, which is located on the axis of the column and which "sees" the gas column through the same small angle $d\omega$ and at the same angle θ at which it saw the black body in Fig. 2a.

The radiant heat flow from the gas to dA will now be dq_g. We define the emissivity of the gas as the ratio between this heat flow and that received by dA (in Fig. 2a) from the black body:

$$\epsilon_1 \equiv \frac{dq_g}{dq_b} \qquad [2]$$

Combining [1] and [2], we note:

$$dq_g = \epsilon_1 \frac{q_b}{\pi} \cos\theta \, d\omega \qquad [3]$$

The columnar emissivity of a particular radiating gas is a function of the number of molecules of the radiating gas in the column under consideration (and of other variables as well). At a given temperature, the number of molecules of the radiating gas in the column is linearly proportional to the pressure-length product term P_gL, in which P_g is the partial pressure of the radiating gas and L the length of the gas column. In most heat transfer texts gas emissivity is usually plotted as a function of P_gL.

The number of molecules in the beam is also linearly proportional to the density-length product term ρL. Meteorologists customarily express gas emissivities as a function of this latter product term, and it is somewhat more convenient for use in problems involving atmospheric radiation. Consequently we shall express gas emissivities as a function of ρL which we write as m. That is

$$m_g \equiv \rho_g L_g \qquad [4]$$

in which ρ_g and L_g are the density and column length, respectively, of the particular radiating gas under consideration. It is seen that m_g has the dimensions g/cm^2, and is numerically equal to the number of grams of the radiating gas contained in a column L_g cm long and 1 sq cm in cross section.

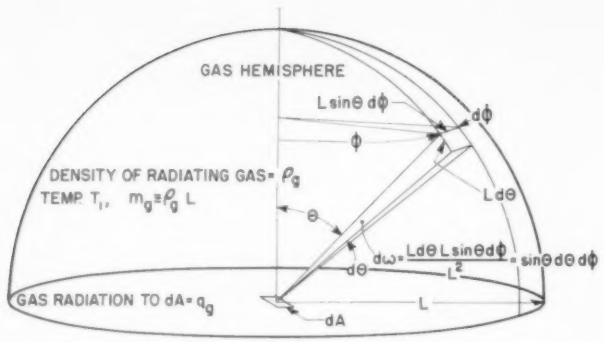

FIG. 3—Radiation from a hemisphere of gas.

We turn to the definition of the emissivity of a hemisphere of gas. Consider Fig. 3. A gas hemisphere at temperature T_1 is radiating to a small area dA at the center of the base. The intensity of radiation striking dA is q_g. The emissivity of the gas is defined as the ratio:

$$\epsilon_2 \equiv \frac{q_g}{q_b} \qquad [5]$$

in which q_b is the intensity of black-body radiation at temperature T_1.

We note that the total radiation from the hemisphere to dA is actually the summation of the radiation from many small columns, each of length L and solid angle $d\omega$. A consideration of Fig. 3 will show that

$$d\omega = \sin\theta \, d\theta \, d\phi \qquad [6]$$

From the above equation and Eq. [3]:

$$dq_g = \frac{\epsilon_1 q_b}{\pi} \sin\theta \cos\theta \, d\theta \, d\phi \qquad [7]$$

Integrating over the entire hemisphere:

$$q_g = \int_{\phi\theta} dq_g = \frac{\epsilon_1 q_b}{\pi} \int_{\phi=0}^{2\pi} \int_{\theta=0}^{\pi/2} \sin\theta \cos\theta \, d\theta \, d\phi \qquad [8]$$

which reduces to:

$$q_g = \epsilon_1 q_b \qquad [9]$$

Comparing Eq. [9] above with Eq. [5], we see that

$$\epsilon_1 = \epsilon_2 \qquad [10]$$

That is, the emissivity of a column and a hemisphere of gas (each having the same value of m_g) are equal. As a matter of fact, columnar emissivity and hemispherical emissivity are essentially merely two ways of defining the same thing. We shall henceforth drop the subscripts 1 and 2 to differentiate between columnar and hemispherical emissivity and refer to either of these emissivities as simply ϵ.

Actual radiation from the atmosphere should be considered neither as radiation from a column nor from a hemisphere, but rather as radiation from a series of horizontal layers (each of varying composition, temperature, or pressure). Each of these layers, for purposes of radiation calculations, may be considered as an infinite slab.

The emissivity of an infinite slab (see Fig. 4) is defined as the ratio

$$\epsilon_s = \frac{q_{gs}}{q_b} \qquad [11]$$

where q_{gs} is the intensity of radiation from the gas striking a small plane area dA lying in one bounding plane of the slab, and q_b is the intensity of black-body radiation at the same temperature as that of the gas.

The density length product m_{gs} of a slab is $\rho_g L_s$ in which L_s is the separation between boundary planes of the slab. The aptly descriptive term "precipitable water" is often used for the water-vapor density-length product m_{ws} of a slab.

Just as in the previous case of the hemisphere, the total radiation from a slab of gas to the small area dA at the "base" of the slab is the summation of the radiation from many small columns. In the case of the slab the length of the various columns is variable and, in general, greater than the separation L_s between the slabs.

A consideration of Figs. 3 and 4, and of the definitions of hemispherical and slab emissivity will suggest, correctly, that the emissivity of a slab must be somewhat greater than that of a hemisphere having the same density-length product as the slab. The nature of this relationship between hemispherical emissivity and slab emissivity is most important in problems of atmospheric radiation. The relationship is somewhat involved, and a further discussion of the matter is deferred to a later section of this article.

The emissivities we have been considering so far are the "average" or "total" emissivities. That is, they are ratios between the total amount of energy of all wavelengths emitted by a gas body under a set of conditions and the total amount of energy which would be emitted by a black body under the same conditions. We consider now the "spectral emissivity" of a gas column.

Again starting with a rather loose definition, the

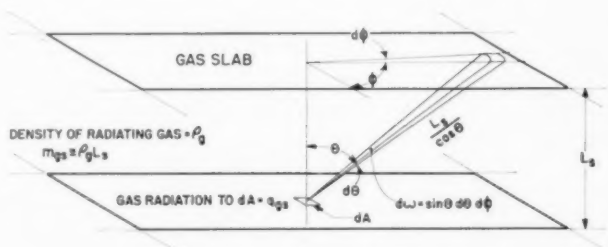

FIG. 4—Radiation from a slab of gas.

VOL. 5 1961

spectral emissivity of a gas column is the ratio between the amount of energy emitted by the column in a particular narrow wavelength region and in a direction closely parallel to the axis of the column, and the amount of energy which would be emitted in the same wavelength region and in the same direction by a black-body at the gas temperature.

To put the matter more explicitly, we again refer to Fig. 2b, and consider the intensity of radiation $d^2q_{\lambda g}$ upon dA which is emitted by the gas in a wavelength region lying between λ and $\lambda + d\lambda$. This may be written:

$$d^2q_{\lambda g} = \frac{I_{\lambda g}}{\pi} d\lambda \cos\theta \, d\omega \qquad [12]$$

Now if the column of gas were replaced by a similarly placed black body at gas temperature (Fig. 2a), the black-body radiation in the same wavelength interval striking dA would be

$$d^2q_{\lambda b} = \frac{I_{\lambda b}}{\pi} d\lambda \cos\theta \, d\omega \qquad [13]$$

We define the spectral emissivity of the gas column as

$$\epsilon_\lambda \equiv \frac{d^2q_{\lambda g}}{d^2q_{\lambda b}} = \frac{I_{\lambda g}}{I_{\lambda b}} \qquad [14]$$

The preceding equation also defines the spectral emissivity of a gas hemisphere.

It is generally considered that the spectral emissivity of a column or hemisphere of a radiating gas, insofar as *monochromatic* radiation is concerned, is correctly given by an exponential expression of the form:

$$\epsilon_\lambda = 1 - e^{-K_\lambda m_g} \qquad [15]$$

It should be emphasized that the above expression is strictly valid only for monochromatic radiation. That is, it becomes increasingly valid as the wavelength interval under consideration approaches zero. For finite wavelength intervals $\Delta\lambda$ it is, in general, a rather poor approximation.

The relationship between total emissivity and spectral emissivity is:

$$\epsilon = \frac{dq_g}{dq_b} = \frac{\int_0^\infty \epsilon_\lambda I_{\lambda b} \, d\lambda}{q_b} \qquad [16]$$

In order to derive the above, we note that from Eqs. [12] and [14] we obtain

$$d^2q_{\lambda g} = \epsilon_\lambda \frac{I_{\lambda b}}{\pi} d\lambda \cos\theta \, d\omega \qquad [17]$$

Integrating the above with respect to λ:

$$\int_{\lambda=0}^\infty d^2q_{\lambda g} = dq_g = \frac{\cos\theta \, d\omega}{\pi} \int_0^\infty \epsilon_\lambda I_{\lambda b} \, d\lambda \qquad [18]$$

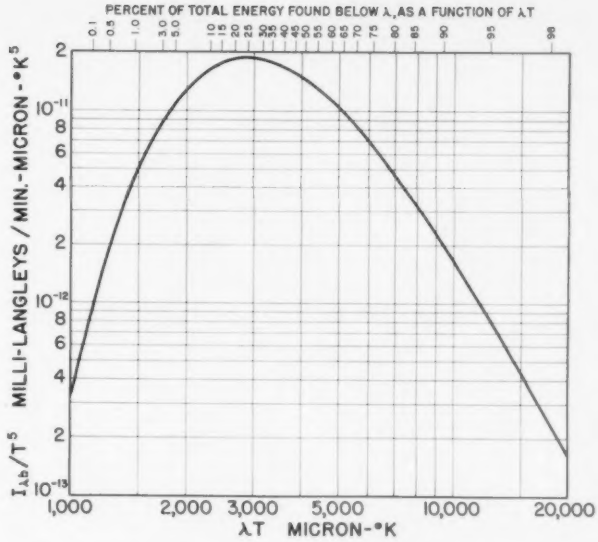

FIG. 5—Planck's black-body function.

Dividing the above equation by dq_b as given by Eq. [1] gives Eq. [16].

The black-body spectral intensity per unit of wavelength $I_{\lambda b}$ is given by Planck's equation. This equation, expressed in cgs units, may be written:

$$I_{\lambda b} \, d\lambda = T^5 \frac{2\pi hc^2}{(\lambda T)^5 (e^{\frac{ch}{k\lambda T}} - 1)} d\lambda \frac{\text{ergs}}{\text{sq cm-sec}} \qquad [19]$$

in which

$h = 6.62 \times 10^{-27}$ erg-sec (Planck's constant)
$c = 2.998 \times 10^{10}$ cm/sec (velocity of light)
$k = 1.380 \times 10^{-16}$ erg/°K (Boltzmann's constant)
λ = wavelength, cm
T = temperature °K

Integration of Eq. [15] may be shown[4a] to give:

$$\int_0^\infty I_{\lambda b} \, d\lambda = q_b = \sigma T^4 \qquad [20]$$

in which

$$\sigma = \frac{2\pi^5 k^4}{15c^2h^3} \text{ (Stefan-Boltzmann constant)} = 5.67 \times 10^{-5} \text{ ergs/sq cm-sec-°K}^4 \qquad [21]$$

In the units used in this article, the Stefan-Boltzmann constant is

$$\sigma = 8.13 \times 10^{-8} \text{ mly/min-°K}^4 \qquad [22]$$

Fig. 5 presents a plot of Eq. [19] in units used in this paper. Graphs such as this are convenient for use in a variety of problems involving the spectral energy distribution of black-body radiation. Limited quantities of a larger and somewhat more accurate and easy-to-read version of Fig. 5 are available from the author. An extensive tabulation of the Planck function, in cgs units,

has been presented by Lowan and Blanch.[5] A shorter tabulation, in English units and in a quite convenient form for many engineering uses, is given by Dunkle.[6]

For the benefit of engineers having only infrequent occasion to use Planck's function, it may be mentioned that the function is presented and tabulated in various ways in the literature. Sometimes the units used are confusing, occasionally the presentation or tabulation may be erroneous.[3b, 7a] Consequently, in using a published tabulation for the first time, it is best to double check that one clearly understands the units employed, and that the tabulation itself appears correct.

EMISSIVITY OF WATER VAPOR

In principle, measurement of the emissivity of water vapor (or of other radiating gases) consists of sighting a calibrated radiometer through a narrow beam into a column of gas of known composition, length, and temperature; and observing the variations in radiometer readings as gas conditions are changed. If the beam of radiation from the gas is sent directly to the radiometer, measurements of total emissivity are obtained. If the beam is first separated into spectral components by a suitable grating or prism, and these components analyzed with the radiometer, a measure of the spectral emissivity is obtained.

The preceding brief description does not do justice to the practical complexity of obtaining accurate measurements of this type. Great care, skill, and fairly elaborate equipment are required to ensure that the composition, temperature and length of the gas column are accurately measured, that the effects of spurious radiation from contaminating gases and other sources are eliminated, and that the radiometer is properly calibrated.

The total emissivity ϵ_w of a column of water vapor and nonradiating gas is a function of the following variables:

1. The density-length product m_w of the water vapor.
2. The partial pressure P_w of the water vapor.
3. The total pressure P_T of the mixture.
4. The temperature T of the mixture.

In general, ϵ_w increases with an increase of any of the preceding variables. However, over the range of P_w and T which occur in our problem, ϵ_w is a weak function of these two variables. Consequently, for purposes of simplification, we assume that ϵ_w is not a function of P_w nor of T. We will allow for the variation of ϵ_w with total pressure P_T, and a discussion of this variation is deferred to a later section.

The total emissivity of water vapor as a function of m_w, according to various authorities, is presented in Fig. 6.

Particularly noteworthy is the slow variation of ϵ_w over an enormous range of m_w. The emissivity of the very small amount of water vapor contained in a few

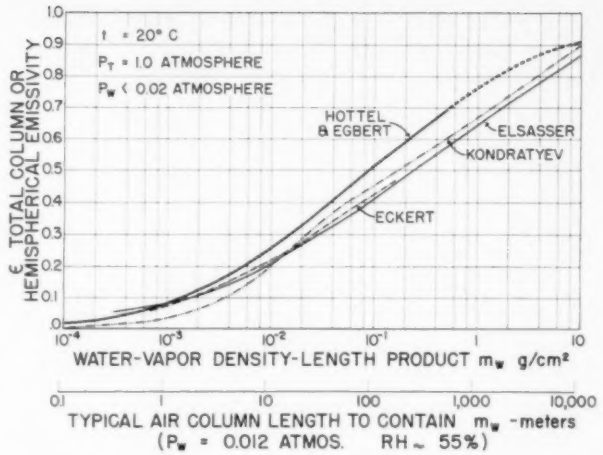

FIG. 6—The column or hemispherical emissivity of water vapor.

centimeters of typically moist air can be detected. The emissivity (and corresponding absorptivity) of the water vapor contained in a fair-sized room may be on the order of 10% or more. This is a large enough value to be of interest in some air-conditioning calculations, as the absorptivity of the water vapor in the air has a noticeable effect on the rate at which incoming air is heated or cooled by radiative effects on entering a room. And it is seen from Fig. 6 that the emissivity of a column of air (of typical moisture content) continues to increase very slowly for very long column lengths—out to 10,000 meters or more. Laboratory measurements do not, of course, involve the measurement of emissivities of such long column lengths of air and water vapor. Laboratory measurements are normally made on columns only a few meters in length at most. Consequently, the use of laboratory-determined emissivities to determine the emissivities to be expected from large bodies of moist outdoor air always involves judicious extrapolation of some sort.

It is also to be noted from Fig. 6 that the various authorities are not in exact agreement The difficulties of making close measurements of water vapor emissivity are such that it is not known to a high degree of accuracy.

The work of Hottel and Egbert[8] was particularly painstaking and thorough, and may represent the best estimate. They were primarily interested in determining the emissivity of water vapor in hot furnace gases and most of their measurements were made at temperatures ranging from about 150 C to 700 C; however, they did make some measurements at room temperatures. The heavy solid line of Fig. 6 is Hottel and Egbert's estimate of the emissivity of water vapor at 70 F (for low values of P_w and a total pressure of one atmosphere). The same data are given in the current edition of McAdams.[1b]

VOL. 5 1961

Eckert's[3e] estimate of water-vapor emissivity for low values of water-vapor pressure is seen from Fig. 6 to be lower than that of Hottel and Egbert. Eckert also was chiefly interested in the radiation of furnace gases, and made most of his measurements at temperatures above 100 C. Although, as indicated on Fig. 6, Eckert's and Hottel's emissivity values do not agree too well for low values of P_w, they are in quite close agreement for saturated steam at 100 C. A discussion of possible reasons for the discrepancy between the two values at low water-vapor pressures is given by Hottel and Egbert.[8, 9]

The other two emissivity curves shown on Fig. 6—those of Elsasser[10] and Kondratyev[11]—are not the result of laboratory measurements of total emissivity by the writers in question. They represent, instead the correlation of a large body of spectral measurements on water vapor by various workers, and the deductions by Elsasser or Kondratyev as to the resulting total emissivity of water vapor. Essentially such a process amounts to breaking down the emission of water vapor into many small spectral components, and then adding all these components to obtain the total emission. This is more easily said than done, as the emission spectrum of water vapor is very complex, and the spectral emissivity ϵ_λ varies violently in very narrow ranges of wavelength. In general, for values of m_w which can be practically attained in experimental columns, the total emissivity ϵ is probably obtained with greater accuracy by direct empirical measurement (as was done by Hottel and by Eckert) than by deductions from spectral measurements. Nevertheless, the deductions of Elsasser and of Kondratyev are seen to agree reasonably well with the (probably) more accurate direct empirical measurements of Hottel and Eckert.

For values of m_w which are larger (or smaller) than can be practically attained in the laboratory, the emissivity can be best extrapolated from measurable values only by deductions from spectral analysis or from quantum-mechanical theory of the water-vapor molecule. This is a matter much beyond the province of this article. The dashed-line extrapolation of Hottel's and Egbert's curve is simply a guess on our part.

It is evident from Fig. 6 that some choice must be made amongst the various authorities. We shall choose the Hottel and Egbert curve as probably being the best available estimate of the total emissivity of water vapor, and will assume that our extrapolation of their curve is satisfactory for the problem at hand.

We turn now to a consideration of the approximate spectral distribution of radiation from water vapor. The actual spectrum of water vapor is made up of literally thousands of spectral "lines", as may be found in the spectral measurements of Randall and co-workers.[12, 13] The monochromatic emissivity ϵ_λ varies rapidly over each of these lines, and this complexity makes it practically impossible to accurately evaluate ϵ_λ over the entire spectrum of interest and thereby accurately obtain the total emissivity by integrating an expression such as Eq. [16].

TABLE 1—The Exponential Absorption Coefficient for Water Vapor (Krondratyev's Estimate)

Wavelength Interval, microns	$K_{\Delta\lambda}$ cm²/g	Wavelength Interval, microns	$K_{\Delta\lambda}$, cm²/g
5.0–5.5	40	19–20	43
5.5–6.0	198	20–21	23
6.0–6.5	198	21–22	58
6.5–7.0	156	22–23	64
7.0–7.5	46	23–24	75
7.5–8.0	12.8	24–25	80
8.0–8.5	3.4	25–26	53
8.5–9.0	0.10	26–27	93
9.0–12.0	0.10	27–28	116
12–13	0.25	28–29	136
13–14	0.84	29–30	152
14–15	1.30	30–31	179
15–16	1.65	31–32	179
16–17	4.40	32–33	179
17–18	17.2	33–34	198
18–19	14.0	34–35	110

However, for our purposes, a fairly good quantitative picture of the intensity of water-vapor emission in various wavelength regions can be obtained by assuming that Eq. [15] holds true over a finite wavelength region. In other words, we assume that over a wavelength region $\Delta\lambda$ the average spectral emissivity is given by

$$\epsilon_{\Delta\lambda} = 1 - e^{-K_{\Delta\lambda} m_g} \qquad [23]$$

in which $K_{\Delta\lambda}$ is a constant. As we have already mentioned, the above simplification is theoretically unjustified. But it does furnish a convenient engineering approximation, it is often used, and it is probably adequate for our purpose of obtaining a rough quantitative estimate of the apportionment of radiant energy to various wavelength regions.

If we wish to use the above approximation to determine the total emissivity of water vapor, the relation will be (compare Eq. [16]:

$$\epsilon = \frac{1}{q_b} \sum_{\lambda=0}^{\lambda=\infty} (1 - e^{-K_{\Delta\lambda} m_g}) I_{\lambda b} \, \Delta\lambda \qquad [24]$$

Table 1 presents Kondratyev's[11] estimates of the exponential absorption coefficient $K_{\Delta\lambda}$. These apply to water vapor at customary atmospheric temperatures —say from −20 to +30 C—and for a total air pressure of 1 atmosphere. As is mentioned by Kondratyev, all the coefficients should be considered as approximations. The emissivity curve attributed to Kondratyev in Fig. 6 is a plot of Eq. [24], using values of $K_{\Delta\lambda}$ from Table 1 and values of q_b and $I_{\lambda b}$ appropriate for black-body radiation at 290 K (17 C).

It will be noted from Table 1 that water vapor is at least slightly emissive over the entire spectrum tabulated. Some regions are very much less emissive (i.e.,

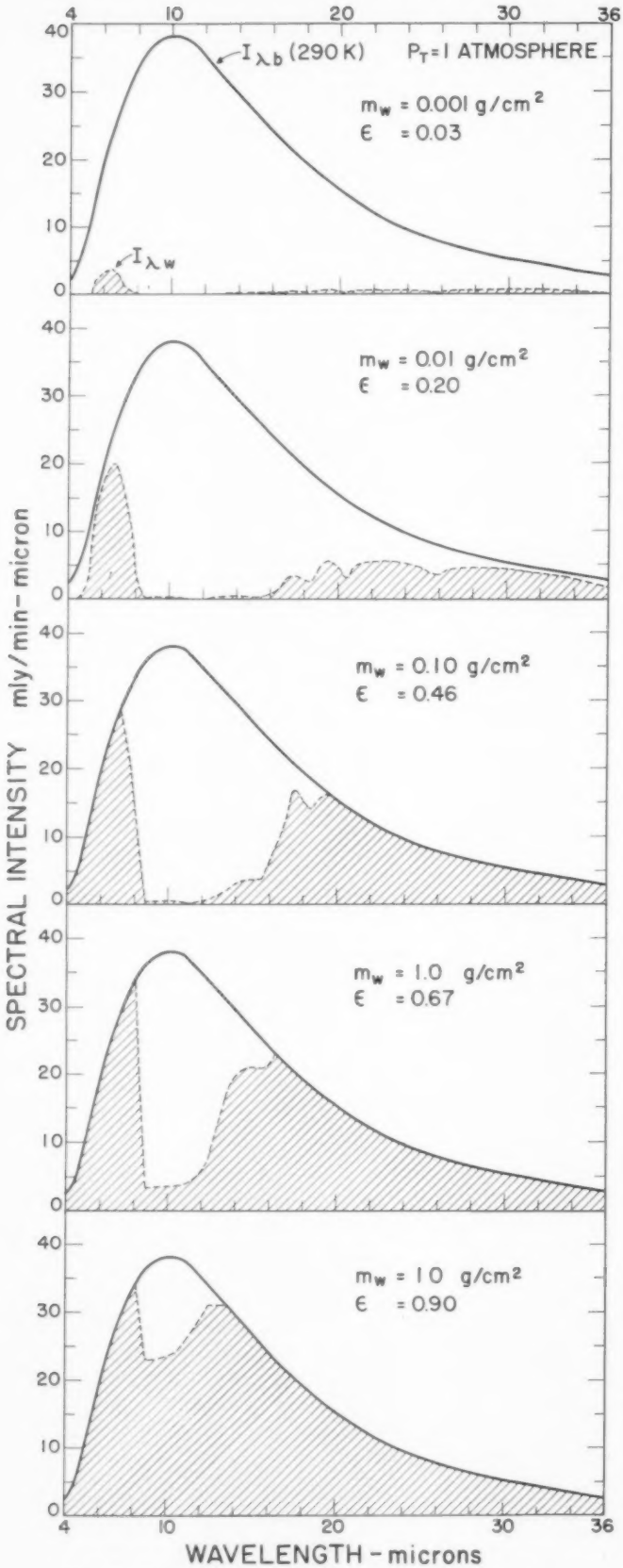

FIG. 7—Spectral intensity of water-vapor radiation.

have very much smaller values of $K_{\Delta\lambda}$) than others. The region around 8.5–13 microns is one of particularly low emissivity, and consequently of particularly high transmissivity. This region of relatively great transparency is aptly known as the "atmospheric window." It happens to be a wavelength region in which a substantial fraction (about 28%) of black-body radiation at ordinary atmospheric temperature is found. Consequently the radiative behavior of water vapor in this wavelength region has a marked effect on radiative transfer in the atmosphere.

As the density-length product m_w of a volume of water vapor is increased, the emission from the water vapor first approaches black-body emission in the spectral regions on each side of the relatively low-emissive "window." As m_w is still further increased, emission from the spectral "window" increases towards black-body values. This situation is graphically shown in Fig. 7, in which the spectral intensity $I_{\lambda w}$ of water vapor is plotted against wavelength for various values of m_w.

The curves of Fig. 7 were calculated from the same data as that used in calculating Kondratyev's estimate of the total emissivity of water vapor given in Fig. 6. That is, the values of $K_{\Delta\lambda}$ given in Table 1 were used, together with an assumed temperature of 290 K. For each of the graphs shown in Fig. 7, the total emissivity ϵ_w of the water vapor is the ratio between the shaded area under the $I_{\lambda w}$ curve and the total area under the black-body $I_{\lambda b}$ curve. These ratios are, of course, the same as those indicated by Kondratyev's curve on Fig. 6.

A consideration of the series of graphs shown in Fig. 7 gives a good understanding of the role which the high-transparency "atmospheric window" plays in the slow build-up of ϵ_w with m_w, a situation which we first noted in Fig. 6.

EFFECTS OF RADIATION FROM CARBON DIOXIDE

The wavelength spectrum of major interest in our problem ranges from about 5 microns to about 40 microns. Water vapor radiates, at least to some extent, throughout this spectrum. But carbon dioxide does not. The only important radiant energy contribution from carbon dioxide in the spectrum of interest lies between 13 and 17 microns. This 13–17 micron region contains 18.5% of the total black-body radiation at 17 C (290 K) and this percentage does not change very much over the range of temperatures of interest to us. Hence, if we assume that carbon dioxide radiates only in the 13–17 micron region, its maximum possible emissivity would be about 0.185.

Actual measurements of the emissivity of carbon dioxide indicate that its maximum emissivity is around 18 to 20%. Fig. 8 presents the results of direct measurements made by Hottel and Mangelsdorf[14] and Hottel

VOL. 5 1961

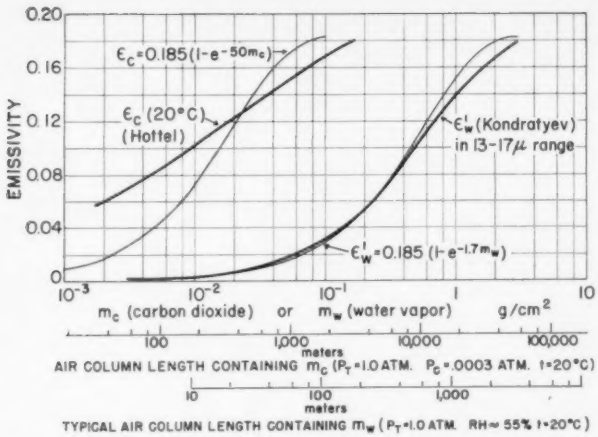

FIG. 8—Emissivity of carbon dioxide and emissivity of water vapor in the 13–17 micron region.

and Smith.[15] These same data also appear in the current edition of McAdams' "Heat Transmission."[16]

Also plotted on Fig. 8 is the approximate emissivity ϵ_w' of water vapor in the 13–17 micron band. This emissivity ϵ_w' is the ratio between the energy radiated in the 13–17 micron band by water vapor at 290 K and total black-body radiation (of all wavelengths) at the same temperature. Expressed as an equation:

$$\epsilon_w' = \frac{1}{q_b} \sum_{\lambda=13\mu}^{17\mu} \epsilon_{a\lambda}\, I_{b\lambda}\, \Delta\lambda \qquad [25]$$

The preceding equation was used to calculate ϵ_w' for 290 K, using the values of $\epsilon_{a\lambda}$ determined from the exponential absorption coefficients $K_{a\lambda}$ given in Table 1.

Fig. 8 illustrates several points of interest:

1) In the 13–17 micron band, water vapor is approaching "blackness" at values of m_w near 2 g/sq cm. Only about $\frac{1}{20}$ as much carbon dioxide is needed to produce the same effect.

2) However, under typical humidity conditions prevailing in air near the earth's surface, the concentration of water vapor is normally so much greater than that of carbon dioxide that either gas will reach maximum emissivity in the 13–17 micron range in about the same column length—in the neighborhood of 2000 meters.

3) Insofar as the total emissivity ϵ of a homogeneous mass of gas containing water vapor having a density-length product greater than about 1 g/sq cm is concerned, it does not particularly matter whether carbon dioxide is present or not, because the water vapor would already be nearly "black" in the 13–17 micron region in which the carbon dioxide radiates.

As will be discussed more fully in a later section, the gas masses to be considered in our problem typically do have a water-vapor content of around 1 g/sq cm or more, but they are not quite homogeneous. That is, they consist of several layers at slightly differing temperatures and pressures. Because of this we need some sort of correction to allow for the radiative effect of the carbon dioxide present in the air. But, as will become more evident as we go along, a rough correction is quite adequate for our particular purpose of determining the intensity of atmospheric radiation near ground level.

To obtain this rough correction we assume that carbon dioxide radiates only in the 13–17 micron band and that, within this band, the emissivity of water vapor and carbon dioxide can each be approximated by exponential expressions of the form:

$$\epsilon_w' = 0.185(1 - e^{-\beta m_w}) \qquad [26]$$

$$\epsilon_c = 0.185(1 - e^{-\gamma m_c}) \qquad [27]$$

According to the above equations, each g/sq cm of carbon dioxide behaves radiationwise in the 13–17 micron band the same as γ/β g/sq cm of water vapor. Consequently a gas containing m_w g/sq cm of water vapor and m_c g/sq cm of carbon dioxide may be treated as if its only radiative component were an amount $m_w + m_w'$ of water vapor, where

$$m_w' = \frac{\gamma m_c}{\beta} \qquad [28]$$

The emissivity in the 13–17 micron band of the carbon-dioxide and water-vapor mixture will be the same as that of the gas containing $m_w + m_w'$ g/sq cm of water vapor only:

$$\epsilon_{c+w} = 0.185(1 - e^{-\beta(m_w + m_w')}) \qquad [29]$$

From Eq. [28]:

$$\beta(m_w + m_w') = m_w\left(\beta + \gamma\frac{m_c}{m_w}\right) = m_w\left(\beta + \gamma\frac{\rho_c}{\rho_w}\right) \qquad [30]$$

From Eqs. [26], [29], and [30], the added emissivity caused by the carbon dioxide is seen to be

$$\Delta\epsilon = \epsilon_{c+w} - \epsilon_w' = 0.185\,(e^{-\beta m_w} - e^{-c_1 m_w}) \qquad [31a]$$

$$c_1 = \beta + \gamma\frac{\rho_c}{\rho_w} \qquad [31b]$$

From the above we see that the correction $\Delta\epsilon$ is a function of m_w and ρ_c/ρ_w. From Fig. 8 we see that reasonable values of β and γ are about 1.7 and 50 sq cm/g respectively, although the fit to the carbon-dioxide emissivity curve is crude.

Using the gas laws and tables of water-vapor saturation pressures, and assuming a carbon-dioxide partial pressure of 3×10^{-4} atmosphere (its approximate sea-level value), the ratio ρ_c/ρ_w can be readily obtained as a function of water-vapor dew point. For a dew point of −20 C the ratio is about 0.7; for a dew point of +20 C it is about 0.03.

Fig. 9 presents a plot of the correction $\Delta\epsilon$ for the presence of carbon dioxide, for various values of ρ_c/ρ_w. The correction corresponding to $\rho_c/\rho_w = 0.10$ is

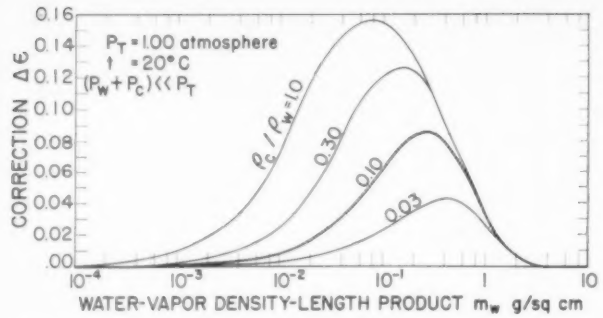

FIG. 9—Correction $\Delta\epsilon$ to be added to water-vapor emissivity to allow for the presence of carbon dioxide.

suggested as an appropriate one for all water-vapor dew points greater than about -10 C. If $P_c = 3 \times 10^{-4}$ atmosphere, the dew point corresponding to $\rho_c/\rho_w = 0.10$ is about 4 C.

This simple scheme for allowing for the effects of carbon dioxide in problems of atmospheric radiation seems to have been first used by Kondratyev.[11] It is probably a good one for our particular purpose, but it could be subject to considerable error in other types of radiative heat transfer problems involving mixtures of water vapor and carbon dioxide.

RADIATION FROM A SLAB OF GAS

As has already been mentioned, the various layers of air above the ground are best treated as infinite slabs for radiation calculations. Hence, to make use of laboratory determinations of emissivity in our problem, we must obtain the relation between the emissivity of radiating gas in the form of a slab and that of the same gas in the form of a column or hemisphere.

This matter is best handled by first determining the emissivity of a slab for monochromatic radiation, and then interpreting this result for the case of radiation of all wavelengths. We refer to Fig. 4, and consider the intensity of monochromatic radiation originating in the solid angle $d\omega$ and striking the small area dA at the base of the slab. From Eqs. [12], [14], [15] and the value of $d\omega$ given in Fig. 4, we see that this intensity is:

$$d^2q_{\lambda g} = \frac{I_{b\lambda}}{\pi}\left(1 - e^{-\frac{K_\lambda m_{gs}}{\cos\theta}}\right)\cos\theta\sin\theta\,d\theta\,d\phi\,d\lambda \qquad [32]$$

To determine the total monochromatic intensity $dq_{\lambda g}$ upon dA from all parts of the slab, we must integrate Eq. [32] over all values of θ and ϕ. Referring to Fig. 4, we see that θ varies from 0 to $\pi/2$ and ϕ varies from 0 to 2π.

The integration with respect to θ is more conveniently carried out, and nomenclature shortened, if we make the substitutions:

$$x = \frac{K_\lambda m_{gs}}{\cos\theta} = \frac{a}{\cos\theta} \qquad [33]$$

It is seen that the limits of integration of the new variable x will be from a to ∞. Also Eq. [33] yields:

$$\sin\theta\cos\theta\,d\theta = \frac{a^2}{x^3}\,dx \qquad [34]$$

Substituting from Eq. [34] into Eq. [32], and indicating the integration:

$$\int_{\theta=0}^{\pi/2}\int_{\phi=0}^{2\pi} d^2q_{\lambda g} = dq_{\lambda g} = \frac{I_{\lambda b}\,a^2\,d\lambda}{\pi} \cdot \int_{\phi=0}^{2\pi}\int_{x=a}^{\infty}\frac{1-e^{-x}}{x^3}\,dx\,d\phi \qquad [35]$$

Performing the indicated integration and simplifying will yield:

$$dq_{\lambda g} = I_{\lambda b}\,d\lambda[1 - 2Ei_3(a)] \qquad [36]$$

in which

$$2Ei_3(a) \equiv 2a^2\int_a^\infty \frac{e^{-x}}{x^3}\,dx \qquad [37]$$

Tabulations of the function $2Ei_3(a)$ are available.[10] Also, by integration by parts, the function will be found equal to:

$$2Ei_3(a) = e^{-a} - ae^{-a} + a^2\int_a^\infty \frac{e^{-x}}{x}\,dx \qquad [38]$$

A tabulation of the integral appearing in the above equation is given by Jahnke and Emde.[16]

The quantity $dq_{\lambda g}$ appearing in Eq. [36] is the radiation in wavelengths lying between λ and $\lambda + d\lambda$ from all portions of the gaseous slab to the small area dA at its base. The amount of black-body radiation $dq_{\lambda b}$ within the same wavelength interval is $I_{\lambda b}\,d_\lambda$. The spectral emissivity $\epsilon_{\lambda s}$ of the slab is then

$$\epsilon_{\lambda s} = \frac{dq_{\lambda g}}{dq_{\lambda b}} = 1 - 2Ei_3(a) \qquad [39]$$

Or, substituting the value of a:

$$\epsilon_{\lambda s} = 1 - 2Ei_3(K_\lambda m_{gs}) \qquad [40]$$

This is to be compared with the value of the spectral emissivity of a hemisphere, which we have already found to be (see Eq. [15]):

$$\epsilon_\lambda = 1 - e^{-K_\lambda m_g} \qquad [41]$$

Evidently the relation between the spectral emissivity of a slab and that of a hemisphere depends upon the relation between the function $2Ei_3$ and the exponential function. From Fig. 10 it is evident that, over a wide range of values of a:

$$2Ei_3(a) \approx e^{-1.8a} \qquad [42]$$

We shall make the simplifying assumption that the

VOL. 5 1961

two functions shown in Eq. [42] are equal, for all values of a.

With this simplifying assumption, it is easily seen from Eqs. [41] and [42] that the spectral emissivity of a slab of density-length product m_{gs} will in all cases be the same as the spectral emissivity of a hemisphere having a density-length product

$$m_g = 1.8\, m_{gs} \qquad [43]$$

If the slab of density-length product m_{gs} has the same spectral emissivity as the hemisphere of density-length product $1.8\, m_{gs}$ for all values of spectral emissivity, then the total emissivity of the slab will also be the same as the total emissivity of the hemisphere of density-length product $1.8\, m_{gs}$. Consequently, using our simplifying assumption, if we wish to determine the emissivity ϵ_{ws} of a slab of water vapor of density-length product m_{ws} we may find it readily from a plot of hemispherical emissivity vs. m_w (such as Fig. 6) by simply reading off the emissivity of a hemisphere of density-length product $1.8\, m_{ws}$.

Figs. 11 and 12 have been prepared to give some idea of the magnitude of the error associated with our simplifying assumption that approximate Eq. [42] is an equality. In Fig. 11 the ratio $\epsilon_{\lambda s}/\epsilon_\lambda$ is plotted against $K_\lambda m_{gs}$ for various values of m_g/m_{gs}. In Fig. 12 are plotted the exact values of the ratios m_g/m_{gs} which make Eq. [42] an equality. The extreme limits of this ratio are 2.00 at $Km_{gs} = 0$ and 1.00 at $Km_{gs} = \infty$. Fig. 11 indicates that the ratio $m_g/m_{gs} = 1.8$ perhaps gives the best approximation over the entire range of Km_{gs} shown. However, if only values of Km_{gs} greater than 0.10 are considered, a somewhat lower value of the m_g/m_{gs} ratio might be a better approximation.

The procedure developed in the preceding paragraphs to determine the best approximation of this m_g/m_{gs} ratio is essentially that used by Eckert.[3]

Meteorologists approach the problem of determining this ratio in a variety of ways, and have suggested values of the ratio ranging from 1.5 to 2.0.[17] Elsasser[10] recommends the value 1.66 which is widely used in meteorological calculations. However, since the value 1.8 is customarily used for this ratio in engineering heat transfer calculations, we shall use that estimate, although it may be a little high, as the best single approximation for calculations of atmospheric radiation.

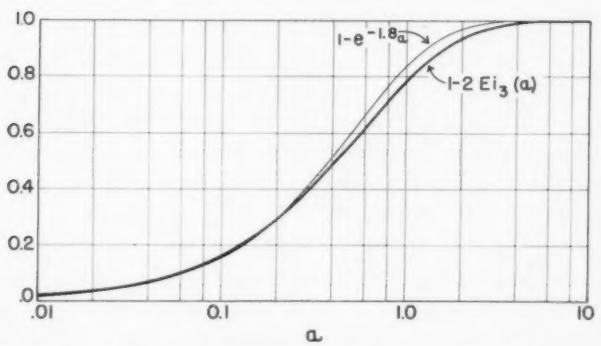

FIG. 10—Comparison of the functions $1 - e^{-1.8a}$ and $1 - 2Ei_3(a)$.

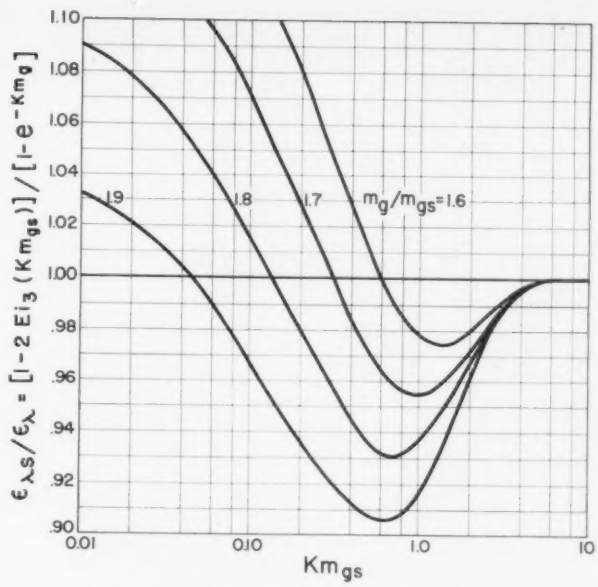

FIG. 11.

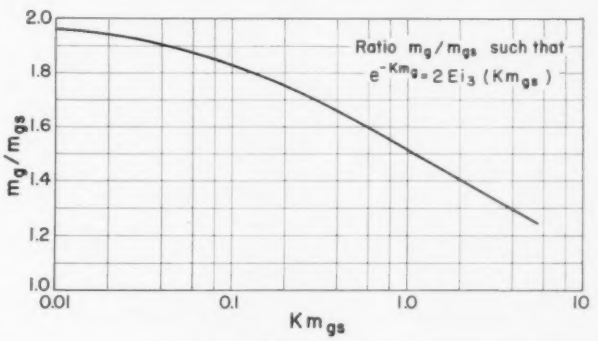

FIG. 12.

Using our estimate of 1.8 for the ratio m_g/m_{gs}, we can replot the Hottel-Egbert curve of Fig. 6 in order that we may read slab emissivity directly. Furthermore we can add the correction $\Delta\epsilon$ for carbon dioxide as developed in the preceding section (see Eq. [31] and Fig. 9). All of this is shown in Fig. 13, which is our final working plot of the slab emissivity of a mixture of water vapor, carbon dioxide, and nonradiating gas, at a total pressure of one atmosphere.

Fig. 13 could be used directly to obtain the slab emissivity of an idealized homogeneous slab of gas at equal pressure and temperature throughout. However, the actual atmosphere should be considered as a series of layers of slabs, of varying pressure, temperature and moisture content. Our procedure for allowing for these variations is described in the next section.

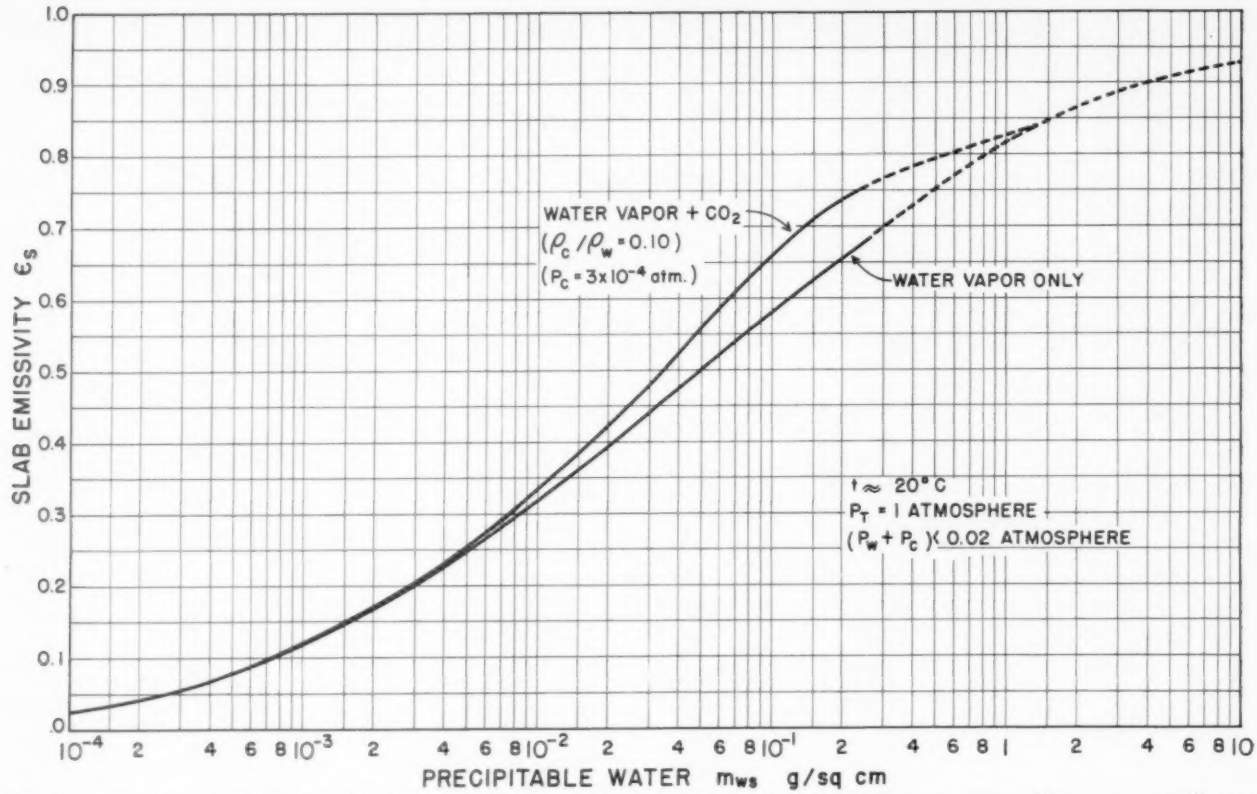
SLAB EMISSIVITY ϵ_s
PRECIPITABLE WATER m_{ws} g/sq cm
WATER VAPOR + CO_2
(ρ_c / ρ_w = 0.10)
(P_c = 3x10^{-4} atm.)
WATER VAPOR ONLY
t ≈ 20° C
P_T = 1 ATMOSPHERE
(P_w + P_c) X 0.02 ATMOSPHERE

FIG. 13—The slab emissivity of an idealized homogeneous slab of moist air at 1 atmosphere pressure. Upper curve indicates typical correction for carbon dioxide content.

LAYERS OF VARYING PRESSURE AND TEMPERATURE

The emissivity of a mixture of water vapor and nonradiating gas is a function of the total pressure P_T. The physical explanation is that the emission of radiation by water-vapor molecules is influenced by collisions with molecules of nonradiating gas (as well as by other effects). If the rate of collisions is lessened by lowering P_T, the rate of emission will also be lowered.

If the emissivity of a slab at total pressure P_0 and containing an amount of water vapor m_w is known, and it is desired to determne the emissivity of a second slab at different pressure P but containing the same amount of water vapor, one way of allowing for the effect of variation in pressure is to assume that the second slab acts radiatively as if it were at total pressure P_0 but contained a "reduced" amount of water vapor

$$m_w' = f_p m_w \qquad [44]$$

in which f_p is a suitable correction factor to allow for the variation in P. This is the scheme customary in meteorological literature. Preference is usually shown for one or the other of two values of f_p.[7b]

$$f_p = \sqrt{\frac{P}{P_0}} \quad \text{or} \quad f_p = \frac{P}{P_0} \qquad [45a] \quad [45b]$$

The first equation implies that the effect of halving the total pressure is the same as multiplying the water-vapor content m_w by $1/\sqrt{2}$. The second equation implies that halving the pressure has the same effect on emissivity as halving the water-vapor content. Because of the very slow increase of emissivity with water-vapor content (see Fig. 6 or 13), either of the above versions of the correction factor f_p will yield about the same corrected emissivity. We shall assume that Eq. [45b], i.e., $f_p = P/P_0$, is the closer approximation. We shall also assume that the emissivity of carbon dioxide, for the purposes of our calculations, varies in the same fashion.

We have already made the simplifying assumption that the emissivity of water vapor does not vary with temperature over the range of temperatures with which we are concerned. This implies that the total energy radiated by a slab of gas of specified water-vapor content will be a function of its temperature only, and will be directly proportional to the fourth power of its absolute temperature. Hence, with the simplifying assumption that emissivity does not vary with temperature, the ratio between the total energy radiated by a slab at temperature T_1 and that radiated by a slab at T_2 will be $\epsilon_1 T_1^4 / \epsilon_2 T_2^4$. If both slabs have the same emissivity, this ratio will be simply $(T_1/T_2)^4$.

VOL. 5 1961

With the above concept of the effect of temperature variation, together with the previously developed assumption regarding the effect of pressure variation, we are now in a position to calculate the emissivity of a system of several layers of slabs, the various layers having different temperatures, total pressures, and amounts of precipitable water.

The procedure for doing this is perhaps best illustrated by a numerical example. Fig. 14 illustrates a hypothetical case of 3 layers of infinite slabs. The layers have different temperatures, precipitable water contents, and total pressures as shown in the figure. Each individual layer is assumed to be at the same temperature and pressure throughout.

The problem is to determine the apparent over-all emissivity ϵ_a of all three layers, measured at the bottom of the lowest layer. This emissivity is to be expressed as the ratio between the intensity of radiation emitted by the three layers to the intensity of black-body radiation at the temperature of the lowest layer. This temperature is seen to be 280 K.

The first step is to "reduce" the water-vapor content of each slab in proportion to its total pressure, in accordance with Eq. [45b]. This yields the equivalent precipitable water m_w' to be used for radiation calculations. These values of m_w' are shown in the last column of Fig. 14.

Then, considering the lowest slab only, we find from Fig. 13 that its emissivity would be 0.335. Since the temperature of the lowest slab is 280 K, this 0.335 is the fraction of black-body radiation at 280 K contributed by this first slab.

Next we consider the radiation contribution from the second layer, which contains the radiation equivalent

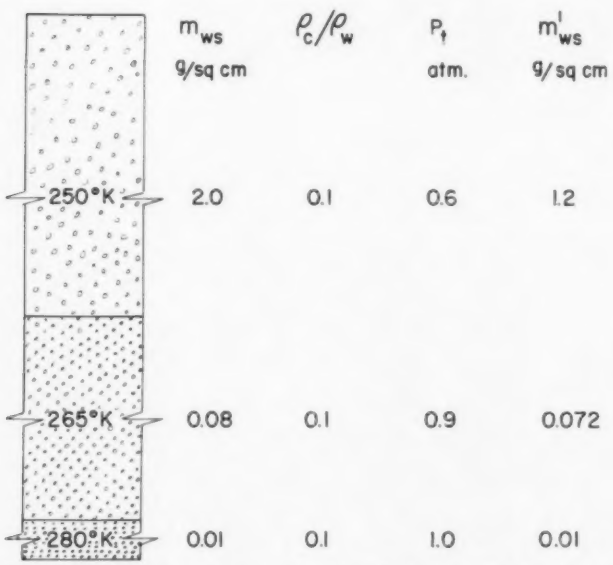

FIG. 14—A numerical example of calculation of apparent emissivity (see text for details of calculation).

of 0.072 g/sq cm of water vapor. From Fig. 13 we see that the addition of this amount of water vapor to the 0.010 g/sq cm contained in the first slab will raise the emissivity from 0.335 to 0.630. The latter value is the emissivity of 0.082 g/sq cm of water vapor plus indicated carbon dioxide ($\rho_c/\rho_w = 0.10$). The change in emissivity due to "adding on" the second slab is thus 0.630 − 0.335, or 0.295. This is the fraction of black-body radiation at 265 K (temperature of the second slab) contributed by that slab. This is $(265/280)^4 \times 0.295 = 0.237$ times black-body radiation at 280 K. Hence the equivalent emissivity contribution of the second slab, calculated as the fraction of 280 black-body radiation, is 0.237.

Proceeding similarly with the third slab, we find that its equivalent precipitable water content of 1.20 g/sq cm would raise the emissivity measured on Fig. 13 from 0.630 to 0.840. The latter emissivity is that of 1.28 g/sq cm of water vapor (again remembering that we are proceeding along the curve $\rho_c/\rho_w = 0.10$). The resulting change in emissivity is 0.840 − 0.630 = 0.210. But since the temperature of the upper slab is 250 K, the equivalent change of emissivity, figured to the 280 K base, is $(250/280)^4 \times 0.210 = 0.134$.

The apparent emissivity of all three slabs, relative to 280 black-body radiation, is then the sum of the contribution from all three layers, or 0.335 + 0.237 + 0.134 = 0.71.

We could carry out this step-by-step procedure for any number of layers, and thereby determine the emissivity of the actual atmosphere for any specified set of conditions of temperature, pressure, and water-vapor content in the various layers. This procedure, for typical atmospheric conditions, is carried out in the next section.

TYPICAL ATMOSPHERIC EMISSIVITIES

The composition of the atmosphere varies, of course, with time, place, and height. Nevertheless, it often varies with height in fairly typical ways, and we can use these typical variations to work out the emissivity of the atmosphere to be expected under average conditions.

The variation of pressure with altitude is, for our purposes, quite constant. It typically follows rather closely the relation shown in Fig. 15, which is a plot of the pressure variation of the "U. S. Standard Atmosphere".[7e] As indicated on Fig. 15, this curve, up to about 4000 meters, can be approximated very nicely by the simple exponential relation

$$P = P_0 e^{-\gamma Z} \qquad [46]$$

in which P is the pressure at height Z centimeters, P_0 is the pressure at ground level, and the constant γ is 1.2×10^{-6} cm^{-1}.

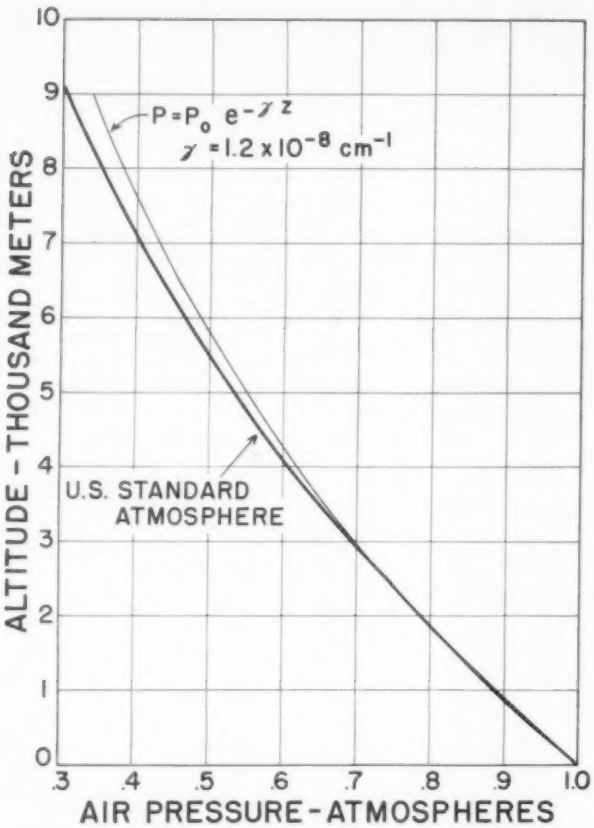

FIG. 15—Typical variation of air pressure with height.

Variation of temperature with height is less uniform, but at heights of a few tens of meters off the actual ground surface, it often obeys the simple relation:

$$T_Z = T_0 - 0.006\ Z' \qquad [47]$$

in which T_Z is the air temperature at height Z' meters, and T_0 is the air temperature measured a meter or two above the surface. The above equation indicates that the air temperature drops 6 centigrade degrees for each 1000 meters increase in altitude. The variation is very much more rapid than this in the first few tens of meters above the ground surface.

Variation of water-vapor density with height is also variable, but it too often exhibits a reasonably regular variation with height,[11, 18] the relation being:

$$\rho_w = \rho_{w-0} e^{-\beta z} \qquad [48]$$

in which ρ_w is the water-vapor density at a height Z centimeters, and ρ_{w-0} is the water-vapor density near ground surface. The quantity β (which we take as a constant) is about 4.5×10^{-5} cm^{-1}.

Equation [48] can be readily utilized to determine the total precipitable water contained below a height of Z centimeters, and the result will be found to be:

$$\int_0^Z dm_w = \frac{\rho_{w-0}}{\beta}\,(1 - e^{-\beta z}) \qquad [49]$$

Since ρ_{w-0} is, to a good approximation, a function of the surface dew point only, we can use the above equation to prepare a plot of the variation of precipitable water with height, as a function of surface dew points. The solid lines of Fig. 16 give this information.

For radiation calculations we need the "reduced" amount of precipitable water m_w' as given by the pressure correction Eq. [45b]. If the pressure variation is assumed to be given by Eq. [46], and the variation of density of actual precipitable water by Eq. [48], it is readily shown that the "reduced" amount of precipitable water below height Z is given by:

$$\int_0^Z dm_w' = \frac{\rho_{w-0}}{\beta + \gamma}\,(1 - e^{-(\beta+\gamma)z}) \qquad [50]$$

A plot of this "reduced" amount of precipitable water below height Z (again plotted as a function of surface dew point) is given by the dashed lines of Fig. 16.

Fig. 16 and Eq. [47] are seen to give us all the information we need to calculate the emissivity of a typical atmosphere. We do this by dividing it into layers, and using the same step-by-step procedure developed in the numerical example of the preceding section.

Table 2 presents an example of such a calculation, for an assumed surface dew point of +10 C. The table, together with its notes, is self-explanatory. A consideration of this tabulation and the calculation procedure behind it reveals several interesting points:

1) The first two or three hundred meters above the surface contributed about 90 per cent of the total radiation received near ground level. We see that atmospheric radiation is predominantly determined by the condition of the first few hundred meters above the surface, although for best accuracy it is necessary to

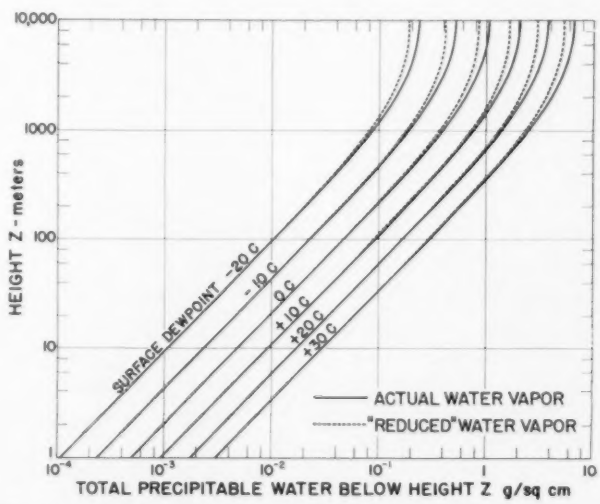

FIG. 16—Typical approximate variation of water-vapor content with height.

VOL. 5 1961

TABLE 2—Example of Emissivity Calculation

(1) ϵ	(2) m'_w, g/sq cm	(3) $\Delta\epsilon$	(4) Z, meters	(5) $\left(\frac{T_z}{T_0}\right)^4$	(6) $\Delta\epsilon'$
.40	.0170	.40	10	1.000	.400
.45	.0245	.05	25	.998	.0499
.50	.0345	.05	30	.997	.0498
.55	.0480	.05	40	.996	.0498
.60	.0660	.05	60	.995	.0497
.65	.0930	.05	80	.992	.0496
.70	.136	.05	120	.990	.0495
.75	.235	.05	210	.987	.0493
.80	.570	.05	510	.958	.0479
.81	.720	.01	870	.930	.0093
.82	.900	.01	1200	.904	.0090
.83	1.10	.01	1650	.871	.0087
.84	1.30	.01	2350	.821	.0082
.85	1.58	.01	~4300	.692	.0069

Total = .8376
Emissivity ϵ_a = .84

Assumptions:
Dew point = +10 C
Surface air temperature = +20 C
"Reduced" water-vapor distribution according to Fig. 16
Temperature-height variation according to Eq. [47]

Explanation of Columns:
(1) Emissivity, from Fig. 13
(2) Corresponding precipitable water, from Fig. 13
(3) Uncorrected emissivity contribution from layer
(4) Approximate average height of layer, from Fig. 16
(5) Temperature correction factor for layer, calculated from Eq. [47]
(6) Corrected emissivity contribution from layer (= Col. 3 × Col. 5)

consider the ever-decreasing radiation contributions from heights up to several thousand meters.

2) If the site is at sea level—that is, if the pressure of the first layer of gas is 1.00 atmosphere—the over-all effect of pressure corrections on total emissivity is very small.

3) The emissivity contributions from the various layers indicated in Table 2 were obtained by moving along the $\rho_c/\rho_w = 0.10$ curve of Fig. 13. Since the total amount of "reduced" precipitable water was fairly high (1.58 g/sq cm) it is evident from Fig. 13 that very nearly the same total emissivity would have been obtained in this case if we had ignored the effect of carbon dioxide and simply proceeded along the base emissivity curve of water vapor only. This corroborates the remarks made in the previous section concerning the effects of carbon dioxide, in which we noted that, if more than about one g/sq cm of water vapor is present, the effect of any added carbon dioxide is small.

4) The over-all effect of the temperature corrections is also small. Furthermore, if the temperature variation with height follows Eq. [47], the over-all effect of the temperature corrections $(T_z/T_0)^4$ will be essentially unchanged over a fairly wide variation in T_0. For example, Table 2 was calculated for $T_0 = 293$ K (20 C), which corresponds to a relative humidity of about 50% for a dew point of 10 C. However, practically identical values of ϵ_a would be found if we had made the calculation for any value of T_0 ranging from 283 K (which corresponds to 100% RH) to 303 K (about 30% RH). Summing up, as a practical matter we can consider the apparent emissivity ϵ_a to be independent of surface temperature T_0, a strong function of the total precipitable water m_{ws}, and a weak function of both the pressure and temperature variation of the upper air containing m_{ws}.

We can determine ϵ_a for typical conditions by calculating it for several dew points, just as was done for the single dew point of +10 C in Table 2, and plotting the results. Such a plot is given by Fig. 17. All the points for dew points of −10 C and greater were calculated with the $\rho_c/\rho_w = 0.10$ curve of Fig. 13, and the calculations indicated that the effect of carbon dioxide was small. But for the low dew point of −20 C the effect of carbon dioxide was more noticeable, and was not properly accounted for by the $\rho_c/\rho_w = 0.10$ curve of Fig. 13. In calculating this point, the correction corresponding to $\rho_c/\rho_w = 1.0$ on Fig. 9 was used. In applying the corrections given by Fig. 9 to the base water-vapor emissivity curve of Fig. 13, it should be remembered that the abscissae m_w of Fig. 9 refer to the water-vapor content of a column, and those of Fig. 13 refer to a slab. We have assumed that 1.0 g/sq cm in a slab is equivalent to 1.8 g/sq cm in a column. Hence, for example, the correction to be applied at $m_{ws} = 1.0$ on Fig. 13 is that obtained by entering Fig. 9 at $m_w = 1.8$.

For typical atmospheric conditions, Fig. 17 is essentially the "answer" towards which we have been working. The intensity of atmospheric radiation is given by

$$A = \epsilon_a \sigma T_a^4 \qquad [51]$$

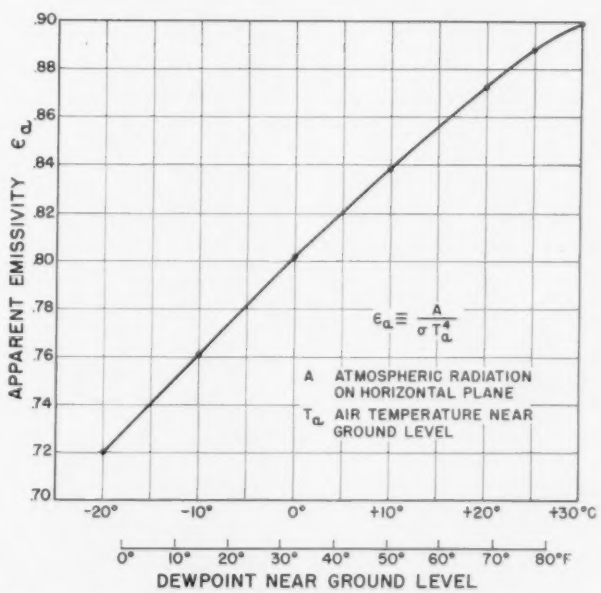

FIG. 17—Typical apparent emissivity ϵ_a of a clear sky at sea level.

If we insert the values of ϵ_a from Fig. 17 into the above, we finally obtain our estimate of the values of atmospheric radiation for the typical conditions used in calculating Fig. 17, viz., cloudless sky, site at sea level, and upper-air variation of temperature, water vapor, and pressure as given by Eq. [47] and Figs. 15 and 16. The resulting values of A are plotted in Fig. 18.

The quantity of particular interest in solar heat collector design, as well as in a variety of similar problems, is the net radiation exchange between an exposed horizontal thermally black surface at air temperature and the sky above it. This is the quantity to which we assign the symbol R.

$$R \equiv \sigma T_a^4 - A = (1 - \epsilon_a)\sigma T_a^4 \qquad [52]$$

This quantity R can be obtained from Fig. 18, by subtracting values of A from values of black-body

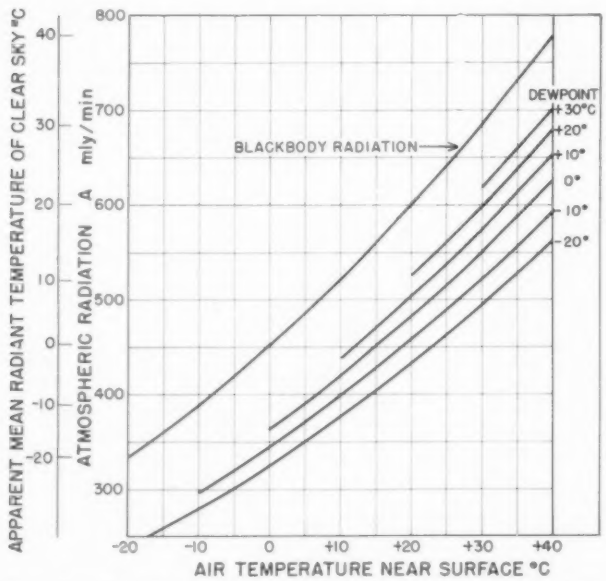

FIG. 18—Typical values of atmospheric radiation from clear skies at sea level.

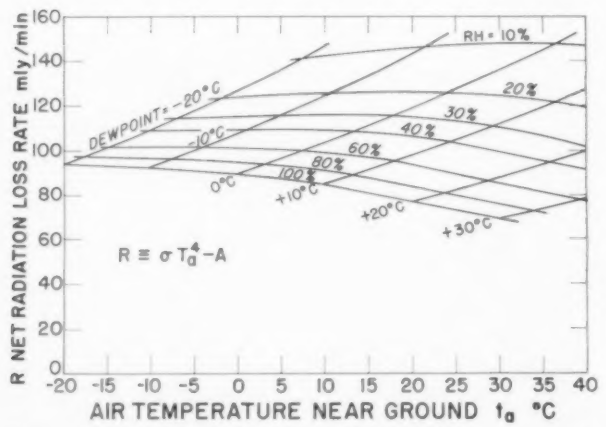

FIG. 19—Typical values of R for clear skies at sea level—metric units.

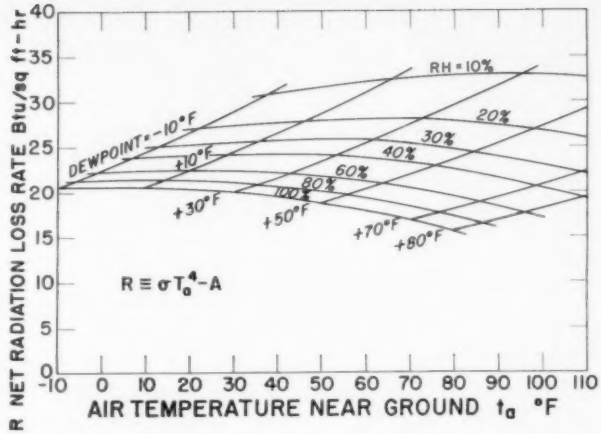

FIG. 20—Typical values of R for clear skies at sea level—English units.

radiation. However, because of its practical importance, we have plotted it separately, in both metric and English units, in Figs. 19 and 20.

EFFECTS OF CLOUDS, ALTITUDE, AND OTHER VARIATIONS

Figures 17, 18, 19, and 20 all refer to clear skies, sea level, and typical atmospheric variations with height of temperature, water-vapor content, and pressure.

The effect of clouds is always to increase atmospheric radiation relative to clear sky conditions. Any cloud which is visually opaque may be assumed to radiate as a black body at the temperature of the cloud base. In general, the radiative effect of clouds is to "close the atmospheric window" of transparency in the 8.5–13 micron region. A rough but reasonable method of allowing for this may be described by numerical example.

Suppose that air temperature near the surface of the ground is 290 K and conditions are such that the calculated clear sky emissivity ϵ_a would be 0.80. However, the sky is completely covered with clouds whose base temperature is 250 K. We wish to determine ϵ_a for the cloudy condition.

We begin by assuming that the 20% deficiency in radiation from the clear sky is entirely due to a region of complete transparency in the region of the "atmospheric window" and that all other portions of the spectrum would be black. This is not too bad an assumption, as can be seen from Fig. 7. Now the "black" cloud will radiate to the ground through this spectral window. The fraction of black-body radiation at 290 K contributed by the cloud will then be $(250/290)^4 \times 0.20 = 0.11$. Hence the clear sky emissivity will be increased by 0.11, and the resulting over-all emissivity ϵ_a will be 0.91.

Provided the cloud base temperature can be estimated, the above scheme is probably a good one for estimating the added apparent emissivity caused by

VOL. 5 1961

clouds. If the clouds do not cover the entire sky, appropriate allowance should be made for the per cent of sky actually covered and the position of the clouds. Clouds directly overhead naturally exert more influence than those off to the sides of the sky.

Other factors being equal, the effect of increasing altitude of site is always to decrease the atmospheric radiation, because of the influence of the pressure correction Eq. [45b]. At sea level, as we have already seen, the influence of the pressure correction on over-all emissivity is quite small. But if the site is at a higher altitude the pressure correction effect may be quite significant, because it "starts off", so to speak, right at ground level, and its influence is felt in the important first few hundred meters of air above the site.

Also, in general, other factors are *not* usually equal at higher altitudes. At a high altitude site the distribution of water vapor above the site is apt to be different from that suggested as typical by Fig. 16. Hence, to estimate atmospheric radiation to be expected at high altitude sites, one should consider both the pressure correction and the water-vapor distribution above the site.

Even at sea level, atmospheric conditions do not, of course, always vary with height in the typical fashions given by Figs. 15, 16, and Eq. [47]. If conditions are known to be different from those indicated by the typical curves, the emissivity ϵ_a should be calculated directly from Fig. 13, using a tabulation procedure similar to that of Table 2. In cases of low amounts of precipitable water (say $m_{ws} < 0.4$ g/sq cm) appropriate carbon dioxide corrections from Fig. 9 should be used.

If one has occasion to make a series of emissivity calculations such as exemplified in Table 2, it should be noted that the form of that tabulation was chosen to best illustrate the basic procedures and reasoning involved, and is not necessarily in the most convenient form for making a series of calculations of this type. In particular, the engineer confronted with making a series of such emissivity calculations should familiarize himself with the meteorologist's customary procedure of expressing heights in terms of pressure units (usually millibars). The utilization of this concept will usually result in more expeditious handling of the various calculations leading up to and embodied in an iteration such as Table 2. An example of a more "streamlined" tabulation than ours is given by F. A. Brooks.[19] Incidentally, at least insofar as the determination of the intensity of atmospheric radiation near ground level is concerned, the graphical methods used by Elsasser[10] or Robinson[20] are more cumbersome than tabulation methods.

In situations where the closest possible estimate of atmospheric radiation is desired, attention should be paid to the rapid variation of air temperature with height in the first few meters above the ground. As has already been mentioned, Eq. [47] does not properly apply in this region. The air temperature measured 20 meters above the ground may, and often does, differ by one or two centigrade degrees from that measured two meters above the ground. And, in turn, the air temperature measured at two meters often differs one or two degrees from that measured 10 centimeters above the ground surface. Much further information on this matter is given in an excellent book by Geiger.[21]

DISCUSSION AND CONCLUSION

We believe that the procedures developed in this article, together with the data presented, are adequate for most engineering problems requiring an estimate of the intensity of atmospheric radiation upon horizontal surfaces near ground level.

The values of apparent atmospheric emissivity ϵ_a which we have derived in this article are a little higher than those usually appearing in meteorological literature. For example, for the atmospheric conditions upon which Table 2 is based, and for which we obtained $\epsilon_a = 0.84$, the values of ϵ_a for the same conditions as determined by F. A. Brooks,[19] Elsasser,[10] and Robinson,[20] would be about 0.80, 0.79, and 0.74 respectively.

No two of the three authorities mentioned use the same set of corrections for slab emissivity, presence of carbon dioxide, and varying pressure, and none of them uses the set used in this article. However, the over-all effect of the various corrections used comes out about the same in all cases, insofar as the determination of ϵ_a is concerned. The chief reason for the differing estimates of ϵ_a lies in differing estimates of the hemispherical emissivity ϵ_w of water vapor. We have taken Hottel's determination of water-vapor emissivity as the basis of our calculations, and his estimate is a little higher than those generally taken by meteorologists.

Hottel and Egbert estimated that their values of water-vapor emissivity were accurate to about five per cent. Since, to a close approximation, $A \sim \epsilon_a \sim \epsilon_w$, the indicated accuracy of A as calculated from their water-vapor emissivity measurements perhaps is also on the order of 5 per cent, certainly should not be considered as much closer than this.

A small fractional uncertainty in A leads to a considerably larger fractional uncertainty in R. As is readily found from Eqs. [51] and [52]:

$$\frac{dR}{R} = \frac{\epsilon_a}{1 - \epsilon_a}\frac{dA}{A} \approx \frac{0.8}{1 - 0.8}\frac{dA}{A} \approx 4\frac{dA}{A} \qquad [53]$$

Hence a 5 per cent uncertainty in A implies something like a 20 per cent uncertainty in R. It may be mentioned that R can be determined by direct outdoor measurement, using various types of radiometers de-

veloped for the purpose. However, the present accuracy of these devices is often considered to be no closer than 10–20 per cent.[11] Consequently, as a practical matter, at the present time there does not seem to be much to choose between the accuracy of R as determined by emissivity calculations such as those developed in this article, and its accuracy as determined by direct measurements.

The heat transfer engineer who has read to this point is by now aware that there is nothing particularly mysterious about atmospheric radiation—in its fundamentals it is a problem quite similar to the problems encountered in connection with radiation from nonluminous gases in furnace design. However, it is hoped that this exposition of the details of atmospheric radiation calculations will be helpful both to designers of solar heat collectors and others who find it necessary to "put some numbers" to the fact that "a clear sky is 'colder' than air temperature near the ground."

ACKNOWLEDGMENT

Grateful acknowledgment is made to Professor J. E. McDonald for his expert and helpful criticism of the entire article; to M. K. Donovan, who worked up most of the graphs and tabulations; and to Robert Solomon, Franz Kurath, W. G. Beck, and R. Stouffer, who assisted greatly on preparation of graphs and manuscript.

REFERENCES

1. McAdams, W. H. *Heat Transmission*, 3d Ed. McGraw-Hill, 1954. 1a, p. 64–65; 1b, Fig. 4–15, p. 85; 1c, Fig. 4–13, p. 83.
2. Jakob, Max. *Heat Transfer*, Vol. I, John Wiley & Sons, 1949. 2a, p. 28–29.
3. Eckert, E. R. G. and Drake, R. M. *Heat and Mass Transfer*, McGraw-Hill, 1959. 3a, p. 360–61; 3b, p. 364 (Values of $i_{bn\lambda}T^5$ given in Table 13-2 are all approximately 8% too low); 3c. fig. 13–19, p. 386.
4. Richtmeyer, F. K. and Kennard, E. H. *Introduction to Modern Physics*, 4th Ed., McGraw-Hill, 1947. 4a, p. 178–83.
5. Lowan, A. N. and Blanch, G. "Tables of Planck's Radiation and Photon Functions" (Project for Computation of Mathematical Tables, Works Project Administration, New York City). *J. Opt. Soc. Am.* **30:** 70–81, February 1940.
6. Dunkle, R. V. "Thermal Radiation Tables and Applications," *Trans. ASME*, **76:** 549–52, May 1954.
7. Haltiner and Martin. *Dynamical and Physical Meteorology*, McGraw-Hill, 1957. 7a, p. 81 (Eq. 6–12 is erroneous. Correct value of integrated Planck's function as given is σT^4, not $\sigma T^4/\pi$); 7b, p. 112; 7c, p. 52.
8. Hottel, H. C. and Egbert, R. B. "Radiant Heat Transmission from Water Vapor." *Trans. Am. Inst. Chem. Engrs.* **38:** 531–568, 1942.
9. Hottel, H. C. and Egbert, R. B. "The Radiation of Furnace Gases." *Trans. Am. Soc. Mech. Engrs.* **63:** (4) 297–307, May 1941.
10. Elsasser, W. M. "Heat Transfer by Infrared Radiation in the Atmosphere." *Harvard Meteorological Studies* No. 6, 1942.
11. Kondratyev, K. Ya. *Radiant Heat Exchange in the Atmosphere* (in Russian). Hydrometeorological Publishing House, Leningrad, 1956. Note: A translation of this book has been made by RCA Corp. for the U. S. Army Signal Intelligence Agcy., Arlington 12, Virginia. A second translation is presently in progress by the U. S. Weather Bureau.
12. Weber, L. R. and Randall, H. M. "The Absorption Spectrum of Water Vapor Beyond 10 Microns." *Phys. Review*, **40:** 835–47, 1932.
13. Randall, H. M. *et al.* "The Far Infrared Spectrum of Water Vapor." *Phys. Rev.* **52:** 160–74, 1937.
14. Hottel, H. C. and Mangelsdorf, H. G. "Heat Transmission by Radiation from Non-Luminous Gases II. Experimental Study of Carbon Dioxide and Water Vapor," *Trans. Am. Inst. Chem. Engrs.* **31:** 517, 1935.
15. Hottel, H. C., and Smith, V. C. "Radiation from Non-Luminous Flames." *Trans. ASME*, **57:** 463–70, 1935.
16. Jahnke, E. and Emde, F. *Tables of Functions*, 4th Ed., Dover Publications, 1945.
17. Brunt, D. *Physical and Dynamical Meteorology*, 2d Ed., Cambridge, University Press, 1952.
18. Byers, H. R. "Significance of Different Vertical Distributions of Water Vapor in Arid and Humid Regions," Tech. Report No. 3, Institute of Atmospheric Physics, The University of Arizona, March, 1957.
19. Brooks, F. A. "Atmospheric Radiation and its Reflection from the Ground." *J. Meteorology*, **9:** (1) 41–52, February, 1952.
20. Robinson, G. D. "Notes on the Measurement and Estimation of Atmospheric Radiation." *Quart. J. R. Met. Soc.*, **76:** 37–51, 1950.
21. Geiger, R. *The Climate Near the Ground*. Harvard University Press, 1950.

VOL.
5
1961

Flow Systems in the Solar Furnace and the Photolysis of Nitrosyl Chloride*

Rudolph J. Marcus and Henry C. Wohlers

Chemistry Department, Stanford Research Institute, Menlo Park, California

This paper reports the design, construction, installation, testing, and use of various flow systems in a 2-ft-diam solar furnace. The flow system finally used is more complex than usual, since it was designed to handle a corrosive solution of nitrosyl chloride in carbon tetrachloride.

In this flow system the focal spot of the furnace is contained in the center of a 15-mm-diam quartz tube through which solution is pumped at the rate of 500 ml per min. Alternatively the focal spot is in a free-falling stream of solution which impinges on a splash plate immediately after illumination.

The flow system achieved two objectives.

1. The separation of the photoproducts before appreciable back reaction occurred.

2. Adequate temperature control without any cooling.

The flow system was used to study the photolysis of nitrosyl chloride in carbon tetrachloride solution to form nitric oxide and chlorine. The results can be summarized and compared with those of the static system which was studied previously.

	Flow System	Static System
Average quantum yield	0.22	0.023
Average energy stored as percentage of available energy in the 3000–6300 Å range	1.71	0.18

These results were obtained without optimization of various experimental parameters such as light intensity, flow rate, concentration, etc.

INTRODUCTION

The photodecomposition of nitrosyl chloride is one promising reaction for the photochemical storage of solar energy. This reaction,

$$2\ NOCl \xrightarrow{h\nu} 2\ NO + Cl_2, \qquad [1]$$

is listed in Daniels'[5] table of photochemical quantum yields. Thermodynamically the photodissociation of nitrosyl chloride is endergonic by 4.9 kcal/mole. The efficiency, Q, of conversion of radiant energy to chemical energy as defined by Calvert[4] is 21.8%. The free energy stored in the products of this reaction is available upon demand by recombination of the nitric oxide and chlorine to form the original nitrosyl chloride.

Many authors[1-5, 7-9, 13, 16-21, 23, 24] have reported on the results of both the thermal and photochemical decomposition and recombination of nitrosyl chloride. These results have been discussed in a previous paper.[14] All available physical, photochemical, and thermochemical data on nitrosyl chloride, nitric oxide, and chlorine are also gathered in that paper.

Reaction [1] occurs in solution as well as in the gas phase. This is significant for possible energy storage applications of this reaction, because it provides separation of the photoproducts. Chlorine stays in solution and nitric oxide, being much less soluble in solvents such as carbon tetrachloride, can be stored in the gas phase.

Neuwirth,[17] using a 500-watt projection lamp as a source of light, found quantum yields ranging from 0.7 to 1.1 for the primary reaction of decomposition of nitrosyl chloride in carbon tetrachloride; these values dropped to 0.05 to 0.1 when a steady state was reached. This author suggested that the best way to reduce the effect of the back reaction was to use a dynamic system in which the carbon tetrachloride solution of nitrosyl chloride was continuously removed from the reaction vessel.

Pitts, Margerum, and McKee[18] discussed the photodecomposition of gaseous nitrosyl chloride for space power generation. These authors calculated that the maximum theoretical efficiency for this reaction, utilizing the 2150–6300 Å range (about 562 w/m^2), was 16.9%. Using a mercury lamp (4750 Å), about 80% decomposition of gaseous nitrosyl chloride at 400 mm Hg pressure occurred in 10 min. The rate of the back reaction was such that half of the photolysis products recombined after about 15 min in the dark.

We have previously reported[13] on the insolation of nitrosyl chloride in carbon tetrachloride at the focus

* This work was supported by the Air Force Cambridge Research Center under Contract AF 19(604)-7302.

of a 2-ft solar furnace.[12] In experiments using a static system, less than 2% of the initial nitrosyl chloride was decomposed—based upon pressure readings and upon the chloride ion titration (Volhard method) of the initial and final solutions. In a preliminary experiment, a gravity feed flow system was used in an attempt to minimize or prevent the recombination of the products, nitric oxide and chlorine. The results with the preliminary flow system approximated those with the static system.

We are now reporting on the photolysis of nitrosyl chloride in carbon tetrachloride in a dynamic system. The light source for the photolysis was, as before, the focal spot of a 2-ft diam solar furnace. This work required the installation of a flow system in the solar furnace. This system will be described first.

DESIGN AND OPERATION OF A FLOW SYSTEM IN THE SOLAR FURNACE

The Solar Furnace as a Light Source

The solar furnace was used as a light source for the nitrosyl chloride reaction. We have found that photochemical reactions generally proceed by the same mechanism in the solar furnace as under laboratory conditions. This use of the solar furnace, rather than unconcentrated sunlight, means that a far greater output will be obtained from reactions which will convert solar energy into various other, storable, forms of energy. Such studies and the equipment to handle such reactions, as well as the instrumentation to follow them, have been developed and described.[10-13].

Advantages of Flow System

Various flow systems were constructed which allowed the reactant molecules only limited time in the focal spot of the 2-ft front-surfaced parabolic mirror. The residence time was controlled by using a direct pumping system to feed a reactant solution through a small insolation cell.

Advantages of a flow system for photochemical reactions are obvious. If the reacting solution (or gas) could be pumped quickly through the highly concentrated light at the focus of a solar furnace, the extent of the reaction could be controlled by the residence time in the focus. Further, the rate of a reverse reaction would be drastically minimized if one product could be removed from the system. Swift passage of the material through the focus would reduce the unwanted decomposition of light- or heat-sensitive chemicals.

Another advantage would be a large reduction in capital costs for heat transfer equipment in commercial installations. Because the residence time of the solution in the focus of the solar furnace would be short, heating would be minimized and the cooling system, if required, would be small.

Although the study of flow systems for the solar furnace is of general value for photochemical reactions in a concentrated light source, the emphasis in the work reported here was on the decomposition of nitrosyl chloride.

Corrosion of NOCl and Solvent Effect of CCl_4

Design of the flow system was hampered by the corrosive action of the nitrosyl chloride and the solvent effect of the carbon tetrachloride. Materials compatibility tests[15] have shown that, among the metals, nickel, monel, tantalum, and Udimet 500 have good resistance to nitrosyl chloride; among the plastics, unplasticized Kel-F film and Teflon have good resistance, and others such as Silastic LS-53, polyethylene, Viton A, Kel-F elastomer, and Hypalon have sufficient resistance to attack to be considered for some applications. Other data[22] have indicated that Teflon, Kel-F elastomer, and Compar (polyvinyl alcohol) have good resistance to carbon tetrachloride. These were the major materials of which the flow system had to be constructed.

Pump for NOCl System

A Teflon pump with a Kel-F elastomer liner was obtained for the nitrosyl chloride flow system. This Vanton Flex-i-liner pump* is unique in that pumping is accomplished by a rotor mounted on an eccentric shaft which rotates within the elastic liner. This creates a squeegee action on the fluid trapped between the liner and the inside of the rigid Teflon body block. No metal parts are in contact with the pumped fluid; the body block and the flexible liner are the only two pump parts in contact with the pumped fluid. Both a Kel-F liner and a Compar liner were tested. During two months of experimentation with solutions up to 0.5 molar nitrosyl chloride in carbon tetrachloride, both liners were satisfactory, although the Compar liner showed some evidence of solvent action.

Other, simpler pumps could be used if less corrosive liquids were used. The one disadvantage of the pump used in these tests was that the squeegee action produced a pulsating solution flow. It was thus necessary to insert a surge vessel into the flow system to minimize this pulsating action.

Pump Motor

In order to obtain a variable solution flow, a $\frac{1}{4}$-hp General Electric Company half-wave thymotrol drive, direct-current motor was connected to the pump. In this electronically controlled system, the controller converts alternating current from the 220-v power line

* Model XB-T6, Maximum capacity 1 gpm H_2O at 70°F, 0 psig, Vanton Pump and Equipment Corp., Hillside, N. J.

VOL. 5 1961

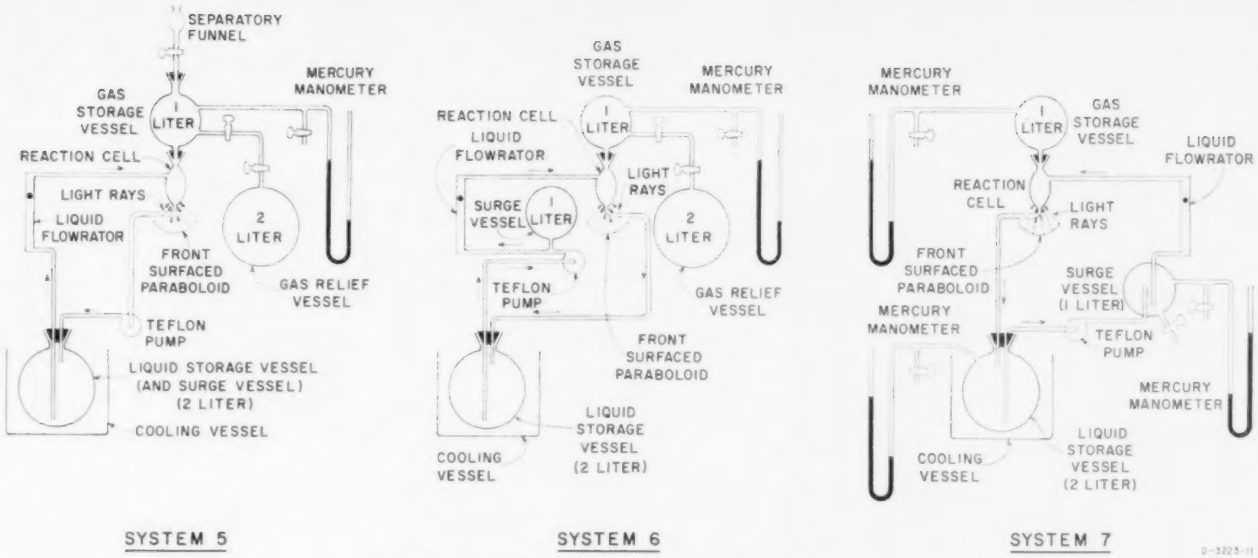

FIG. 1—Flow systems for liquid phase photochemical reactions.

to direct current to drive the motor; the d-c shunt motor is designed for use with the controller. The motor speed was adjustable over a wide, stepless range from 0 to 1750 rpm. Specifications stated that with constant line voltage and motor temperature the sustained change in speed would not exceed 3% of top speed from "no load" to "full load" for any speed within the rated speed range.

Flow Apparatus

Three different flow systems were used; these are shown in Fig. 1. Figure 2 shows the flow system in actual operation. In system 5 (Fig. 1), the nitrosyl chloride storage vessel and the surge vessel to minimize the pulsating flow were combined into a single unit; pressure from the discharge side of the pump forced the solution from the liquid storage vessel through the system. For system 6, a separate surge vessel was used, so the suction side of the pump was connected directly to the solution in the liquid storage vessel. System 7 was a modification of system 6; in system 7, the surge vessel was an integral part of the flow apparatus so that there was a minimum holdup of liquid in that vessel. The three systems worked equally well in the flow experiments. Each system may have a particular advantage depending upon the photochemical reaction under investigation, and it was felt that system 7 was most advantageous for the nitrosyl chloride-carbon tetrachloride system.

Reaction Cells

Four quartz reaction cells, shown in Fig. 3, were designed, constructed, and tested. Cells H and I were designed with a splash plate to facilitate quick separation of nitric oxide from the dissolved chlorine. In these cells the focal spot could be located at any point of the free-falling stream between the nozzle and the splash plate. In practice, the focal spot was located either at the nozzle tip or at the splash plate itself. In the latter

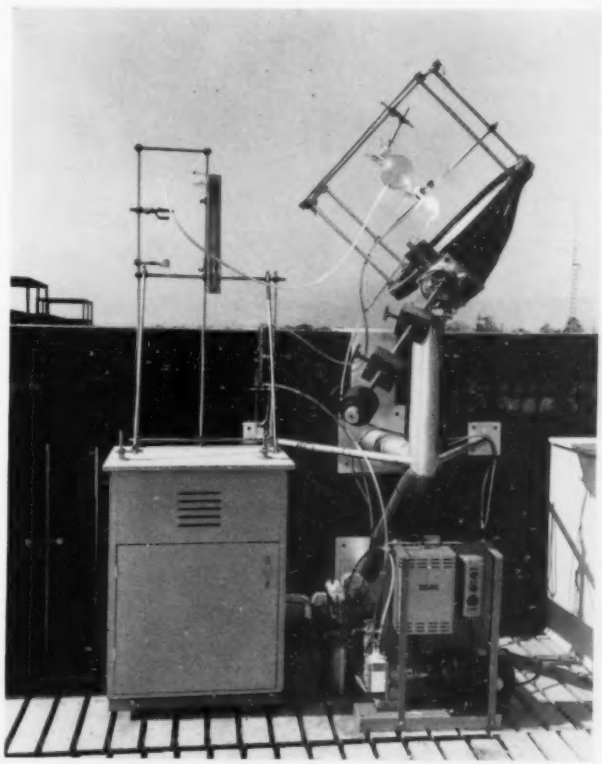

FIG. 2—Flow apparatus showing system 5 and reaction cell H in operation.

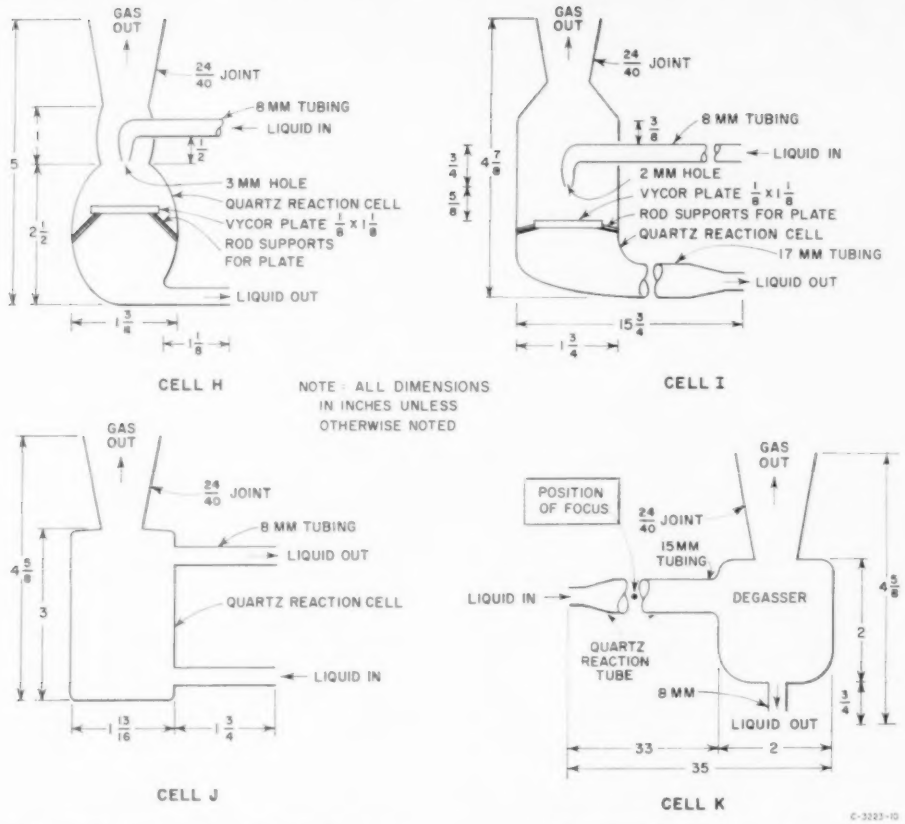

FIG. 3—Reaction cells used for liquid photochemical flow systems—In cells H and I, the focal spot is located in the stream between nozzle and splash plate. In cells J and K, the focal spot is at the center of the liquid.

FIG. 4—Flow apparatus showing cell H in operation (photograph taken at f 32, 1/400 sec).

FIG. 5—Flow apparatus showing cell K in operation (photograph taken at f 32, 1/400 sec).

case, concentrated illumination of a thin film was obtained. Cells J and K were designed so that the focal spot was in the body of the solution; these two cells were not designed specifically for the nitrosyl chloride

VOL. 5 1961

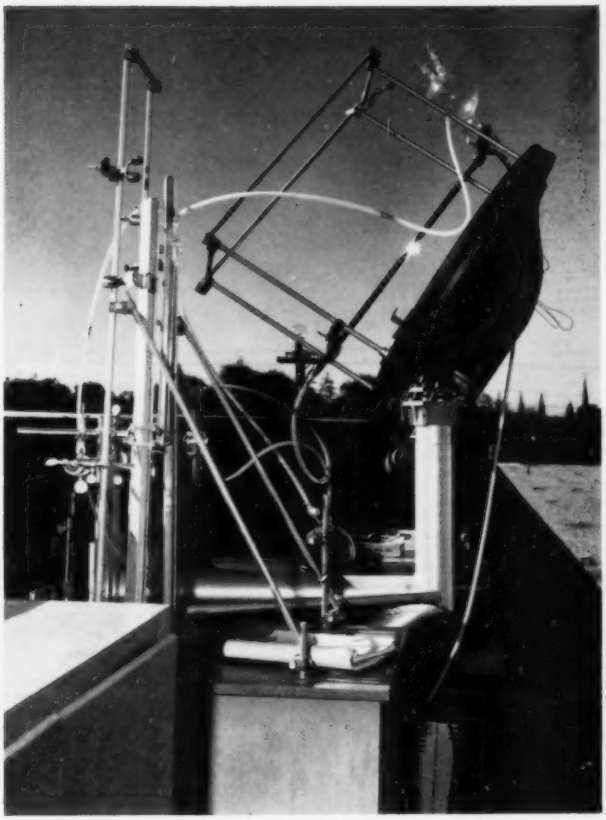

FIG. 6—Flow apparatus showing system 7 and reaction cell K in operation.

reaction. Cell J was, however, similar to the cell used in the static system, but without any provision for cooling in the area of the focal spot. Cell K provided a greater light flux for a small instantaneous volume of solution and had provisions for degassing. Figures 4 and 5 show detailed photographs of cells H and K, respectively, in actual operation. Figure 6 shows cell K in operation in system 7.

Operating Procedure

At the start of a run, the entire system was flushed with argon to displace atmospheric oxygen. The storage vessel, containing the nitrosyl chloride-carbon tetrachloride solution, was attached to the apparatus after aliquots were removed for analysis of the nitrosyl chloride by the Volhard method.

The pump was then started to force the solution through the system; after flow equilibrium was attained, the reaction cell was exposed to concentrated light. During the run, changes in gas pressure were recorded. At the conclusion of a run, aliquots of the photolyzed carbon tetrachloride solution were taken for chloride analysis.

During these experiments, solution flow rates of 50 to 600 ml/min were used without evidence of any appreciable heating of the solution in either the reaction cell or the liquid storage vessel.

EXPERIMENTAL DATA

Preliminary experiments showed that flow system 7 produced the most reliable data of the photolysis of nitrosyl chloride. It was designed so that the gas pressure at the three major vessels could be measured; the type of surge vessel used in these experiments minimized the holdup of the circulating liquid.

During the experiments with concentrated light, it was noted that the gas pressure in the gas storage vessel increased. This pressure decreased when the cover was placed on the furnace, exposing the cell only to the unconcentrated light of the sun. To determine the effect of the concentrated light on the net decomposition of nitrosyl chloride in the flow system, the pressure-volume products of the three parts of the system were algebraically added.

The necessity for this procedure is demonstrated in Fig. 7, in which the liquid flow rate is plotted against the speed of the pump motor for two experiments (nos. 44 and 46). The flow rate was increased and decreased several times in these experiments; the numbers represent the sequence in which the readings were taken and thus show whether the flow rate was increased or decreased at each point. The range indicates, where it is given, the spread of readings over a period

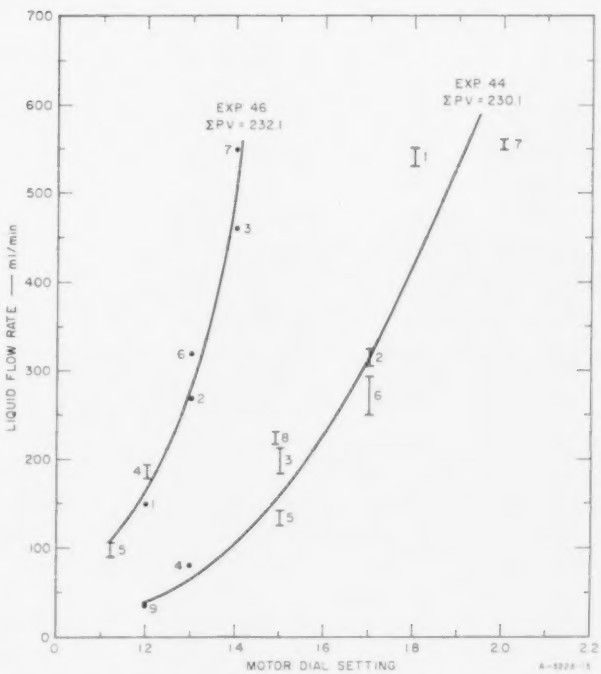

FIG. 7—Liquid flow rate dependence on speed of pump motor at constant sum of the pressure-volume products (ΣPV) of the three components of the flow system—$NOCl$-CCl_4 solution in unconcentrated light; system 7 and cell K; numbers show sequence of readings.

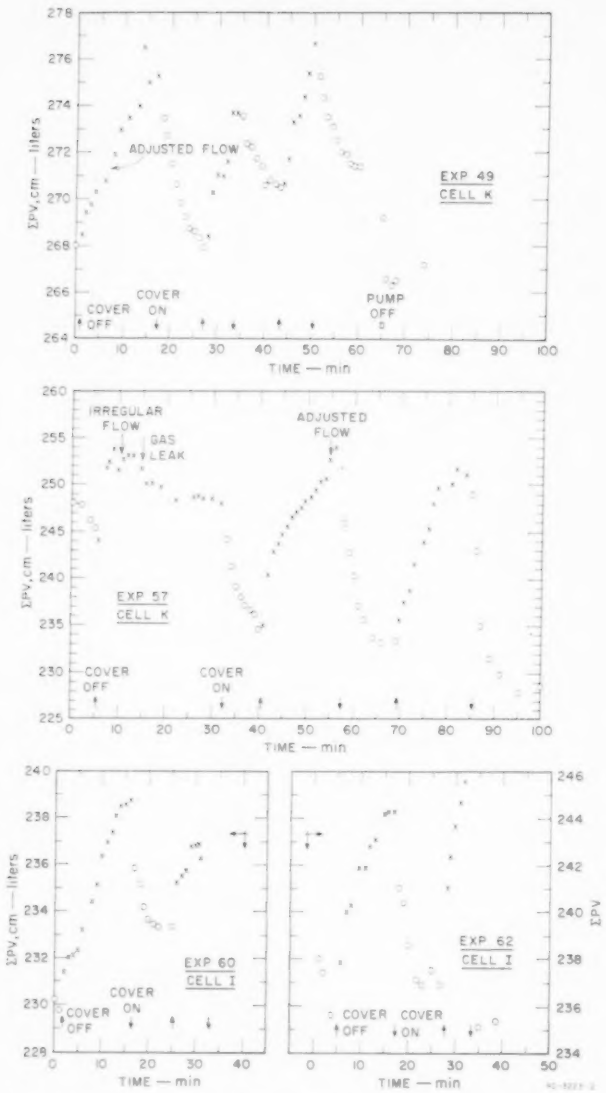

FIG. 8—Results of four typical experiments with concentrated (X) and unconcentrated (O) light.

of time. It should be noted that these readings make sense only when they are taken at a constant sum of the pressure-volume products of the three components of the flow system, viz., the liquid storage vessel, the surge tank, and the gas storage vessel.

Experiments 44 and 46 (shown in Fig. 7) also serve as blank runs. They were performed with unconcentrated light (i.e., with the cover on the furnace). Any effect which is due to the unconcentrated light should be reflected in these curves.

Results of three typical experiments with concentrated light are shown in Fig. 8. Data for experiment 57 show that the pressure-volume increase upon exposure to concentrated light was 19 and 20 cm-l respectively, for the time period 41–58 min and 70–86 min; based upon a gas volume of 3.0 l, the increase in pressure was 6.5 cm Hg. The increase in pressure for experiment 49 was 1.8 cm Hg; for experiments 60 and 62 it was 2.9 and 2.7 cm Hg, respectively. This pressure increase may be considered as the net effect of concentrated light on the carbon tetrachloride solution of nitrosyl chloride—or expressed differently, the excess of nitrosyl chloride decomposition over the recombination of the reaction products, nitric oxide and chlorine. The magnitude of the pressure increase upon illumination may be gauged by subtracting 228 (i.e., three times atmospheric pressure) from the ΣPV figures.

DISCUSSION OF RESULTS

The results may be expressed in terms of the photodissociation of nitrosyl chloride and of the recombination of the photoproducts nitric oxide and chlorine. The pressure rise upon exposure to concentrated light ("cover off" in Fig. 8) shows that gas is being given off, and that the rate of production of that gas rapidly approaches a steady state. The location of the steady state is governed by the speed of the back reaction, which occurs mainly where the gas storage system joins the liquid circulating system.

Once the steady state has been established, the gas is generated only as fast as it is consumed by the back reaction. On the other hand, if the gas were withdrawn continuously to feed a nitrosyl chloride fuel cell, the steady state would be upset and the gas would be generated at the rate at which it is generated in the approach to the steady state in our experiments.

Rate of Reaction

On this basis we can calculate a forward rate of reaction [1] as it occurs in the solar furnace. The net rate (R_n) of reaction [1], which is the quantity we observe, is the difference between the forward rate (R_f) and the backward rate (R_b), which can be calculated from known rate constants

$$R_n = R_f - R_b = k_f I[\mathrm{NOCl}] - k_b[\mathrm{NO}]^2\,[\mathrm{Cl_2}] \quad [2]$$

These calculations are carried out for some flow experiments in this series in Table 1. It should be noted that the backward rate is a small, but noticeable part (of the order of 3%) of the net rate, and that the rate of gas evolution perforce decreases to that value when the steady state is established.

The same calculation can be carried out for experiments with the static system, which are shown in Fig. 5 of ref. 13. The backward rate was somewhat higher in these experiments than it was in the flow experiments, and the net rate of gas evolution was of the same order of magnitude as that found in the flow experiments.

VOL. 5 1961

TABLE 1—Rates, Quantum Yields, and Calculated Energy Storage for Photolysis of Nitrosyl Chloride in Flow System [7]

Expt.	Net rate of gas evolution: R_n moles/l-min	Rate of backward reaction: $2NO + Cl_2 \rightarrow 2NOCl$: R_b moles/l-min	Rate of forward reaction: $2NOCl \xrightarrow{h\nu} 2NO + Cl_2$: R_f moles/l-min	Net quantum yield ϕ_n	Quantum yield for forward reaction ϕ_f	Initial NOCl concentration $[NOCl]_0$ moles/l	Flow Rate l/min	Light Saturation Factor $\frac{N\,h\nu}{[NOCl]_0}$ time %	Maximum Energy Storage cal/min	Rate of energy storage $\phi\Delta F^\circ_{h\nu_{4500}}$ min^{-1} Energy Storage in 3000–6300 Å Range %
Flow System										
49	1.04×10^{-4}	3.32×10^{-6}	1.07×10^{-4}	0.075	0.077	0.243	0.350	4.9	1.53	0.58
	2.26×10^{-4}	1.67×10^{-6}	2.28×10^{-4}	0.16	0.16	0.243	0.350	4.9	3.32	1.2
	2.26×10^{-4}	3.66×10^{-6}	2.30×10^{-4}	0.16	0.17	0.243	0.350	4.9	3.32	1.2
52	1.67×10^{-4}	1.13×10^{-6}	1.68×10^{-4}	0.12	0.12	0.190	0.350	6.3	2.45	0.92
	2.38×10^{-4}	10.2×10^{-6}	2.48×10^{-4}	0.17	0.18	0.190	0.350	6.3	3.51	1.3
55	1.30×10^{-4}	2.14×10^{-6}	1.32×10^{-4}	0.094	0.095	0.059	0.250	2.8	1.92	0.72
57	10.0×10^{-4}	33.8×10^{-6}	10.3×10^{-4}	0.72	0.74	0.283	0.300	3.6	14.7	5.5
	3.73×10^{-4}	53.0×10^{-6}	4.26×10^{-4}	0.27	0.31	0.283	0.300	3.6	5.47	2.1
60	1.65×10^{-4}	6.15×10^{-6}	1.71×10^{-4}	0.12	0.12	0.146	0.400	7.1	2.45	0.91
62	1.47×10^{-4}	5.98×10^{-6}	1.53×10^{-4}	0.11	0.11	0.265	0.350	4.5	2.16	0.81
	6.47×10^{-4}	5.98×10^{-6}	6.53×10^{-4}	0.47	0.47	0.265	0.350	4.5	9.6	3.6
Average				0.224						1.71
Static System										
46	3.77×10^{-4}	1.83×10^{-5}	3.95×10^{-4}	0.038	0.040	0.162	—	130	0.78	0.29
Ref: 13	2.24×10^{-4}	1.51×10^{-5}	2.40×10^{-4}	0.022	0.024	0.162	—	210	0.45	0.17
Fig. 5	2.10×10^{-4}	1.63×10^{-5}	2.27×10^{-4}	0.021	0.023	0.162	—	230	0.43	0.16
	1.82×10^{-4}	2.34×10^{-5}	2.04×10^{-4}	0.018	0.020	0.162	—	310	0.36	0.14
	1.68×10^{-4}	0.67×10^{-5}	1.75×10^{-4}	0.017	0.018	0.162	—	230	0.35	0.13
Average				0.023						0.18

Light Utilization

Nitrosyl chloride in solution absorbs light fairly continuously[14] between 3000 Å and 6300Å. This absorption covers 38% of the solar spectrum.[6] Since the 2-ft-diam solar furnace collects 49 w,[12] it collects 18.6 w in the wavelength range absorbed by nitrosyl chloride. This corresponds to a rate of energy collection of 266 cal/min in the 3000–6300 Å wavelength range. If the average energy of a mole of photons is taken as 64 kcal/einstein in that wavelength range, a photon flux ($h\nu_{4500}$ min^{-1}) of 4.16×10^{-3} einsteins/min exists at the focal spot.

This figure enables us to estimate a quantum yield, ϕ, for gas evolution. When these are calculated from the net rate of gas evolution, they are listed as ϕ_n in Table 1. When they are calculated from the rate of the forward reaction, they are listed as ϕ_f in Table 1. The average of these quantum yields is 0.224, which is of the same order of magnitude as the value reported for a laboratory determination of the optimum quantum yield.[1]

For comparison, quantum yields have also been calculated for experiments with the static system.[13] These average 0.023 and are a whole order of magnitude smaller than those for the flow system.

It should be pointed out that these rough quantum yields have been obtained without knowing optimum values of such experimental parameters as concentration, flow rate, and configuration of irradiation cell, and also without extrapolation to zero light intensity. Such optimization should be performed when a nitrosyl chloride fuel cell can be attached to the system. Under those conditions the power output and power storage can be measured in terms of light input and the other parameters already mentioned.

One of the differences between the flow system and the static system is illustrated by a light saturation factor. This factor compares the number of molecules of nitrosyl chloride with the number of photons in the focal plane in unit time. It is seen from values of this factor in Table 1 that the static system was light-saturated, while the flow system was not light-saturated.

Energy Storage

The most precise indication of energy storage in these experiments would be to measure output from a nitrosyl chloride fuel cell. Since no such device was available, we have added to Table 1 two columns showing what this energy storage would be if all of the

gas evolved were converted to electrical power. One of these is the product of photon flux (4.16×10^{-3} einstein/min), quantum yield, and free energy of recombination (4.9 kcal/mole). This is the rate of energy storage in cal/min; it can be seen that this is a fraction of a watt. We can also compute the efficiency of this storage by dividing the rate of energy storage by the rate of energy collection (266 cal/min); this efficiency averages 1.71%.

These quantities have also been evaluated for experiments with the static system. The energy storage was somewhat smaller in the static system than in the flow system. The efficiency of this storage averaged 0.18%, or a whole order of magnitude less than the efficiency shown by the flow system.

What we have shown, then, is that a flow system is capable of separating the products of the photolysis of nitrosyl chloride.

REFERENCES

1. Atwood, K., and G. K. Rollefson. *J. Chem. Phys.* **9,** 506 (1941).
2. Bailey, C. R., and A. B. D. Cassie. *Proc. Roy. Soc.* (London) **A145,** 336 (1934).
3. Bowen, E. J., and J F. Sharp. *J. Chem. Soc.* **127,** 1026 (1925).
4. Calvert, J. G. *Ohio J. Sci.* **53,** 293 (1953).
5. Daniels, F. *J. Phys. Chem.* **42,** 713 (1938).
6. Friedman, D. *NRL Memorandum Report* 1005, December 1959.
7. Goodeve, C. F., and S. Katz. *Proc. Roy. Soc.* (London) **A172,** 432 (1939).
8. Kiss, A. *Rec. trav. chim.* **42,** 665 (1923).
9. Kistiakowsky, G. B. *J. Am. Chem. Soc.* **52,** 102 (1930).
10. Marcus, R. J., and H. C. Wohlers. *Ind. Eng. Chem.* **51,** 1335 (1959).
11. Marcus, R. J., and H. C. Wohlers. *Ind. Eng. Chem.* **52,** 377 (1960).
12. Marcus, R. J., and H. C. Wohlers. *Ind. Eng. Chem.* **52,** 825 (1960).
13. Marcus, R. J., and H. C. Wohlers. *Solar Energy* **4**(2), 1 (1960).
14. Marcus, R. J., and H. C. Wohlers. *Solar Energy* **5,** 44 (1961).
15. Margerum, J. D., and E. Findl. Sundstrand Turbo Division of Sundstrand Corporation. Private communication.
16. Natanson, G. L. *Acta Physiocochim.* USSR **11,** 521 (1939).
17. Neuwirth, O. *J. Phys. Chem.* **63,** 17 (1959).
18. Pitts, J. N., J. D. Margerum, and W. E. McKee. "Photochemistry and Space Power Generation." Presented at American Rocket Society Meeting, May 1960.
19. Rosenberg, N. "Photochemical Processes and Their Utilization for Solar Energy." *Proceedings* of a Seminar on Advanced Energy Sources and Conversion Techni ques **1,** 139 (1958). ASTIA No. AD 209301.
20. Taylor, H. S. *J. Phys. Chem.* **34,** 2049 (1930).
21. Trautz, M. and W. Gerwig. *Z. anorg. allgem. Chem.* **146,** 1 (1925).
22. Vanton Pump and Equipment Corp., Hillside, New Jersey, Bulletin 10.3.
23. Waddington, G., and R. C. Tolman. *J. Am. Chem. Soc.* **57,** 689 (1935).
24. Welinsky, I., and H. A. Taylor. *J. Chem. Phys.* **6,** 466 (1938).

VOL. 5 1961

Equilibrium Temperatures of Ideal Spectrally Selective Surfaces

R. R. Hibbard

Lewis Research Center, National Aeronautics and Space Administration, Cleveland, Ohio

Spectrally selective surfaces were assumed for which the monochromatic emissivity changed abruptly at specific wavelengths. These surfaces could be completely characterized by two parameters: the height of the step change in emissivity, and the wavelength of the change. This characterization is more general than the widely used α/ε ratio.

Equilibrium temperatures were calculated for such surfaces when exposed to both focused and unfocused solar radiation at the earth's orbit distance. Varying step heights at wavelengths between 0.3 and 20 microns were assumed. With unfocused radiation, temperatures as low as 40 K were found for surfaces for which the emissivity increased from zero to unity at long wavelengths, and temperatures as high as 2400 K when the change was from unity to zero at short wavelengths. For focused radiation, much higher temperatures were found. Such surfaces may find application in power-generation cycles or in the storage of cryogenic propellants in space.

INTRODUCTION

Spectrally selective surfaces, that is, surfaces for which the monochromatic emissitivity, ϵ_λ, varies with wavelength, are capable of controlling the temperatures of bodies where heat exchange is primarily by radiation. They are now being so used for the passive temperature control of payloads in space. Their use also has been proposed for power-generation systems both terrestrial (e.g., by Shaffer[1]) and in space (e.g., by Whitaker[2]); for such applications both high solar-energy absorption and low reradiation losses are desired.

Shaffer[1] has shown analytically that for ideal spectrally selective surfaces, i.e., those for which ϵ_λ changes stepwise with increasing wavelength from 1.0 to 0.0, the maximum efficiency of a solar-driven Carnot cycle is obtained with a collector surface which has the step change at 1.224 microns. His calculations were based on unfocused radiation and with the cycle discharging heat to a 300 K reservoir. Shaffer also considered the efficiencies of cycles in which the ϵ_λ steps were from 0.9 to 0.01 and 0.02 and in which there were parasitic conduction-convection heat losses. Whitaker[2] has considered the form of the analytic solutions required to specify the optimum surfaces for the generation of power in space.

Presented herein are the results of a further study of the performances of such surfaces in regard to their equilibrium temperatures when exposed to solar radiation at the earth's orbit distance. Ideal surfaces were considered in which the cutoff wavelength varied from 0.35 to 20 microns, for surfaces for which smaller step changes in ϵ_λ were made, and for surfaces for which the ϵ_λ change with increasing wavelength is from lower to higher values. The last type might find applications as coatings for cryogenic fuel tanks in space. These equilibrium temperatures were calculated for both unfocused and focused radiation and are presented as curves in which the step height and the wavelength for the step are parameters.

MODEL AND PROCEDURE

Spectrally selective surfaces were assumed in which ϵ_λ is a step function of wavelength as shown in Figs. 1(a) and (b). These surfaces can then be fully described by the wavelength, λ, and by the departures Δ_1 and Δ_2 from total absorption or total reflection as also shown in Fig. 1. In this analysis it was further assumed that $\Delta = \Delta_1 = \Delta_2$. Where $\Delta > 0.5$, ϵ_λ is greater at short wavelengths than at long ones, and where $\Delta < 0.5$, ϵ_λ is greater at longer wavelengths. Where $\Delta = 0.5$, the surface is gray with an emissivity of 0.5.

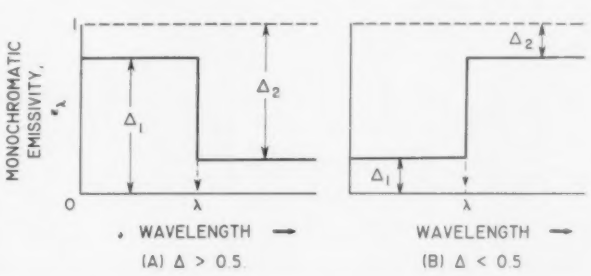

FIG. 1—Model of step changes in monochromatic emissivity.

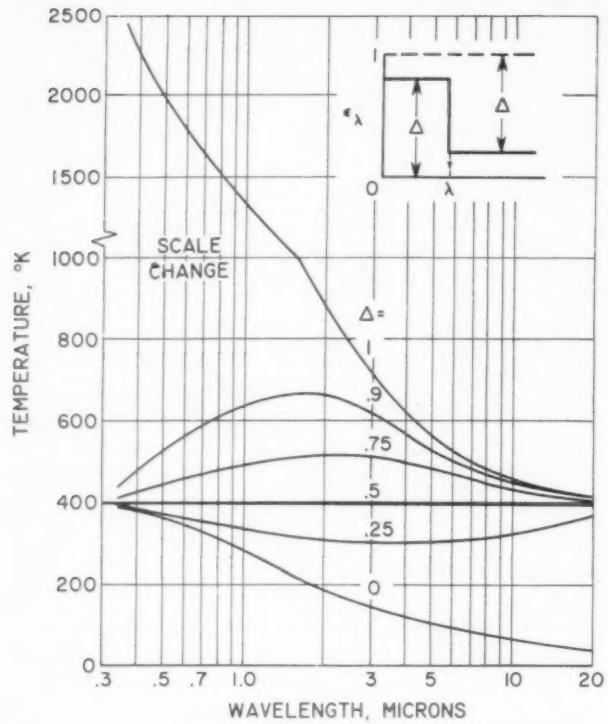

FIG. 2—Equilibrium temperatures of back insulated plate at earth's orbit as functions of Δ and λ.

For unfocused radiation, an incident flux of 1350 w/m² with an energy-wavelength distribution characteristic of a 5800 K black (or gray) source was used. It was assumed that there were no other energy sources; that is, that the plate was outside the influence of the earth's albedo and radiation, and that the plate reradiated to 0 K space. It was also assumed that the plate was perfectly insulated on the back side and was normal to the incident flux.

The radiant flux absorbed per m² of surface is then

$$q_{abs} = 1350\left[\left(\frac{R_{S,0-\lambda}}{R_{S,0-\infty}}\right)\Delta + \left(\frac{R_{S,\lambda-\infty}}{R_{S,0-\infty}}\right)(1-\Delta)\right] \quad [1]$$

where

$\left(\frac{R_{S,0-\lambda}}{R_{S,0-\infty}}\right)$ is the fraction of the total radiant flux from the sun found at wavelengths shorter than λ

$\left(\frac{R_{S,\lambda-\infty}}{R_{S,0-\infty}}\right)$ is the fraction at wavelengths longer than λ

and

Δ is the previously mentioned departures from total reflectivity and total absorbtivity.

Similarly the flux radiated away per m² of surface is:

$$q_{rad} = \sigma T^4\left[\left(\frac{R_{T,0-\lambda}}{R_{T,0-\infty}}\right)\Delta + \left(\frac{R_{T,\lambda-\infty}}{R_{T,0-\infty}}\right)(1-\Delta)\right] \quad [2]$$

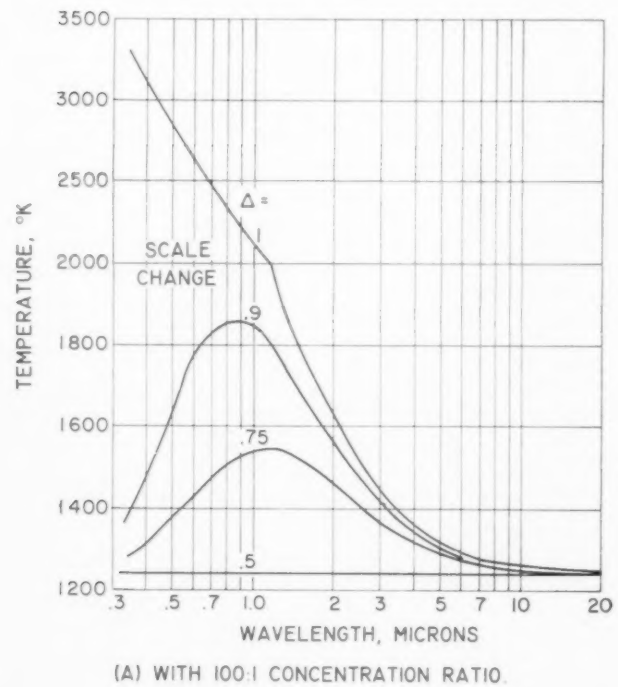

(A) WITH 100:1 CONCENTRATION RATIO.

FIG. 3A—Equilibrium temperature of back-insulated plate at earth's orbit using focused radiation.

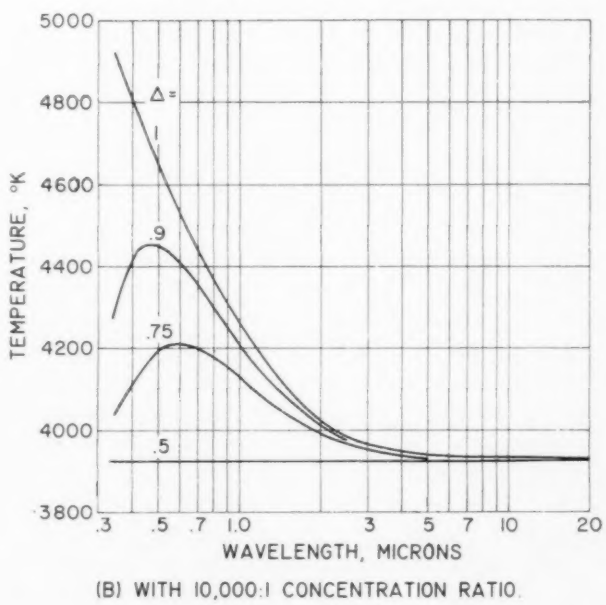

(B) WITH 10,000:1 CONCENTRATION RATIO.

FIG. 3B—Concluded. Equilibrium temperature of back-insulated plate at earth's orbit using focused radiation.

VOL. 5 1961

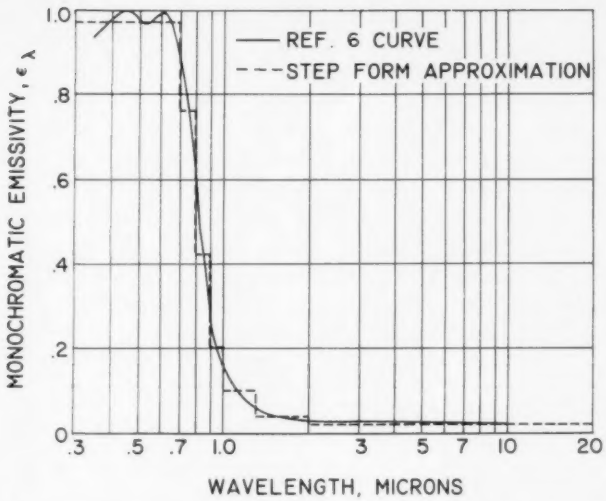

FIG. 4—Spectral emissivity of Cu-Ge-SiO filter (Redrawn from Ref. 6, Fig. 6).

where

$$\left(\frac{R_{T,0-\lambda}}{R_{T,0-\infty}}\right) \quad \text{and} \quad \left(\frac{R_{T,\lambda-\infty}}{R_{T,0-\infty}}\right)$$

are the same functions as described for Equation [1] but are now evaluated at the collector temperature T, and where σ is the Stefan-Boltzmann constant.

The temperatures for the surfaces were calculated for various values of λ and Δ by setting q_{abs} equal to q_{rad}. The calculations were done using values of Planck's functions taken from the Lowan and Blanch tables.[3]

Similar calculations were also made for focused radiation at concentration ratios of 100:1 and 10,000:1. These ratios might be attained with parabolic cylinder and parabaloidal collectors, respectively. The same effects would also be obtained by moving the surface, without focusing, towards the sun to about $\frac{1}{10}$ and $\frac{1}{100}$ of the earth's orbit distance.

RESULTS

With Unfocused Radiation

For $\Delta = 0.5$, or for any other uniformly gray (or black) surface, the equality of Equations [1] and [2] reduces to

$$1350\,\epsilon = \sigma T^4 \epsilon \qquad [3]$$

or

$$1350 = \sigma T^4 \qquad [3a]$$

and $T = 393$ K. This, then, is the temperature of a semi-insulated plate with a nonspectrally selective surface under the simplifying assumptions used herein. The more real situation of an earth satellite exposed to albedo and earthlight has been treated elsewhere (e.g., Tousy[4]), as has the problem of nonrotating and rotating spheres (Jenness[5]).

For spectrally selective surfaces, the results are shown in Fig. 2 for λ between 0.35 and 20 microns and for values for Δ of 1.0, 0.90, 0.75, 0.50, 0.25, and 0.0. The curves show that very high or very low temperatures are obtained only with surfaces in which ϵ_λ changes abruptly from 1.0 to 0.0. Under these conditions equilibrium temperatures range from as high as 2470 K for $\Delta = 1.0$ and $\lambda = 0.345$ microns to as low as 40 K for $\Delta = 0.0$ and $\lambda = 20$ microns.

For surfaces where $\Delta \neq 1.0$ or 0.0, interesting but far less extreme equilibrium temperatures result. These surfaces approach gray-body temperatures at each end of the wavelength scale because they are effectively near-gray bodies. For example, a surface with $\Delta = 0.9$ and a cutoff wavelength of 0.35 is a light gray body (with $\epsilon = 0.10$) to 93 percent of the solar radiation and to substantially all of the collector-plate radiation; the high ϵ_λ of 0.9 operates only on 7 percent of the solar radiation. These curves have broad maxima and minima in the neighborhood of 2 microns.

With Focused Radiation

Again, when $\Delta = 0.5$ or for any other uniformly gray (or black) surface, the equality of Equations [1] and [2] reduces to

$$\sigma T^4 = 1.35 \times 10^5 \text{ w/m}^2 \qquad [4]$$

for a concentration ratio of 100:1 with $T = 1242$ K, and

$$\sigma T^4 = 1.35 \times 10^7 \text{ w/m}^2 \qquad [5]$$

for a concentration ratio of 10,000:1 with $T = 3928$ K.

For spectrally selective surfaces the results are shown in Fig. 3(a) and (b) for Δ values of 1.0, 0.9, 0.75, and 0.5 and for wavelengths between 0.3 and 20 microns. Calculations were not made for $\Delta < 0.5$ since there is no point in using focused radiation while working towards reduced temperatures with this type of surface.

Figure 3 again shows the very high temperatures that can be obtained with surfaces in which ϵ_λ changes abruptly from 1.0 to 0.0 at the shorter wavelengths. Much lower temperatures are attained when $\Delta = 0.9$ and 0.75. For these latter types the wavelength that yields highest temperatures shifts from about 2 microns for unfocused radiation to about 1 micron for 100:1 concentrated radiation to about $\frac{1}{2}$ micron at 10,000:1 concentration.

DISCUSSION

Figures 2 and 3 show the theoretical promise of surfaces having sharp changes in monochromatic

emissivities. This may be of no great importance to the control of payload temperatures in satellites where surfaces having but moderate changes in monochromatic emissivity can hold temperatures to near 300 K. They may also be of minor importance to space radiators where high-emissivity surfaces are most effective. However, for applications where either very high temperatures are desired or where very low temperatures would be useful, as for the storage of cryogenic propellants in space, surfaces giving the temperatures shown in Figs. 2 and 3 are worthy of consideration.

Surfaces with Δ very near to 1.0 have, in fact, been made experimentally. Haas, Schroeder, and Turner[6] prepared multilayer filters in which the monochromatic reflectance changes quite abruptly from near 100% to near 0% as wavelength increases. Their data for a Cu-Ge-SiO filter has been replotted, assuming monochromatic emissivity to be equal to unity minus monochromatic reflectivity, and is presented as the solid line in Fig. 4. This curve is not much different than the step-change models assumed herein. It might be considered a $\Delta = 1.0$, $\lambda = 0.82$ surface, since the curve crosses 0.5 emissivity at 0.82 microns.

A calculation was made with unfocused radiation for this filter surface, using the step form approximation shown as the dotted line in Fig. 4. An equilibrium temperature of 1465 K, which is but little lower than the 1500 K temperature shown for the $\Delta = 1.0$, $\lambda = 0.82$ surface of Fig. 2, was found. However, it must be recognized that the reflectance measurements reported by Haas et al.[6] were made at room temperature and that somewhat different values might be obtained at 1465 K. In addition, this particular surface would almost certainly not be stable to such high temperatures, especially since the melting point of germanium is only 1232 K. Nevertheless, this example does indicate the promise of highly selective surfaces.

REFERENCES

1. Shaffer, L. H., "Wavelength-Dependent (Selective) Processes for the Utilization of Solar Energy," *Solar Energy*, **2**(3–4), 21, 1958.
2. Whitaker, R. O., "Methodology for Determination of Performance Characteristics of Spectrally Selective Absorbers," *Solar Energy*, **4**(2), 40, 1960.
3. Lowan, A. N., and Blanch, G., "Tables of Planck's Radiation and Photon Functions," *Jour. Optical Soc. Am.*, **30**, 70, 1940.
4. Tousy, R. "Optical Problems of the Satellite," *Jour. Optical Soc. Am.*, **47**, 261, 1957.
5. Jenness, James R., Jr. "The Effect of Surface Coatings on the Solar Radiation Equilibrium Skin Temperature of an Earth Satellite," *Solar Energy*, **2** (3–4), 17, 1958.
6. Haas, G., Schroeder, H. H., and Turner, A. F., "Mirror Coatings for Low Visible and High Infrared Reflectance," *Jour. Optical Soc. Am.*, **46**, 31, 1956.

VOL. 5 1961

On Radiant Energy in High-Temperature Research

Tibor S. Laszlo

AVCO Manufacturing Company, Wilmington, Massachusetts

The mechanism of heating solids with radiant energy is reviewed and the need for measuring radiative properties is pointed out. Image furnaces are suitable for such measurement at high temperatures. The limitations of image furnace operations are discussed and methods as well as equipment offered to overcome the limitations. The importance of artificial black bodies in high-flux measurements is described and a new shape for such cavities is proposed. Data comparing this shape with hitherto used shapes are tabulated. Design for a fast-action on-off shutter for image furnaces is presented. In its retracted position the shutter does not cast any shadow on the mirror and it does not require artificial cooling even when exposed to radiation.

INTRODUCTION

During the past two centuries the transfer of thermal energy has become of great interest to scientists and engineers. The fundamental measurements which support the theory of thermodynamics are based on transfer of heat by conduction or convection (i.e., measurements concerning specific heat, heat of reaction, heat of phase transformation, etc. For example, engineers use steam extensively as the main heat-transfer medium in industrial processes and the generation of steam and its utilization for heating are based on transfer by conduction and convection.

As a consequence these two forms of heat transfer have been studied extensively. Not only have the relevant fundamental laws been developed but also the constants necessary for the application of these laws to specific problems were determined for a wide range of conditions. This fortunate situation came about because these data were badly needed by industry in its development from empirical operations to a well-defined and controlled technology. The collection of these data did not present great difficulties; methods and instruments once developed could be applied easily to the measurement of the constants for any new material.

The same situation does not hold true for the third method of heat transfer, i.e., radiation. The definition of the fundamental laws of radiation engaged the interest of such foremost scientists as Kirchhoff, Boltzmann, and Lambert; and problems arising from the explanation of the spectral distribution of radiant energy ("The Ultraviolet Catastrophe"), among other reasons, led Planck to the development of the quantum theory. Nevertheless, the detailed study of the more intricate problems in radiation and the measurement of specific data were lagging behind until recently.

The cause of this state of affairs is just the opposite to those presented for the more abundant knowledge on conduction and convection phenomena. Below 2200 F only a small fraction of the heat is transferred by radiation. Until recently, industrial processes were seldom performed above this temperature range, thus the need for radiation data was not very pressing. The academic interest in radiation measurements in the past was dampened by the extreme experimental difficulties connected with the use of intense radiant energy.

During the past 15 years this situation changed considerably. Industrial processes were developed or conceived which require operation at temperatures far in excess of 2200 F. At the same time laboratory tools became available which permit experimentation and measurements in the range of 7000–100,000 F, and sometimes even higher. With a few exceptions these tools utilize radiant energy for heating as well as for observation and measurements.

EFFECT OF THERMAL RADIATION ON SOLIDS

When electromagnetic radiation impinges on a metal, an oscillating electric field is set up at the surface. In terms of classical mechanical theory the free electrons of the metal begin to oscillate due to the electromagnetic field. The oscillating electrons collide with the atoms of the metal and transfer to it part of their energy. The atoms take up this energy in the form of lattice vibrations and the metal heats up. The net effect of this process is that the metal absorbs the impinging radiation and it becomes hot.

Not all of the energy of the free electrons is transmitted to the atoms of the metal. As the oscillation of the electrons increases under the effect of the electromagnetic wave, the electrons begin to emit radiation and the entire material becomes a radiator. Since part of the incident radiation is reradiated, only the net heat input increases the temperature of the substance.

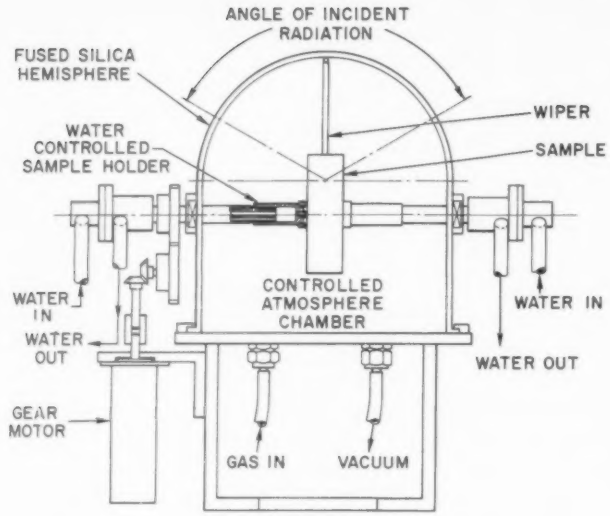

FIG. 1—Controlled atmosphere rotating sample holder.

The effect is somewhat different in dielectrics which do not have free electrons. Their electrons can oscillate only with the natural frequency of the atoms to which they are bound. If the impinging radiation has a frequency indentical with or close to the natural frequency of the atoms, it is absorbed, thus producing the same effect as in metals. If radiation of a different frequency impinges on a dielectric, it will not be absorbed and the dielectric will not heat up.

From these considerations it follows that two important parameters determine the effect of radiation on a substance. The first is the frequency of the radiation, the second is the resonant frequency of the elementary particles of the substance. These two parameters will determine what fraction of the radiant energy is absorbed and what fraction is reradiated by the substance. The thermodynamic state of the substance is determined by the net energy retained in it. The reradiated fraction of the energy is an important indicator of certain properties of the substance, e.g., temperature and emissivity.

Emissivity is an intrinsic property of a substance and it is a function of the wave length of the radiation, the temperature of the substance and the direction of observation. For nonisotropic substances it may also depend on the altitude and azimuth of observation relative to the surface. Unfortunately, there is no theoretical knowledge available which could be used to calculate emissivity from parameters defining the structure of a substance. Accordingly, emissivity has to be measured as a function of each applicable parameter. Since the knowledge of emissivity is required during most high temperature experiments (optical pyrometry, radiant emission, etc.) methods were sought for the measurement of emissivity at high temperatures. Image furnaces, utilizing radiant energy for the heating of a specimen appear to be the most suitable tools for such measurements.

USE OF IMAGE FURNACES

The principle of operation of image furnaces and their advantages in high-temperature research have been discussed before.[1,2] Here only the two most important characteristics of such furnaces will be mentioned: the high heat fluxes (temperatures), and the pure condition of heating which can be obtained.

However, image furnaces place certain limitations on experimentation. For successful operation it is therefore important to develop special equipment as well as special methods which take into account these limitations.

The first limitation is the small size of the hot zone in an image furnace. It is not technically possible to increase the image size without decreasing the flux in carbon-arc image furnaces. In solar furnaces a larger image may be obtained by increasing the collector. However, the manufacturing problems involved in the building of large solar furnaces are considerable. It appears that a better solution to this problem is to change experimental techniques so as to make use of the small image size. The precision of the measurements is not necessarily affected by the reduction of the size of a heated sample. If the experience of microanalytical techniques can be applied here, the decrease in sample size may even increase the accuracy of certain tests.

The second limitation, namely, that heating takes place only on one side of the sample is more restrictive. Heating in a cavity has been suggested[3] to overcome this difficulty. It appears, however, that the refractoriness of the cavity material sets a rather low temperature limit on such a technique. In addition, owing to the presence of a sample in the cavity it is unlikely that a uniform wall temperature can be reached. A more promising technique is the rotation of the sample around an axis perpendicular to the optical axis of the image furnace to achieve even heating around the entire circumference.

Figure 1 shows a sample holder mechanism designed for this purpose. The sample holder clamps are mounted in ball bearings. One of the clamps is driven by a servomotor through a gear train, the other rotates freely. Both are water-cooled. The entire sample holder is covered with a fused-silica bell jar thus permitting operation in controlled atmospheres.

Figure 2 illustrates a sample holder in which the sample rotates around the optical axis of the image furnace. Asymmetry of the image can be reduced greatly with this technique. This sample holder is also equipped for operation in controlled atmospheres or in vacuum. An oscillating wiper is provided to remove

VOL. 5 1961

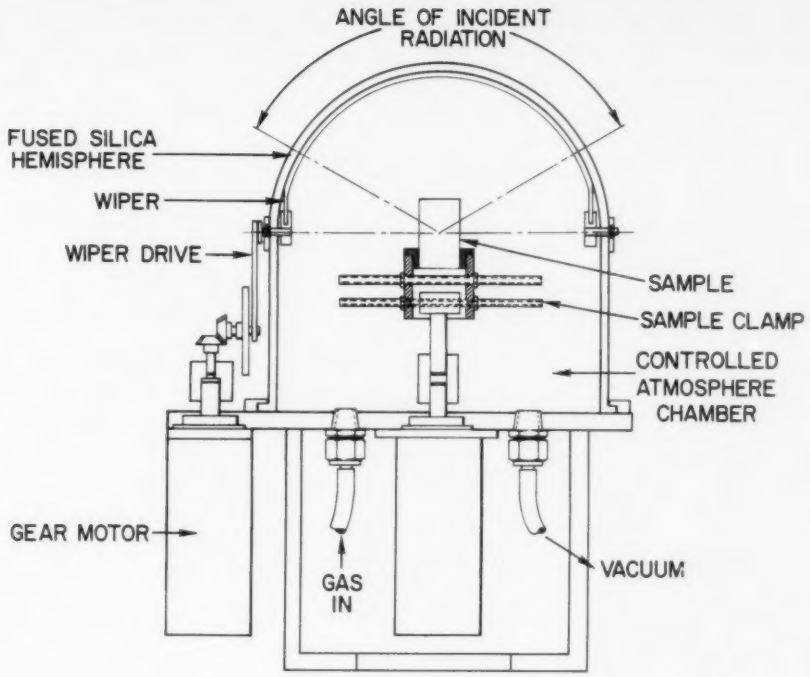

FIG. 2—Controlled atmosphere sample holder with wiper.

deposits from the inside of the silica jar, which would reduce the flux inside the sample holder. The blade of the wiper is a steel wire wrapped with a refractory tape, tailored to the shape of the bell jar.

The third limitation imposed by the fundamental optics of image furnaces is the nonuniformity of the flux across the image area. Owing to the ratio of radiation-source diameter and its distance from the image furnace, the recreated image has a more or less regular bell-shaped flux distribution. Accordingly, a sample heated in an image furnace will have a similar temperature distribution. The measurement of a property, e.g., electrical resistivity, performed on this sample yields a value which cannot be related to any one temperature and is therefore meaningless.

A new experimental technique has been developed which makes it possible to obtain meaningful values of a property for narrow temperature intervals from measurements in the wide-range temperature distribution of an image furnace if the distribution is well defined. Such is the case in the solar furnace.

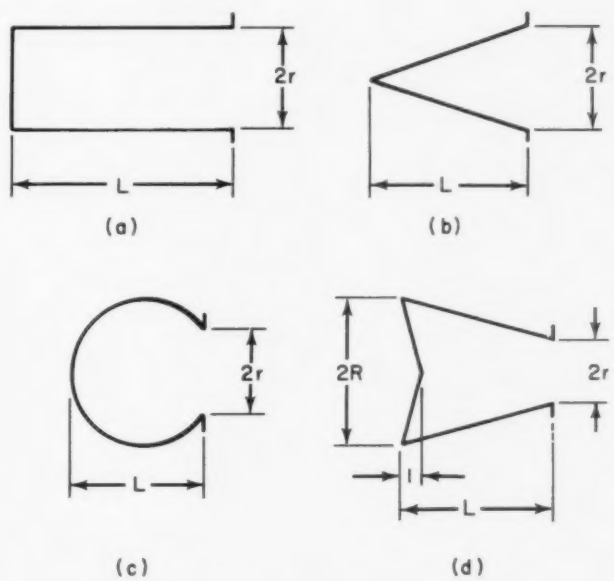

FIG. 3—Shapes of artificial black bodies.

FLUX MEASUREMENTS

The high temperatures encountered when using radiant energy are usually determined by measuring the flux impinging upon or emitted by the sample. The flux is measured with calorimeters or with radiometers calibrated with calorimeters. Several water-cooled calorimeters have been designed which are suitable for use in image furnaces.[4, 5] These calorimeters contain a spherical cavity as an artificial black body to absorb the incident radiation.

The problem of finding the optimum shape for an artificial black body has been investigated extensively. Buckley studied the radiation from the inside of a circular cylinder.[6] He derived an expression for the radiation from an annulus to any other annulus in a cylinder of infinite length taking into account multiple

reflections. He then applied the same method to the case of a finite uniformly heated cylinder and obtained an approximate solution. Finally, he adapted the method to the problem of a uniformly heated finite cylinder closed at one end; a shape which closely approximates some artificial black bodies being used in optical pyrometry.

One of the most interesting results of his work is the relationship between cylinder length and orifice radius. It is shown that if the emissivity of the cylinder wall is 0.75 a cylinder length/orifice radius ratio of 3.8 gives radiation intensities within 1 per cent of black-body radiation. This ratio decreases rapidly as the emissivity of the wall increases, with the result that for materials of high emissivity the length of the cavity can be greatly reduced without reducing the orifice radius.

Gouffé compared the sphere, the cylinder, and the cone in his search for the optimum artificial black-body shape.[7] He based his comparison on the value L/R, where L is the length of the black body and R is the radius of the orifice. From these data he calculated the total surface area of the cavity, S, and the surface area of the orifice, s. The ratio s/S then expresses the relative value of the cavity as an absorber. It should be pointed out, however, that in his calculations S includes the area of the orifice s which is not an absorbing surface. A more precise expression for the evaluation of the cavity would be $s/(S - s)$. The shapes considered by Gouffé are shown in Fig. 3(a, b, c).

TABLE 1—Comparison of Proposed Black-body Shapes

$\frac{L}{R}$	$\frac{s}{S}$				$\frac{s}{S} - \frac{s}{S_0}$ *		
	Sphere*	Cylinder*	Cone*	Double Cone**	Cylinder*	Cone*	Double Cone**
1	0.500	0.250	0.415	0.175	−0.250	−0.085	−0.325
2	0.200	0.167	0.309	0.094	−0.033	+0.109	−0.106
3	0.100	0.125	0.241	0.059	+0.025	+0.141	−0.041
4	0.059	0.100	0.195	0.041	+0.041	+0.136	−0.018
5	0.039	0.083	0.164	0.030	+0.044	+0.125	−0.009
8	0.016	0.056	0.111	0.015	+0.040	+0.095	−0.001

* Shapes considered by Gouffé
** Shape proposed by present investigation
* Comparison of shapes with sphere (s/S_0)

A NEW SHAPE FOR ARTIFICIAL BLACK BODIES

During the present investigations a new shape for artificial black bodies was conceived, consisting of a truncated right cone with the smaller end as the orifice. The bottom of the cavity is a right circular cone, Fig. 3(d). In a cavity of this shape only a very small fraction of the total area "sees" the orifice perpendicularly, and accordingly losses due to reradiation are low.

Gouffé's method of evaluation has been applied to this shape. The results, together with Gouffé's data for the shapes he has considered are presented in Table 1.

The data in Table 1 show that if the L/R value is greater than 2 both the cylinder and the cone are inferior to the sphere as far as the s/S value is concerned. However, the double-cone shape results in a s/S value which is more favorable than that for a sphere even for L/R ratios as high as 8.

It should be pointed out that the ratio s/S does not completely express how closely an artificial cavity approximates the radiation characteristics of a black body. The effect of multiple reflections has to be considered in order to determine what fraction of the radiation entering the cavity will finally escape from it.

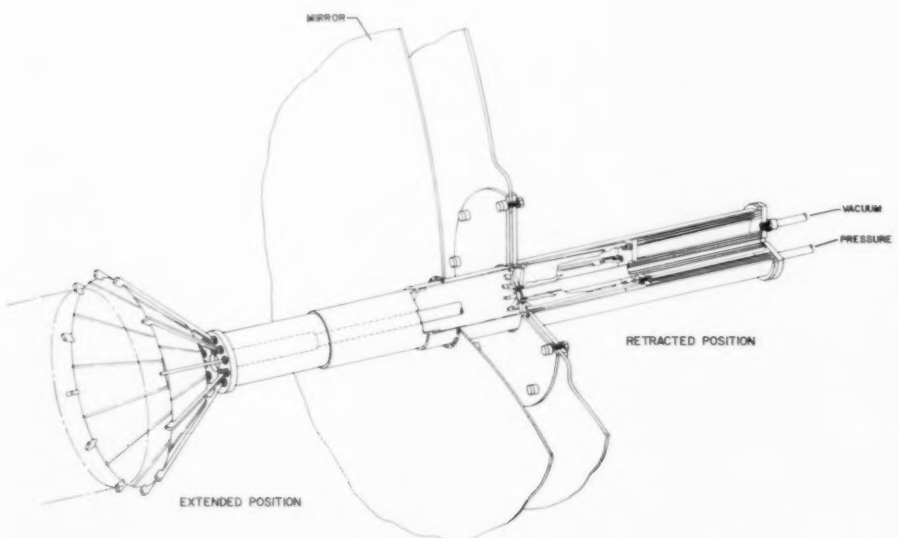

FIG. 4—Solar furnace shutter.

VOL. 5 1961

It is planned to perform this study for the proposed cavity shape in the near future.

A water-cooled calorimeter has been built to this design and is currently undergoing tests. These tests will help to determine its efficiency in absorbing incident radiation.

THE SHUTTER

In most image furnaces the intensity of the flux impinging on a specimen is controlled by a cylinder moving along the optical axis. For many experiments, however, an instantaneous on-off flux control is necessary. Venetian-blind-type shutters are now in use on some furnaces[8] which combine the effect of flux attenuation and on-off control. A disadvantage of this mechanism is that even in the fully open position it blocks somewhat the passage of radiation due to the thickness of the slats and to the need of using support members.

A fast-action on-off shutter has been designed, which does not cast a shadow on the collector when in the retracted position. Figure 4 illustrates the mechanism of the shutter. The flux inceptor has a ribbed umbrella structure which is supported by a telescoping tube. In its retracted position the entire structure is behind the mirror and, when not needed, it can be swung away from the observation hole. It is extended by the application of compressed air and retracted by vacuum. In the center of the telescope there is another telescoping tube, which permits observation of the sample during the entire operation.

CONCLUSIONS

Radiant energy is an excellent heat source for experimentation and measurements at high temperatures, and image furnaces are suitable tools for such work. However, for successful experimentation it is important to take into consideration the special operating conditions of image furnaces. In most cases conventional instruments and techniques cannot be used because of the small size and uneven flux distribution at the hot zone. A completely fresh approach has to be taken for each type of experimentation when using high-intensity radiant energy. The size, shape, and mounting of the specimen may require unconventional arrangements. New methods of observation and measurement must be developed together with instruments of special design. Because of the novelty of image furnaces, very little work has been done to date. However, with progress in this field a unique and very versatile tool will soon be available for high-temperature research.

ACKNOWLEDGMENT

The author wishes to express his appreciation to S. Motta for the shutter design, A. Shores for the design of the sample holders, A. Cicco for the art work, P. Sheehan for his assistance, and R. Barriault for valuable suggestions in the preparation of this paper.

The research reported in this paper was sponsored by the Electronics Research Directorate of the Air Force Cambridge Research Laboratory, Air Research and Development Command under contract AF19 (604)-7204. This paper, although based on work sponsored by the U. S. Air Force, has not been approved or disapproved by that Agency.

REFERENCES

1. Laszlo, T. S., "Solar Furnace in High-Temperature Research," *Science*, **124**, 797 (October 1956)
2. Laszlo, T. S., "Temperature and Flux versus Geometrical Perfection," *Solar Energy*, **1**, 78 (April-July, 1957)
3. Glaser, P. E., "Engineering Research with a Solar Furnace," *Solar Energy*, **2**, 7 (April 1958)
4. Farber, J., "Images of Very High Temperature Sources," *Proceedings* of the Symposium "High Temperature — A Tool for the Future," Stanford Research Institute (1956)
5. Glaser, P. E., "High Radiation-Flux, Absolute Water-Flow Calorimeter," *Rev. Sci. Instr.*, **28**, 1084 (December 1957)
6. Buckley, H., "On the Radiation from the Inside of a Circular Cylinder," *Philosophical Magazine;* **4**, 753 (1927); **6**, 447 (1928); **17**, 576 (1934)
7. Gouffé, A., "Corrections d'ouverture des corps-noir artificiels compte tenu des diffusions multiples internes," *Revue D'Optique*, **24**(1–3), 1 (January–March 1945)
8. Davies, J. M., and Cotton, E. S., "Design of the Quartermaster Solar Furnace," *Solar Energy*, **1**, 16 (April 1957)

Notes on a Solar Collector with Unique Air Permeable Media

M. J. Shoemaker

Research Products Corporation, Madison, Wisconsin

Tests on plate heat collectors reveal that they are highly efficient in transferring heat and thus in increasing the temperature of a stream of air provided that the space between the cover and the bottom of the collector is filled with slit-and-expanded aluminum foil blackened on the one side, which is turned toward the sun. The air stream traverses the collector parallel to the general plane of the foil layers. The high radiant-energy exchange should reduce the cost of heat collectors and hasten wider utilization of solar heat.

A solar-energy plate collector using novel air-permeable media is very effective in raising the temperature of an air stream. Its high efficiency may be attributed to the arrangement in layers of slit-and-expanded aluminum foil having one black side upon which the solar energy falls. The general construction is otherwise similar to a conventional plate collector in that it employs an insulated shallow tray, painted black inside, with a transparent cover. The foil, which is placed inside the tray, fills the space between the cover glass and the bottom of the tray.

The foil used in these experiments is illustrated in Fig. 1 which shows the openings enlarged approximately 2.3 times. The foil is 0.002 in. thick and is coated on one side with black vinyl enamel. It averages about 85 sq ft per lb and costs approximately $1.85 per lb in rolls. The material cost per sq ft of seven layers is aproximately 15¢.

Due to the expansion pattern, when a number of layers of the slit-and-expanded foil are superimposed without pressure, the thickness of a layer is approximately 0.065 in. per layer. The reduction of light incident to each successive layer of foil is shown in Table 1 for a stack laid up at random, as determined by a Weston light meter.

The heat collector is 18 in. wide with an effective length of approximately 5 ft; the frame is constructed of $\frac{3}{4}$-in. plywood lined with 22 gauge galvanized iron. The frame is insulated at the bottom only with approximately $3\frac{1}{2}$ in. of fiber-glass blanket between the wood and the galvanized iron. The two single-strength glass covers are spaced $\frac{1}{4}$ in. apart. Tape prevents air leakage

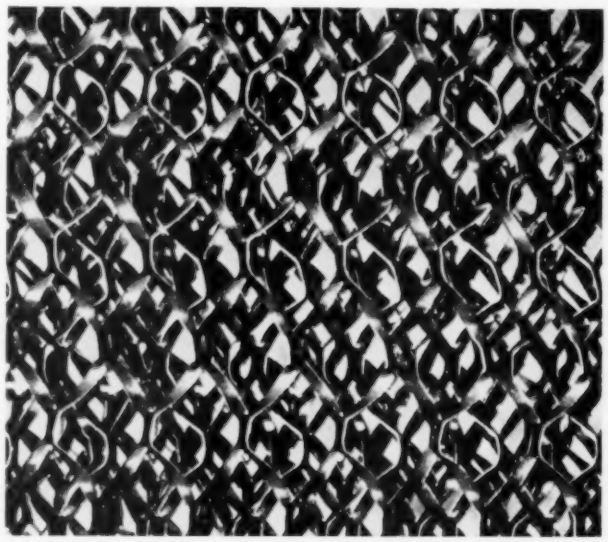

FIG. 1—Close-up of 7 layers of the slit and expanded aluminum foil used in the experiments described. Approximately 2.3 × actual size.

TABLE 1—Light Transmission Through the Meshes of a Stack of Layers of Expanded Foil

No. of Layers	% Light Reduction	% of Total Light Incident on Each Sheet of Foil
0	0	—
1	33.3	33.3
2	50.0	16.7
3	63.3	13.3
4	73.3	10.0
5	79.0	5.7
6	86.0	7.0
7	90.0	4.0

at the edges of the glass panes which are recessed into the wood frame. The collector is mounted normal to the rays of the sun during tests. Air was drawn through an orifice meter at controlled rates at the lower end of the

VOL.
5
1961

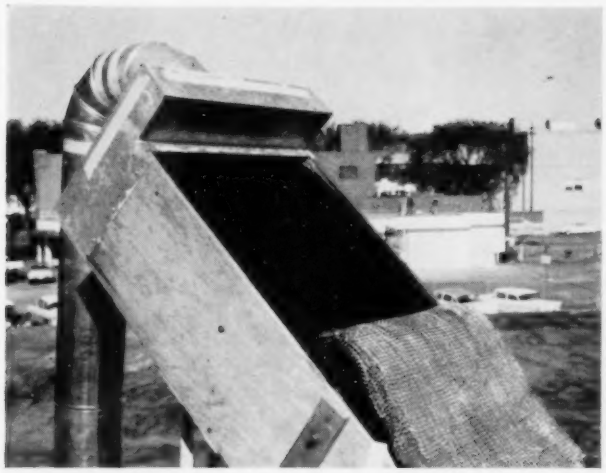

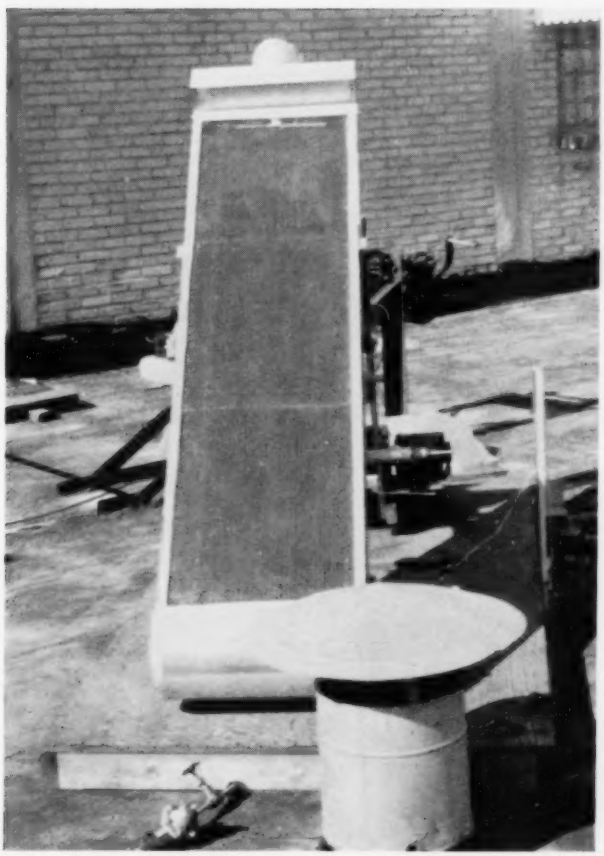

FIG. 2—Two views of the experimental heat collector showing the slit and expanded foil used in the tests reported by the author.

collector and discharged at the upper end by a blower; Fig. 2 shows two views of the test set-up. Temperatures of the inlet and outlet air were recorded.

In the first series of tests the distance between the glass and the bottom of the collector was 1 in. Tests

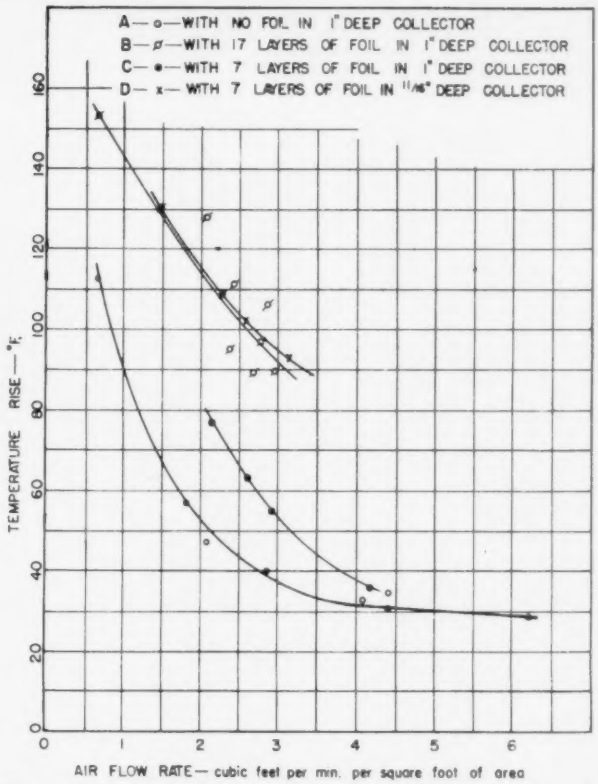

FIG. 3—Temperature rise of the air passing through the collector vs. flow rate (a) With no foil in the 1 in. deep collector. (b) With 17 layers of foil filling the 1 in. deep space in the collector. (c) With 7 layers of foil and insufficient to fill the 1 in. deep space. (d) With 7 layers of foil adjusted to fill a collector space 11/16 in. deep.

were run with the collector empty and also with 17 layers of the foil slightly compressed to fill the space between the glass and the bottom. The tests for curves (a) & (b) shown in Fig. 3 were run on clear days between Aug. 31 and Sept. 26 between the hours of 9:30 A.M. and 1:10 P.M. standard time. These curves show the temperature rise of the air passing through the collector with no foil and with 17 layers of foil, respectively. It may be noted that the temperature rise of the air is from 50 to 60 F greater in the flow rate range of 1 to 3 cfm per sq ft of area when the foil is used. In terms of heat collected, curves (a) and (b) in Fig. 4 illustrate the performance of the collector without and with the foil, respectively. At an air flow rate of about 4 cfm/sq ft, the heat collected levelled off at about 5.3 Btu/min-sq ft. This rate is more than double that of the black-box type collector without foil. Assuming that the glass transmitted 85–90% of the incident solar energy, it is suggested that the performance, as reflected by the temperature rise, is remarkably close to a maximum for the avilable solar energy.

In the second series of tests, the number of layers of foil was reduced from 17 to 7 and the same distance of 1 in. between the glass and the collector bottom was

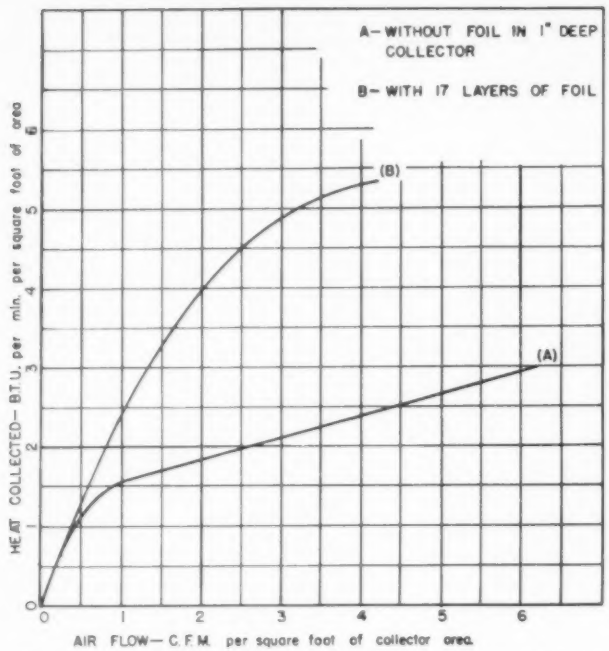
A—WITHOUT FOIL IN 1" DEEP COLLECTOR
B—WITH 17 LAYERS OF FOIL
(B)
(A)
HEAT COLLECTED—B.T.U. per min. per square foot of area
AIR FLOW—C.F.M. per square foot of collector area

FIG. 4—Heat collected vs. air flow rate (a) With no foil in the 1 in. deep collector. (b) With 17 layers of foil in the same collector.

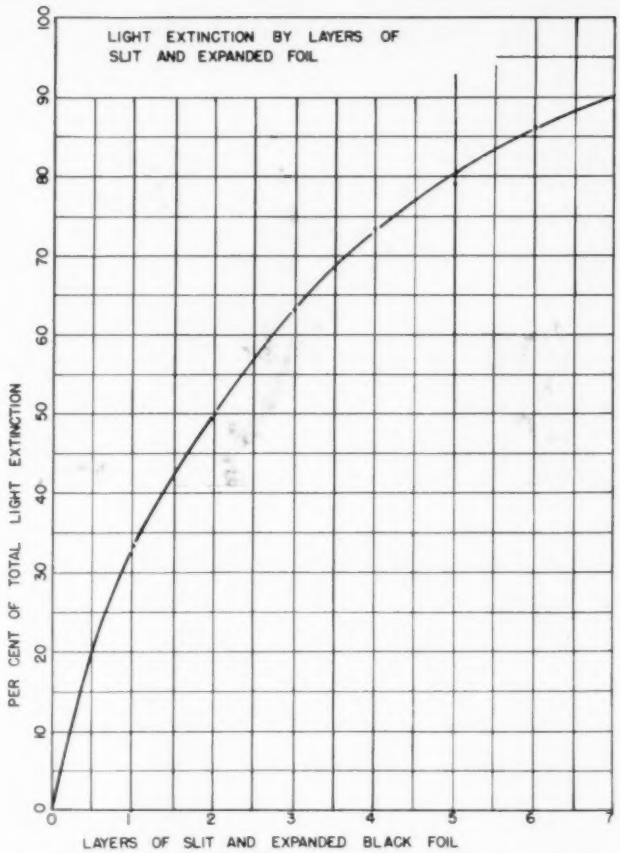
LIGHT EXTINCTION BY LAYERS OF SLIT AND EXPANDED FOIL
PER CENT OF TOTAL LIGHT EXTINCTION
LAYERS OF SLIT AND EXPANDED BLACK FOIL

FIG. 5—Light extinction by layers of slit and expanded foil.

retained as formerly. The foil no longer filled the available space, there being a clearance of about $\frac{5}{16}$ in. between the glass and the top of the foil stack. Observations made on Oct. 17 between 9:30 and 10:30 A.M. established curve (c) in Fig. 3. The reason for the greatly reduced temperature rise in curve (c) as compared to curve (b) is probably due to the free-air space betweeen the glass and the foil, which, offering less resistance, resulted in some of the air stream by-passing the foil layers and therefore not absorbing available heat in the foil stack.

In the third series of tests, the clearance between the glass and the top of the foil stack was reduced to $\frac{3}{16}$ in. so that 7 layers of foil virtually filled the space. The data for curve (d) in Fig. 3 were obtained on Oct. 24 between 10 A.M. and 12 noon. It will be observed that curves (b) and (d) are virtually the same thus showing that for air flow confined to the space occupied by the foil stack, 7 layers are just as effective as 17 for heat exchange.

In accounting for the greatly improved performance of a plate heat collector when used with slit and expanded foil blackened on the side which is turned toward the sun, it may be observed that, in effect, the incident radiant energy is transferred to the air stream by reradiation as well as forced convection. According to the data in Table 1, the first layer of foil transfers by reradiation and convection about one-third of the energy. The actual area of the foil is 38.5% of the apparent or gross area of the slit-and-expanded foil, but due to inclination of the baffles, the light intercepted in a plane perpendicular to the solar rays is 33.3%. The second layer transfers about half as much as the first layer, and the third about 13%, while the remaining four layers in the 7 layer stack convert about 27%, thereby leaving only about 10% of the total radiant heat to be transferred at the bottom of the collector. Due to this mechanism of energy transfer in the space traversed by the air stream, the boundary temperatures in the collector are greatly reduced; hence the temperature gradient and the heat loss by conduction through the bottom and sides of the collector are correspondingly reduced. Since the bright side of the foil is turned downward, the preponderance of reradiation is diverted upward and laterally. The baffles of the foil being turned at an angle, the reradiation from the foil occurs in many directions throughout the pervious mass thereby providing rapid and efficient heat transfer to the air streaming through it. It is believed that this explanation may account for the excellent performance of a plate-type heat collector filled with the expanded foil.

The apparent low value for the light intercepted by the fifth layer is believed due to the fortuitous arrange-

VOL. 5 1961

ment resulting from stacking the various layers at random. From the light study, it is apparent that it would be desirable to intercept less light on the first layer and this can easily be accomplished by employing a more open pattern. By selecting patterns, the heat can be transferred uniformly throughout the layers in the stack.

The work described should make possible lower original and maintenance costs in the collection of solar energy. It also demonstrates that for any air rate within the observed range and area of exposure, consistently higher air temperatures are obtainable with foil-stack collectors than with conventional plate-type collectors.

L.
61

Solar Abstracts

Milton D. Lowenstein

Technical Research Service Center, AFASE

VOL. 5 1961

I—Evaporative Processes

Grune, Werner N. and Zandi, Iraj, "Improved Solar Still Process for Desalting Sea and Brackish Waters." *Journal American Water Works Assn.* **52** (8): 993–1005, Aug. 1960. Illus.

Several new design features have been investigated to improve the yield of existing solar stills. One of the improvements is the mechanical separation of the collector-evaporator unit from the condenser. A further improvement is the use of air as an intermediate substance that substitutes forced convection for natural convection to increase evaporation. In addition, this design utilizes droplet evaporation in lieu of flat-sheet evaporation to increase the interfacial area between carrier and water droplet.

* * *

Ozisik, N. and Schutrum, L. F., "Solar Heat Gains Through Slat-Type Between-Glass Shading Devices," The American Society of Heating, Refrigerating & Air-Conditioning Engineers, Cleveland, Ohio, 1960. 8 p. Illus.

Instantaneous heat gains through slat-type between-glass shading devices have been predicted with engineering accuracy from the incident solar radiation, the outdoor air temperature, and the K and U values reported in the paper.

The use of these shading devices results in a reduction of instantaneous heat gains as compared with a window of single glass. For a west-oriented window, the design (Aug. 1, 40° N. Lat.) instantaneous heat gain from 12 noon to 5 p.m., using a slat-type between-glass shading device constructed with ordinary window glass, would be about 35 to 60 per cent of the gain through a window of single regular plate glass. These percentages also hold for the maximum instantaneous heat gains.

* * *

U. S. Department of the Interior, "Saline Water Conversion," National Academy of Sciences-National Research Council, Pub. 568, Proceedings of a Symposium, 4–6 Nov., 1957, 3–459 p. Illus.

This symposium brings together for the first time those in the world concerned with the development of solutions of the problems of saline water conversion. The proceedings of the symposium can be regarded as representing the current state of knowledge in this field, and to present accurately the status of world progress toward solution of one of the critical problems facing man. Details of commercial equipment are included only incidentally, the primary emphasis being on the state of knowledge rather than details of commercial practice.

CONTENTS

SOLAR DISTILLATION METHODS AND EQUIPMENT

Summary of Solar Distillation Processes	J. J. Strobel
Solar Distillation Research and its Application in Australia	B. W. Wilson
Solar Distillation Developments in the Eastern Mediterranean	C. Gomella
Solar Still Theory and New Research	M. Telkes
An Air Film Osmotic Stack for Low Cost Multiple Evaporation	G. L. Hassler
Design and Cost Factors of Large Basin Type Solar Stills	G. O. G. Lof
An Experiment with a Plastic Tubular Solar Still	G. Nebbia

* * *

II—Space Water Heating and Absorptive Collectors

Deo. Suresh, "Heating of Water in a Flat Solar Energy Collector." Nagpur University, 1956, September, 1960, 2–82 p. Illus.

The flat-plate collector constructed by the writer is a "sandwich" of eight component parts. The experimental thermal efficiencies of this unit, 33 to 53 per cent, compare favorably with efficiencies of 32 to 57 per cent for similar type of units designed and tested by other investigators.

Data obtained from the Department of Home Economics at the University of Mississippi indicate that a temperature of approximately 118 F is just about right for the purpose of washing dishes and clothes in household use, but is a bit high for bathing purposes. It thus appears that the water temperatures of 126 to 135 F attained in the experimental solar heater are not too low and, in fact, may be accepted favorably by many households. Brooks has indicated that with ordinary care, a family of five uses about 100 gal of hot water per day with an extra 25 gal for clothes washing. The hot water supply capacity of the experimental solar heater, about 975 lb or 116 gal in the temperature range of approximately 135 to 125 F (the ambient air temperatures being 80 to 93 F), therefore, appears very encouraging.

* * *

Mathur, K. N., Khanna, M. L., Davey, T. N., and Suri, S. P., "Domestic Solar Water Heater." *Journal of Scientific Industrial Research 18A* (2): 51–58, 1959. Illus.

An arrangement for heating water with solar energy for supplying the domestic needs of a small family at Delhi, using easily available and inexpensive construction materials (galvanized iron sheets), has been described. The heat collector unit consists of a wooden box, insulated at the bottom, in which are formed the flow channels for water by one corrugated and one plane galvanized iron sheet. The upper side of the box is glazed with one or more layers of $\frac{1}{8}$ in. thick window glass sheets to reduce heat losses, keeping a 2 in. gap between the glass sheets and the water flow channels.

As the length of the day is short and water requirements large during the winter, the heating unit is set up at an angle of 45° to the horizontal to make the best use of sunlight. Flow rates of water, through the collector unit, in the range 4–21 gal/hr have been used and a rate of 7–10 gal/hr has been found to be optimum under the experimental conditions employed. The efficiency of heat transfer on a clear day is about 70 per cent which is more than that for the usual types of heat collector units using copper pipes soldered to flat copper sheets.

III—Cooling Processes: Refrigeration and Heat Rejection Systems

No abstracts this issue.

IV—Heat Collectors and Solar Cookers

Yappel, A. Ralph, "Solar Energy Steam Generator: Parabolic-Cylinder Mirror Type." Contributed by the Solar Energy Applications Committee for presentation at the Winter Annual Meeting, New York, N. Y., Nov. 27–Dec. 2, 1960, American Society of Mechanical Engineers. 10 p. Illus. 60-WA-89

This paper presents a summary of performance data for a solar steam generator along with a rough estimate of power cost. After a brief discussion of the equipment, an analysis of performance data at different saturation temperatures is presented. A theoretical study of predicted performance is made for use of an improved focus tube. Abbot's original steam generator is very briefly described in Appendix A. Owing to high cost of power production, this type of power plant may be useful on the earth's surface only in remote regions. However, this type of power generator may be utilized on space vehicles to advantage.

* * *

V—Thermoelectric

Bloom, Justin L. and Weddell, James B., "13-Watt Isotope-Powered Thermoelectric Generators for Space and Lunar Impact Missions." Presented at ARS Space Power Systems Conference, Santa Monica, Calif., Sept. 27–30, 1960. 11 p. Illus. (1332–60)

Two small thermoelectric generators which derive their power from the radioactive decay of Curium-242 have been designed.

The first is intended for use in space and is capable of delivering an essentially constant power output of 13 electrical watts over a 6 month operational life. It weighs 16.6 lb and occupies a volume of 230 cu in.

The second generator is designed to operate for 2 months, both in lunar day and night, after a hard (500 ft/sec) impact on the moon. The principles of design are described. The complete power supply weighs 6.2 lb and occupies a volume of 350 cu in., including allowances for mounting a structure and radiator surfaces.

In both cases, external radiation levels may be reduced to the point where personnel exposure in ground handling and photon dosage to neighboring instrumentation are minimized.

Thermal-to-electrical conversion principles, properties of the radioisotope fuel, method of encapsulation of the fuel and techniques for obtaining constant power output are discussed. Safety considerations in the event of accidents during launch-to-operation sequence are presented briefly.

* * *

Danko, J. C., Kilp, G. R., and Mitchell, P. V., "Irradiation Effects on Thermoelectric Materials." Presented at ARS Space Power Systems Conference, Santa Monica, Calif., Sept. 27–30, 1960. 5 p. Illus. (1276–60)

The prime subject of a research and development program on a thermoelectric nuclear fuel element was $Li_xNi_{1-x}O$. In-pile measurements of the Seebeck coefficient and electrical resistivity were made at reactor ambient temperatures and elevated temperatures. In addition, pre-postirradiation measurements of the Seeback coefficient, electrical resistivity, and thermal conductivity were performed. The following compositions were tested: 1. $Li_{.013}Ni_{.987}O$, 2. $Li_{.05}Ni_{.95}O$.

Post-irradiation measurements on $Li_{.013}Ni_{.987}O$ samples after exposure to a total integrated thermal neutron flux of 1.4×10^{19} revealed that the electrical resistivity had returned to the pre-irradiation value; the Seebeck coefficient had increased slightly; and the thermal conductivity had remained essentially unchanged. In-pile measurements of the Seebeck coefficient and electrical resistivity of $Li_{.05}Ni_{.95}O$ at 464 C and up to 8×10^{18} nvt (thermal) did not show much variation from out-of-pile values.

* * *

Gardner, Edward E. and Woisard, Edwin L., "Thermoelectric Materials for Space Cooling." Presented at ARS Space Power Systems Conference, Santa Monica, Calif., Sept. 27–30, 1960. 7 p. Illus. (1280–60)

Thermoelectric devices are particularly suited to space applications. Since these are electronic devices there is no mechanical motion involved, no moving parts. Immediately this implies long life and dependability with minimum upkeep. Of equal importance, this also means there are no vibrations or gyroscopic moments to interfere with guidance or stabilizing systems. The demands which space applications make on thermoelectric materials will be discussed as well as the problems inherent in the materials themselves. In particular, the properties of n-type and p-type thermoelectric elements belonging to the bismuth telluride class of compounds will be examined in terms of the various thermoelectric parameters. Other promising thermoelectric materials will also be presented. Conclusions will be drawn as to the degree to which materials available today meet the demand of space applications and, finally, the outlook for improved materials in the future will be discussed.

* * *

Greenfield, H. H., "Optimized SNAP III Power Generator Design for Spacecraft." Presented at ARS Space Power Systems Conference, Santa Monica, Calif., Sept. 27–30, 1960. 18 p. Illus. (1278–60)

Design performance studies on the original SNAP III type of thermoelectric generator were made to optimize its use as a power system for special spacecraft missions. From laboratory and analytical studies on the generator's performance and thermal energy rejection characteristics in a space environment, it was determined that the initial available electrical power can be increased by as much as a factor of four. The electrical power is increased by increasing the thermal input of the generator at the expense of conversion efficiency. The modification to the SNAP generator consists of increasing the diameter of the thermoelectric elements and decreasing their length as well as modifying the fuel container and hot shoes to physically accommodate the thermoelectric element. However, the over-all physical characteristics of the SNAP III generator—dimensions, number and type of thermoelectric elements, method of hot and cold junction contacting, hot and cold junction temperature limits, radial arrangement, number of thermoelectric element rows, and thermal insulation—remain unchanged in the modified design.

* * *

Mayer, S. E. and Ritchie, I. M. "The Use of High Temperature Thermoelectric Materials (Silicides) for Power Generation in Space." Presented at ARS Space Power Systems Conference, Santa Monica, Calif., Sept. 27–30, 1960. 4 p. Illus. (1279–60)

This paper discusses the possible use of some developmental high temperature thermoelectric materials—the silicides—for space applications. Calculations of efficiency and power-weight ratio are carried out for present typical materials and materials which might reasonably be expected to result from present work. It is shown that even though these materials leave a lot to be desired in terms of efficiency, the power-weight ratios are more favorable than other materials industrially

available for cases in which the rejected heat can only be lost by radiation. For a given efficiency and Seebeck coefficient for materials having the same efficiency it is shown that the particular combination of parameters in these materials viz low electrical resistivity and high thermal conductivity is the most desirable.

* * *

Vickery, R. C., Muir, H. M., and Kleber, E. V., "Thermoelectric Properties of some Rare Earth Systems." Presented at ARS Space Power Systems Conference, Santa Monica, Calif., Sept. 27–30, 1960. 4 p. Illus. (1275–60).

Compositions of gadolinium with other metals and metalloids have been examined for value as high temperature thermoelectric materials. In systems containing bismuth, antimony, silicon, boron, phosphorus, iron, nickel, cobalt and manganese, Seebeck emf's and resistivities are generally low (20–30 uv/C and 200–400 u-cm respectively). The gadolimium-selenium system presents however, intermetallic compounds with Seebeck outputs up to 600 uv/C and resistivities ranging from 0.2 to 1000 $\times$ 10^{-3}-cm. Specific considerations are made of the potential of this system.

* * *

VI—Vapor, Hot Air, and Fluid Heat Engines

Bullock, Robert O., "Vapor Turbine for Space Power." Presented at ARS Space Power Systems Conference, Santa Monica, Calif., Sept. 27–30, 1960. 20 p. Illus. (1327–60)

Vapor turbines for space power will require the use of unfamiliar fluids in unfamiliar conditions. In order to achieve long life, reliability, and efficiency, attention must be given to problems that previously were either nonexistent or could be economically ignored. Several prominent problems are raised; the background information about them is reviewed, and the research and development required to solve them is outlined.

* * *

Parker, M. D. and Smith, C. L., "Stirling Engine Development for Space Power." Presented at ARS Space Power Systems Conference, Santa Monica, Calif., Sept. 27–30, 1960. 34 p. Illus. (1315–60)

The basic Stirling cycle is reviewed with respect to its advantages and limitations for space power applications. An engine design for space power is discussed with particular emphasis on problems associated with the space environment. Conditions for exact balance of dynamic forces are examined. Design and development approach to the lubrication and sealing problems in a zero gravity environment for long periods of unattended operation is outlined. Finally, a Stirling cycle engine, designed and constructed by the Allison Division of General Motors Corporation, is discussed.

* * *

VII—Solar Furnaces

Hiester, Nevin K. and De La Rue, R. E., "The Image Furnace as a Research Tool." Reprinted from *ARS Journal*, Oct. 1960, 928–938 p. Illus.

The purpose of this paper is to provide a guide to the literature covering some of the important theoretical and practical aspects of image furnaces and their operation. In addition, some of the research areas where these devices have been used will be briefly described in the hope that it may trigger ideas for other ways in which they can be used to solve research problems.

Kevane, Clement J., "Report on the Measurement of Thermal Diffusivity Using a Solar Furnace." Office of Naval Research Contract No. NR-032-419, June 1958.

In order to develop a method for measurement of thermal diffusivity of materials, the propagation of temperature waves set up by periodic modulation of the heat flux in a solar furnace was studied at moderate temperatures. The experimental results were compared with an analysis of one-dimensional heat flow under periodic excitation to determine thermal diffusivity.

Because of small temperature oscillation amplitudes and rather large temperature fluctuations at the focal spot, work was limited to temperatures less than 1000 C. The results are only in rough order of magnitude agreement with known thermal diffusivities because of the temperature fluctuation noise and undetermined systematic errors.

* * *

VIII—Thermionic

Oman, Henry and Street, George, Jr., "Experimental Solar Thermionic Converter for Space Use." AIEE Pacific General Meeting, San Diego, Calif., August 8–12, 1960. Conference Paper, May 10, 1960. 8 p. Illus. (60–1040).

1. A high-pressure cesium-vapor type thermionic converter heated by sunshine concentrated by a lightweight mirror appears to be a promising power source for space vehicles.
2. A procedure for designing solar-thermionic space-vehicle power sources has been developed.
3. Tests of a 15 watt solar heated thermionic converter should establish valid design criteria for these converters.

* * *

IX—Photochemical Processes: Biological, Botanical and Inorganic

Hardwick, R., "Kinetic Studies of the Thionine-Iron System II," Dept. of Chemistry, Univ. of California, Los Angeles, Calif., 5 p. Illus.

The observed inhibitory effect of ferric ions on the bleaching of aqueous thionine-ferrous ion solutions has been formerly attributed to direct quenching of excited thionine. The results of the present experiments, reinforced by recent data of other authors, are used in an interpretation of the reaction mechanism which assigns a chemical, not quenching, role to ferric ions.

* * *

X—Photoelectric: Photovoltaic, Photogalvanic, Piezoelectric

Dale, B., and Rudenberg, H. G., "Photovoltaic Conversion-High Efficiency Silicon Solar Cells." Transitron Electronic Corporation, Reprinted from 14th Annual *Proceedings*, Power Sources Conference, May 17–19, 1960. 4 p. Illus.

The improvements made in high efficiency silicon solar cells under a research study have been described. They have raised the over-all conversion efficiency of the units from 10% to 15%, by careful design of the cell structure. The work has raised the output voltage of the cell, substantially lowered the series resistance, and has provided various surfaces with differing optical characteristics. A new tetrahedral surface structure, as well as clear silicon surfaces and adjustable optical coatings have been shown. The improved cells are capable of use with light concentrators to increase the output per cell and lower costs by factors of 5 to 10 times. Thus a

VOL. 5 1961

five cell array capable of 1 watt output in bright sunlight is now possible. Radiation studies show that the decrease of efficiency can be predicted from laboratory measurements of lifetime.

* * *

Escoffery, C. A. and Luft, Werner, "Silicon Photovoltaic Cells and the Utilization of Solar Energy." International Rectifier Corp., June, 1960. 16 p. Illus.

Silicon photovoltaic cells are being widely used in numerous applications, both celestial and terrestrial, for the direct conversion of solar radiation into electric power. The possibility of relieving the world energy problem by the photovoltaic process is discussed. Present day silicon solar cells have conversion efficiencies of 12 per cent or more, and the preparation, operating principles, and characteristics of silicon solar cells are presented. The control of cell temperature in space vehicles is discussed in terms of the absorptance and emittance of radiation by the silicon cell surface, and measured values of these parameters are shown for uncovered cells and for cells provided with glass or with silicon oxide films.

* * *

Gordon, G. D., "Measurement of Ratio of Absorptivity of Sunlight to Thermal Emissivity." *The Review of Scientific Instruments,* **31** (11): 1204–1207, Nov. 1960. Illus.

Direct measurements of the ratio of the surface absorptivity of sunlight to the thermal emissivity have been made, and the apparatus is described. A thin plate to be measured is suspended in a vacuum, surrounded by walls cooled by liquid nitrogen, and illuminated by an arc light, which simulates solar radiation. The desired ratio is determined from the equilibrium temperature, which ranged from 0 to 250 C for the samples measured. Possible errors in the procedure have been analyzed theoretically, and corrections introduced where necessary. Intensity fluctuations in the present light source have limited the accuracy to 10%, but this is not a fundamental limitation in the method. Values of the thermal emissivity are also obtained from the rate of change of sample temperature.

* * *

Kracher, Richard W., "Advent." Presented at ARS Space Power Systems Conference, Santa Monica, Calif., Sept. 27–30, 1960. 3 p. Illus. (1343–60)

The vehicle will be positioned so that its antenna will be continually oriented toward the earth by means of the attitude control system. The electrical power for the vehicle will be drawn from the sun and converted to electricity by silicon photovoltaic cells. The tens of thousands of cells required will be distributed over one side of two paddles deployed on each side of the vehicle.

* * *

Spitzer, C. F., "Solar Cell Measurement Standardization." Lockheed Aircraft Corp., Missiles & Space Div., Sunnyvale, Calif. LMSD-288184, Feb. 29, 1960. 84 p. Illus.

This report on solar cell standards and measurements covers the preparation of standard solar cells, methods for measuring the direct solar radiation intensity, the latitude of the observing location, and atmospheric conditions necessary to accurate measurement. Calibration and maintenance of standard solar cells are also included. Laboratory light source and instrumentation of cell measurements are discussed. Definitions of the various terminologies and a literature survey for 1949 to the present is included for the convenience of the reader.

Grace, W. R., "Investigation of Thin Sheets of High-Quality, Single-Crystal Silicon." U. S. Army Signal Research & Development Laboratory, Report No. 3, ARPA Order No. 80–59, Sept. 10, 1960. 31 p. Illus.

The purpose of this contract is to investigate and determine the feasibility of a concept advanced by Dr. W. Shockley of floating a thin layer or film of molten silicon upon a liquid metal surface, preferably lead, and pulling the silicon horizontally through a temperature gradient to obtain a single crystal in the form of thin sheet. The objective is to develop a method for the continuous production of thin sheets of high-quality, single-crystal silicon of less than 1 mm thickness and of appreciably greater dimensions than currently available.

* * *

Wysocki, Joseph J., and Rappaport, Paul, "Effect of Temperature on Photovoltaic Solar Energy Conversion," *Journal of Applied Physics,* **31** (3): 571–578, March 1960. Illus.

Photovoltaic solar energy conversion is investigated theoretically over a temperature range of 0–400 C using semiconductor materials with band gaps varying from 0.7 to 2.4 ev. Three cases are considered. In Case I, the junction current is the ideal current. In Case II, the junction current is the ideal plus a recombination current; and in Case III, a recombination current. The best conversion performance is obtained for the ideal current; the worst, for the recombination current. The maximum conversion efficiency occurs in materials with higher band gap as the temperature is increased. GaAs is close to the optimum material for temperatures below 200 C. Experimental measurements are presented on Si, GaAs, and CdS cells. The measurements on Si and GaAs agree with theoretical expectations as far as the gross behavior is concerned. The CdS cell behaves anomalously as if it were made from a material with band gap of 1.1 ev.

* * *

XI—Radiation Mechanics: Insolation, Spectroscopy, Spectral Distribution

Fritz, Sigmund, "Solar Radiation Measurements in the Arctic Ocean." *Geophysical Research Paper No. 63,* Scientific Studies at Fletcher's Ice Island, T-3, 1952–1955, **II:** 6–10, Dec. 1959. Illus.

For several years the U. S. Air Force Cambridge Research Center has made various measurements on ice islands in the Arctic Ocean. Among the measurements was the amount of solar energy received on a horizontal surface from sun and sky, and this report summarizes the data taken on Fletcher's Ice Island, T-3, during the year 1953. During the period March through October, the solar energy is measurable. In 1953 at that time T-3 was located near 86°N and 90°W, which is in the Arctic Ocean north of Hudson Bay, Canada.

* * *

Stearns, Forest W., and Carlson, Charles A., "Correlations between Soil-Moisture Depletion, Solar Radiation, and other Environmental Factors," *Journal of Geophysical Research, 65* (11): 3727–3732, Nov. 1960.

To extend the usefulness of a soil-moisture prediction method, solar radiation, temperature, and other environmental factors were studied in relation to moisture loss in the surface 12 inches of soil. Data were obtained in an upland meadow on loessial soil near Vicksburg, Mississippi. Comparisons were made only for drying periods, and only when soil moisture was in the wetter half of its range.

Highest correlations of single factors with moisture loss were obtained with soil temperature and evaporation-pan data

(r = 0.79 each), and with solar radiation (r = 0.76). Values for air temperature, vapor pressure deficit, humidity, and wind were progressively lower. Correlations with soil temperature or evaporation-pan data were somewhat improved by the addition of other factors in combination. Highest correlation was obtained with a site-derived depletion curve (r = 0.85) from the previous year.

* * *

XIII—Accessories: Batteries, Tracking, and Control Systems

Jordan, Richard C., "Solar Energy Storage Practical Application," *American Artisan*, Oct. 1960, 53–56 Illus.

Stones, water, concrete or change-of-phase materials supply stored heat when solar radiation is below requirements. Since solar energy source is highly variable, it is manditory that any solar space heating be designed with either an energy storage system, auxiliary heat, or both.

* * *

XIV—Geophysical and Meteorolgical: Weather, Climate, Sundials, Telescopes, Magnetism, and Gravity

Hubert, L. F., Fritz, S., and Wexler, H., "Pictures of the Earth from High Altitudes and their Meteorological Significance." U. S. Weather Bureau, Washington, D. C. 10 p. 1960. Illus.

Rocket pictures provide an excellent preview of an important new source of meteorological data that will soon be available from satellites equipped with television cameras. A mosaic picture, resulting from a moving picture of the Atlas flight of August 24, 1959, is presented. It illustrated the meteorological potential of cloud pictures taken simultaneously over millions of square miles.

While a television picture will not have the same resolution as the Atlas film, it will show significant cloud patterns. This is illustrated with the aid of two versions of a rocket photograph mosaic taken over Texas in October 1954. The original version of the mosaic shows macro- and meso-scale meteorological phenomena including an upper vortex; the second version has been scanned with 250 lines to simulate satellite television pictures. Despite the low resolution of the simulated picture, significant features are still visible.

* * *

Fritz, Sigmund, "Absorption and Scattering of Solar Energy in Clouds of Large Water Drops." U. S. Weather Bureau, *Journal of Meteorology*, Feb. 1958, **15:** 51–58. Illus.

A brief description of the basic method used to compute the absorption of solar energy in clouds is given. The numerical results of computations are presented. These include: 1. the absorption in thick clouds as a function of wavelength; 2 the total absorption in thick clouds as a function of certain cloud parameters; and 3. the absorption as a function of thickness for a particular cloud. The effect of the water vapor above the cloud on absorption in the cloud is discussed; the influence of the sun's zenith distance is indicated. For some cases, the albedo of the clouds is also given.

* * *

Fritz, Sigmund, "On Observing the Atmosphere from Satellites," *Weatherwide*, U. S. Weather Bureau, Washington, D. C. **12** (4): 139–165. Aug. 1959. Illus.

The observation of clouds involves at least three types of information. First we can measure cloud amount; secondly we will often be able to determine cloud type; and third, we can observe cloud patterns such as vortices, cloud "streets," frontal cloud fields, etc. Features such as vertical shear can sometimes also be determined.

* * *

Fritz, Sigmund, "Radiational Inversions and Surface Temperature Changes," *Monthly Weather Review*, U. S. Weather Bureau, Washington, D. C., April 1958, 129–132. Illus.

When air stagnates in dark polar regions, an inversion forms. The change of the inversion magnitude is studied under the assumption that the snow surface radiates about as much energy as it receives from the atmosphere. It turns out that the inversion magnitude may either decrease or increase as the surface temperature falls, depending on the rate of change of atmospheric "emissivity" with air temperature.

* * *

Maxwell, A., Howard, W. E. III, and Garmire, G., "Some Statistics of Solar Radio Bursts at Sunspot Maximum" *Journal of Geophysical Research*, **65** (11): 3581–3588, Nov. 1960. Illus.

This paper discusses the occurrence and intensity of solar radio bursts at four frequencies in the band 100 to 600 Mc/s. The observations cover 4010 hours during a 12 month period at sunspot maximum; the results refer essentially to bursts of intensity greater than 10^{m} mks unit and duration greater than 0.3 second; and the statistical information has been interpreted in terms of the spectral characteristics of the bursts. The experimental data were taken at Fort Davis, Texas, and the analysis shows that at 125 Mc/s burst radiation was recorded for 560 hours, of which 380 hours were of low intensity. At 200 Mc/s the burst radiation covered 350 hours, of which 240 hours were of low intensity. For these two frequencies the bursts occurred mainly in the form of noise storms (spectral type I). At 425 and 550 Mc/s the total times of the solar bursts were much less, being respectively 21 and 23 hours; for the most part, however, this radiation was of high intensity and appeared in the form of continuum radiation (spectral type IV) over a wide frequency range.

* * *

Wexler, Harry, and Fritz, Sigmund, "Tiros Reveals Cloud Formations," *Science*, **131** (3415): 1708–1710, June 10, 1960. Illus.

Tiros 1, the experimental weather satellite, in the first month of its operation, orbited the earth about 450 times and took about 9000 pictures of various cloud formations. The pictures have revealed a large degree of organization in cloud systems over much of the earth's surface.

VOL.
5
1961

L.
61